New catalysts for miniaturized methanol fuel cells

Pedersen, Christoffer Mølleskov; Chorkendorff, Ib; Stephens, Ifan

Publication date:
2016

Document Version
Publisher's PDF, also known as Version of record

Citation (APA):
Pedersen, C. M., Chorkendorff, I., & Stephens, I. (2016). New catalysts for miniaturized methanol fuel cells. Department of Physics, Technical University of Denmark.

Center for Individual Nanoparticle Functionality

DTU

DANISH
TECHNOLOGICAL
INSTITUTE

New catalysts for miniaturized methanol fuel cells

Ph.D. Thesis by

Christoffer Mølleskov Pedersen

Supervisor: Professor Ib Chorkendorff
Co-supervisor: Associate Professor Ifan E. L. Stephens

December 2015

Center for Individual Nanoparticle Functionality
Department of Physics
Technical University of Denmark

Preface

This Ph.D. thesis was submitted as part of the requirements for a Ph.D. degree under the Industrial Ph.D. Programme under The Danish Council for Technology and Innovation (DCTI). The Ph.D. project was carried out as collaboration between Center for Individual Nanoparticle Functionalities (CINF) at the Technical University of Denmark (DTU), Department of Physics and the Danish Technological Institute (DTI). The project was funded by DCTI and DTI. I would like to thank my supervisors Professor Ib Chorkendorff (CINF), Associate Professor Ifan E. L. Stephens (CINF) and Leif H. Christensen (DTI) for this opportunity and for all their help and support during this project.

The work has been performed both at CINF and DTI, and I have been very grateful to my colleagues at both places. In particular, I would like to thank Brian P. Knudsen, Amado Velázquez-Palenzuela, Maria Escudero-Escribano, Paolo Malacrida and Arnau Verdaguer-Casadevall from CINF, and Christian Kallesøe, Henrik F. Clausen, Patricia Hernández-Fernández, Erik Wisaeus, Solveig R. Madsen, Oscar Tynelius, Torsten Lund-Olesen, Jan H. Hales and Elisa A. Paoli from DTI.

Furthermore, part of the work took place at the Center for Materials Crystallography (CMC), at Department of Chemistry, Aarhus University. I would like to thank Jakob Becker for agreeing to let me try my experiments on their equipment and Muhamed Aref Hasen Mamakhel for his help in conducting my experiments.

Finally, I would like to thank my family for their support and understanding during this project and especially my sister Sabine Mølleskov Pedersen who has helped me proofreading the thesis.

Kgs. Lyngby, 31th December 2015
Christoffer Mølleskov Pedersen

Abstract

The methanol fuel cell is an interesting energy technology, capable of converting the chemical energy of methanol directly into electricity. The technology is specifically attractive for small mobile applications such as laptops, smartphones, tablets etc. since it offers almost instantaneously recharging by simply replacing the methanol liquid. The technology is currently being developed for hearing instruments in order to ease the handling of the device for users complaining about difficulties replacing the very small batteries in the hearing instrument. The technology has already been demonstrated by the Danish Technological Institute; however, for the technology to become more widely adapted, the power density of the fuel cell must be increased.

It is well known that a considerable part of the energy from the methanol is lost in the fuel cell during the conversion due to poor kinetics. The kinetics can however be improved by using a superior catalyst. Therefore, the aim of this thesis is to identify new catalyst material for methanol fuel cells. By analysing the performance of the standard catalysts (PtRu and Pt) currently being applied in methanol fuel cells as anode and cathode respectively, a benchmark is defined. This benchmark is used to compare catalysts for the different reactions taking place in a fuel cell such as hydrogen oxidation, methanol oxidation and oxygen reduction. In addition, different phenomena in the fuel cell such as CO poisoning of the hydrogen oxidation and methanol poisoning of the oxygen reduction are studied. Consequently, promising new candidates for replacing the standard catalyst are identified. One of these, Pt_5Gd, exhibits improved oxygen reduction reaction activity even in the presence of methanol, thus making Pt_5Gd an interesting candidate to replace the Pt catalyst in the methanol fuel cell cathode.

Having identified a potential new catalyst material, a fabrication method is needed. Because the catalytic properties of the catalyst material is inherent in the surface of the catalyst, the surface to volume ratio for the material must be

as high as possible, which usually can only be achieved by making the material as nanoparticles. However, the problem of Pt_5Gd and other Pt alloys with lanthanides or early transition metals is that these materials are very difficult to synthesise chemically, especially in the more technological relevant nanoparticulate form. Therefore, a second objective of this thesis has been to investigate different synthesis routes. The thesis is able to demonstrate for the first time, chemical synthesised carbon supported metallic Pt_xGd, Pt_xY and Pt_xTb alloy nanoparticles. The synthesised nanoparticles are more active than Pt nanoparticles, but not as active as expected for these materials. Thus, the synthesis route is promising but needs further optimisation.

Dansk Resumé

Metanol brændselscellen er en interessant energiteknologi, der kan konvertere den kemiske energi fra metanol direkte til elektricitet. Teknologien kan især finde anvendelse inden for mindre mobile enheder, såsom bærbare computere, smartphones, tablets osv., da teknologien kan tilbyde næsten øjeblikkelig genopladning af disse enheder ved blot at udskifte metanolvæsken. Teknologien bliver i øjeblikket udviklet til anvendelse i høreapparater for at gøre brugen af disse lettere for de mange brugere, der har problemer med at udskifte de meget små batterier i hørerapparaterne. Teknologien er allerede blevet demonstreret af Teknologisk Institut, men for at teknologien kan blive mere udbredt, er det nødvendigt at forøge den elektriske effekt per volumen.

Det er velkendt, at en stor del af energien fra metanolen går tabt i energikonverteringen på grund af dårlig reaktionskinetik, der imidlertid kan forbedres ved at bruge bedre katalysatorer. Formålet med denne afhandling er derfor at forsøge at finde og fremstille nye katalysatorer til metanol-brændselsceller. Afhandlingen analyserer indledningsvis, hvordan metanol-brændselscellen til hørerapparater præsterer, og hvilke energitab den har. Denne analyse bliver efterfølgende brugt til at finde et sammenligningsgrundlag for brændselscelle reaktioner så som brint oxidation og metanol oxidation på anoden, plus ilt reduktion på katoden. Sammenligningsgrundlaget er basseret på aktiviteterne for katalysatorerne Pt og PtRu, som er standard katalysator til henholdsvis katoden og anoden, i disse reaktioner. Derudover bliver fænomener, så som CO forgiftning af brint oxidation og metanol forgiftning af ilt reduktion studeret. Dette grundlag bliver brugt til at lede efter lovende alternative til Pt og PtRu katalysatorer. En af disse er Pt_5Gd, som havde en højere aktivitet for ilt reduktion reaktionen sammenlignet med Pt både med og uden metanol tilstede. Dette betyder, at Pt5Gd er en lovende materiale til at erstatte Pt som katode katalysatoren i metanol-brændselsceller.

De katalytiske egenskaber af en katalysator sidder i overfladen og der er derfor nødvendigt at fremstille katalysatoren i en form med så høj overflade til volumen ratio som muligt, hvilket i de fleste tilfælde betyder at materialet skal fremstilles som nanopartikler. Pt_5Gd er et lovende materiale, men for at bruge det i en brændselscelle er det nødvendigt at finde en fabrikations metode til at lave legeringen som nanopartikler. Dette er særdeles vanskeligt både for Pt_5Gd og andre interessante Pt legeringer med lanthanider eller tidlige overgangsmetaller, og især at fremstille legeringerne som nanopartikler ved hjælp af kemisk syntese. En stor del af denne afhandling undersøger derfor, de mulige syntese metoder for at fremstille disse legeringer. Kemisk fremstillede metalliske Pt_xGd, Pt_xY og Pt_xTb nanopartikler supporteret på karbon, bliver demonstreret for første gang. De syntetiserede nanopartikler var mere aktive end Pt for ilt reduktion, men ikke så aktive som forventet for disse materialer. Dette viser at syntese metoden er lovende, men kræver yderligere optimering.

List of publications

Paper 1

Benchmarking Pt-based electrocatalysts for low temperature fuel cell reactions with the rotating disk electrode: oxygen reduction and hydrogen oxidation in the presence of CO (review article)
Christoffer M. Pedersen, María Escudero-Escribano, Amado Velázquez-Palenzuela, Leif H. Christensen, Ib Chorkendorff, Ifan E.L. Stephens
Electrochimica Acta **179** (2015) doi: 10.1016/j.electacta.2015.03.176
Paper included in Appendix B.

Paper 2

Probing the nanoscale structure of the catalytically active overlayer on Pt alloys with rare earths
Anders F. Pedersen, Elisabeth T. Ulrikkeholma, María Escudero-Escribanoa, Tobias P. Johansson, Paolo Malacrida, Christoffer M. Pedersen, Martin H. Hansen, Kim D. Jensen, Jan Rossmeisl, Daniel Friebel, Anders Nilsson, Ib Chorkendorff, Ifan E. L. Stephens
Submitted 2015, abstract included in Appendix C.

Paper 3

Relating direct methanol fuel cell performance to measurements in a liquid half cell
Christoffer M. Pedersen, Elisa. A Paoli , Oskar Tynelius, Torsten Lund-Olesen,

Jan H. Hales, Leif H. Christensen, Ifan E. L. Stephens, Ib Chorkendorff
In preparation, abstract included in Appendix D.

List of Abbriviations and Symbols

Abbreviations

Pt_5Ln	Pt alloy with a lanthanide
Pt_xM	Pt alloy with M metal, where M is either a lanthanide, early transition metal or alkali earth
µ-DMFC	Miniaturised DMFC by DTI
AR-XPS	Angle Resolved X-ray Photoelectron Spectroscopy
BF	Bright Field
CE	Counter electrode
CINF	Center for Individual Nanoparticle Functionalities
COR	CO Oxidation Reaction
DMFC	Direct Methanol Fuel Cell
DTI	Danish Technological Institute
ECSA	Electrochemical surface area
EDX	Energy Dispersive X-rays
EDX	Energy-Dispersive X-ray
FWHM	Full width at half maximum
GDL	Gas Diffusion Layer

HAADF	High Angle Annular Dark Field
HER	Hydrogen Evolution Reaction
HOR	Hydrogen Oxidation Reaction
M	M is either an early transition metal, lanthanide or alkali metal
MEA	Membrane Electrode Assembly
MOR	Methanol Oxidation Reaction
MPL	Micro Porous Layer
OCV	Open Circuit Voltage
ORR	Oxygen Reduction Reaction
PDF	Pair Distribution Function
PEMFC	Proton Exchange Membrane Fuel Cell
PVP	Polyvinylpyrrolidone
PXRD	Powder x-ray diffraction
RDE	Rotating Disk Electrode
Ref	Reference electrode
RHE	Reversible Hydrogen Electrode
RRDE	Rotating ring disk electrode
SAXS	Small Angle X-ray Scattering
SCF	Supercritical Fluid
SEM	Scanning Electron Microscopy
SGEIS	Staircase Galvanostatic Electrochemical Impedance Spectroscopy
STEM	Scanning Transmission Electron Microscopy
TEM	Transmission Electron Microscopy
TEM	Transmission Electron Microscopy
TKK	Tanaka Kikinzoku Kogyo
UHV	Ultra High Vacuum
WE	Working electrode

XPS	X-ray Photoelectron Spectroscopy
XRD	X-ray Diffraction
YCp3	Cyclopentadienyl Yttrium(III)

Symbols

α_{A}	Anodic transfer coefficient
α_{c}	Cathodic transfer coefficient
β_{obs}	Observed broadening for sample
β_{size}	FWHM broadening from crystallite size
β_{std}	Instrumental broadening
β_{strain}	Broadening from microstrain
β_{tot}	Total broadening
δ	Distance between lattice planes
ΔG	Change in Gibbs free energy
$\Delta G(T)$	Temperature dependant change in Gibbs free energy for the reaction
ΔG_{r}	The change in Gibbs free energy for the reaction
$\Delta G_{\mathrm{H_2O}}$	Change in Gibbs free energy to form water from its elements
$\Delta G_{\mathrm{M_2O_3}}$	Change in Gibbs free energy to form $\mathrm{M_2O_3}$ from its elements
$\Delta G_{\mathrm{Pt_xM}}$	Change in Gibbs free energy to form $\mathrm{Pt_xM}$ from its elements
ϵ	Microstrain
η_{anode}	Overpotential of anode
η_{cathode}	Overpotential of cathode
η_{Conc}	Overpotential due to concentration limitations of reactants
η_{Methanol}	Overpotential from methanol crossover
η_{MOR}	Overpotential due to MOR kinetics
$\eta_{\mathrm{transport}}$	Overpotential from transport losses
Γ	Shape parameter
γ	Reaction order

λ	Wavelength of the radiation
ν	Viscosity
$\nu_{\mathrm{X-ray}}$	Frequency of x-ray
ϕ	Work function
ρ	Resistivity
θ	Bragg angle
A_k	Absorption correction
B	Constant
C	Constant
c_0	Solubility of gas in electrolyte
C_{DL}	Double layer capacitance
C_P	Specific heat capacity
d	Thickness
$E_{\mathrm{a}}^{\mathrm{rev}}$	Activation energy at zero overpotential
E_{F}	Energy of fermi level
E_{kin}	Kinetic energy
E_{vac}	Energy of vacuum level
E_b	Binding energy
E_k	Extinction correction
F	Faradays constant
f_j	Scattering factor
F_k	Structure factor
$G_{\mathrm{Pt_xM}}$	Gibbs free energy for the alloy
G_{ik}^{p}	Normalised profile function
h	Planck's constant
H_0	Standard enthalpy
H_k	FWHM of peak

I	Current
i	Integer
J	Current density
J_0^*	Reference exchange current density
$J_{\mathrm{Crossover}}$	Methanol crossover current density
J_{Kin}	Kinetic current density
J_{Lim}	Mass transport limited current density
K	Equilibrium Constant
K	Shape factor
L_k	Lorentz polarisation factor
m_{Pt}	Pt molar mass
M_k	Multiplicity
n	Integer
$n_{\mathrm{O_2}}$	Moles of oxygen
p	Phase
P_{HCl}	Partial pressure of HCl
$P_{\mathrm{O_2}}$	Partial pressure of O_2
$P_{\mathrm{O_2}}^*$	Partial pressure of O_2 under reference conditions
P_k	Factor related to preferred orientation
$P_{\mathrm{H_2O}}$	Partial pressure of water
$P_{\mathrm{H_2}}$	Partial pressure of H_2
Q	Flow rate
R	Gas constant
R_{Ohmic}	Ohmic resistance
$r_{20\%}$	Radius at 20% of the cumulative size distribution
$r_{50\%}$	Radius at 50% of the cumulative size distribution
$r_{80\%}$	Radius at 80% of the cumulative size distribution

rf	Roughness factor
S	Scale factor
$S_{\mathrm{M}}(25\ ^{\circ}\mathrm{C})$	Entropy of M at 25 °C
$S_{\mathrm{Pt}}(25\ ^{\circ}\mathrm{C})$	Entropy of Pt at 25 °C
T	Temperature
T^{*}	Temperature at reference conditions
T_{mix}	Mixing temperature
T_{reactor}	Temperature of reactor
U	Parameter to Caglioti broadening function
$U(J)$	Cell voltage as a function of current density
U°	Standard cell potential
$U^{\circ}(T)$	Thermodynamic cell potential at a given temperature
$U^{\circ}_{\mathrm{Anode}}$	Thermodynamic potential of methanol oxidation
$U_{\mathrm{Compensated}}$	Ohmic drop compensated potential
U_{Measured}	Measured potential
$U_{\mathrm{OCV,H_2}}$	Open circuit potential when electrolyte is saturated with H_2
U_{RHE}	Potential vs RHE
V	Parameter to Caglioti broadening function
$V(Q,t)$	Volume from a certain flow and a certain time
W	Parameter to Caglioti broadening function
w_{Pt}	Pt weight
y_{iB}	Intensity of the background at point i
y_{iC}	Net intensity at point i
z	Number of electrons transferred in the reaction
*	Free site on the metal

Contents

1

Introduction

Today's hearing instruments use disposable zinc-air batteries, which require replacement ranging from once a week to daily. The frequency of replacement depends on specific characteristics of the hearing aid, counting the size of the battery, the capacity of the device as well as its application. The usage of zinc-air batteries is undesirable as numerous hearing aid users face difficulties replacing their batteries [1]. At the same time, many users also prefer less visible hearing instruments, which require smaller batteries that in turn make exchanging the batteries even more difficult. Therefore, The Danish Technological Institute and partners have since 2010 tried to develop an alternative to the disposable batteries used in hearing instruments. The requirements for such a technology are:

- The cost must be the same as the total cost of using batteries for the entire life-time of the hearing aid.
- The alternative cannot take up more space inside the hearing aid than the combined space of battery and battery lid.
- The recharging procedure must be simple and also easy to perform for people with lower dexterity.
- The recharging time should be comparable to that of exchanging the batteries.

As a result Direct Methanol Fuel Cell (DMFC) was chosen as a suitable alternative as the refuelling can be performed in a simple and fast manner, where the liquid fuel is replaced using a docking station that contains a pump and fuel reservoir. This makes for a more simple recharging process where the actual hearing aid is placed in a docking station as opposed to separating the battery from the device for recharging. In addition the recharging can be performed as fast as the liquid can be replaced. The concept is shown in Figure 1.1. Since the start of its development in 2010 the size of the DMFC plus fuel tank has been miniaturised to the point where it now can fit inside the hearing aid and provide enough power for about 24 hours of operation for a medium sized hearing aid. However, to power larger and more powerful hearing instruments and the new smarter hearing instruments with wireless communication, DMFCs with a higher power density are required.

Figure 1.1: Hearing aid with build-in DMFC placed on a docking station that is replacing the fuel. Image courtesy of DTI.

This thesis aims at improving the miniaturised DMFC by DTI, which for the rest of the thesis will be referred to as µ-DMFC, by furthering the understanding of how they function and which losses are limiting the performance. Then this knowledge will be used to test new catalyst and finally synthesise new catalyst for the DMFC. Before analysing the µ-DMFC performance it is necessary to introduce some concepts. In the remaining part of this chapter a literature study is performed for fuel cells, catalysts and synthesis of catalysts, which is relevant for the other chapters of the thesis. First the general concepts of fuel cells and specifically proton exchange membrane fuel cells will be introduced followed by the specifics for the DMFC.

1.1 Fuel Cells

A fuel cell is a device that converts chemical energy directly into electricity and exhibits many similarities to batteries; both are comprised of an anode and cathode where oxidation and reduction takes place respectively, separated by a membrane or electrolyte. The fuel cell works by oxidising a fuel on the anode side of the device into ions and electrons, which are then passed to the cathode side of the device through a membrane and external circuit respectively. At the cathode a reduction takes place to balance the overall reaction. The main difference between batteries and fuel cells is that in the case of batteries, the anode and cathode participate in the reaction and is also the fuel. In a fuel cell, the anode and cathode does not react but only facilitates the reaction with the fuel. This is an important distinction; since increasing the capacity of a battery requires more cells or larger cells containing more anode/cathode material is needed. In comparison the size of the of the fuel cell depends on the maximum power required while increasing capacity can be accomplished by scaling the size of the fuel tank rather than the fuel cell itself [2, 3].

1.1.1 Proton Exchange Membrane Fuel Cells

Several types of fuel cell exist e.g.: Proton Exchange Membrane Fuel Cell (PEMFC), Direct Methanol Fuel Cell (DMFC), Phosphoric Acid Fuel Cell (PAFC), Alkaline Fuel Cell (AFC), Molten Carbonate Fuel Cell (MCFC), Solid Oxide Fuel Cell (SOFC) etc. [2]. The different fuel cell types have different advantages/disadvantages, but the only one of them that operates around room temperature is the DMFC [2], which is important as it is not possible to have the fuel cell running at elevated temperatures (>80°C) inside the hearing aid. Besides most of the alternative fuel cell technologies uses gases as fuel and it is not practical for a miniaturised fuel cell to have a pressure tank inside a hearing aid. The DMFC is a variant of the PEMFC since it uses the same membrane, but a different fuel i.e. methanol instead of H_2. Therefore the PEMFC will be explained first in general terms and the specifics of the DMFC will follow. The Proton Exchange Membrane Fuel Cell (PEMFC) is named after the type of membrane that is used in the fuel cell. The membranes are based on perfluorosulfonic acid ionomers, which is proton conducting if humidified. The conductivity increases with relative humidity and temperature. The relative humidity is most important for the conductivity and therefore normally only fully humidified gasses are used. The PEMFC run on H_2 and O_2 gasses, which are fed to the anode and cathode respectively. The PEMFC function by oxidising H_2 on the anode side into protons and electrons, which is also known as the hydrogen oxidation reaction (HOR):

$$\mathrm{H_2(g)} \longrightarrow 2\,\mathrm{H^+} + 2\,\mathrm{e^-} \tag{1.1}$$

The protons travels through the proton exchange membrane whereas the electrons go through an external circuit to the cathode where oxygen is reduced into water, which is also known as the oxygen reduction reaction (ORR):

$$\frac{1}{2}\mathrm{O_2(g)} + 2\,\mathrm{H^+} + 2\,\mathrm{e^-} \longrightarrow \mathrm{H_2O} \tag{1.2}$$

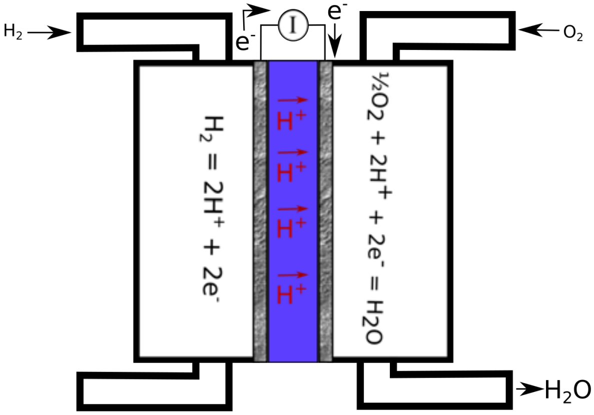

Figure 1.2: Illustration of how a PEMFC works. H_2 enter from the left and is oxidized to protons and electrons. The electron passes through an external circuit to the cathode and the protons go through the membrane. On the cathode O_2 is reduced to water.

The generated water then evaporates and is carried away in the O_2 gas stream. The reaction is also shown in Figure 1.2. The thermodynamic open circuit voltage (OCV) for galvanic cell, which is when no external current is running, is given as [4]:

$$U^\circ = -\frac{\Delta G(T)}{zF} \tag{1.3}$$

Where U° is the standard cell potential, $\Delta G(T)$ is the temperature dependant change in Gibbs free energy for the reaction, z is the number of electrons transferred in the reaction and F is Faradays constant. In case of the hydrogen fuel cell with the half-cell reactions (1) and (2), the standard cell potential at 25 ℃ is 1.23V. Drawing a current from the cell will decrease the cell voltage due to different losses. The cell voltage under operating conditions is [2]:

$$U(I) = U^\circ(T) - J\rho d - \eta_{\text{anode}}(J,T) - |\eta_{\text{cathode}}(J,T)| - \eta_{\text{transport}}(J,T)$$

Where $U(J)$ is the cell voltage for a given current density, $U^\circ(T)$ is the thermodynamic OCV cell potential for a given temperature, ρ is the resistivity of the membrane, d is the thickness of the membrane, η_{anode} and η_{cathode} is the overpotential for the anode and cathode reaction respectively for a given temperature and current, and $\eta_{\text{transport}}$ is the overpotential from transport losses. The overpotential for the cathode is due to slow kinetics of the oxygen reduction reaction. The overpotential depends on the catalyst used, loading of the catalyst, temperature and pressure, which makes it difficult to talk about a general overpotential for ORR. Neyerlin, Gasteiger et al found that the overpotential could be described under different experimental condition using the same equation and some fitted kinetic parameters [2,5]:

$$|\eta_{\mathrm{ORR}}| = \frac{2.303RT}{\alpha_c F} \log\left(\frac{J}{rfJ_0^*}\left(\frac{P_{\mathrm{O}_2}}{P_{\mathrm{O}_2}^*}\right)^{\gamma} \exp\left[\frac{-E_a^{rev}}{RT}\left(1-\frac{T}{T^*}\right)\right]\right) \tag{1.4}$$

Where R is the gas constant, T is the temperature, α_c is the cathodic transfer coefficient, J is the current density, rf is the roughness factor i.e. the ratio between catalyst surface area and electrode surface area, J_0^* is the catalyst exchange current density measured under reference conditions, P_{O_2} is the partial pressure of oxygen, $P_{\mathrm{O}_2}^*$ is the partial pressure of oxygen under reference conditions, γ is the reaction order, $E_\mathrm{a}^{\mathrm{rev}}$ is the activation energy at zero overpotential, T^* is temperature for reference conditions. The different losses in eq. 1.1.1 are plotted in Figure 1.3. The ORR overpotential was calculated using eq. 1.4 and assuming ambient conditions at 25 °C, a roughness factor of 400 (corresponding to 0.5 mg/cm^2 and 80 m2/g) and using the kinetic data for Pt/C reported in [2,5]. The potential losses from ohmic drop and transport resistance was adjusted to show similar overpotential as in [2]. The overpotential from anode kinetics was neglected since it was lower than 3 mV, even with very low Pt loadings of 0.05 mg/cm^2 [6], which is an order of magnitude lower than for the cathode. Figure 1.3 shows that the most significant loss in a H_2-PEMFC is the ORR kinetics. The ORR kinetics and catalyst will be discussed further in Section 1.3.3.

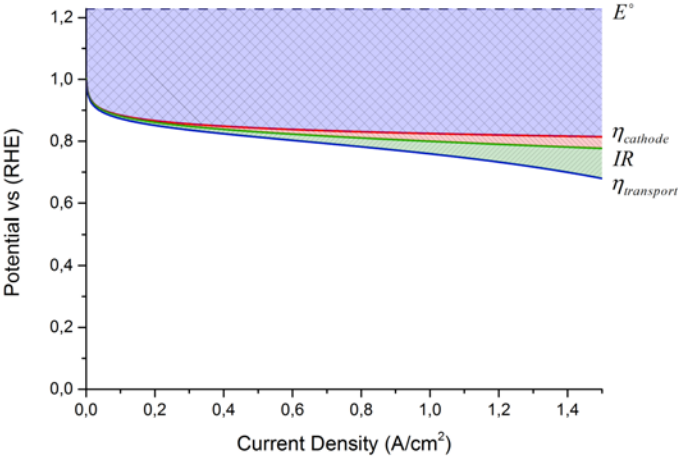

Figure 1.3: Losses in a H2 -PEMFC. The figure was adapted from fig 19 in [2], to show the losses at 25 °C and ambient pressure. The η_{ORR} was calculated using equation 1.4 applying the kinetic parameters from [2,5] calculated for ambient pressure and temperature assuming a roughness factor of 400. Ohmic and transport resistances were selected to achieve similar potential losses as in [2].

1.1.2 Direct Methanol Fuel Cells

The Direct Methanol Fuel Cell (DMFC) is a variant of the PEMFC where the DMFC instead of H_2 runs on a mixture of methanol and H_2O. The DMFC works by oxidizing the methanol into CO_2 on the anode side:

$$CH_3OH + H_2O \longrightarrow CO_2(g) + 6\,H^+ + 6\,e^- \tag{1.5}$$

Then, similarly to the PEMFC, the protons pass through the membrane and the electron through an external circuit to the cathode side. On the cathode side O2 is reduced to water, the exact reaction as for PEMFC seen in eq. 1.2.

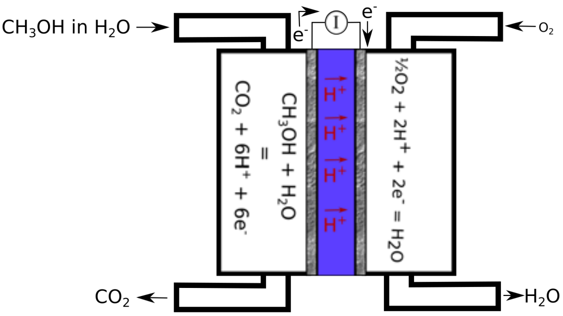

Figure 1.4: Illustration of how a DMFC functions. A methanol/water mixture is fed to the anode side, where the methanol and water reacts to form CO_2, protons and electrons. The CO_2 leaves through the exit stream. The protons go through the membrane and the electrons are collected in an external circuit. On the cathode side O_2 is reduced to H_2O.

The thermodynamic standard potential of the cell can also be calculated for a DMFC using equation 1.3 which is 1.21 V at 25 °C [7]. The performance of a DMFC can be calculated similar as for the PEMFC in Figure 1.3. The ORR kinetic losses are the same as in a PEMFC and can be calculated from equation 1.4 applying the kinetic data from [2,5], and assuming that the DMFC is running at 80 °C, with ambient air and 0.5 mg/cm^2 Pt catalyst loading, with an electrochemical surface area (ECSA) of 80 m2/g Pt. The anode kinetic losses from the methanol oxidation reaction (MOR) is approximated from the average Tafel curve from Figure 27 in [2] assuming 1 M methanol and a catalyst loading of 1 mg/cm^2 with an ECSA of 80 m2/g PtRu. The ohmic drop and methanol crossover is calculated assuming a Nafion 117 membrane that is 183 µm thick. The overpotential from methanol crossover was approximated using the work of Thomas et al. [8] and their equation:

$$|\eta_{\text{crossover}}| = \frac{2.303RT}{\alpha_c F} \log\left[\frac{1+J}{J_{\text{crossover}}}\right] \tag{1.6}$$

Where η_{Methanol} is the potential shift due to methanol crossover and $2.303RT/(\alpha_c F)$ is the Tafel slope, J is the cell current density and $J_{\text{Crossover}}$ is the methanol crossover current density which for Nafion 117 at 80 °C is about 0.12 A/cm^2 [8]. The ideal DMFC performance is plotted on Figure 1.5. Contrary to the H2 PEMFC the anode kinetic loss is quite significant for the DMFC and larger than the kinetic loss on the cathode. The methanol crossover is mainly causing losses at low current densities (<0.05 A/cm^2) and then becomes negligible at high current densities (0.5 A/cm^2). The ohmic losses are much higher than for the PEMFC in Figure 1.3 which is due the thicker membranes (183 µm) used in DMFCs compared to the H_2-PEMFC (25 µm). Thicker membranes are used to reduce the methanol crossover, but increase the ohmic losses. The ohmic losses are mainly a problem at high current densities, where in this case the ohmic loss is 8% at 0.5 A/cm^2. However at low current densities (0.05 A/cm^2) the ohmic loss is (<1%), which is less than the loss from methanol crossover (3%). Since the µ-DMFC for hearing instruments is designed to operate at the low current densities, the methanol crossover is a greater problem than the ohmic resistance.

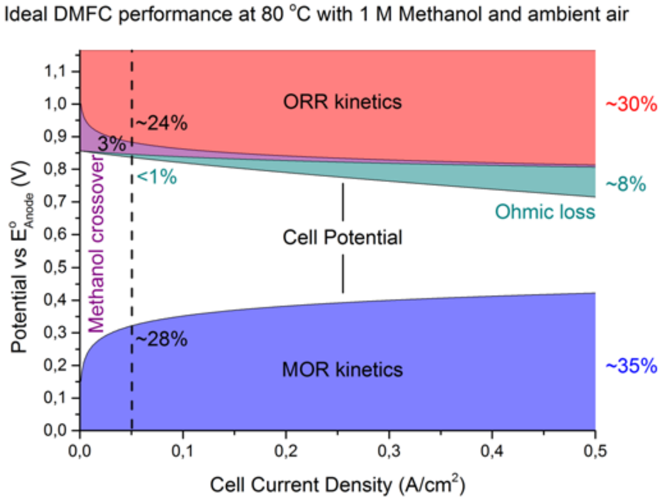

Figure 1.5: Shows the ideal DMFC performance adapted from Figure 28 in [2]. ORR kinetics (red) are based on kinetic data from [2,5] and calculated for 80 °C, ambient air and 0.5 mg/cm^2 catalyst loading with ECSA of 80 g/cm^2. MOR kinetics (red) are calculated using the average Tafel curve in Figure 27 from [2] assuming 1 M methanol and 1 mg/cm^2 catalyst loading with ECSA of 80 g/cm^2. The ohmic loss (dark cyan) is based on a Nafion 117 (183 µm thick) membrane. The methanol crossover (purple) is based on data [8] for the Nafion 117 membrane at 80 °C and 1 M methanol. The values are taken at 0.05 and 0.5 mA/cm^2 respectively.

The data used to calculate the losses shown in Figure 1.5 stems from an active DMFC, whereas the µ-DMFC is a passive DMFC. The difference between an active and passive DMFC is whether the fuel is supplied actively with pumps and where the DMFC is possibly heated and pressurised, or the fuel is supplied by diffusion.

The active DMFC is more efficient, but requires external components to function, whereas the passive DMFC only need the fuel cell and fuel tank. Because of the strict space limitations in a hearing aid it is only possible to use passive DMFC inside it. The passive DMFC have more losses due to mass transport limitations, which can be caused by limited diffusion of fuel, too much or too little water at the anode and cathode [9]. Therefore controlling the generation, diffusion and evaporating is quite impotent and is also referred to as water management.

1.2 µ-DMFC for hearing instruments

In the last section it was established how the PEMFC and DMFC work and their main potential losses in an ideal fuel cell. Having introduced the general concepts of the fuel cell, the current design of the µ-DMFC developed by DTI, can be presented.

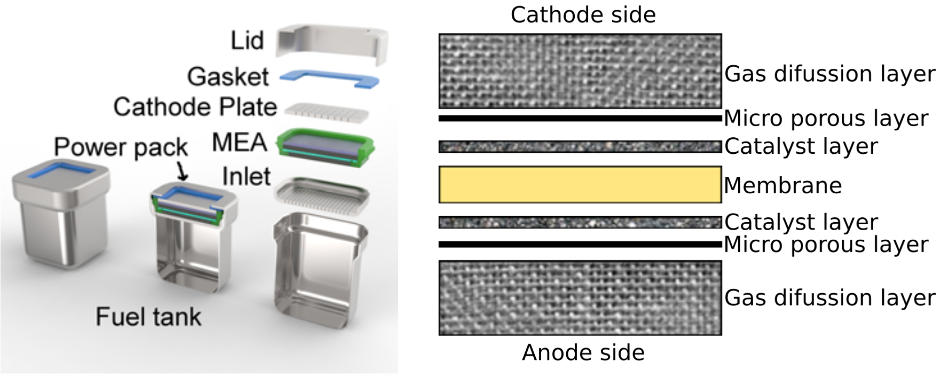

(a) µ-DMFC **(b)** MEA

Figure 1.6: design of the µ-DMFC a) and the MEA inside the µ-DMFC b).

The different parts of the µ-DMFC are seen on Figure 1.6a, which main components are a fuel tank and a DMFC power pack. The main layers in the DMFC power pack are part of the membrane electrode assembly (MEA) shown in Figure 1.6b. The MEA consist of a membrane separating two catalyst layer. The catalyst on the anode is carbon supported PtRu nanoparticles and on the catalyst on the cathode is carbon supported Pt nanoparticles. The size of the anode and cathode is 6.3x6.3 mm and 6.0x6.0 mm respectively. To achieve good electrical conductivity and reactant/product transport the catalyst layers are fabricated on a substrate consisting of a micro porous layer (MPL) which is on top of a gas diffusion layer (GDL). The GDL have larger pores than the MPL and the function of these layers are mainly to control the water management. Water is needed to keep the membrane fully humidified, which is required to sustain the high conductivity. Water is also part of the anode reaction and is required to completely oxidize the methanol and at the same time water is generated from the ORR on the cathode. Ideally water would be created on the cathode, pass through the membrane and used on the anode side. Unfortunately some of the water will also leave through the MPL and GDL in which case it must evaporate, otherwise droplets will form in the GDL blocking the gas transport of oxygen to the cathode. Another problem is methanol crossover, as stated in Section 1.1.2, which reduces the performance of the cathode and wastes fuel. The most effective way of reducing methanol crossover is by using lower concentrations on the anode side [2, 8]. However, this is not a possibility with the µ-DMFC, because of the small volume, which in turn requires concentrated methanol in the fuel tank to operate for 24h per charge. To reduce the problem of methanol crossover, methanol vapour feed [10] is used instead of a liquid feed to the anode. The vapour feed works by having a perforated film together with a membrane to separate the anode from the concentrated fuel, in this case by a Nafion 117 membrane. Only a tiny amount of methanol will permeate the membrane and will continue in vapour form to the anode. A cathode plate is placed on top of the MEA to act both as a current collector and to control the air flow to the cathode. The assembly is closed with a gasket and a lid. In addition there is a valve for refuelling and ventilation holes for the CO2 exhaust, though neither is shown in the figure. The fuel cell is connected to the hearing aid via a DC-DC converter in order to supply a voltage of at least 1V for the hearing aid. The DC-DC converter requires at least 350 mV to function and the hearing aid requires between 1.5-8 mW power during operation.

1.3 Catalysts

As stated in the previous section the DMFC uses PtRu/C and Pt/C catalysts for the anode and cathode respectively. In this section it will be defined what a catalyst is and how catalyst catalyses the different fuel cell reactions. A catalyst is a material that increases the reaction rate of an otherwise favourable but slow reaction by providing an alternative reaction path with a lower energy barrier. A great example, but unrelated to fuel cells, is the ammonia synthesis where nitrogen and hydrogen reacts to form ammonia. The overall reaction is:

$$\mathrm{N_2(g)} + 3\,\mathrm{H_2(g)} \longrightarrow 2\,\mathrm{NH_3(g)}$$

The overall reaction is favourable and the change in Gibbs free energy for the reaction is negative, meaning that the reaction could happen spontaneously. However, this is not the case because that there are several steps in the reaction and the first step that occur, is the splitting the molecular nitrogen into atomic nitrogen, which is very unfavourable. The dissociation of nitrogen only happens at very high temperatures and at these temperatures, it is practically impossible for nitrogen and hydrogen to form ammonia [11]. Alternatively, the reaction can be catalysed on iron in what is known as the Haber-Bosch process [11]. Instead of having atomic nitrogen, the nitrogen and hydrogen gases are dissociated on the iron surface, forming bonds with iron instead. Then on the iron surface, the nitrogen and hydrogen reacts to form ammonia that subsequently desorbs from the surface making space for more nitrogen and hydrogen to react. In this case the iron facilitates the reaction thus making iron a catalyst for this reaction.

1.3.1 Hydrogen oxidation reaction and CO poisoning

PEMFC have an energy barrier associated with the electrochemical reactions, similar to that of the ammonia example. In order to overcome this, an overpotential is needed for the reaction to proceed. The higher the overpotential, the lower the cell voltage is. To put it simply in order to achieve high electrical efficiency, good catalysts must be used. The hydrogen oxidation reaction (HOR), is the reaction taking place on the anode side of a fuel cell and is shown in equation 1.1. This reaction can be catalysed almost perfectly by Pt; the overpotential for the reaction is so low that it is difficult to measure [6]. Only about 0.05 mg/cm^2 Pt is needed for the anode in a H_2-PEMFC to achieve an anode overpotential of less than 3 mV [6], which is about an order of magnitude lower Pt loading than used on the H_2-PEMFC cathode. Therefore there is little focus on the HOR reaction and catalyst in the case where pure H_2 is used. However, since most H_2 is produced from reforming hydrocarbons the H_2 contains trace amounts of CO. CO is poisonous for the HOR and trace amounts of CO as little as 10 ppm can significantly degrade the performance of the fuel cell [2,12,13]. A selective CO oxidation catalyst can be placed in the gas feed to reduce the CO concentration, but for application with a varying power demand the gas flow will fluctuate making it difficult to get below 10 ppm CO [2]. It is possible to mitigate the CO poisoning by adding about 2% O2 to the H_2 feed, which is known as air bleed [14]. The membrane however, tend to degrade due to increased H_2O_2 formation [15]. Alternatively, a CO tolerant catalyst could be developed and it has also been reported that alloying Pt with Ru [16–18], Sn [19], Mo [20,21], Ni, Fe and Co [22,23] improves the CO tolerance. The CO poisoning is due the strong adsorption of CO on the Pt surface which blocks the surface and lowers the catalytic activity by reducing the number of available sites. The HOR only has a little overpotential, less than 3 mV in an optimized fuel cell [6], which mean the anode potential should be close to the equilibrium potential for HOR. The equilibrium potential between hydrogen evolution reaction (HER) and HOR is also called the reversible hydrogen electrode (RHE) and this electrode is commonly used as a reference electrode when working with fuel cell catalysts. The electro oxidation of CO (CO oxidation reaction, COR) requires a much higher overpotential than for HOR since OH is required in the reaction. The OH comes from water activation (10) and starts at potentials around 0.4-0.45 V vs RHE [7,24]. The OH is used to oxidise the CO (11).

$$\mathrm{H_2O} + {}^{*} \longrightarrow \mathrm{H^+} + \mathrm{e^-} + {}^{*}\mathrm{OH} \tag{1.7}$$

$$^{*}\mathrm{CO} + {}^{*}\mathrm{OH} \longrightarrow \mathrm{CO_2(g)} + \mathrm{H^+} + \mathrm{e^-} + 2\,{}^{*} \tag{1.8}$$

Bifunctional alloy such as PtRu can perform reaction 1.7 and 1.8 at lower potentials since Ru can activate water at lower potentials than Pt [25, 26]. However the CO oxidation still takes place at potentials above 0.3-0.4V which is much higher than the HOR operating potentials at 0-20 mV vs RHE [2]. CO tolerant catalyst work by lowering the CO bond strength and thereby lowering the CO coverage, the same mechanism driving non-bifunctional alloys such as Pt-Fe, Pt-Ni, Pt-Co works. The Pt-Ru is the best CO tolerant alloy since it has the highest residual activity in the low potential range 0-0.2V vs RHE [27]. The CO overpotential is marginal when using 0.2 mg/cm^2 PtRu on the anode [2]. However, due to instability of the PtRu alloy, Ru tend to leach out, crossover and degrade the cathode [28–30]. Therefore a better CO tolerant catalyst is needed.

1.3.2 Methanol oxidation reaction

The methanol oxidation reaction (MOR) is the electro oxidation of methanol and water into CO2, protons and electrons which occur on the anode in a DMFC. The overall reaction is shown in equation 1.5. There are several reaction routes with different intermediates that form the overall reaction in eq. 1.5 which is shown in Figure 1.7. The intermediates, reaction route and limiting steps, depend on which metal surface the reaction is taking place on [31]. The reaction path on Pt, shown with green, red and blue arrows, consists of seven steps. The first steps are the dehydrogenation of methanol [7]:

$$\mathrm{CH_3OH} + {}^* \longrightarrow {}^*\mathrm{CH_2OH} + \mathrm{H^+} + \mathrm{e^-} \tag{1.9}$$

$${}^*\mathrm{CH_2OH} \longrightarrow {}^*\mathrm{CHOH} + \mathrm{H^+} + \mathrm{e^-} \tag{1.10}$$

$${}^*\mathrm{CHOH} \longrightarrow {}^*\mathrm{COH} + \mathrm{H^+} + \mathrm{e^-} \tag{1.11}$$

$${}^*\mathrm{COH} \longrightarrow {}^*\mathrm{CO} + \mathrm{H^+} + \mathrm{e^-} \tag{1.12}$$

The stars denote sites on the Pt surface. The adsorption of methanol can be observed at low potential 0.05 V vs RHE, which is close to the open circuit potential for methanol oxidation 0.02 V vs RHE [7]. The dehydrogenation of methanol starts at 0.1-0.2 V vs RHE seen by adsorbed CO on the surface and the onset potential is structure dependent [7]. The next steps in the reaction are the oxidation of the adsorbed CO molecules, which is the same reaction shown in equation 1.7 and 1.8 in the previous section. At about 0.4 V vs RHE, CO_2 can be observed, which suggest that reaction 1.7 and 1.8 takes place. The intensity of CO_2 increases with overpotential until around 0.7 V vs RHE where water start competing with methanol for surface sites [7]. However, since anode potentials above 0.5 V have no practical use in real DMFC applications, the mechanism at higher potentials is not important for this thesis. The limiting steps can be summarised as follows: At lower potentials, 0.02-0.3 V vs RHE, the limiting step is the adsorption and dehydrogenation of methanol, reaction 1.9-1.12. Between 0.3-0.7 V vs RHE the reaction is limited by the activation of water eq. 1.7 and the oxidation of CO equation 1.8. At potentials above 0.7-0.75 the adsorption of methanol is the limiting step. The reaction is not exclusively going through the CO intermediate as a parallel pathway through HCOOH and HCHO intermediates have been reported [7].

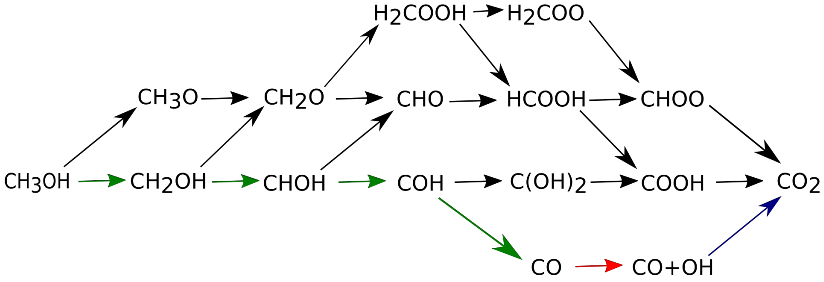

Figure 1.7: Possible reaction intermediates and reaction routes for the electro oxidation of methanol. The green arrows shows the reaction path on Pt, which is not rate limiting. The red arrow shows the rate limiting step on Pt. The figures was adapted from [31].

The high overpotential for MOR on Pt is mainly due to the high potential needed to activate water and the strong adsorption of CO. Ru, on the other hand, activates water easily but methanol does not adsorb on Ru below 60 °C [7, 32]. When combining the two elements in an alloy, the methanol can be dehydrogenated on Pt sites and water activated on Ru sites and then CO and OH can react at lower potentials than for Pt, which is also known as the bifunctional mechanism [7, 33]. The reaction in equation 1.7 and 1.8 then becomes:

$$\mathrm{H_2O} + \overset{*}{_{\mathrm{Ru}}} \longrightarrow \mathrm{H^+} + \mathrm{e^-} + \overset{*}{_{\mathrm{Ru}}}\mathrm{OH} \tag{1.13}$$

$$\overset{*}{_{\mathrm{Pt}}}\mathrm{CO} + \overset{*}{_{\mathrm{Ru}}}\mathrm{OH} \longrightarrow \mathrm{CO_2(g)} + \mathrm{H^+} + \mathrm{e^-} + \overset{*}{_{\mathrm{Pt}}} + \overset{*}{_{\mathrm{Ru}}} \tag{1.14}$$

Where * denotes a free site on the metal and the subscript denotes which metal the species is adsorbed on. The specific activity, measured at constant potential of either 0.4 or 0.5 V vs RHE, increases by several orders of magnitude for $\mathrm{Pt_xRu}$ alloys compared to Pt [7,32,34]. Bulk alloys of $\mathrm{Pt_xRu}$ shows an order of magnitude higher activity compared to Pt(111)/Ru surface alloys [7, 34], meaning that Ru surface atoms are not sufficient and that the bulk alloy is required for achieving the highest activity. The MOR is highly temperature dependent, and raising the temperature from 25 °C to 60 °C can increase the specific activity with an order of magnitude [32]. In addition, MOR activity also depends on whether the electrolyte is acidic or alkaline as MOR shows higher activity in alkaline electrolytes than in acidic [2, 35].

1.3.2.1 Measuring the activity of MOR catalysts

The Pt-Ru bifunctional catalyst for MOR was discovered in 1975 [33] and since then the Pt-Ru system have been optimised, alternative catalysts have been reported and new or improved catalysts are reported every year. However the method for measuring the MOR activity can vary notably from paper to paper, making comparison difficult. The methods vary between cyclic voltammetry [36, 37], potentiostatic at various potentials [36, 38, 39], the ratio between the MOR peak current in the anodic and cathode sweep [36] and DMFC measurements [40]. Although the various methods might provide different insights into the reaction mechanism, the relevant parameter when comparing catalysts for MOR in a DMFC, is the steady-state activity. The cyclic voltammetry and potentiostatic techniques can show very different results for MOR activity. Gasteiger et al [32, 41] showed that the relative MOR activity between sputter cleaned Pt and PtRu was very different depending on whether the cyclic voltammetry or potentiostatic technique were used. At lower concentrations (5 mM) Pt was more active compared to PtRu on the short timescale (<2 min) whereas on the long timescale (>5 min) PtRu is more active than Pt [41]. Similar behaviour was observed for higher concentrations (0.5 M) but in this case the performance degradation was much faster (<10 s) [41]. For a clean surface the limiting step is the dehydrogenation of methanol on the short timescale, and the CO oxidation on the long timescale [7, 32, 41, 42]. Therefore, is potentiostatic measurements better for determining the long term activity, which is relevant for the DMFC [32, 41, 43–45]. In this thesis the focus will be on relating the DMFC performance with MOR catalyst activity.

1.3.3 Oxygen reduction reaction

The oxygen reduction reaction (ORR) takes place on the cathode of both the H2-PEMFCs as well as on DMFCs. The overall reaction is the reduction of oxygen to water:

$$\mathrm{O_2(g) + 4\,H^+ + e^- \longrightarrow 2\,H_2O} \tag{1.15}$$

Pt is the best pure element catalyst for this reaction, but still has an overpotential of 300 mV for high current densities (>0.2 A/cm^2) as also seen on Figure 1.3 for a typical H_2-PEMFC. According to the theoretical model developed by Rossmeisl, Nørskov and co-workers, the reaction steps on Pt are [46, 47]:

$$\mathrm{O_2 + H^+ + e^- + {}^* \longrightarrow {}^*OOH} \tag{1.16}$$

$$\mathrm{{}^*OOH + H^+ + e^- \longrightarrow {}^*O + H_2O} \tag{1.17}$$

$$\mathrm{{}^*O + H^+ + e^- \longrightarrow {}^*OH} \tag{1.18}$$

$$\mathrm{{}^*OH + H^+ + e^- \longrightarrow H_2O + {}^*} \tag{1.19}$$

The changes in free energy compared to the final state for the different reaction steps are plotted in Figure 1.8a, based on density functional theory (DFT) calculations. The figure was adapted from [48] where the calculation was made at 0.9 V vs RHE on a Pt(111) surface. The overall reaction 1.15 is down in energy, but there are two of the reaction steps eq. 1.16 and 1.19 where the change in free energy ΔG_1 and ΔG_4 respectively is positive as seen in Figure 1.8a. Positive changes in free energy limit the reaction, and the step with the most positive change in free energy is the overpotential determining step. The change in free energy for the three intermediates in the ORR reaction is plotted in Figure 1.8b as a function of the change in free energy for the OH intermediate. The lines are regression lines based on calculated binding energies for different surfaces from [49–51]. It turns out that the change in free energy of the different intermediates scales with each other. This is known as scaling relations and the consequence is that it is impossible to change ΔG_1 and ΔG_4 individually since the OOH*, O* and OH* intermediates bind through the oxygen atom and thus changing the O binding energy affects all of the intermediates. If a catalyst was optimised to reduce the binding towards the OH* intermediate, thus having ΔG_4 be equal to or lower than zero, then the OOH* binding energy would be lowered as well, increasing the ΔG_1 and making the reaction in eq. 1.16 the limiting step instead of eq. 1.19. Because of the scaling relations, the optimal binding energy to the intermediates is when ΔG_1 is equal to ΔG_4, also shown in Figure 1.8b with a dashed line. The catalysts for ORR can be divided into two categories; the ones that bind to weakly too O_2, meaning ΔG_1 is potential determining, and the ones that binds OH too strongly, in which case ΔG_4 determines the overpotential. This is contrary to bifunctional catalyst like PtRu for the MOR, where the binding energy can be optimized for the two intermediates CO and OH individually since they bind to different atoms on the surface.

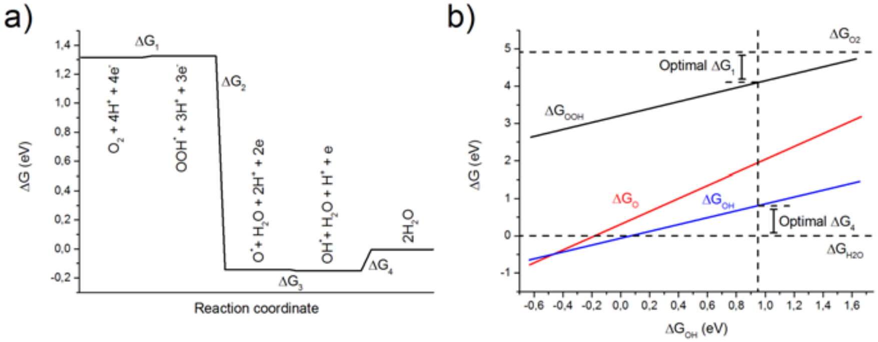

Figure 1.8: a) Change in Gibbs free energy from the final state for different reaction intermediates in the ORR. The overall reaction goes down in free energy, but for to intermediates the free energy change is positive namely for ΔG_1 and ΔG_4. The energy changes was calculated at 0.9V vs RHE for Pt(111) and the figure is adapted from [48]. b) Shows how the change in free energy for the different intermediates scales with each other. The dashed lines shows the free energy level of O_2 and H_2O, and the horizontal line shows the optimal free energy of the different energies. The figure was adapted from [49] where the lines are regression lines calculated using data from [50, 51].

In Figure 1.9 the ORR activity enhancement over Pt versus the difference in OH binding energy from a Pt surface is plotted for a number of very active ORR catalysts. The data stems from [48, 49, 52–55]. It is seen that there is a trend in activity following the dashed lines. The dashed lines forms sort of a volcano and therefore this type of plot is called volcano plot. The top of the volcano is placed at the optimal binding energy towards OH i.e. when ΔG_1 is equal to ΔG_4. The catalysts of the left side are limited by ΔG_4, meaning that OH is binding too strongly. The catalysts on the right side of the volcano are limited by ΔG_1, meaning that the binding towards OOH is too weak. The most active catalyst on the plot is the $Pt_3Ni(111)$ which shows about an order of magnitude higher activity than Pt. Pt is placed on the strong OH binding side and the ideal catalyst should have a OH binding energy about 0.1 eV lower than for Pt.

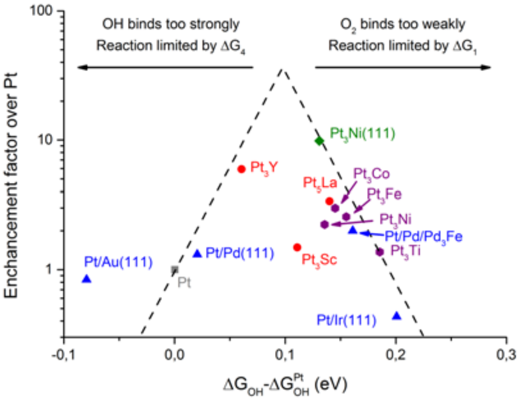

Figure 1.9: hows a volcano plot for the ORR where the enhancement factor in activity over Pt is plotted against the difference in OH binding energy compared to a Pt surface. Data from: (red circles) sputter cleaned polycrystalline bulk alloys [48,49]; (purple hexagons) vacuum annealed alloys [52]; (green diamonds) vacuum annealed single crystal alloy [53]; (blue triangle) Pt monolayer on single crystals [54,55]. Figure adapted from [49].

1.3.3.1 Pt Alloys as improved ORR catalysts

The alternatives to Pt is rather limited since the environment inside a PEMFC is very acidic (pH = 0) and only a few elements like Pt, Au and other noble metals are stable under these conditions. The alternative is to alloy Pt with another metal to slightly change the OH binding energy. The most active alloy surface is the $Pt_3Ni(111)$ [53], but it is difficult to synthesise nanoparticles with the $Pt_3Ni(111)$ facets. Most Pt_3Ni nanoparticles are therefore only slightly more active than Pt (about a factor two [56]). In cases where the morphology of the Pt_3Ni nanoparticles could be controlled and the (111) facets favoured, large increases in mass activity was observed (up to 17x) [56–58]. Similar to Ni, other late transitions metals also form Pt alloys that are very active towards ORR [59–63]. The disadvantage of Pt and late transition metal alloys are that the less noble metal tend to leach out, thus lowering the activity over time [3,64–66] and the leach out metal may in term damage the membrane performance [67]. The instability of the second metal have also been used to form active catalytic structures by synthesising nanoparticles rich on the second metal, which form a active/stable structure after acid treatment [68, 69]. Electrochemical treatment have also been used to form hollow nanoparticles by utilizing the Kirkendall effect, and which resulted in more active nanostructures [66, 70, 71]. Some groups also report that the Pt- late transition metal alloys can be stabilised in certain structures such as the Pt-Ni nanoframe [72] or by doping the octahedral structure with Mo [58].

1.3.3.2 Pt_xM alloys for the oxygen reduction reaction

At CINF/CAMD, DTU, computational screening was used to identify other promising bimetallic alloys for the ORR. The screening first identified Pt_3Y and Pt_3Sc alloys as potential candidates [48]. In the screening, the main parameters were the difference in O binding energy compared to Pt and the heat of formation of the alloy. The assumption was that the more negative the heat of formation, the higher diffusion barrier, which lowers the leaching of the less noble metal. The connection between heat of formation and diffusion barrier have recently been shown in calculations by Vej-Hansen et al. [73], where the diffusion barrier was calculated for different Pt_3X, Pd_3X and Al_3X alloys. The screening by Greeley et al. [48] found that Pt_3Sc and Pt3Y has a heat of formation that is about 0.9-1 eV more negative per atom than the late transition metals such as Pt_3Ni, Pt_3Co, Pt_3Cu and Pt_3Fe. The Pt_3Y alloy turned out to be very active when tested electrochemically and was about 5 times more active than Pt measured at 0.9 V vs RHE. The activity enhancement was predicted under the assumption that the surface consisted of a single Pt monolayer on top of the alloy, which would lower the oxygen binding energy due to a ligand effect. However angle resolved x-ray photoelectron spectroscopy (AR-XPS) later showed the overlayer to be around 1 nm thick [74], which makes a ligand effect unlikely. It has therefore been proposed that the overlayer is under a compressive strain, which would lower the OH binding energy and increase the activity [49, 74, 75]. Several more Pt_xM catalysts have since been found: Pt_5Y [74], Pt_5Gd [75], Pt_5La and Pt_5Ce [**?**, 49], Pt_5Ca and Pt_5Sr [76], and Pt_5Ln where Ln is the lanthanide series [76]. The most active are the Pt_5Tb, Pt_5Gd and Pt_3Y, which shows a 5-6 time enhancement over Pt [48, 75, 76].

Most of the studies have been performed on sputter cleaned polycrystalline alloy disks, produced by standard melt techniques by Mateck (Germany), which are useful for studying trends in activity. However, nanoparticles are technologically more relevant for the fuel cells and it is thus necessary to make these very activity surfaces on nanoparticles. At our laboratory, the Pt_xY and Pt_xGd alloys have also been tested in nanoparticulate form. The nanoparticles were produced in a UHV chamber by sputtering, then aggregated, size-selected and finally placed on a substrate [77–79]. The specific activity and mass activity as a function of particle size are shown in Figure 1.10. It is seen that the activity increases with size and that the very active nanoparticles are 6 nm or larger. The smaller ones (2-4 nm) have similar activity to the same sized Pt nanoparticles. The strain of the overlayer was also measured using Extended X-ray Absorption Fine Structure technique and for the 9 nm Pt_xY and Pt_xGd, the average strain in the overlayer were -2.1% and -2.2% respectively [78, 79], which shows that the activity enhancement is due to a strain effect. The stability of the nanoparticles was also tested by accelerated stress test where the electrode with catalyst was cycled 10000 times between 0.6 and 1.0 V vs RHE. The Pt_xGd nanoparticles retain about 30-50% of their original activity and interestingly the decrease in activity was accompanied by a decrease in compressive strain [79].

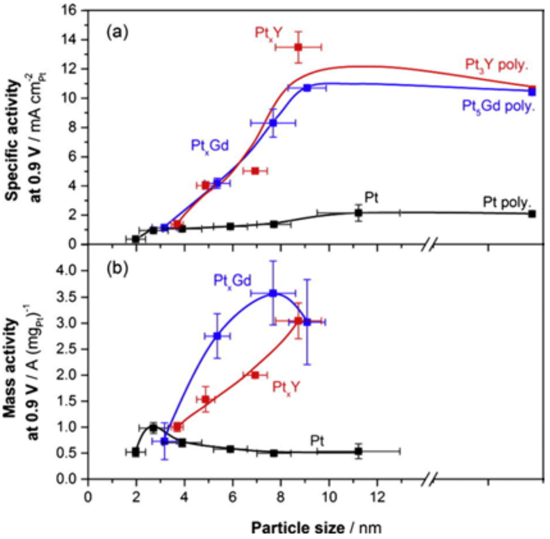

Figure 1.10: ORR specific activity a) and mass activity b) of mass selected Pt (black), Pt_xY (red) and Pt_xGd (blue) nanoparticles measured at 0.9V vs RHE. The specific activity and mass activity increases with size for the Pt_xY and Pt_xGd nanoparticles and the high activity are seen for alloy nanoparticles larger than 6 nm. The figure was adapted from [79].

1.3.3.3 Benchmarking of ORR catalysts

Comparing the catalytic activities of different catalysts can be challenging since different groups measures the activity in slightly different ways, which can have a large impact on the result. Most new ORR catalyst are analysed using the rotating disk electrode (RDE) [80, 81], which is a fast method compared to fuel cell testing. Activities measured with RDE are not necessarily the same as if measured in a fuel cell, but trends in activity seen from RDE measurements are also seen in fuel cell testing [82] and RDE measurements are therefore good for comparing catalysts. Several papers have been published that describes how to perform the measurements correctly [82–87]. However, there is still a large variance in the way activities are measured. Parameters such as temperature; scan rate; correction for ohmic drop; and subtraction of capacitive currents change from paper to paper. In Figure 1.11 a comparison between some of the most active nanoparticles reported in literature [56–58, 60, 62, 68, 69, 71, 72, 78, 79, 88–93] is shown. The different catalysts have been measured with different scan rates, which affect the activity and thus potentially could change the ranking of the catalysts. I will come back to how the activity is affected in Section 4.2. The Pt_xY and Pt_xGd nanoparticles performs well in comparison and ranks 3rd and 5th in mass activity and 1st and 4th in specific activity. These materials are clearly interesting if they can be produced on a large scale.

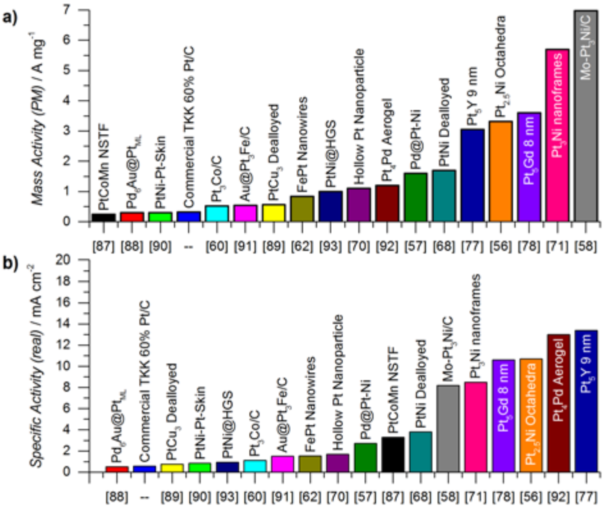

Figure 1.11: Mass activity a) and specific activity b) for a selection of the most active nanoparticles for ORR. The figure was made with data from [56–58, 60, 62, 68, 69, 71, 72, 78, 79, 88–93]. In cases where either the mass activity or specific activity was not specified at 0.9 V vs RHE it has either been found from digitised data in supporting information found in [92]; converting between mass activity and specific activity using specified electrochemical surface area [56, 72]; or in the case of [71, 89] using extrapolated data by Baldizzone et al [93]. Note that the mass activities of $Pd_5Au@PtML$ and $Au@Pt_3Fe/C$ have been normalised to Pt mass and not precious metal (PM) like the rest. The figure is an updated version of Figure 1 in [94] which is included in Appendix B

1.3.3.4 Methanol poisoning of the oxygen reduction reaction

In a DMFC it is practically impossible to avoid at least some methanol crossover. Methanol poisons the ORR by a parasitic MOR current that reduces the effective reduction current, since the total current is a sum of the ORR and MOR currents [95]. The methanol poisoning is different from other ORR poisons like halide anions, cations and different sulphur compounds that poisons the ORR by blocking sites on the Pt catalyst [95]. Methanol can also block sites on Pt by dehydrogenation into CO, which then blocks the surface. CO can however also be oxidised on a Pt surface in the potential range of the cathode [34]. To reduce the effect of methanol poisoning it is necessary to reduce the MOR current without reducing the ORR current. Catalyst such as Ru, Ru_xSe_y and $Ru_xMo_ySeO_4$ are practically not poisoned by methanol since methanol does not adsorb [96–99]. However, none of the catalysts can compete with Pt in methanol free conditions, where they require an additional overpotential of about 100 mV [96]. Measurements in active DMFC have shown that for high current densities (>100 mA/cm^2), the overpotential induced from methanol poisoning is less than 20 mV, which is much smaller than the overpotential from using the methanol tolerant catalyst with poorer kinetics. Pt is thus used as cathode catalyst despite of methanol poisoning. The methanol tolerant catalyst could find use in special cases where the DMFC is using more concentrated fuel and the methanol crossover is difficult to control, but this is more of a DMFC design issue. Alternatively to completely methanol tolerant catalyst, it has been reported that catalysts such as Pt-Ni [100, 101] and Pt-Co [102], provides a higher ORR activity also in the presence of methanol. This type of catalyst seem as a more promising replacement for Pt cathode catalyst in the DMFC than Ru, $\mathrm{Ru_xSe_y}$ and $\mathrm{Ru_xMo_ySeO_4}$.

1.3.4 Catalyst performance in the DMFC

The most common way to test DMFC performance and fuel cells in general is to measure the cell voltage while drawing a specific current with a load box. The load box is basically an electronic controlled adjustable resistor that changes value in order to draw the specified current. While this type of measurement shows the performance at close to real application conditions it does not show the performance of the individual components. Impedance spectroscopy is used to identify the ohmic and polarisation resistances, which shows the different losses in the fuel cell [103–105], but it can however be very difficult to interpret. Another approach is to add a reference electrode, which makes it possible to measure the absolute potential of the anode and cathode. The overpotential as a measure of catalytic activity can be calculated from the absolute potential as well as other contributions such as mass transport limitations, ohmic resistance etc. In any case, electrode potentials reveal the real conditions in the fuel cell, which can then be used to set up more realistic half-cell measurements of the catalyst. A reference electrode can be made by simply extending the membrane out of the MEA and connecting it to reference electrode in an electrolyte, but this reference potential might be skewed by fringe effects at the edge of the MEA. Hinds et al [106] showed an alternative design where the reference electrode is connected via a Nafion tube, which is connected through one of the electrodes to avoid fringe effects. Alternatively to a build-in reference electrode, the cathode can be used as reference electrode by flushing it with hydrogen, which makes it possible to measure the anode potential isolated and then by subtracting the anode from the full cell potential, the cathode potential can be calculated [8, 103].

1.4 Prior work in the chemical synthesis of Pt_xM alloy nanoparticles

In the previous section the importance of the catalyst and the possible gains when using alloy catalyst were described. However, a requirement for using these alloy catalyst in the DMFC is that they can be chemically synthesised as nanoparticles. Possible synthesis routes are discussed later in the thesis. First a selection of synthesis attempts by others will be presented. For future reference the Pt_xM alloys are where M is defined as an early transition metal, lanthanide or alkali earth. Ln refers to the lanthanides throughout the thesis.

The problem of forming the alloy nanoparticles lies mainly in reducing the yttrium or lanthanide precursors. The most common precursors are found in the 3^+ oxidation state, which is difficult to reduce because of this very negative standard reduction potential, and have a much different reduction potential than that for Pt precursors. The standard reduction potential for $Y_3{}^+$ is -2.38V whereas $Pt_2{}^+$ has a standard reduction potential of +1.18V, which is a larger difference than for other ORR Pt alloys with Ni or Co that have a standard reduction potential of -0.257 V and -0.28 V respectively [107]. The very different reduction potential makes challenging to reduce both precursors at the same time. In addition, yttrium and lanthanides forms very stable oxides making it difficult to synthesize alloys with these elements if oxygen is present in any form.

A popular way of making nanoparticles is the water-in-oil micro emulsions technique [108, 109]. The idea is to have small droplets of water with water-soluble precursors and reducing agents surrounded by oil. The particles size is then controlled by size of the water droplets. This method has also been employed with Pt, YCl_3 and $GdCl_3$ salts in the paper by Luo et al [110] who report the formation of Yttrium/Gadolinium oxide decorated Pt nanoparticles. They did report improved ORR activity of up to 60% for the oxide decorated Pt particles over Pt particles, although the alloy was not formed. The increased mass activity could be explained by the particles very small size (2.3 nm) and by a slight compression of the Pt lattice (0.19 – 0.27%). The method does not seem suitable to form the Pt_xM alloy nanoparticles. It might be that oxide formation is too favourable in the presence of water, but if the micro emulsions could be done without water, it might be possible to form the metallic alloy.

Lux et al [111, 112] have demonstrated 25 nm Pt_2Pr and Pt_2Ce nanoparticles by cyanide complexing. $K_2[Pt(CN)_6]$ was complexed with $Ln(NO_3)_3$ (where Ln is either Pr or Ce) to form a $HLn[Pt(CN)_6]_2$ complex, which then can be quickly reduced in H_2 at 800-1000 °C (shock reduction technique) to Pt_2Ln. The measured XRD structure was mainly an $MgCu_2$ Laves phase that is well known for Pt_2Ln alloys. The synthesised catalyst was also tested for the ethanol oxidation reaction but was not more active than PtRu, which might be related to the very large size of the synthesised nanoparticles.

Yan et al [113] report the formation of stable Gd@Au core-shell nanoparticles using alkalide reduction. In this technique crown-ether is complexing with NaK metallic alloy to form an alkalide where NaK metal is stabilized in a K+, Na- state. The alkalide then have the reduction power corresponding to that of a free electron (-3 V) which is enough to reduce the yttrium/lanthanide precursors. The synthesis is a two-step synthesis where the metallic Gd particles are formed and then subsequently gold is formed on top of them. There is no direct evidence of metallic Gd in the paper, but they do display an TEM image showing a core-shell structure and EDX of the particles, which show that they contain both Au and Gd. XRD measurements shows two phases, one that is clearly an Au phase and a HCP phase which is attributed to nano Gd. Although there is no direct evidence of metallic Gd, this method would be interesting for forming Pt@Gd core-shell nanoparticles that later can be annealed to create a Pt_5Gd alloy. The group have also reported formation of metallic Gd and Dy nanoparticles using this method [114, 115].

It has recently been reported that Pt_3Gd could be formed under solvothermal conditions. Dipankar et al [116] reports the formation of Pt_3Gd from an in-situ experiment where 0.5M $H_2PtCl_6 \cdot 3\,H_2O$ and $GdCl_3 \cdot 6\,H_2O$ was mixed in a 1:1 molar ratio in ethanol. The solution was put in a sapphire reactor, which was pressurised to 250 bar and heated to 250 °C while X-ray scattering measurement was performed. From the scattering experiment an atomic pair distribution function was calculated. Pair distribution function for different structures were simulated and the best fit to the measured data was the Pt_3Gd structure.

Finnally, a high temperature reduction method has been reported by Erdmann et al [117, 118] and Bronger [119] in which Pt_xM alloys can be formed by annealing Pt powder with yttrium/lanthanide oxides or fluorides under a ultrapure H_2 [117, 118] or NH_3 [119] flow. The resulting product was in most cases a powder that was characterised using x-ray diffraction techniques. The structures and lattice constants are in agreement with the reported XRD measurements from arc-melted alloys [120–122]. The structures for the Pt_2Y and Pt_3Y also match the reported one for the active ORR catalyst by Stephens et al [74]. The Pt_5M structures however differs from reported active ORR catalyst Pt_5Y [74] and Pt_5Ln [75, 76]. Erdmann [117, 118], Bronger [119] and Krikorian [120] reports a orthorhombic structure for both Pt_5Y and Pt_5Ln alloys whereas the ORR active Pt_5Y was a cubic structure [74] and the ORR active Pt5Ln structures are hexagonal structures [75, 76]. Interestingly the orthorhombic and hexagonal Pt_5Ln structures have very similar a lattice constants.

All of the mentioned methods have been conducted bottom up meaning that the alloy particles have been formed by one atom at a time. Another approach is a top down method where a bulk alloy is broken down into alloy nanoparticles. One way of doing this is by using laser ablation where a pulsed laser break down a bulk material into nanoparticles in a solution [123, 124]. This method is already being offered commercially by companies like Strem and Nanograde although there have been no reports of formation of Pt_xM nanoparticles from laser ablation. Another top down method is cathodic corrosion where nanoparticles are formed in a alkaline electrolyte by applying very cathodic (-10 V) pulses on a bulk wire. The method has been demonstrated to make alloy nanoparticles, including Pt [125] and PtxRh alloy [126]. The idea would be to produce the Pt_xM alloy using standard melt techniques as a wire and then use either laser ablation or cathodic corrosion to make the alloy nanoparticles.

1.5 Thesis outline

The purpose of this chapter was to explain the motivation behind making µ-DMFC a possible replacement for batteries in hearing instruments. Next the different concepts used in the thesis was introduced, including fuel cells in general and in particular the DMFC and the µ-DMFC. Then as this thesis is focused on the catalyst side of the DMFC, the different catalytic reactions in a fuel cell were presented. In addition a new class of catalysts, the Pt_xM alloys, were also introduced including reported synthesis methods for forming the alloys.

The goal of the thesis is to find new active catalyst for the DMFC and methods to produce them as nanoparticles. This is achieved in six chapters, starting with Chapter 2 where the common experimental techniques for the other chapters are presented. In Chapter 3 the performance of the µ-DMFC is measured and the main performance losses are identified. Chapter 4 looks at the catalytic activity from a different perspective than Chapter 3, namely by making RDE experiments approach the condition of the fuel cell, whereas in Chapter 3 the activity is extracted from the fuel cell measurements. Pt_5Gd is identified as a potential replacement for the DMFC cathode catalyst in Chapter 4, but to use it in a DMFC the catalyst must be made in a nanoparticulate form. This is attempted in Chapter 5 where several synthesis routes are attempted, but only one that is the high temperature reduction, is successful in forming a Pt_xM alloy. The synthesis method is studied in details in Chapter 6 and the whole thesis is concluded in Chapter 7.

2

Methods

This chapter explains the general techniques used in chapters 3-6. Specific techniques for a chapter will be introduced in the beginning of their respective chapters. The general electrochemistry and the rotating disk electrode method in particular will be presented in this chapter. Powder x-ray diffraction, x-ray photoelectron spectroscopy and electron microscopy will be introduced along with a description of the data analysis performed in Chapters 3-6.

2.1 Electrochemical measurements

All of the electrochemical experiments were performed with a three-electrode setup. A drawing of the setup is shown in Figure 2.1. The sample is placed on the Working Electrode (WE) where the reaction happens. The Counter electrode (CE) will perform some reaction to balance the charge transfer. It is not necessarily of importance which reactions are taken place on the CE or which potential the CE has. The important potential is the potential of the WE compared to some known reference potential and thus a third electrode is required. The reference electrode (Ref) provides a well-known and stable reference potential, which is then used to measure the absolute potential of the WE. The potential of the Ref depends on the chemistry inside the reference electrode. The electrodes are connected to a potentiostat, which is capable of performing numerous techniques, but basically it either controls the potential between WE and REF or the current between WE and CE while measuring both the potential and current.

2.1.1 The rotating disk electrode method

Electrochemical experiments involving gaseous reactants in a liquid electrolyte are difficult to perform since the solubility of gasses is very low. The rotating disk electrode (RDE) method enables control of the mass flow of reactants towards the

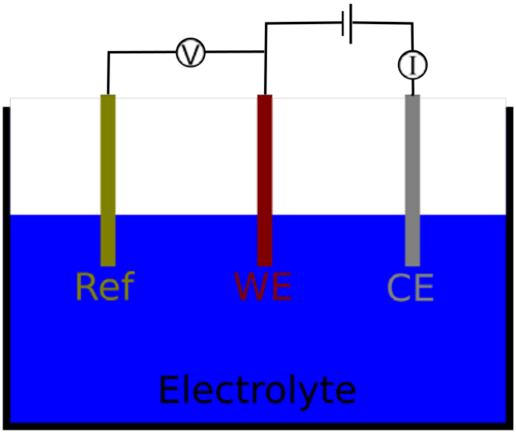

Figure 2.1: Drawing of the three-electrode setup. The setup consists of three electrodes in an electrolyte where WE is the working electrode, CE is the counter electrode and Ref is the reference electrode. The electrodes are connected to a potentiostat which can either control the potential difference between the WE and Ref or current between WE and CE and at the same time record the current and potential.

electrode, which can be controlled by the rotation speed of the electrode. The setup is shown in Figure 2.2a and consist of a rotator that rotates the sample in the liquid half-cell. A Pt wire functions as counter electrode while a luggin capillary with an Hg|Hg_2SO_4 reference electrode serve as reference. The temperature is controlled by flowing heated or cooled water through the jacket of the cell. Different nanoparticles samples for the RDE setup are shown in Figure 2.2b. In order to perform measurements on nanoparticles a thin film with nanoparticles must be form on the glassy carbon in the RDE tip. The preparation of nanoparticles is described in Section 2.1.1.3.

Prior to performing the experiments the glass cell was cleaned in piranha (98% H_2SO_4 (Merck, Emsure) and 30% H_2O_2 (Merck, Emsure), 3:1 v/v) for 12-24 hours and then the cell was cleaned five times in 18.2 MΩcm Millipore water at 86 °C to remove possible traces of piranha. The electrolyte, either 0.1 M $HClO_4$ or 0.5 M H_2SO_4, was prepared from 70% $HClO_4$ Merck Suprapur and 96% H_2SO_4 Merck Suprapur respectively.

2.1.1.1 Preparation of polycrystalline Pt disk electrodes

A polished polycrystalline 99.99% Pt disk from Pine Instruments with a diameter and thickness of 5 mm was used for the polycrystalline Pt experiments. The disk was prepared by annealing it with a butane torch for 5 min and immediately after placed under a glass bell jar with an Ar atmosphere. The disk subsequently cooled

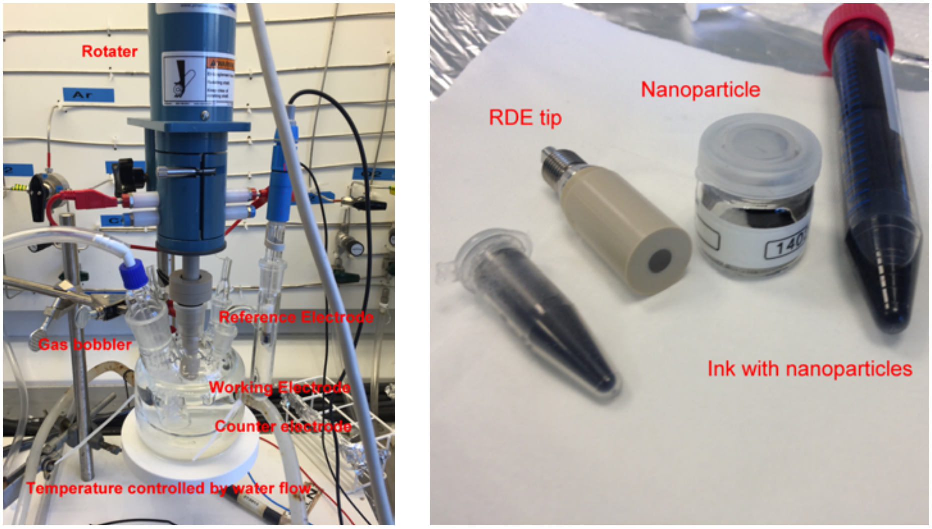

(a) RDE setup **(b)** Samples for RDE setup

Figure 2.2: The rotating disks setup a) which consist of a temperature controlled cell with a bobble tube, luggin capillary with reference electrode, Pt wire as counter electrode, and a working electrode mounted in a RDE tip that is connected to the rotator. b) Shows samples for the RDE setup. The sample is placed in a RDE tip either by changing disk or by depositing on the disk. Nanoparticles are deposited from a dispersion of nanoparticles in a solvent.

down for 3 minutes and then a droplet of Millipore (18.2 MΩcm) saturated with H_2 was put on the surface. The disk was then put on a piece of pre cleaned polypropylene film from Chemplex, placed face down. The disk was then mounted in a changedisk rotating ring disk electrode (RRDE) tip from Pine instruments. The electrode was inserted into the electrolyte under potential control at 0.05V vs RHE and then cycled between 0.05 and 1V vs RHE at 50 mV/s until the CV was stable.

2.1.1.2 Preparation of polycrystalline Pt alloy disk electrodes

The polycrystalline Pt_5Gd disk cannot be flame annealed since the treatment would likely destroy the alloy. Instead, the Pt alloy was sputter-cleaned in a UHV chamber for 40 min at 0.5 keV. Immediately after removing the disk from the UHV chamber a droplet of Millipore (18.2 MΩcm) water saturated with H2 was placed on the surface. The disk was then transferred to the electrochemistry lab where it was placed face down on a pre-cleaned polypropylene film from Chemplex. The disk was then mounted in a Changedisk RRDE tip from Pine Instruments. The electrode was inserted into the electrolyte under potential control at 0.05V vs RHE. The electrode was cleaned by cycling in N_2 saturated 0.1 M $HClO_4$ at 50 mV/s for several hundreds of cycles. Even though special care was taken in keeping the sample clean, it is extremely difficult to keep it clean, due to longer duration between annealing and mounting compared to flame annealing, because the sample had to be transferred from another lab.

2.1.1.3 Preparation of glassy carbon electrodes with nanoparticle

The glassy carbon electrodes with nanoparticles were prepared by drop casting ink with nanoparticles onto the glassy carbon. The nanoparticle dispersion was inspired by the recipe of Garsany et al [84] and consisted mainly of Millipore water and absolute ethanol (99.8%, Fluka, puriss. p.ap, ACS Reagent). The ratio between ethanol and water determines the success of the drop casting. The ratio must be optimised for every catalyst, but in general 1.4 g of water was used with 4.8 g of absolute ethanol for the Pt/C catalyst and 0.7 g of water to 5.8 g of ethanol for the PtRu/C catalyst. In addition, 7.5 mg of PVP (2% in ethanol) and 20 mg of Nafion solution was added. The ink was sonicated in a sonic horn for 5 min when prepared and for 1-2 min before deposition. The glassy carbon disks were polished before deposition using Buehler MicroPolish™ 0.05 µm alumina particles on a Buehler MicroCloth PSA and then sonicated in both isopropanol and water. The ink was deposited while the glassy carbon electrode was placed on an analytical balance to measure the mass of the ink droplet in order to calculate the Pt mass on the electrode.

2.1.1.4 Determining the RHE potential

The potentials for the RHE scale was found by measuring a CV between -.02 to 0.3 V vs RHE at 20 mV/s and 1600 RPM in a H_2 saturated electrolyte. The measured potential was then corrected using this value and the following equation:

$$U_{\mathrm{RHE}} = U_{\mathrm{Hg|Hg_2SO_4}} - U_{\mathrm{OCV,H_2}} \tag{2.1}$$

Where U_{RHE} is the corrected potential, $U_{\mathrm{Hg|Hg_2SO_4}}$ is the measured potential vs Hg|Hg2SO4 and $U_{\mathrm{OCV,H_2}}$ is the OCV value for Pt in H_2. The measured potentials ranged from-0.725 to -0.717 V at 23 °C and from -0.711 to -0.704 V at 60 °C, with respect to the Hg/Hg2SO4 reference electrode.

2.1.1.5 Ohmic resistance

The ohmic resistance was measured by using potentiostatic impedance spectroscopy from 100 kHz to 10 Hz with 10 mV pulse. The ohmic drop value was found from the fitted high frequency intercept from the impedance measurement. The potentials were compensated for ohmic drop using the following formula:

$$U_{\mathrm{Compensated}} = U_{\mathrm{Measured}} - IR_{\mathrm{Ohmic}} \tag{2.2}$$

Where $U_{\mathrm{Compensated}}$ is ohmic drop compensated potential, U_{Measured} is the measured potential, I is the measured current and R_{Ohmic} is the ohmic resistance. The typical Ohmic resistance in 0.1 M $HClO_4$ ranged from 24–33 Ω at 23 °C, and from 17 to 22 Ω at 60 °C. The typical Ohmic resistance in 0.5 M H_2SO_4 ranged from 7 to 8 Ω at 23 °C and from 4 to 5 Ω at 60 °C.

2.1.1.6 Hydrogen oxidation reaction and CO poisoning

The measurements were performed at both 23 °C and 60 °C and in both 0.1 M $HClO_4$ and 0.5 M H_2SO_4. The RHE potential and Ohmic drop compensation was determined in each case. CO poisoning experiments were performed by bobbling a CO/H_2 mixture (either 100 ppm CO in H_2 or 2% CO in H_2) at 2500 rpm. To ensure reproducibility it was necessary to perform a number of cycles at 100 mV/s between 0 and 0.8V vs RHE before each experiment. After the pre-treatment one of two experiments were performed either a potentiostatic or a CV experiment. For the potentiostatic experiments the potential was held at 0.1 V vs RHE until the electrode was completely poisoned, then the potential was stepped by 0.05V every 5 minutes through the potential reached 0.8 V vs RHE. The CV experiments were performed with the same pre-treatment as for the potentiostatic experiment, and then the potential was held at 0.1 V until the electrode was completely poisoned and subsequently the CV started at 1 mV/s up to 0.8 V vs RHE.

2.1.1.7 Oxygen reduction reaction and methanol poisoning

The ORR experiments were performed in O_2 saturated 0.1 M $HClO_4$ at 1600 rpm, 23 °C and 50 mV/s unless stated otherwise. The ORR measurements were analysed in different ways depending on the sample, but in all cases the RHE potential scale was used and mass transport correction applied, which was derived from the relationship between measured current density J, kinetic current density J_{Kin} and mass transport limited current density J_{Lim} [80]:

$$\frac{1}{J} = \frac{1}{J_{\text{Kin}}} + \frac{1}{J_{\text{Lim}}}$$

The bulk polycrystalline samples were compensated for RHE potential, ohmic drop and mass transport limitations. The nanoparticles were compensated for RHE potential, ohmic drop, mass transport limitations and capacitive currents unless stated otherwise. Activity values was measured at 0.9 V vs RHE and normalised either to geometric area in case of the bulk disks; CO stripping determined surface area in case of the nanoparticles; or Pt mass also in the case of nanoparticles.

2.2 Powder x-ray diffraction

Powder x-ray diffraction (PXRD) was used to determine crystal structures and crystallite/particle sizes of synthesised nanoparticles. In the following text I will shortly explain the technique and then focus on the data treatment. The data treatment was performed using the software HighScore Plus from PANalytical, which is the same company that manufactured the diffractometer used in the experiments. In order to understand the data analysis, it is necessary to understand how the software fits the measurements and how the software calculates the crystallite size. The following description of the technique and data refinement is based on material from the Microstructural Characterization of Materials book by Brandon Kaplan [127] and the documentation included for the software [128].

PXRD is used to measure crystal structures and their properties such as lattice parameters, crystallite size, strain etc. Generally, the technique is based on inelastic scattering with the crystal lattice where a well-defined radiation wave of sufficiently small wave lengths (x-rays, neutrons or electrons) is transmitted towards a crystal lattice at an angle and the wave is the in elastically scattered on the lattice and reflected in a direction. This is shown in Figure 2.3. When the incoming wave is in phase with the scattered wave positive interference occurs which amplifies the wave. The condition for this is given by Braggs equation [127]:

$$n\lambda = 2\delta \sin\theta$$

Where n is an integer, λ is the wavelength of the radiation, δ is the distance between the lattice planes and θ is the angle between the incoming wave and the lattice plane. Whenever the Bragg condition is fulfilled the incoming wave is interacting with a specific lattice plane in the crystals thus causing a given reflection. However not all reflections, are allowed as some reflections causes destructive interference that cancel out the scattered wave. Whether a reflection is allowed or not depends on the crystal class and lattice type.

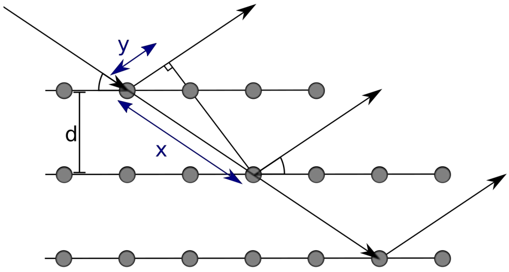

Figure 2.3: Drawing of a crystal lattice with lattice planes separated by a distance d. The incoming x-ray with vector x is scattered when interacting with atoms in the lattice and that scattered x-ray have a vector y. Drawing adapted from [127].

2.2.1 PXRD Setup and measurements

An Empyrean diffractometer from PANalytical with a spinner stage was used for the experiments. The powder samples were placed on zero background plates and packed to achieve uniform height over the sample. The measurements were repeated twice for each sample to monitor time dependent changes in the sample and increase measurement statistics. It was observed that powder samples containing dry chloride salts grew during the measurements due to hydration of the salt. Prior to measuring samples, a LaB6 standard was measured using the same optics. The standard measurement was used to determine instrumental broadening of the diffraction peaks.

2.2.2 Size broadening and data analysis using HighScore Plus

The data treatment was done using the program HighScore Plus from PANalytical, which includes many different methods for analysing PXRD data. The program was mainly used for identifying the different crystal phases in the samples and to perform structure fit to determine the composition and particle size of the samples. The particle size was determined from the crystallite size, which for nanoparticles usually is assumed to be the same. The crystallite size is related to the peak broadening, however other effects contribute to the peak broadening too. The different contributions to the peak broadening must therefore be identified in order to determine the crystallite size. These include the instrumental and micro strain broadening. The instrumental broadening, which comes from optics, sample position, detector position and more, can usually be determined by measuring a standard. For these measurements a LaB_6 standard was measured in the setup using the same optics and sample holder prior to the experiments. Micro strain broadening is more difficult to determine since it is convoluted with the size broadening. However, since the two broadenings have different dependencies on the θ angle it is possible to separate the effects. The broadening from crystallite size described by the Scherer equation [127] is:

$$\beta_{\text{size}} = \frac{K\lambda}{L\cos\theta} \tag{2.3}$$

And for microstrain (mean lattice distortion) [127] the broadening can be described as:

$$\beta_{\text{strain}} = C\epsilon\tan\theta \tag{2.4}$$

Where K is the shape factor, λ is the x-ray wavelength, θ is the Bragg angle. β_{size} is the full width at half maximum (FWHM) broadening from crystallite size given by $\beta_{\text{size}} = \beta_{\text{obs}} - \beta_{\text{std}}$ where β_{obs} is the observed broadening and β_{std} is the instrumental broadening. β_{strain} is the broadening from strain where the instrumental broadening have been subtracted. ϵ is the micro strain and C is a constant depending on the assumptions made on ϵ.

If the broadening, due to size effects and the microstrain, is known, then the size and micro strain can be determined from 2.3 and 2.4 respectively. However, this is seldom the case and further analysis has to be performed in order to deduce the different broadenings. One way to separate the size and microstrain dependent broadening is to utilize their different dependencies on the Bragg angle, which is also seen on equation 2.3 and 2.4. A simple way of achieving this is to construct a so-called Williamson-Hall plot [129] where it is assumed that the total broadening is a sum of the different contributions. By combining equation 2.3 and 2.4 the following relation can be obtained:

$$\beta_{\text{tot}} \cos\theta = C\epsilon \sin\theta \frac{K\lambda}{L} \tag{2.5}$$

By plotting β_{tot} $\cos\theta$ as a function of θ and performing a linear regression on the points. The microstrain can be determined from the intersection $C\epsilon$ and the crystallite size from the slope $K\lambda/L$. The Williamson-Hall method is most applicable when many reflections are present, in cases with only few reflections e.g. for a FCC structure like Pt, which only have 5 reflections in the 15-90 ° 2θ range, it is difficult to achieve a meaningful regression line.

Both the Williamson-Hall method and the Scherer equation depends on a precise description of the peaks or peak broadening, which in the ideal case is simple, but when taking the instrumental factors into account becomes more difficult. Diffraction peaks are, when using an x-ray source, shaped like a Voight function which is a convolution of a Gaussian and Lorentzian function. Since calculating the convolution of the Gaussian and Lorentzian part of the peak is computational heavy an approximation is used instead which is called a Pseudo-Voight function:

$$G_{jk} = \Gamma \frac{C_0^{\frac{1}{2}}}{H_k \pi} \left[1 + C_0 X_{jk}^2\right]^{-1} + (1 - \Gamma) \frac{C_1^{\frac{1}{2}}}{H_k \pi^{\frac{1}{2}}} e^{-C_1 X_{jk}^2} \tag{2.6}$$

Where $C_0 = 4$, $C_1 = 4 \ln 2$, H_k is the full-width at half-maximum (FWHM) of the k^{th} bragg reflection, $X_{jk} = (2\theta_j - 2\theta_k)/H_k$ and Γ determines the mix between the Lorentzian and Gaussian component. The mixing can be 2θ dependent and is described in terms of shape parameters (Γ_1-Γ_3):

$$\Gamma = \Gamma_1 + \Gamma_2 2\theta + \Gamma_3 (2\theta)^2 \tag{2.7}$$

The three shape parameters can be refined from the standard measurement. In addition, the instrument can also cause asymmetry in the peaks, but this asymmetry can be described as a asymmetry function convoluted with the peak function [128]. The Finger, Cox & Jephcoat asymmetry function [130] was used to describe the asymmetry of the diffraction peaks for these measurements. The asymmetry parameters can also be determined by fitting the profile to a standard measurement. When the shape and asymmetry parameters are known the line profile described by equation 2.6 can be fitted to the sample measurement and the peak broadening extracted.

2.2.2.1 Rietveld refinement

Rietveld refinement is different from the other methods presented since Rietveld refinement requires the crystal structure to be known, as the PXRD curve is simulated from the structure. Subsequently the fit is performed by changing the structural parameters. The simulated spectrum is calculated from the following equation [128]:

$$y_{iC} = y_{iB} + \sum_{p} \sum_{k_{1,p}}^{k_{2,p}} G_{ik}^{p} I_k$$

Where y_{iC} is the net intensity of the pattern at point i, y_{iB} is the background at point i, p is the phase, $k_{1,p}$ to $k_{2,p}$ is the range of valid reflections of phase p that contribute to the intensity of point i, G_{ik}^{p} is the normalized profile function eq. 2.6 for a given reflection k in phase p at point i. I_k is the intensity of the peak for reflection k in phase p. The intensity is given as [128]:

$$I_k = S M_k L_k |F_k|^2 P_k A_k E_k$$

Where S is the scale factor, M_k is the multiplicity, L_k is the Lorentz polarisation factor, P_k is a factor from preferred orientation, A_k is the absorption correction, E_k is the extinction correction, and F_k is the structure factor described by [128]:

$$F_k = \sum_{j=1}^{n} f_j \exp\left[2\pi i (\mathbf{h}_k^{\mathrm{T}} \mathbf{r}_j - \mathbf{h}_k^{\mathrm{T}} \mathbf{B}_j \mathbf{h}_k)\right]$$

Where f_j is the scattering factor of atom j, $\mathbf{h}_k$, $\mathbf{r}_j$ and $\mathbf{B}_k$ are matrices representing the miller indices, atomic coordinates and anisotropic thermal vibration parameters respectively. The matrices denoted by a T superscript are transposed. The FWHM can also be described in terms of a Caglioti function [131], which is the description used in the Rietveld refinement:

$$H_k = \sqrt{U \tan^2\theta + V \tan\theta + W} \tag{2.8}$$

Where U, V and W are parameters, which all must be refined from the standard and then depending on the type of analysis some of them are refined for the samples. In case of a size analysis, U and W are refined with the constraint that $U_{\mathrm{obs}} - U_{\mathrm{std}} = W_{\mathrm{obs}} - W_{\mathrm{std}}$. Inserting the constraints into 2.8 yields:

$$H_k = \sqrt{(W_{\mathrm{obs}} - W_{\mathrm{std}}) \tan^2\theta + (V_{\mathrm{std}} - V_{\mathrm{std}}) \tan\theta + (W_{\mathrm{obs}} - W_{\mathrm{std}})}$$

Which can be reduced to:

$$h_K = \sqrt{W_{\mathrm{obs}} - W_{\mathrm{std}}}\sqrt{\tan^2\theta + 1} = \sqrt{W_{\mathrm{obs}} - W_{\mathrm{std}}}\sec\theta \tag{2.9}$$

By inserting 2.9 into 2.3 the angle dependence cancel out and the expression for crystallite size only depends on the fitted parameter W:

$$L = \frac{\lambda}{\sqrt{W_{\mathrm{obs}} - W_{\mathrm{std}}}} \tag{2.10}$$

2.2.2.2 Data treatment

The data was loaded into a file containing instrument calibration made from a standard measurement with LaB_6. The calibration contains the θ dependent instrumental broadening. The repeated measurements were summed and then a constant background was determined for the summed signal. Peaks were in part obtained by an algorithm in the program and by manually adding any additional peaks. The peak form was fitted to equation 2.6 where Γ is known from the calibration. Having fitted the profile function, it was possible to determine the crystallite size, assuming that all the fitted peaks were from the same phase, using the Williamson-Hall plot eq. 2.5. To determine the phases in the sample a search program was executed, which found structures matching the fitted profile. The relevant phases were added to the structure model and the program performed a structure refinement.

The structure model was used in the structure/Rietveld refinement. The Rietveld refinement simulated the spectrum from the structure model and the changed parameters in the structure model to fit the simulated pattern to the measured pattern. First the zero-shift, which was due to a slight sample displacement, and lattice parameters were determined. It was easier to determine, if either the zero shift or the lattice constant for at least one of the phases were known, otherwise the fitting might not have found the right values. To fit the zero shift and lattice parameters i.e. the peak positions, the program needed to describe the peak shape and broadening reasonable well. This was achieved by entering the shape and asymmetry parameters, determined in the standard measurement, and a reasonable guess for peak broadening parameters eq. 2.8. Having determined the zero shift and lattice parameters the crystallite size was determined by a "size-only" fit, where the constraints that $U_{\text{obs}} - U_{\text{std}} = W_{\text{obs}} - W_{\text{std}}$ and $V = V_{\text{std}}$ were applied. The U and W parameters were fitted for each phase and then the size was determined from equation 2.10.

An example of a Rietveld refinement is shown in Figure 2.4, where the same PXRD measurement of Pt nanoparticles is refined in two different ways: In the first case, seen in Figure 2.4c, the spectrum was refined for the crystallite size of a single Pt phase. In the second cases, seen in 2.4d, two Pt phases were refined and allowed to have different crystallite sizes. The refinement in 2.4d describes the measurement much better than the refinement in 2.4c, which also can be seen in Figure 2.4a and 2.4b. These figures display the difference between the measured and simulated spectrum. The difference is an order of magnitude larger in 2.4a than in 2.4b. While the measurement cannot be described by a single size, but there is no guarantee that it makes physical sense to describe it with two; it is always possible to add more phases to a model, and at some point it is possible to make a perfect fit to the data, at least from a mathematically perspective. The simple interpretation of the measurement is that the size distribution is so broad that it does not make sense to talk about one size. The example showed that it is not always possible to determine the size from the peak broadening. In cases where PXRD cannot be used to determine the particle size, other techniques can be used instead. The Small Angle X-ray Scattering technique is presented in the next section, which can be used to measure the size distribution of nanoparticles.

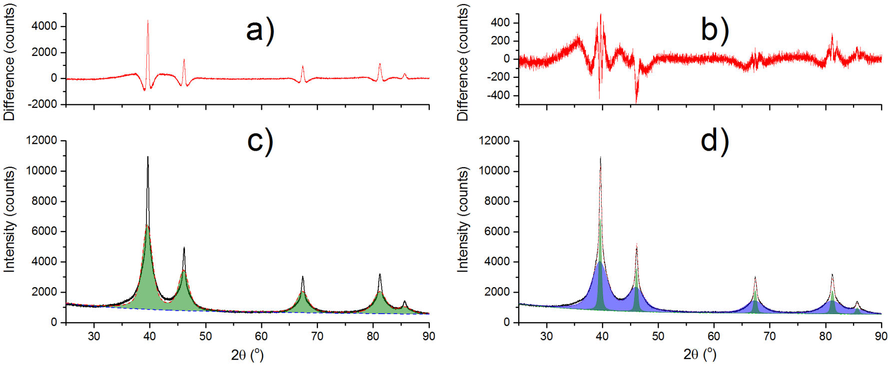

Figure 2.4: Shows two different Rietveld refinements of the same PXRD measurement of Pt nanoparticles. The spectrum in c) was refined with a single phase whereas the spectrum in d) was refined using two Pt phases. The difference between the simulated spectrum and the measured spectrum is shown in a) and b). It is clear that the difference is much larger in a) than in b).

2.3 Small angle x-ray scattering

In addition to PXRD, Small Angle X-ray Scattering (SAXS) was used to measure the size of nanoparticles. SAXS, as the name implies, measures the x-ray scattering at small angles compared to PXRD where the scattering is measured at wider angles. PXRD probes the electron density at length scales corresponding to the lattice spacing whereas SAXS probes the electron density on a 1-100 nm length scale [132,133]. This enables SAXS to measure particle and pore sizes in materials. Monodisperse nanoparticles give rise to oscillations in the intensity, which is size dependent and decays with the scattering vector. Simulated spectra for a 20 nm particle with different Gaussian size distributions are shown in Figure 2.5, which is adapted from [132]. In the monodisperse case (relative standard deviation = 0%), oscillations is found in the intensity, but as the relative standard deviation increases the oscillations disappear, since the measured signal is a sum of different oscillations depending on the particle size. A real measurement is shown in Figure 2.5b for Pt/C nanoparticles, which will be properly introduced in Chapter 6. No oscillations are visible in the figure because the particles are polydisperse. The size distribution can be found by performing a Fourier transform [132, 133].

The SAXS measurements were performed on the same diffractometer as the PXRD measurements, however using a special vacuum pumped stage. The Pt/C samples were measured as well as the carbon support. The carbon support measurement was subtracted from the Pt/C measurements. The analysis was performed by Solveig Røgild Madsen, DTI, using the EasySAXS program from PANalytical.

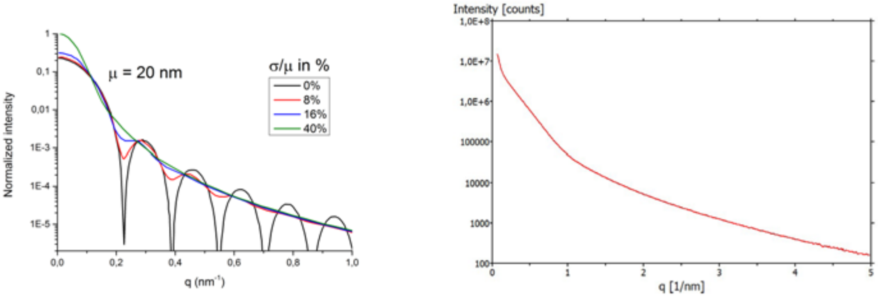

(a) Simulated SAXS spectrum of 20 nm particles

(b) Measured SAXS spectrum of Pt/C

Figure 2.5: a) Simulated SAXS spectrum for 20 nm particles with different Gaussian distributions. The periodicity in the signal disappears as the standard deviation increases. The figure was adapted from [132]. b) Shows a SAXS measurement of a Pt/C sample, which will be presented in Chapter 6. The measurement was performed by Solveig Røgild Madsen, DTI.

2.4 X-ray Photoelectron Spectroscopy

X-ray Photoelectron Spectroscopy (XPS) is used to measure the chemical composition and state of a conducting surface. The technique is based on the emission of photoelectrons from the surface when eradiated with x-rays. The process takes place when a monochromatic x-ray of energy $h\nu_{\mathrm{X-ray}}$ hits an electron in a bound state with energy E_{b} where after the electron is emitted with the kinetic energy:

$$E_{\mathrm{kin}} = h\nu_{\mathrm{X-ray}} - (E_{\mathrm{b}}\phi)$$

Where h is Planck's constant, $\nu_{\mathrm{X-ray}}$ is the frequency of the x-ray and ϕ is the work function, which is the energy required to transfer the electron from the Fermi level E_{F} to the vacuum level E_{vac}. The process is also shown for Cu2p in Figure 2.6a. The mean free path of an electron versus the electron energy is plotted in Figure 2.6b. It is seen that there is a large range where the mean free path is less than 20 Å, signifying that only electrons emitted from the initial 20 Å will reach the detector, which is why XPS is surface sensitive. The XPS instrument measures the kinetic energy of the emitted electrons, but the software is able to calculate the binding energy of the electrons from the measured kinetic energy. The binding energy of orbitals changes from element to element and the measured peak positions can thus be used to fingerprint the chemical composition on the surface. The intensity of the peaks depends on the cross-section of the electron, which changes for orbitals and elements. It is therefore necessary to know sensitivity when quantifying the amounts of the different elements.

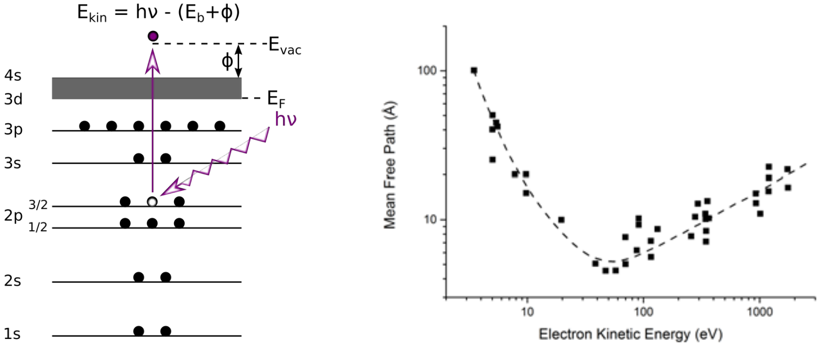

(a) XPS Process **(b)** Mean free path of an electron

Figure 2.6: The excitation of a 2p photoelectron from Cu. A x-ray with energy $h\nu_{\text{X-ray}}$ is exiting an electron with a binding energy E_b that then leaves with a kinetic energy E_{kin}. The figure was adapted from [127]. b) The mean free path for an electron with certain energy. It is seen that in the energy range 10-2000 the mean free path is less than 2 nm which is what makes the XPS technique surface sensitive. The figure was adapted from [11].

2.4.1 Sample preparation and data analysis

The XPS method was used to measure powder samples of nanoparticles. The nanoparticles were attached to a two-sided adhesive carbon tape, which was placed on a piece of Al foil. The samples were prepared immediately before loading them in the machine. The data analysis was done in the Thermo Advantage software. The software controls the XPS and converts the measurement into a binding energy spectrum. For each sample a survey spectrum was recorded to determine which peaks are present and thus which elements are present. Detailed spectra were subsequently recorded for the most intense peak of the species present which were Pt4f, Y3d, C1s, and O1s. The peaks were quantified using a Shirley background and integrating the peaks. The sensitivity factor for Y3d on the equipment had previously been determined by Paolo Malacrida [134], and additional sensitivity factors were found in the XPS software database. In cases where peaks were overlapping, the individual peaks were determined by fitting, using the build-in fitting functionality in the software package. The fitting was done with as few peaks as possible to describe measurement i.e. reducing the difference between measurement and the fit, to the apparent noise level for the measurement.

2.5 Electron microscopy

Electron microscopes offer nanometre resolution and in some cases even atomic resolution, which allow us to visualise nanostructures that would not be visible in optical microscopes due to a fundamental limit in resolution of about 0.5 µm when using visible light [127]. Electrons have a much smaller wavelength and therefore it is possible to visualise nanometre structures. The electrons can interact with matter in different ways as illustrated in Figure 2.7. Backscatter electrons are backscattered after having interacted with electrons of the elements in the sample and thus have mass contrast. Secondary electrons are scattered inside the sample but eventually escapes and hit the detector. As more electrons escape close to edges, these have higher intensity and this adds topography to the image. The incoming electrons will also inelastic scatter with the electron in the sample and thereby ionize the atom. In the following relaxation of the atom either x-rays or Auger electrons can be emitted. The energy of the Auger electron corresponds to the difference in energy between the excited core electron, the electron that relaxes to the core level and the emitted electron. Different elements will emit Auger electrons with different energies, thereby allowing for the element to be identified. The emitted x-rays will also have characteristic energies depending on the element, and the emitted x-rays can thus be used to identify the elements in the sample. Elemental identification using this method is called Energy-Dispersive X-ray (EDX) spectroscopy. Electrons can also transmit through the sample if the sample is thin enough. There are generally two kinds of transmitted electrons; those that pass through without interacting with the sample (called bright field) and the diffracted electrons (called dark field).

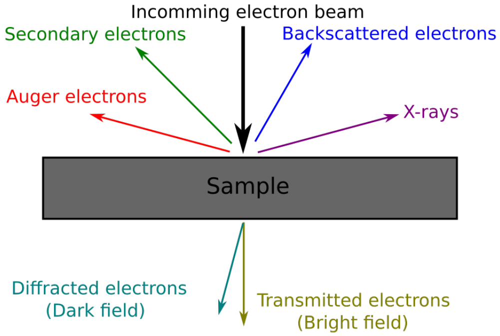

Figure 2.7: Shows the principle of electron microscopy. An incoming beam of electrons interact with the sample and different types of electron beams leave the sample.

2.5.1 Scanning electron microscopy

Scanning Electron Microscopy (SEM) was used to visualise large nanoparticles and to determine the average elemental composition of the sample using EDX. The samples, nanoparticulate powder, were dispersed on a Cu TEM grid. The SEM images shown in Chapter 5 were recorded using a secondary electron detector. For the elemental composition two or three images were recorded at different positions with a low magnification 2.5 k in order to get the average composition over a large area. The spectra was analysed in the EDX detectors software where the peaks were assigned to different elements, and the composition was determined from fitting the spectrum. The resulting values are based on the average value of the 2-3 measurements per sample.

2.5.2 Transmission electron microscopy and scanning transmission electron microscopy

Both Transmission Electron Microscopy (TEM) in Bright Field (BF) mode and Scanning Transmission Electron Microscopy (STEM) with High Angle Annular Dark Field (HAADF) were used to characterise nanoparticles. In both cases the nanoparticles samples were dispersed on a Cu TEM grid. The TEM images were recorded at 80 kV in a FEI Tecnai T20 G2 and the STEM at 300 kV in a FEI Titan Analytical 80-300ST TEM.

3

Catalyst performance in the DMFC

The goal of my PhD project was to develop new catalyst for a µ-DMFC in order to increase the power density of the µ-DMFC. To develop the right catalyst it is important to know where the losses are in the µ-DMFC and how the catalyst performs. It is quite tedious and time consuming to test new catalyst in a fuel cell and performance gains/losses can also be related to how the design and assembly of the fuel cell and thus it can be difficult to extract the kinetic performance from the measurement. Catalyst for the ORR and MOR may alternative be tested in liquid half-cells, but it can be difficult to mimic the conditions from the DMFC in the liquid half-cell.

This chapter examines the performance of the µ-DMFC and the catalytic performance of the electrodes used in the DMFC. To achieve this it is necessary to measure the absolute potential of the anode and cathode in the DMFC, since it makes is possible to measure the overpotential of the anode and cathode. In addition the operating potentials of the electrodes are relevant for designing half-cell experiments, so the catalyst can be tested in the half-cell under realistic conditions. For these measurements a modified version of µ-DMFC, presented in Section 1.2, is fabricated where it was possible to connect the DMFC to a reference electrode. In addition the half-cell measurements of the anode electrode will also be explored, to determine how the performance relates to the anode in the DMFC.

3.1 Experimental setup and fabrication of fuel cells

DMFCs and fuel cells in general are mostly measured with what is called a load box. The load box is basically an adjustable resistor, which the load box changes automatically in order to draw a specified current. The load box can simulate the real usage of the fuel cell and measure the overall performance; however it is not good for diagnostics and probing the individual components of the fuel cell. Using a potentiostat/galvanostat it is possible to measure the anode and cathode potential individually, if a reference electrode is used. In addition impedance spectroscopy can be performed with a potentiostat to determine the ohmic and polarisation resistance of the fuel cell.

3.1.1 Fabrication of fuel cell and setup

This is the procedure for producing the modified version of the µ-DMFC presented in Section 1.2, where the design is explained and the different layers are also shown in Figure 1.6.

The first step in the fabrication of the µ-DMFC is the fabrication of the electrodes. The electrodes were made with HiSPEC 13100 70% wt. loading Pt/C and HiSPEC 12100 75% loading PtRu/C catalyst from Johnson Matthey. The catalyst was dispersed in inks based on isopropanol, polyvinylpyrrolidone (PVP) and Nafion solution. The inks were sonicated using a sonic horn before deposition. The deposition was performed on a gas diffusion layer consisting of a carbon cloth with a thin microporous layer on top by using a robot-controlled airbrush. The loadings were 14.6 mg/cm^2 PtRu/C and 3.53 mg/cm^2 Pt/C for the anode and cathode respectively. The anode and cathode electrodes were punched out in sizes of 0.63 x 0.63 mm and 0.60 x 0.60 mm respectively. The casing for the fuel cell was custom made and consisted of two parts, a fuel tank and a power pack where the DMFC was placed. The power pack was assembled first; a Nafion 117 membrane was placed in the bottom of the power pack, which is where the inlets to the fuel tank are, and enclosed by placing a perforated plate on top. Next, a carbon cloth followed by the anode electrode, which was placed on top. The membrane Nafion 117 was placed on top of the anode catalyst layer and then the cathode catalyst layer was placed on top of that. After the cathode a carbon cloth was added followed by the cathode plate, which was followed by a gasket. The whole power pack was hot pressed together. The fuel tank was welded together with the power pack and cables were consecutively welded to the anode and cathode connections. The fuel cells were fabricated by Torsten Lund-Olsen from DTI.

An important distinction in this design compared to the one presented in Section 1.2, was the longer membrane, which was used in order to have some extra membrane that could be led out of the DMFC as seen in Figure 3.1a, where the membrane is protrudes from the cathode side. This is not an optimal design because fringe electric fields on the edge of the MEA can affect the potential. A more optimal design would be that of Hinds et al [106], where the connection to the membrane is made through the electrode. This was also attempted, but not successful as the µ-DMFC is too small for that kind of procedure and thus the design with the extended membrane was used instead. The cell was placed in Millipore water prior to use to ensure the membranes were hydrated. The setup is seen in Figure 3.1b where the very small cell is placed close to one of the inlets in the glass cell where the extended membrane goes into the glass cell filled with 0.5 M H_2SO_4 electrolyte. An $Hg|Hg_2SO_4$ reference electrode is also placed in the cell. The WE is connected to the cathode, the CE to the anode and the Ref to the $Hg|Hg_2SO_4$ reference electrode. The µDMFC was placed inside a small plastic holder with venting holes. In cases where H_2 gas atmosphere is needed on the cathode, the gas is fed through the small venting holes in plastic casing.

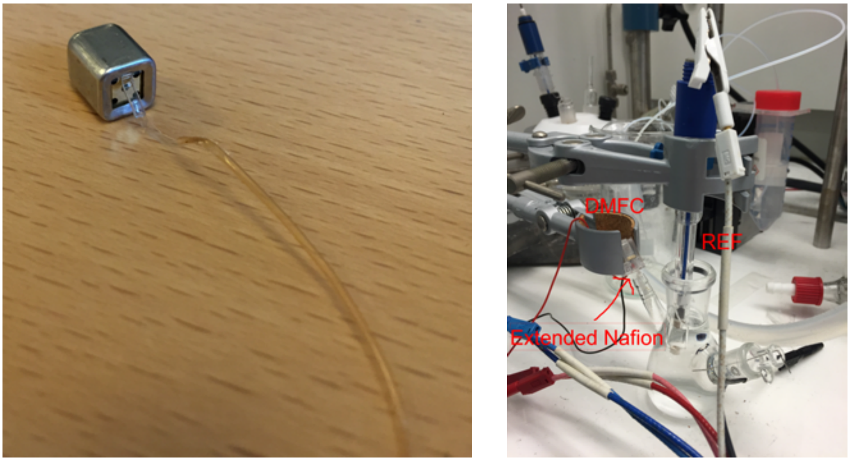

(a) µ-DMFC with reference electrode

(b) Setup for measuring µ-DMFC

Figure 3.1: Shows µ-DMFC with extended membrane a) and the µ-DMFC connected to a reference electrode via a cell with 0.5 M HClO4. The small red and black cables are welded to the cathode and anode respectively. The large red cable (WE) is connected to the cathode and the blue cable (CE) is connected to the anode. The white cable is connected to a $Hg|Hg_2SO_4$ reference electrode.

3.1.2 Measurements of anode and cathode potentials

Before measuring the DMFC, the reference potential was calibrated by flowing H_2 over the cathode while measuring the open circuit voltage (OCV) of both the anode and cathode as seen in figure 3.2a. The potential of the cathode drops considerably when the H_2 flows and then it reach a somewhat stable potential as seen on the insert. The average cathode potential is then used to calculate the potential vs RHE for the anode and the cathode. Figure 3.2a further shows that the anode potential decreases when the H_2 flows over the cathode. This is due to H_2 leaking to anode and since the methanol is in a gaseous phase H_2 will compete with methanol for adsorbing on the anode catalyst. Figure 3.2b shows how the I-V curves were recorded for both the anode and cathode. The experiment was recorded using a Staircase Galvanostatic Electrochemical Impedance Spectroscopy (SGEIS) technique, where the experiment would run at constant current for 15 min and then the impedance spectroscopy would start measuring from 100 kHz to 5 mHz with an amplitude of 1 mA. The measurements were done in steps of 2 mA and the potential was extracted after 15 min at each current. The potential never reaches a stable plateau for the final current, which is when the mass transport resistance starts, and it is not possible to increase the current without the cell going to zero as seen at the end time om figure 3.2b.

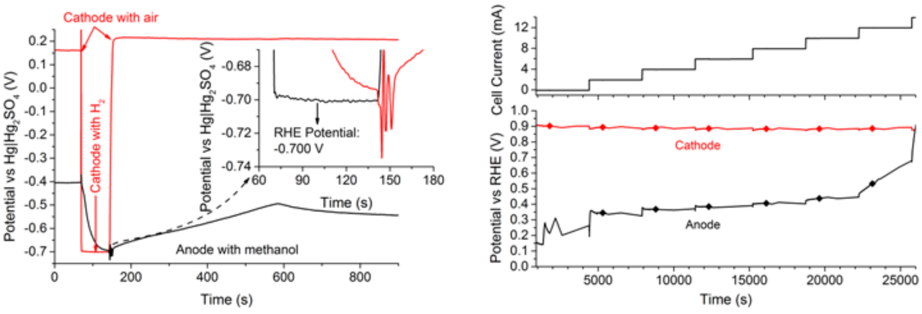

(a) OCV

(b) Galvanostatic

Figure 3.2: Shows a) the open circuit potential of the anode (black) and cathode (red) while the cathode is breathing air and while H_2 is flowing over the cathode (60-140s). The open circuit potential, while H_2 is flowing, was used to calculate the zero point of the RHE scale. b) Shows a galvanostatic experiment where the anode and cathode potential is measured for different cell currents. The cell currents are shown in the top graph. The points mark the values used in the I-V curve for the DMFC measurements and are recorded after 15 min for each current.

3.1.3 Half-cell measurements of DMFC anode electrodes

The electrodes used for the anode in the DMFC were also tested outside of the fuel cell in a liquid half-cell setup. The setup shown in Figure 3.3a and 3.3b consist of two glass half-cells that can be put together. The electrode was placed in between the two glass pieces, using a metal clamp to keep the pieces together. 0.5 M H_2SO_4 was added to cell on the catalyst side of the electrode. A platinum mesh was used as counter electrode and the electrolyte was purged with Ar prior to measurements. An Hg|Hg$_2$SO$_4$ reference electrode was used and was connected to the main chamber via a porous frit. Lastly the right part of the cell was filled with gas, either Ar, CO or H_2 depending on the experiment.

3.1.3.1 Determining the RHE potential

The potentials for the RHE scale was found by measuring the OCV while flowing H_2 on the backside of the electrode for 1 min and then using the average value. The measured values where in the range -0.706 - -0.709 V vs Hg|Hg$_2$SO$_4$. The measured potential was then corrected using this value and equation 2.1

3.1.3.2 Ohmic resistance

The ohmic resistance was measured by using galvanostatic impedance spectroscopy from 100 kHz to 1 Hz with 1 mA pulse. The ohmic drop value was found from the fitted high frequency intercept from the impedance measurement. As the value changed slightly at high current densities, the impedance measurements were performed for each methanol oxidation current measured. The ohmic drop compensation was calculated using the equation 2.2.

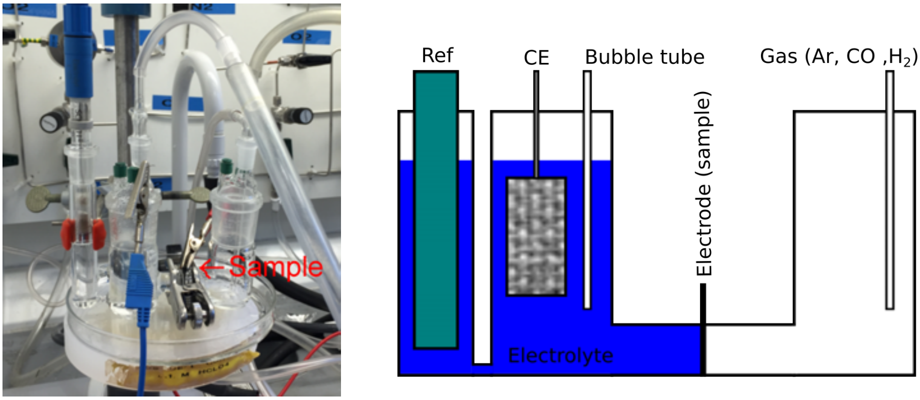

(a) Picture of setup

(b) Drawing of setup

Figure 3.3: Shows a picture a) and a drawing b) of the H-cell setup. The H-cells consist of two halves that are put together with the fuel cell electrode in between them. The catalyst is facing the electrolyte side and the gas diffusion layer the gas side.

3.1.3.3 Electrochemical surface area measurement from CO stripping

The electrochemical surface area (ECSA) was measured using CO stripping. A reference CV was first recorded while Ar was flowing on the backside. The CV was recorded with 85% online ohmic drop compensation, since the larger current densities, due to the high catalyst loading caused significant potential shifts. The CO stripping was recorded at 1-5 mV/s depending on the catalyst loading, since the large capacitive current from the high loading combined with the residual resistance in some cases caused severe potential shifts. The CO stripping cycle were performed by keeping the potential at 0.05 V vs RHE for 30 min. Gas was changed to CO for 5-10 min and then changed back to Ar. The stripping cycle was performed at same scan speed as the reference cycle and the area was calculated from the integrated CO stripping peak area using a line as background, and assuming a CO stripping charge of 420 $\mu C/cm^2$ [135].

3.1.3.4 Methanol oxidation reaction

Methanol oxidation reaction activity was measured by changing the electrolyte, 0.5 M H_2SO_4 , to one containing 0.5 – 2M methanol. The electrolyte was flushed with Ar prior to the experiment and Ar was flowing on the backside on the electrode for the duration of the experiment. It was attempted to measure the MOR activity potentiostatically, however the large currents and residual ohmic drop made it difficult to predict the uncompensated potential. Therefore the galvanostatic technique was applied, for the same current densities as for the DMFC measurements. It was observed that the ohmic drop could change at higher current densities. The galvanostatic technique was therefore combined with the impedance technique for the MOR measurements. At each current the potential was first recorded for 5 minutes and then the impedance measurement was performed as in Section 3.1.3.2.

3.2 Fuel cell measurements

The measurements presented in this section are mainly focused on two supposedly identical cells that have been prepared in the same manner described in Section 3.1.1 and using the same anode and cathode electrode material. The cells are named cell A and cell B where cell A is representative of a well-constructed cell which is able to deliver minimum 420 mV continually while drawing 8 mA. Cell B is an example of a substandard cell that initially was able to deliver above 420 mV, but after a day the performance degraded and after a week the cell could only deliver 274 mV continuously at 8 mA. However, long term measurement have shown that the µ-DMFCs are stable and only degrade about 2.8% per 1000 hours [1], and thus making the major degradation of Cell B unusual. In the following measurements, the operating potentials of the functional cell will be identified as well as the main losses of both cell A and B.

Figure 3.4a shows the anode and cathode potential vs RHE for Cell A (green) and Cell B (red) compared to the average potential measured for five well-constructed cells including Cell A (purple). The measurements were done galvanostatic as described in Section 3.1.2. The anode and cathode potentials were measured simultaneously. However, due to different electrode areas for the anode (0.63 x 0.63 cm) and cathode (0.6 x 0.6 cm), the anode and cathode points are slightly shifted from each other on the current density scale. The figure shows that Cell B has a larger anode (40-80 mV) and cathode (110-120 mV) overpotential compared to cell A. The anode potential for Cell A is close to the average value of the well-constructed cells for lower current densities (<30 mA/cm^2), and the cathode potential is slightly higher than the average value, and thus Cell A is representative for the well-constructed cells. For all cells the anode potential increases sharply with current density. The anode is thus setting the limit for maximum current density that can be drawn continuously. The standard deviation for the anode potential (purple) is increasing for higher current densities (>30 mA/cm^2), which is due to different limiting current densities for the different cells. In Figure 3.4b the cell potential and cell power density is plotted as a function of the anode current density for cell A and B. The peak current density is achieved around 25 mA/cm^2 for both cells, but the maximum current density is almost doubled for cell A compared to cell B. Comparing Figure 3.4a and 3.4b reveals that the maximum in power density is due to the sharp increase in anode overpotentials for both cells around 30 mA/cm^2. If the anode potentials increased less with current density, then the cells would have a higher maximum power density as seen for the average power density of the well-constructed cells.

Staircase Galvanostatic Impedance Spectroscopy (SGEIS) was used to measure the impedance spectra of the DMFCs in order to determine their ohmic losses. The impedance spectra of cell A and B are seen in Figure 3.5a together with the

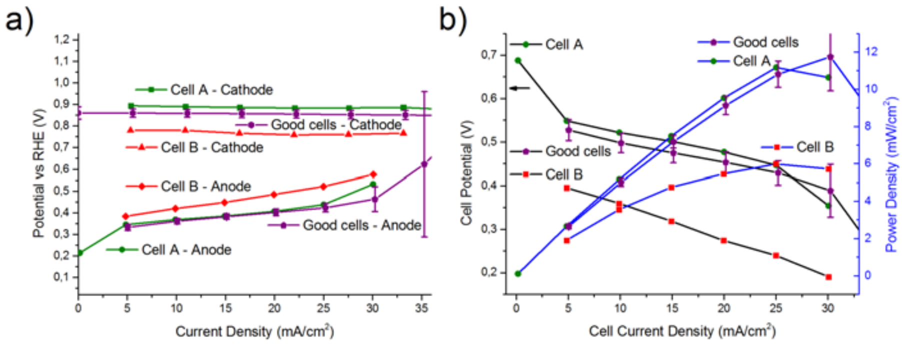

Figure 3.4: Shows the performance of two DMFCs: Cell A and Cell B compared to the average value of five well constructed cells. a) The anode and cathode potential plotted for different current densities. b) Shows the cell potential and power density as function of the cell current density (anode). The black lines are the potentials and the blue the power densities.

spectra of two standard DMFCs without the reference electrode modification. The two extra cells (C and D) were measured to determine if the reference electrode modification would change the impedance spectrum. From Figure 3.5a it is evident that the overall spectra of cell B, C and D are quite similar and at the high frequency range, seen in the insert, all four cells show similar spectra. All spectra were recorded while drawing 8 mA from the cells. The spectra consist of a general shift in impedance, R_0, as well as four arcs, which are all marked in the figure. The negative arc, arc 4, is only observed for the unmodified cells, which could be due to lower frequency limit, meaning that if the limit was set even lower, the negative arc might also become visible for the modified cells. The spectra can be compared with the spectrum of an active DMFC seen in Figure 3.5b, which was adapted from [136]. Evidently arc 1, 3 and 4 are also observed in the Figure 3.5b. In the paper by Lai et al 2008 [136] and 2007 [137], they attribute the different arcs: Arc 1 is related to the interfacial impedance, Arc 3 to an electrochemical reaction and arc 4 to an anodic reaction involving adsorbed CO. Arc 1 has also been observed by other groups [103, 138, 139] and the negative loop is likewise observed elsewhere too [103, 103, 138, 140, 141]. The purpose of the impedance measurements was not to completely model the DMFC, although interesting differences are seen in the spectra between the well performing cell A and the others. Instead, impedance measurements were used to identify the ohmic losses, which from the insert in Figure 3.5a appear to be no more than 0.5 Ωcm^2 for the sum of ohmic and interfacial resistance, which corresponds to an internal resistance of the cells of less than 1.3 Ω. This small resistance has little impact on the performance of the cells; as at the highest current draw in these measurements, 12 mA, the ohmic loss would be 15.6 mV which is about 1% of the theoretical cell potential.

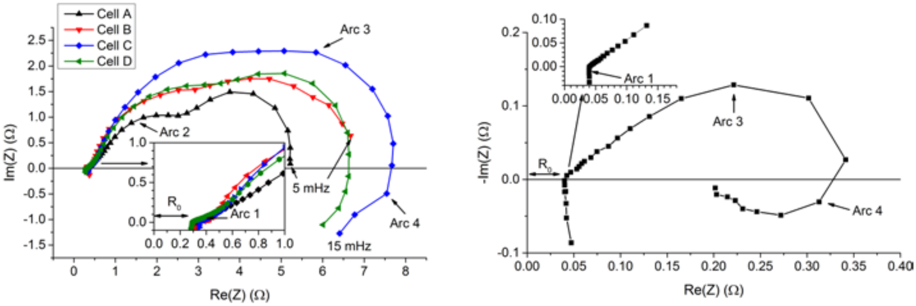

(a) Nyquist plot of µ-DMFCs **(b)** Nyquist plot of an active DMFC [136]

Figure 3.5: a) Impedance spectra of µ-DMFC at 8 mA where cell A and B are modified with reference electrode and cell C and D are standard cells with similar performance as cell B. Four arcs are visible in the spectra. b) Impedance spectrum of an active DMFC adapted from [136] shown for comparison with a). The spectrum shows some of the same features as in a). The small arc 1 is present in both a) and b) as well as arc 3 and the negative arc 4.

3.2.1 Fitting of cathode potential data

To determine the losses due to ORR kinetics and methanol crossover the cathode potential data from the two cells was fitted to the model in equation 1.4 and 1.6. It is assumed that the kinetics can be described by equation 1.6 using the kinetic data from [2,5] with a roughness factor calculated from the electrode loading. The fitting is shown in Figure 3.6a and 3.6b for cell A and B respectively. The blue expected kinetics curve is calculated from equation 1.6 at 25°C with an ambient air partial O_2 pressure of 21.17 kPa and roughness factor of 2118 corresponding to a loading of 3.53 mg/cm^2 Pt with an ECSA of 60 m^2/g. The fitted roughness factor was 588, which is 28% of the expected value. This may be interpreted in two ways: Either that only 28% of the cathode catalyst material is being utilised, or the catalysts activity is only 28% of the Pt/C in [5], or a combination of the two. The fitted methanol crossover current density was 40 mA/cm^2, which is comparable to the measurements of Thomas et al [8], who measured the methanol crossover through a Nafion 117 membrane at 60-120 °C. Extrapolating from their data by means of linear regression, the methanol crossover should be 49 mA/cm^2 at 25 °C and 1 M methanol. The overpotential of the cathode in cell B seen in Figure 3.3b, is too high to fit the roughness factor as it would be unrealistic low 3, and it is likewise unrealistic that methanol crossover alone can explain it as that would correspond to at crossover current of 5700 mA/cm^2. It is more likely a combination of methanol crossover and mass transport limitations. In case of a mechanical failure where concentrated methanol could travel to the cathode, that would severely poison the cathode and the methanol liquid could also start blocking the O_2 transport if a methanol layer is formed on top of the catalyst layer. The fit shown in figure 3.6b assumes the same kinetics as fitted in figure 3.6a and then fits the methanol crossover to fit the measurement.

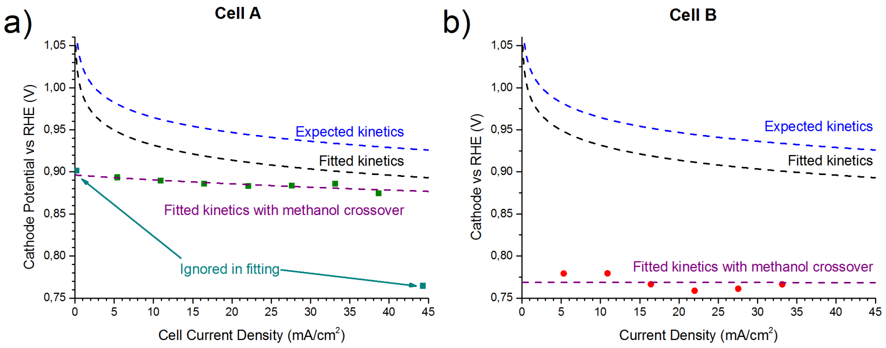

Figure 3.6: Shows the cathode potential of cell A and B in a) and b) respectively. The potentials are plotted with fitted kinetics with and without methanol crossover and the expected kinetics calculated from the catalyst loading.

3.2.2 Fitting of anode potential data

The anode potential data from the fuel cell measurements shown in Figure 3.1 were also fitted. To describe the anode potential, a model consisting of a kinetic part and a concentration limitation part from [142] was used:

$$\begin{aligned} U_{\text{Anode}} &= U^{\circ}_{\text{Anode}} + \eta_{\text{MOR}} + \eta_{\text{Conc}} \\ &= U^{\circ}_{\text{Anode}} + \frac{2.303RT}{\alpha_{\text{A}}F}\left(\log\left[\frac{J}{J_0}\right] - \log\left[\frac{J_{\text{lim}} - J}{J_{\text{lim}}}\right]\right) \end{aligned} \tag{3.1}$$

Where U°_{Anode} is the thermodynamic reversible potential of methanol oxidation, η_{MOR} is the overpotential due to MOR kinetics; η_{Conc} is the overpotential due to concentration limitations of reactants, R is the gas constant, T is the temperature, α_{A} is the anodic transfer coefficient, F is Faradays constant, J is the current density, J_0 is the exchange current density, and J_{lim} is the limiting current density, proportional to reactant concentration. The temperature was fixed at 298.15 K. To verify the kinetic data a simpler model was also employed which only consisted of the kinetic overpotential [142]:

$$U_{\text{Anode}} = U^{\circ}_{\text{Anode}} + \frac{2.303RT}{\alpha_{\text{A}}F}\log\left[\frac{J}{J_0}\right] \tag{3.2}$$

The fitted data is shown in Figure 3.7a and 3.7b for cell A and B respectively. Two models were applied for the data from cell A to determine the effect of the transport limiting term in eq. 3.1 on the fitted kinetic parameters. Model 1 includes both kinetics and mass transport limitations and is described by equation 3.1. The second model is purely kinetics, eq. 3.2, and is only fitted in the 5-20 mA/cm^2 range, where the points fit a Tafel line. The two models result in different exchange current densities which are seen from the black and yellow line in Figure

3.7a. Evidently model 2 have a higher overpotential for MOR of about 26 mV at 20 mA/cm^2 compared to model 1. The fitted parameters are shown in Table 3.1, in which the transfer coefficient changes from 0.79 in cell A to 0.55 in cell B, corresponding to a change in Tafel slope from 75 to 106 mV/dec. The transfer coefficient should be the same in all cases and thus the difference could suggest that the fitted parameters are not only describing the kinetics. Because of the different Tafel slopes it is not possible to compare the exchange current densities directly however, the activities will be discussed further in Section 3.3, and compared to catalyst kinetic date. The limiting current density is similar for the two cells and the values match the experimental observations that the cell potential of the two cells would approach zero, when the current density was increased further.

	Cell A	**Cell B**	**Average of well-constructed cells**
Model 1			
J_0 [mA/cm^2]	3.6E-4	0.0026	3.24E-3 ± 4.46E-3
α_A	0.79	0.55	0.68 ± 0.1
J_{Lim} [mA/cm^2]	30.42	32.63	41.16 ± 6.72
Model 2			
J_0 [mA/cm^2]	0.0021		0.0097 ± 0.0064
α_A	0.62		0.54 ± 0.06

Table 3.1: Shows the fitted values and standard deviation in fitting from the fitting shown in figure 3.7 plus the average fitted values of cells not shown. Model 1 is based on equation 3.1 and model 2 on equation 3.2.

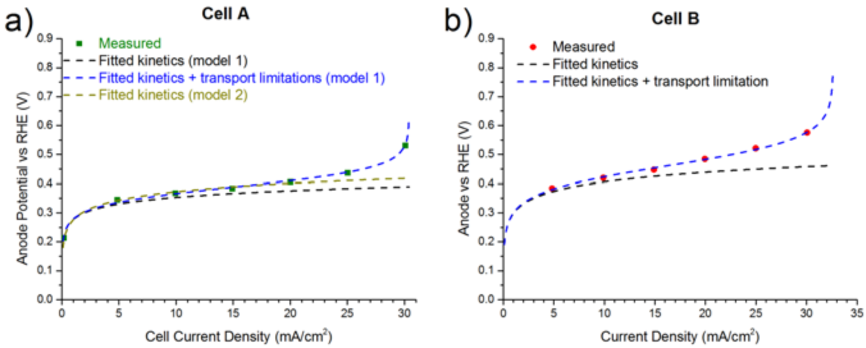

Figure 3.7: Shows the anode potential for cell A and B on a) and b) respectively. Model 1 is based on equation 3.1 and model 2 on equation (3.2.

3.2.3 Losses in the µ-DMFCs

By combining the results of fitting the anode and cathode in Section 3.2.1 and 3.2.3 it is possible to visualise the main losses in cell A and B shown in Figure 3.8a and 3.8b respectively. The figures show that the two largest losses in the two cells are the kinetics of MOR and ORR. Both cells are also limited by a low limiting current density of about 30-32 mA/cm^2, which limits the max power density of the cell. Methanol crossover is also an issue for both cells although it is not as big a problem in a well-constructed cell (cell A) than in a substandard cell (cell B). The performance of the cells could be improved by using a more methanol tolerant ORR catalyst, however, the methanol crossover is not severe enough to justify using Ru and Ru_xSe_y type catalyst, because the kinetic overpotential penalty for using these catalyst [2,96], is larger than the overpotential from methanol crossover. Alternatively the DMFCs could use a more active MOR and ORR catalyst, which would result in a higher cell potential. However, to gain significantly higher power densities, the cells need to operate at higher current densities than cell A and B. The limiting max current density is related to the methanol and water concentrations at the anode, and one or both are limited. It should be noted that these cells with reference electrodes are built slightly different with the membrane being extended out through the cathode. The piece of membrane outside the cell can act as a source or drain of water and explains why the water management is sub optimal on these cells. Ideally, these measurements should have been performed without extending the membrane and rather having the reference electrode contact to the membrane inside the fuel cell assembly. That is however difficult to achieve when the fuel cells are so small.

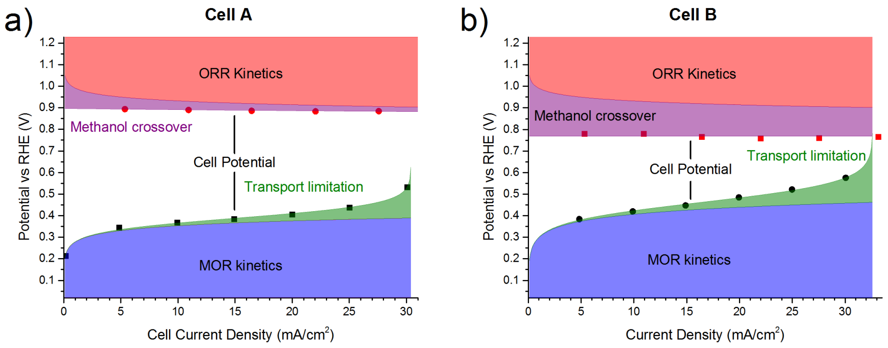

Figure 3.8: Shows the qualitative losses in cell A and B on a) and b) respectively. The filled areas are based on the fitting performed in figure 3.6 and 3.7.

3.3 Measurements on fuel cell electrodes

To measure the activity of the catalyst on the anode electrodes, the electrodes was measured in a H-Cell as shown in Figure 3.3, using the procedure described in Section 3.1.3. In half-cells measurement of MOR, the experiment is either done with potential cycling or potentiostatic at 0.4 - 0.6 V vs RHE [7,32,35,45]. These procedures are not practical in a liquid electrolyte with a high loading where high ohmic resistance and high currents in turn makes it difficult to control the potential. Rather, the measurements were done galvanostatic using the same current densities as for the DMFC measurements. A commercial DMFC anode from Alfa Aesar with 4 mg/cm^2 loading of PtRu/C catalyst was measured galvanostatic. The ohmic drop compensated potential vs RHE is shown in Figure 3.9a. Here, the red points have been compensated using the ohmic resistance measured at OCV, while for the black points the ohmic drop was measured for each point during the experiment, and the potentials have been corrected with the resistance measured at each current. The difference between the two corrections is seen at high current densities above 35 mA/cm^2. The two dataset were fitted to the Tafel equation 3.2, showing that for the point corrected data the fitted curve passes through all of the points, whereas for the other dataset the Tafel equation does not fit. The ohmic restances measured at different currents are shown in Figure 3.9b, demonstrating that the resistance is more or less stable until about 35 mA/cm^2 and upon which starts to decrease slightly. The difference between the highest and lowest resistance is less than 3%, but the impact on the measurement is quite significant as seen in Figure 3.9a.

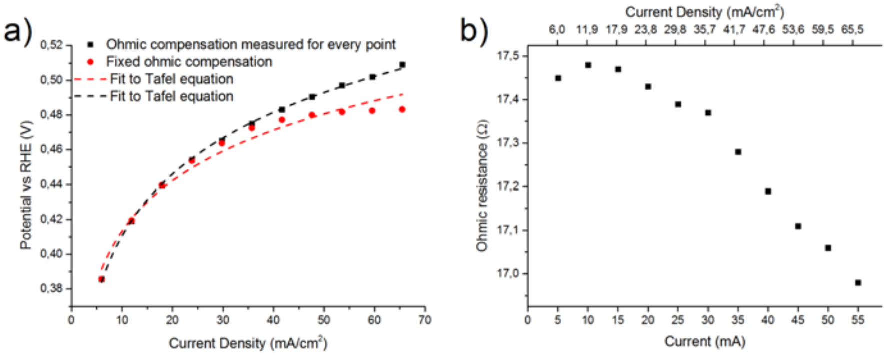

Figure 3.9: Shows galvanostatic measurements of MOR with 2 M methanol in 0.5 M H_2SO_4 at room temperature. a) The red points have been compensated for ohmic drop by using the ohmic resistance measured with GEIS at OCV. The black line has been compensated for ohmic drop by using ohmic resistance measured during the experiment. b) Shows the fitted ohmic resistance from the GEIS measurements.

The Tafel slope for the point corrected measurement from Figure 3.9a is displayed in Figure 3.10 (black points) together with a linear regression (black line). The linear regression fits very well with a R^2 value of 0.999 and a slope of 117.9 ± 1.2 mV/dec, which is close to the expected 120 mV/dec thus indicating a transfer coefficient α close to 0.5 [143–145]. The Alfa Aesar 4 mg/cm^2 PtRu anode measured in the H-cell (black) is compared to 14.6 mg/cm^2 PtRu anodes measured in the DMFCs and normalised to Pt mass. The mass activities of the Alfa Aesar electrode are in between the measurements of unmodified DMFC cells and DMFC cells with build-in reference electrode. The data from the H-Cell and DMFC Cells are not directly comparable since the measured potential in the DMFCs are not only related to kinetics and because the evaporation membrane in the DMFCs makes it difficult to define the methanol concentration at the anode. In addition, data from measurements of thin film nanoparticulate electrodes with the anode catalyst in 0.5 M methanol in 0.1 M $HClO_4$ [45] was also added for comparison. The anode potential in the DMFC was around 0.4V vs RHE in the measurements as seen in Figure 3.7a and thus comparison of activity should be done at 0.4 V vs RHE. At this potential the mass activity of cells with reference electrodes, the Alfa Aesar electrode and the catalyst measurement are all within a factor of two of each other.

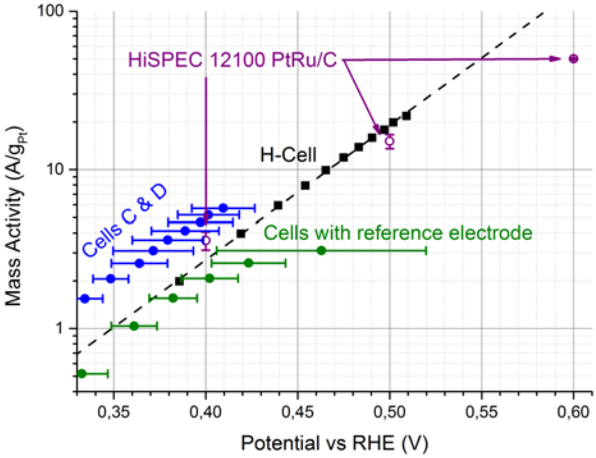

Figure 3.10: Tafel slope (black line) of the point corrected MOR measurement of a Alfa Aesar 4 mg/cm^2 PtRu DMFC Anode in 2 M methanol in 0.5 M H_2SO_4 at room temperature. The H-Cell data is co-plotted with the current densities normalised to mass vs anode potential for the DMFC (green and blue triangles) and liquid half-cell (0.5 M methanol in 0.1 M $HClO_4$) measured activity of the catalyst used in the electrodes [45]

3.4 Summary

The aim of this chapter was to measure performance of the DMFCs, the anode and cathode electrodes, in order to both determine the losses in the DMFCs and the conditions in which DMFC catalysts should be tested. The performance of the µ-DMFC was measured for a well-constructed and poor cell. It was possible to measure the absolute potential of the anode and cathode by extending the membrane out of the fuel and into a reference cell with a reference electrode. From the anode and cathode measurement is was seen that the anode was limiting the maximum power density as the anode potential increased suddenly around 30-48 mA/cm^2 in galvanostatic measurements. Impedance measurements were performed on both cells and showed that the ohmic resistance was close to identical about 1.3 Ω for the two cells. The operating potentials of the anode and cathode electrodes in the DMFC were approximately 0.4 V vs RHE and 0.9 V vs RHE for the anode and cathode respectively, thus establishing that activity measurements of catalysts should be performed at these potentials. The losses were mainly due to kinetics where about 56% of the theorectical potential is lost. Only 2% of the cell potential was lost to methanol crossover, for the well-constructed cell and ohmic losses were about 1% for all of the cells.

The measured cathode potentials were fitted to a kinetic model with methanol crossover, demonstrating that for the well-constructed cell the cathode only exhibited 28% of the expected activity, which can be explained by either the catalyst utilization or the catalyst being less active than expected in the model. The fitted crossover current density was 40 mA/cm^2, which is reasonable compared to literature measurements of methanol crossover for the membrane used. The model was also applied to the cathode data of the poor functioning cell, but fitted values were not realistic, which suggest more than kinetics and methanol poisoning to be limiting the cathode.

The anode potential data was likewise fitted to a model consisting of a kinetic term and concentration-limited term. The model fitted the poor working cell best, but in both cases the limiting current density was fitted to 41 mA/cm^2 in average. Anode electrodes were measured for MOR in an H-cell setup. The measurement was highly depended on ohmic drop compensation because the ohmic resistance in the electrolyte changed at high currents. The ohmic compensated measurements could be fitted to the Tafel equation and had a Tafel slope of 118 mV/dec, which suggest a transfer coefficient α of 0.5. The activities of the H-Cell measurements were compared to the DMFC anode measurements, both normalised to mass activity, and at 0.4 V vs RHE the mass activities were within a factor of two of each other.

4

Catalyst activity in a rotating disk electrode setup

The rotating disk electrode (RDE) is a fast and easy method for measuring the activity of catalysts compared to fuel cell testing. However, there is a large variance in how the activity is measured in the RDE setup, which makes it difficult to compare catalysts reported in the literature. This chapter will examine how RDE experiments should be performed to achieve a comparable benchmark of catalysts, for the HOR in presence of CO, ORR, and ORR in the presence of methanol. In addition, the Pt_5Gd ORR catalyst will be tested for both HOR in the presence of CO and ORR in the presence of methanol. The Pt_5Gd catalyst has a 5x higher ORR specific activity than Pt [75] because of its weaker binding energy towards OH [75, 79]. It is expected that it also binds CO more weakly and that might make it an excellent catalyst for HOR and ORR under poisoning conditions. This chapter therefore starts by establishing a procedure for measuring the CO poisoning of HOR on Pt and PtRu. Then Pt_5Gd will be tested using this procedure. This will be followed by measurements showing how different experimental parameters change the activity for ORR, which will be used for establishing a benchmark for Pt ORR activity. Finally, the influence of methanol on the ORR will be studied and also used to compare the ORR activity of Pt and Pt_5Gd in the presence of methanol.

4.1 CO poisoning of the Hydrogen Oxidation Reaction

The CO poisoning of the HOR is related to the MOR through the oxidation of CO and the high overpotential required to start the oxidation. The difference though is that for a H_2-PEMFC that is suffering from CO poisoning the goal is to keep the CO coverage as low as possible so the remaining sites can oxidise H_2 whereas in MOR the CO is an intermediate and thus cannot be avoided. Thus the HOR, will ideally run with a slight overpotential of 20-40 mV [2] and the MOR with an overpotential of 300-500 mV [2]. PtRu is the best catalyst both for CO poisoned HOR and for the MOR but for different reasons; PtRu improves the MOR due to a lower water activation potential than for Pt, while the weakened CO binding energy and thus lower coverage makes it great for CO poisoned HOR [146–149]. A catalyst that has a lower CO binding energy and thus is more CO tolerant could prove a good MOR catalyst and increase the kinetics of the final step in the MOR where adsorbed CO and OH reacts to form CO_2. The less bound the CO, the faster it will reach an adsorbed OH molecule.

The HOR on Pt poly is shown in Figure 4.1a in both 0.1 M $HClO_4$ and 0.5 M H_2SO_4 at 60 °C and different rotation speeds. This measurement and the following were all performed at 60 °C to mimic the real conditions since H_2-PEMFC operates at around 80-90 °C and because the CO poisoning is temperature depended [150]. 60 °C was chosen as the limit since evaporation of the electrolyte becomes a problem at higher temperatures [81]. The figure shows the mass transport limiting current shows that the limiting current is higher in 0.1 M $HClO_4$ than in 0.5 M H_2SO_4. This have been quantified in Figure 4.1b where a Levich plot was constructed from the limiting current density measured at 0.2 V vs RHE using the Levich equation:

$$J_{\text{lim}} = 0.62nFD^{\frac{2}{3}}\nu^{-\frac{1}{6}}c_0\omega^{\frac{1}{2}} = Bc_0\omega^{\frac{1}{2}} \tag{4.1}$$

Where J_{lim} is the limiting current density, n is the number of electrons, F is faradays constant, ν is the viscosity, c_0 is the solubility of H_2 in the electrolyte, ω is the rotation speed and B is a constant. From the Levich plot Bc_0 was determined to be 7.9 × 10-2 mA cm^{-2} $rpm^{-\frac{1}{2}}$ and 8.7 × 10-2 mA cm^{-2} $rpm^{-\frac{1}{2}}$ for 0.5 M H_2SO_4 and 0.1 M $HClO_4$ respectively. The data for the 0.5 M $HClO_4$ is close to those reported by Gasteiger et al [151], which is also evident in Figure 4.1 where their data is co-plotted (dotted line).

RDE setups are in general not suited for HOR measurements since the HOR reaction has so little overpotential on Pt that it cannot be observed in a RDE experiment because of mass transport limitations [6]. When the HOR is CO poisoned the overpotential becomes sufficiently large, enabling the HOR reaction to be measured. The CO poisoning on polycrystalline Pt and Pt/C nanoparticles are shown in Figure 4.2 in 0.1 M $HClO_4$ saturated with either 100 ppm CO in H_2 (dashed) or 2% CO in H_2 (solid) at 60 °C, 2500 rpm and 0.1 V vs RHE. Seemingly, it takes longer time to reach a plateau when using 100 ppm CO instead of 2% and in the case of Pt/C the poisoning is so slow that a plateau is not reached within an hour. Ideally, CO poisoning would be measured with a realistic CO concentration; however, the low gas saturation concertation in the liquid electrolyte combined with the low concentration of CO in the gas makes the poisoning too slow for RDE experiments. Instead 2% CO in H_2 was used to establish the HOR in the presence of CO benchmark, since a steady-state is reached within 15 min for both extended surfaces and nanoparticles.

The experiments can either be performed with potential cycling or potentio-

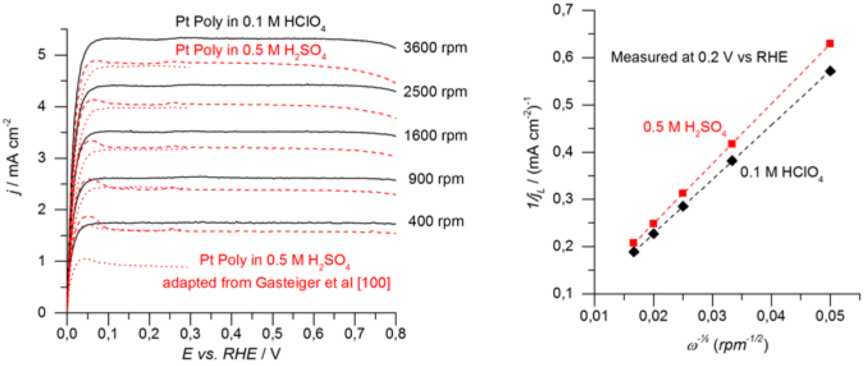

(a) HOR anodic sweep on Pt

(b) Levich plot

Figure 4.1: a) HOR on Pt poly in H2 saturated 0.1 M HClO$_4$ (black solid) and 0.5 M H$_2$SO$_4$ (red dashed) at 60 oC and different rotation speeds. For comparison measurements performed by Gasteiger et al [151] on Pt poly (red dotted) in 0.5 M H$_2$SO$_4$ at 60 °C were also added. b) Levich plot constructed using the limiting current density in a) at 0.2 V vs RHE. The dashed lines are regression lines.

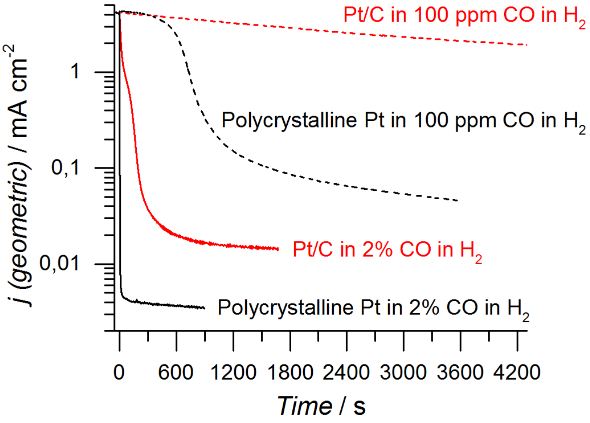

Figure 4.2: CO poisoning of HOR on a polycrystalline Pt disk (black) and Pt/C nanoparticles (red) measured in 0.1 M HClO$_4$ saturated with either 100 ppm CO in H$_2$ (dashed) or 2% CO in H$_2$ (solid) at 60 °C and 2500 rpm.

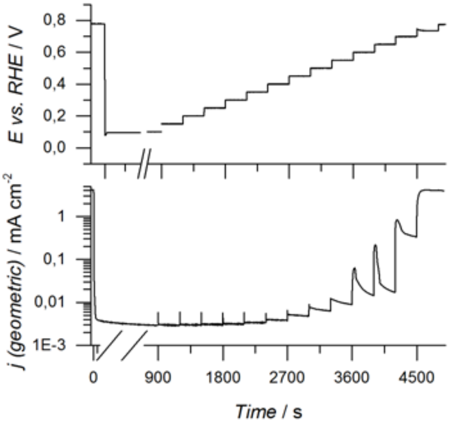

Figure 4.3: Figure 4.3 Potentiostatic experiment with a Pt disk at 60 °C, 2500 rpm in 2% CO/H_2 saturated 0.1 M $HClO_4$. The potential is held at 0.1 V vs RHE until the current density becomes stable, and then the potential is stepped 50 mV every 5 minutes until the current density reaches the limiting current density.

static. In the CV the onset of the CO oxidation and poisoning can be seen where the potentiostatic measurement shows the remaining HOR current under poisoning conditions. The potentiostatic experiment is depicted in Figure 4.3 where the applied potential is shown at the top and the measured current density at the bottom. The experiment starts at an oxidizing potential in orderto keep the surface free of CO, next the potential is stepped down to 0.1 V vs RHE to poison the surface. The potential is held at 0.1 V until the current density is stable (15 min) and then the potential is stepped 50 mV every five minutes until the current density reach the limiting current density at 0.8 V vs RHE. The measured current density is the last point before each potential step.

4.1.1 CO poisoning on polycrystalline Pt

The CO poisoning was measured on a polycrystalline Pt disk to verify that the CO poisoning was similar to those reported in literature. This is depicted both as CV and potentiostatic points in Figure 4.4a. The blue line and points were measured in 0.5 M H_2SO_4 whereas the black line and points were measured in 0.1 M $HClO_4$. Evidently the potentiostatic measurements follow the CVs, and that the CVs have similar onset but different poisoning in the cathodic sweep. The Pt surface is poisoned faster in 0.1 M $HClO_4$ than in 0.5 M H_2SO_4 which may be related to the stronger anion adsorption of H_2SO_4 where $HClO_4$ is hardly adsorbed [152]. The CV for Pt in 0.5 M H_2SO_4 was also compared to data reported by Gasteiger et al [16]. The CVs are similar although the onset of CO oxidation is slightly different. The difference in onset potential might be due to our measurement being done after potential cycling. We added pre potential cycling to our procedure in order

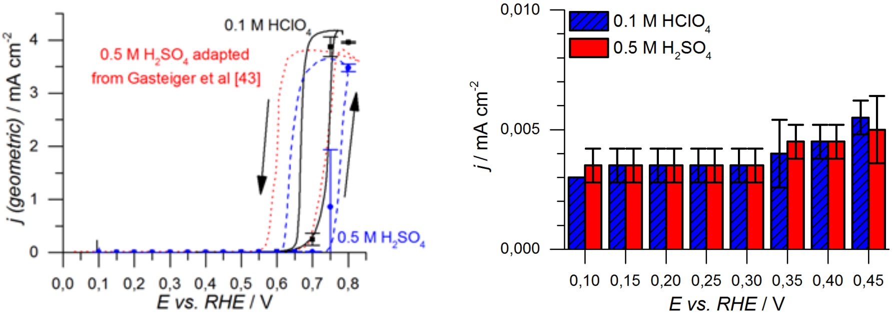

(a) CV of CO poisoned HOR on Pt poly

(b) Potentiostatic CO poisoned HOR on Pt poly

Figure 4.4: a) CO poisoned HOR on Pt Poly in 0.1 M $HClO_4$ (black) or 0.5 M H_2SO_4 (blue) saturated with 2% CO in H_2 at 60 °C, 2500 rpm and 1 mV/s. Measurement on Pt Poly in 0.5 M H_2SO_4 by Gasteiger et al [16] was included for comparison. CVs were recorded after holding the potential at 0.1 V vs RHE for 15 min. b) Shows potentiostatic measurements of CO poisoning of HOR on Pt poly performed under the same experimental conditions as for a).

to have reproducible CVs as we observed that repeating the experiment did not necessarily result in the same CV unless the pre cycling was applied. The onset of the oxidation occurs at potentials much higher than seen for an HOR anode. Therefore, the more relevant data is the steady-state residual HOR under CO poisoning, plotted in Figure 4.4b, which was recorded under the same conditions as for Figure 4.4a. The current densities for Pt in 0.1 M $HClO_4$ and in 0.5 M H_2SO_4 are the same. The measured current densities are so low that it could be noise although we still assign the activity to HOR. The Pt disks surface area is too small to produce significant HOR currents under these conditions, but the measurements did show that the Pt surface was poisoned as expected.

4.1.2 CO poisoning on Pt/C and PtRu/C nanoparticles

The CO poisoning of HOR measurements were also performed for Pt/C and PtRu/C nanoparticles, which is shown in Figure 4.5, measured under the same conditions as for the polycrystalline Pt disks. While the figure shows the onset of CO oxidation for Pt/C to be similar to that of polycrystalline Pt, the half way potential in case of PtRu/C is about 250-300 mV lower than for Pt/C, consistent to what has been reported in literature [16, 17].

The potentiostatic measurements shown as points on the plot follows the CVs, but the points for PtRu/C show a larger standard variation, which is due to difference in PtRu loading of 14 and 18 µg/cm^2 respectively for the measurements. When normalising the data to either the electrochemical surface area or Pt mass the standard deviation becomes insignificant, this is seen in Figure 4.6a and 4.6b respectively. Both in the case of specific and mass activity PtRu/C have an order

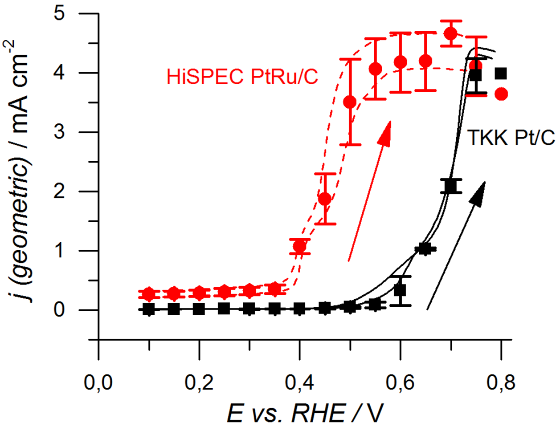

Figure 4.5: CO poisoning of Pt/C (black) and PtRu/C (red) nanoparticles in 0.1 M $HClO_4$ saturated with 2% CO in H_2 at 60 °C, 2500 rpm and 1 mV/s. The CVs was recorded after holding the potential at 0.1 V vs RHE for 15 min. The catalyst loading was 13 and 14 µg/cm^2 for the Pt/C and 14 and 18 µg/cm^2 for the PtRu/C. The points show potentiostatic measurements with 5 min per potential.

of magnitude higher residual activity than for Pt/C.

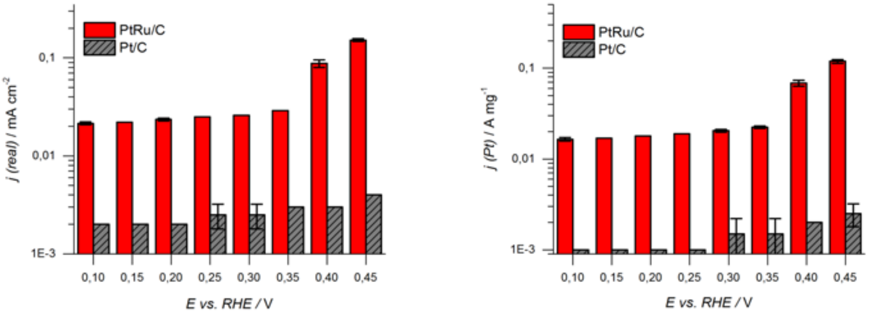

(a) Normalised by electrochemical surface area

(b) Normalised by Pt mass

Figure 4.6: CO poisoning of HOR on PtRu/C (red) and Pt/C (grey) measured potentiostatic with 5 min at each potential. The measurements were performed in 0.1 M $HClO_4$ saturated with 2% CO in H_2 at 60 °C and 2500 rpm. a) is normalised by the surface area determined from CO stripping and b) is normalised by Pt mass.

4.1.3 CO tolerance of Pt_5Gd

The Pt_5Gd alloy is a highly active catalyst for ORR showing 5x improvements over Pt [75]. The enhancement is due to a core shell structure with an alloy

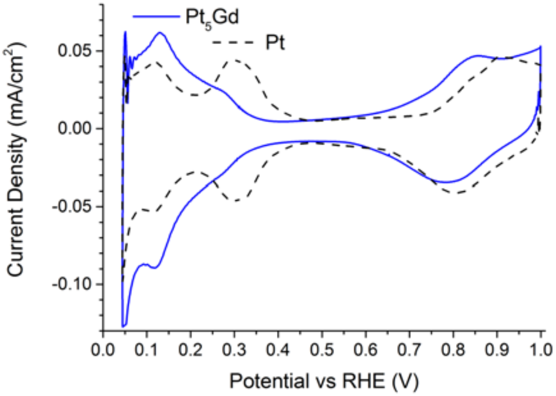

Figure 4.7: CVs of polycrystalline Pt (dashed black) and Pt$_5$Gd (solid blue) in N$_2$ saturated 0.1 M HClO$_4$ at 23 °C and 50 mV/s.

core and a compressed Pt shell where the compression of the overlayer reduces the OH binding energy thereby increasing the ORR activity [75, 79]. Since the compressed overlayer reduces the OH binding energy it might also reduce the CO binding energy. Therefore the CO poisoning on Pt$_5$Gd was studied. The Pt$_5$Gd sample was sputter-cleaned in a UHV chamber prior to experiments as described in Section 2.1.1.2. After mounting the sample in the cell, the sample was cycled until the CV was stable. A stable Pt$_5$Gd CV is shown in Figure 4.7 together with the polycrystalline Pt it will be compared to. The cyclic voltammetry experiment is shown in Figure 4.8a. Prior to the CV, the potential was held at 0.1 V vs RHE until the current density was stable. The CV was performed at 1 mV/s. Pt and Pt$_5$Gd have the same onset around 0.35-0.4 V vs RHE, but the oxidation process is faster for Pt$_5$Gd as it reaches the limiting current density faster than Pt. This indicates that Pt$_5$Gd have higher kinetics for oxidising CO once OH are present. In the cathodic sweep Pt$_5$Gd is poisoned slower, which might indicate a lower CO binding energy compared to Pt. The potentiostatic measurement is shown in Figure 4.8b. It appears that Pt$_5$Gd might be slightly better in the low potential range since it has a higher current density than Pt. The difference is however, insignificant for practical applications. The measurement could indicate a slightly lower CO binding energy. Overall Pt$_5$Gd, is not more CO tolerant than Pt.

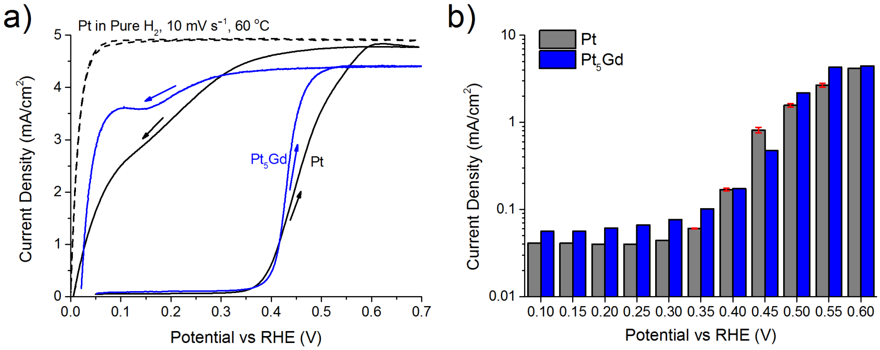

Figure 4.8: Cyclic voltammetry and potentiostatic measurements of polycrystalline Pt and Pt$_5$Gd in 100 ppm CO/H$_2$ saturated 0.1 M HClO$_4$ at 60 °C and 2500 rpm. a) Shows a CV after potentiostatic CO poisoning at 0.1 V vs RHE recorded at 1 mV/s. Pt and Pt$_5$Gd have the same onset of oxidation (0.35-0.4 V vs RHE), but the oxidation process is faster for Pt$_5$Gd and similar the poisoning seen in the cathodic sweep is slower than for Pt. b) Shows potentiostatic measurements of Pt and Pt$_5$Gd.

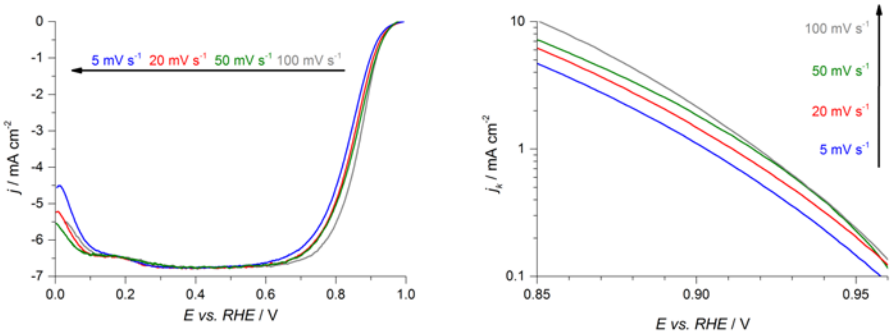

(a) Anodic sweep **(b)** Specific activity

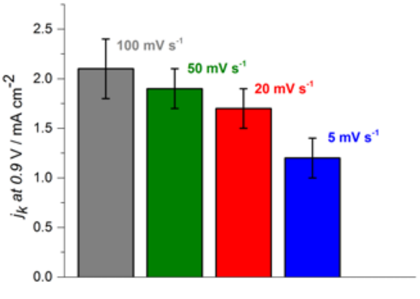

(c) Average specific activity

Figure 4.9: a) Anodic sweep of Pt poly in O_2 saturated 0.1 M $HClO_4$ at 23 °C, 1600 rpm and different scan speeds. b) Specific activity which were extracted from the data in a). Average specific activity on polycrystalline Pt at different scan speeds. The measurements were performed by Maria Escudero-Escribano, CINF.

4.2 Oxygen reduction reaction in a RDE setup

The RDE method is a fast way of measuring ORR and requires less preparation than measuring ORR activity in a fuel cell and the method is preferred in ORR catalyst development. It is important to understand how the RDE method differs from fuel cell testing. ORR measurements are different in a RDE setup compared to the measurements in the fuel cell because of the low solubility of gasses in liquid electrolytes which gives mass transport limitations although the mass transport can be controlled by the rotation speed. A polycrystalline disk was used a benchmark in these measurement. The sample was prepared as described in section 2.1.3.1. The ORR was measured by performing a CV in O_2 saturated electrolyte at 1600 rpm. The anodic sweep from the measurements is shown in Figure 4.9a, and has been compensated for ohmic drop and shift of the RHE scale. The CVs consist of a kinetic region (0.75-0.95 V vs RHE), and a mass transport limited region (0-0.7 V vs RHE). Evidently the kinetic region shifts to lower potentials for lower scan speeds, which means that the activity decreases. The mass transport corrected specific activity is shown in Figure 4.9b, which shows that activity increases with scan speed, which likewise is evident on the average values shown in Figure 4.9c. The activity at the highest scan speed (2.1 mA/cm^2) is roughly twice as high as for the activity at the slowest scan speed (1.2 mA/cm^2).

The average activities are similar to what have been reported by others [153]. It is not clear what the origin of the increased activity with scan speed is, but since it is visible on the untreated data as well, it not due to the corrections. There are several possible explanations for the different activities, including contamination of the surface, adsorption of O and OH intermediates, or time dependent surface effects [82]. The same measurements were also performed on carbon supported Pt. The catalyst was TEC10F60TPM, a 60% wt. Pt/C from Tanaka Kikinzoku Kogyo (TKK). The specific activity for different scan speeds and corrections are shown in Figure 4.10a. While all bars have been corrected for mass transport limitation, the grey bars have no additional corrections, the red bars have been compensated for ohmic drop, and the blue bars have been corrected for both ohmic drop and subsequently for background capacitive currents. The difference between the background corrected bars and the others increase with scan speed, which is due to the capacitive currents J_{DL} increases with scan speed $J_{\mathrm{DL}} = C_{\mathrm{DL}} dU/dt$ where C_{DL} is the double layer capacitance [4]. At low scan speeds (5 mV/s) the difference in activity from the background correction is so small that one could argue that using it introduces more error than not correcting it. At higher scan speeds (50 mV/s and 100 mV/s) the difference is significant and the scan speed trend depicted in Figure 4.9c is only seen for the background corrected bars. The background correction is thus necessary for scan speeds higher than 5 mV/s. The mass activities are shown in Figure 4.10b.

Gasteiger et al. [82] showed that RDE experiments performed at 60 °C and at scan rates of 5 and 20 mV/s show the same ranking of Pt/C catalyst as fuel cell testing in a H_2-PEMFC, and absolute values within a factor of two of the fuel cell testing. Lower scan speeds measurement resemble the fuel cell more, but are difficult to perform with low surface area electrodes in liquid electrolytes as the electrolyte always contains a finite amount of contaminants and the slower the scan rate the more can attach to the surface. For that reason, and experiment time considerations, it is favourable to perform the experiments at higher scan rates. RDE measurements are also mostly used to compare activities to other catalysts that also have been measured with RDE. Therefore the absolute activity in the fuel cell is not important for the comparison, as long as the same ranking of the catalyst is seen in both RDE and fuel cell experiments. The problem, however, is that group's use widely different scan rates (5 – 100 mV/s) and do not always apply the corrections, which makes it difficult to perform a fair ranking of catalysts. This problem also applies to the ranking shown in Figure 1.11 where the reported activities were measured using different scan speeds. To illustrate how the scan rates changes the ranking, I have tried to calculate a "correction factor" to normalise the activities to measurements performed at 50 mV/s. The "correction

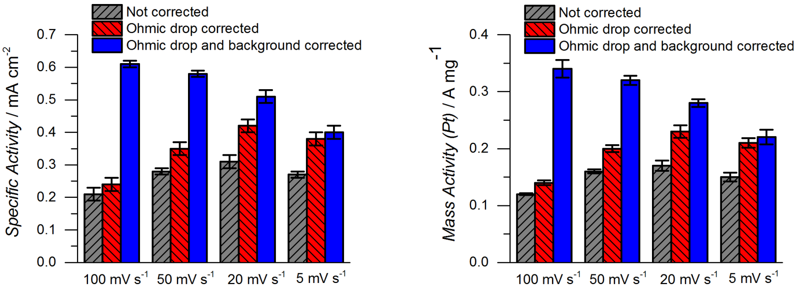

(a) Normalised by ECSA **(b)** Normalised by mass

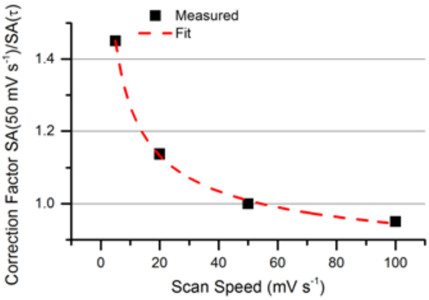

(c) Normalisation factor for scan rate

Figure 4.10: a) Mass transport corrected specific activity of Pt/C 60% wt. from Tanaka in O_2 saturated 0.1 M $HClO_4$ at 23 °C and 1600 rpm. The grey bars have no further correction, the red bars have also been compensated for ohmic drop and the blue bars have been compensated for ohmic drop and capacitive currents. b) Shows the same as a) but normalised to Pt mass. c) Shows the factor that has to be applied to convert activity data measured at different scan speeds normalised to 50 mV/s. The factor is based on the blue curves in a). Measured by Amado Andres Velazquez-Palenzuela, CINF

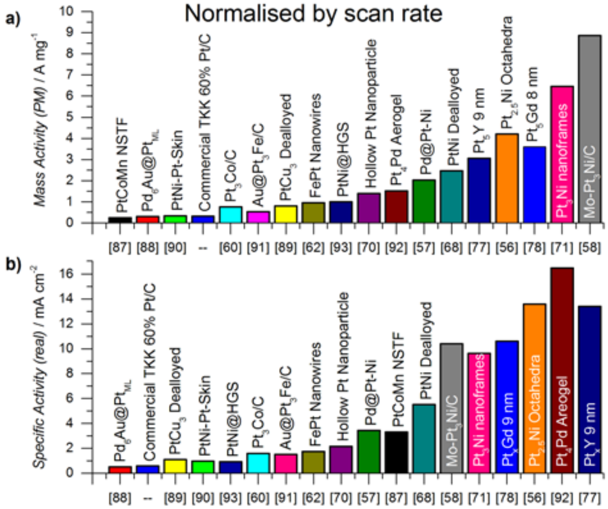

Figure 4.11: Show a ranking of catalysts reported in literature. This plot is a normalised version of Figure 1.11 using the same data as for figure 1.11 and applying the "correction factor" from Figure 4.10c.

factor" was calculated using the data from the blue bars in Figure 4.10a, and is depicted on figure 4.10c. The normalised activity ranking is shown in Figure 4.11, where it is observed that the ranking have changed. For the mass activity the third and fourth place are switched and for the specific activity the first, second and third place are switched. This illustrates how big a difference the scan speed has on activity although I would not say that the normalised ranking is more correct since it is not known how the activity of the literature data changes with scan rate.

4.3 Methanol Poisoning of ORR in a RDE setup

RDE measurements show that Pt_5Gd and other of the PtxM alloys show a 5-6 times activity enhancement over Pt [48,75,76]. A similar enhancement is expected to be seen in a H_2-PEMFC if the alloys can be made as active in a nanoparticulate form. However, it is more difficult to predict how the alloys would perform in a DMFC cathode, since at least some methanol crossover to the DMFC cathode will occur. DMFC measurements are cumbersome because the catalyst material would have to be made as nanoparticles in order to build a DMFC, and all the steps would likely have to be optimized for the new catalyst. It is much simpler and faster to test it in a RDE setup, if the methanol poisoning conditions can be mimicked. There are several reports of methanol poisoning of ORR RDE experiments in literature [95, 96, 98] where methanol concentration as low as 10 mM is severely impeding the ORR. In this section I will investigate how different experimental

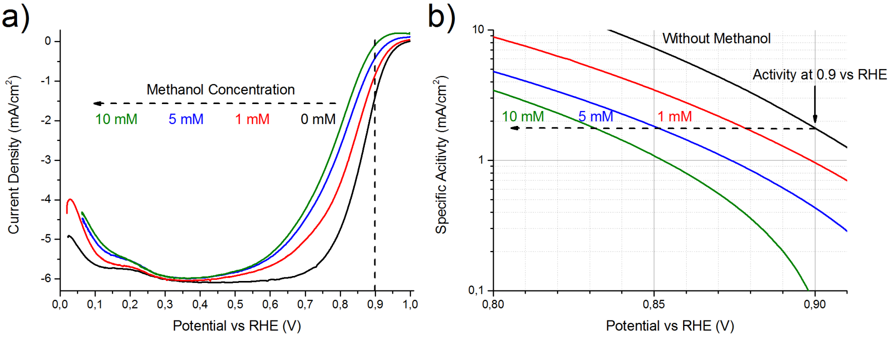

Figure 4.12: RDE measurements of polycrystalline Pt in O_2 saturated 0.1 M $HClO_4$ at 23 °C, 1600 rpm, 50 mV/s and different concentrations of methanol. a) Shows the ohmic drop compensated RDE measurements where it is seen that the kinetic region is moving to lower potential i.e. higher overpotential for increasing methanol concentration. b) Shows the specific activity normalised to geometric area. The activity @ 0.9 V vs RHE decreases with increasing methanol concentration. The potential shift is also shown, which is calculated from the initial activity at 0.9 V vs RHE.

parameters affect the methanol poisoning of the RDE experiment.

Polycrystalline Pt was prepared as described in section 2.1.3.1 and measured in O_2 saturated 0.1 M $HClO_4$ at 23 °C, 1600 rpm and 50 mV/s. The measurement is shown in Figure 4.12a (black line). Following the initial measurement, methanol was added to the cell and the ORR measurement repeated. The figure shows the half way potential moving to lower potentials when increasing the methanol concentration, and that the shift from zero to 10 mM methanol is 93 mV. The calculated specific activity is shown in Figure 4.12b where the black line weas measured before adding methanol and then as methanol is added the curves shift to the left towards lower potentials. One way of quantifying the methanol poisoning is the decrease in specific activity at 0.9 V vs RHE. However, for higher concentrations of methanol, in this experiment 10 mM, the kinetic region is shifted below 0.9 V vs RHE. This is seen in Figure 4.12b where the lines for the lower concentrations 0-5 mM are fairly straight lines, but the 10 mM line (green) is deviating from that behaviour at about 0.87 V vs RHE. Thus the potential shift can be so severe that it is not possible to compare activity due to the narrow potential width of the kinetic region in a RDE experiment. Another way of quantify the poisoning is by using the potential shift of the initial activity. In this case the potential shift is defined as at change in potential from 0.9 V vs RHE where the activity is the same as for the methanol free experiment. This is shown in Figure 4.12b where the dashed line marks the initial activity level and the crossing with the methanol poisoned measurements marks the

Figure 4.13 shows the temperature effect on the potential shift from methanol poisoning. It is seen that the potential shift increases with temperature and concentration. This can be explained since measured current in a linear combination

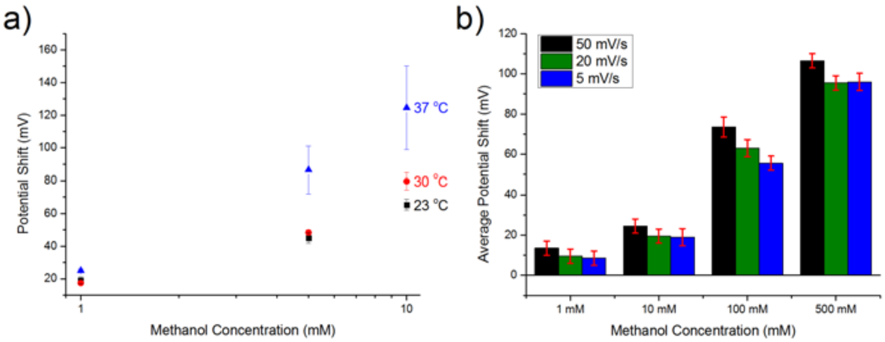

Figure 4.13: RDE measurements of polycrystalline Pt in O_2 saturated 0.1 M $HClO_4$ at 1600 rpm. a) Shows the average potential shift for different methanol concentrations and at different temperatures measured at 50 mV/s. b) Shows the average potential shift as function of methanol concentration and scan rates at 23 °C.

of MOR and ORR currents [95] and that MOR and ORR have different temperature dependence. The activity of ORR increases slightly with temperature. We have measured an activity increase of 10-25% on Pt disks and nanoparticles when increasing the temperature from 23 °C to 60°C and other have reported up to about 50% increase for polycrystalline Pt disks [83]. Additionally MOR have been found to be more temperature dependent where the MOR peak current increase by a factor of four when increasing the temperate from 18 °C to 60 °C [154] (numbers extracted from digitized data). In a RDE measurement, the ORR is mass transport limited with a limiting current whereas the MOR is not. Because the measurement is more sensitive to the MOR, the potential shift will be as temperature sensitive as the MOR. This is also seen comparing the points with 10 mM methanol in Figure 4.13, where raising the temperature from 23 °C to 30 °C increases the potential shift by 14.3 ± 6.5 mV.

The effect of scan rate on the potential shift from methanol poisoning is shown in Figure 3.15b. It is seen that the scan rate mainly has an effect for the higher concentrations of 100 mM and higher and scan rates at 50 mV/s where the potential shit is significantly higher than at the lower scan rates. At the lower concentrations the difference in potential shift for different scan rates is within the statistical error. MOR activity takes time to stabilise for a potential, and it often seen that MOR activity measurements from cyclic voltametry gives widely different results than potentiostatic measurements [41, 45] thus, a methanol poisoning potential shift measured in RDE would likely be different than a steady-state measurement.

4.3.1 Methanol poisoning on carbon supported Pt nanoparticles

The methanol poisoning was additionally measured on a high surface area carbon supported Pt to determine which effect the surface area has on the potential shift

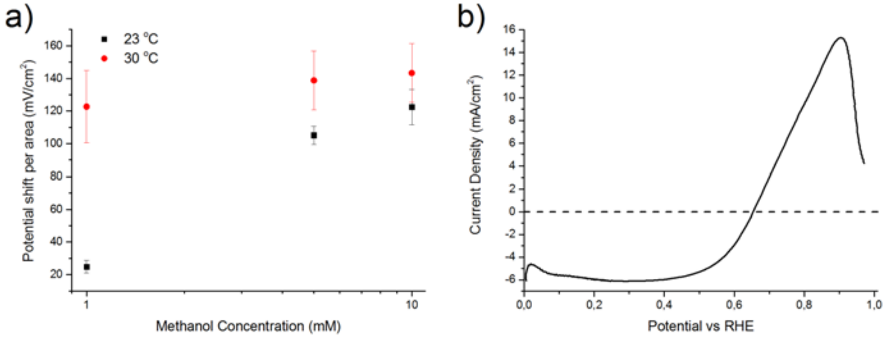

Figure 4.14: a) Average potential shift per electrochemical surface area from methanol poisoning on TKK 60% wt. Pt/C for different methanol concentrations and different temperatures. b) CV in O_2 saturated 0.1 M $HClO_4$ with 5 mM methanol at 37 °C, 1600 rpm and 50 mV/s.

from methanol poisoning. The catalyst used was TEC10F60TPM, a 60% wt. Pt/C from Tanaka Kikinzoku Kogyo (TKK). The measurements were corrected for ohmic drop and background capacitive currents. The potential shift per area is plotted in Figure 4.14a. It was necessary to normalise to the electrochemical surface area because the potential shift seems to scale with surface area. The temperature effect is more striking for the nanoparticles where the potential shift per area increase by about 100 mV/cm^2 when going from 23 °C to 30°C, in only 1 mM methanol. Interestingly, at higher methanol concentrations the change is much smaller, only 20-33 mV. The difference might be an artefact from the RDE measurement since peak MOR current is close to the kinetic region of the ORR measurement. Therefore some ORR currents will be on the right side of the MOR peak and some on the left side. Depending on the MOR peak current and the initial activity at 0.9 V vs RHE, the potential shift can be quite different, based on which side of the MOR peak the potential of the initial activity is shifts to.

The potential shift was also measured for nanoparticles at 37 °C. However, due to very high MOR currents, it was not meaningful to quantify the potential shift as seen in Figure 4.14b where the peak MOR current is more than twice the limiting ORR current. It seems that methanol poisoning can only be measured for a limited range of parameters in a RDE setup. The surface area, methanol concentration and temperature must be kept low, meaning that a low MOR current is a prerequisite to get meaningful results. This also shows that it is not possible to measure the methanol poisoning quantitatively in a RDE setup, since the result depends on so many conditions and these conditions are not transferable to the DMFC. Rather the RDE method can be used to qualitatively show if one catalyst is more methanol tolerant than another, if both are measured under the exact same conditions.

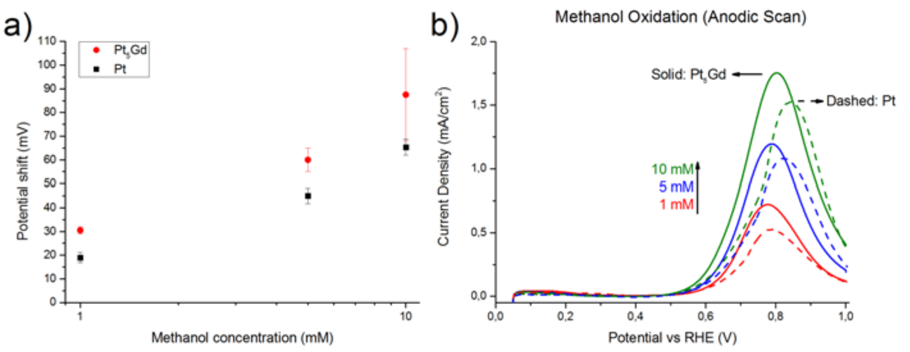

Figure 4.15: a) Potential shift from methanol poisoning of ORR for polycrystalline Pt_5Gd (red circles) and Pt (black squares). b) Anodic sweep of MOR measured in N_2 saturated 0.1 M $HClO_4$ with different concentrations of methanol and measured at 23 °C and 50 mV/s.

4.3.2 Methanol poisoning on polycrystalline Pt_5Gd

RDE measurements in a clean electrolyte have shown that Pt_5Gd is five times more active than Pt [75], but it is not known if it retains its activity enhancement in the presence of methanol. I therefore tested this using the method just shown. The polycrystalline Pt_5Gd disk was sputter-cleaned in a UHV chamber prior to experiments as described in section 2.1.3.2. After mounting and electrochemically cleaning, the ORR activity was measured in pure electrolyte to assure that the activities reported in [75] could be reproduced, which showed that the cell and sample were in good conditions. Methanol was subsequently added and the ORR measurements were repeated. A comparison of potential shifts for polycrystalline Pt_5Gd (red circles) and Pt (black squares) is shown in Figure 4.15a. Evidently Pt_5Gd has a larger potential shift than Pt for all concentrations. To explain this, the MOR was measured using the same methanol concentrations in N_2 saturated electrolyte. Figure 4.15b shows that the MOR peak is larger for Pt_5Gd (solid lines) than for Pt (dashed lines), which suggest that Pt_5Gd is more active for MOR than Pt at high potentials and that this is what give rise to the additional potential shift for Pt_5Gd.

Figure 4.15a indicates that Pt_5Gd is more sensitive to methanol poisoning and losses more activity than Pt. However, Pt_5Gd started with a much higher activity than Pt, how the activity compares after methanol poisoning is thus a more relevant measure. This is shown in Figure 4.16a where the average specific activity is measured before/after adding 1 mM methanol to the electrolyte. The activity measurement before, which is the line above the filled areas shows that Pt_5Gd is about five times more active than Pt as expected. The active measurement after adding 1 mM methanol, which is the line below the filled areas, shows that poisoned Pt_5Gd though having lost activity still is more active than Pt, both before/after poisoning the Pt. Figure 4.16b shows the poisoning with 10 mM methanol and in this case the activity of Pt_5Gd drops below the activity of the

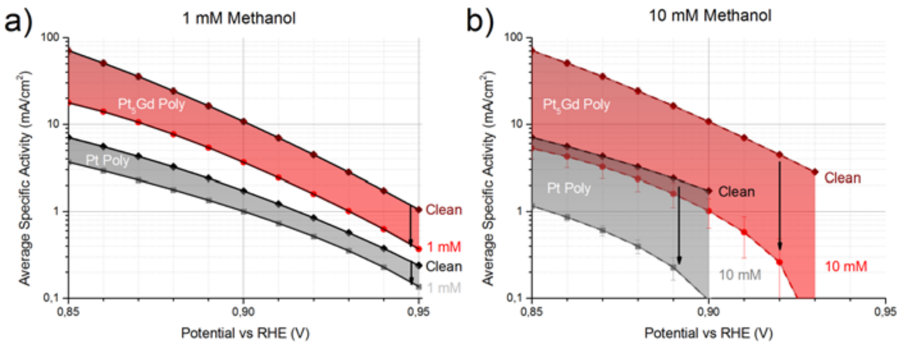

Figure 4.16: a) Average specific activity of Pt_5Gd (red) and Pt (grey) measured in O_2 saturated 0.1 M $HClO_4$ at 23 °C, 1600 rpm and 50 mV/s. a) Specific activity before/after adding 1 mM methanol. The clean measurements are shown in dark red and black whereas the poisoned measurements are shown in red and grey. b) Specific activity before/after adding 10 mM methanol. The top line in the filled areas are the before measurement and the lines below are the after measurements.

clean Pt, but still retain an activity enhancement of 2-3 times over Pt poisoned with the same methanol concentration. These measurements suggest that it could be advantageous to use Pt_5Gd instead of Pt as DMFC cathode. As mentioned in Section 1.3.3.4 alloys such as Pt-Ni [100, 101] and Pt-Co [102] also provide improved ORR activity in the presence methanol. An comparison of Pt_5Gd, Pt-Ni and Pt-Co alloys ORR activity in the presence of methanol would be interesting. However, as shown in this section, the methanol poisoning in a RDE setup is very dependent on the experimental conditions, and thus the data for Pt_5Gd presented in this work is not comparable to the data for Pt-Ni [100, 101] and Pt-Co [102] presented in literature.

4.4 Summary

In this chapter it was studied how to perform RDE measurements of HOR in the presence of CO, ORR, and ORR in the presence of methanol in order to make reproducible benchmark measurements of catalyst activity that are relevant for fuel cells. Two methods of measuring CO poisoning were presented. One method measures the onset of the CO poisoning from cyclic voltammetry in a RDE setup. The other measures the residual current density during poisoning and under potentiostatic conditions i.e. the CO tolerance. The most relevant method for fuel cell testing was the potentiostatic method where the residual current density was measured. An activity benchmark was performed for polycrystalline Pt, Pt/C and PtRu/C nanoparticles. These methods were also applied for comparing the CO tolerance of Pt with that of Pt_5Gd. Pt_5Gd showed the same onset of CO oxidation as Pt, but had faster kinetics once this onset potential was reached. Under potentiostatic conditions the Pt_5Gd showed a slightly higher residual activity but not enough for practical applications.

ORR measurements were performed in a RDE setup both for polycrystalline Pt and carbon supported Pt nanoparticles. The measurements showed that the ORR activity is dependent on scan speed and when increasing the scan speed from 5 to 100 mV/s the average activity increased by 75%. Similar increase was observed for carbon supported Pt, if ohmic drop and background subtraction of capacitive currents were applied. Using the data from Pt/C measurements, a normalisation factor was calculated and applied to the literature data shown in figure 1.11, which showed a different ranking after applying the normalisation. Showing that scan rate, ohmic drop and other corrections are important for the measured ORR activity, and the variation in experimental conditions in literature makes it difficult to compare data.

Methanol poisoning in a RDE setup was studied to see if the RDE method could be used to measure the methanol tolerance of catalysts in a DMFC. I found that the poisoning to be very depended on several experimental parameters such as temperature, electrochemical activity surface area and methanol concentration. Since the measured current is a linear combination of ORR and MOR currents and since ORR is mass diffusion limited whereas MOR is not, the MOR current can easily dominate the experiment. Therefore the MOR current must be kept low by keeping the temperature, surface area and methanol concentration low. It was not possible to construct the experiment to measure the methanol tolerance quantitatively. Instead catalyst could be compared qualitatively if measured under the same conditions. The methanol tolerance of Pt and Pt_5Gd were measured under the same conditions. The measurements show a larger potential shift from methanol poisoning on Pt_5Gd than on Pt, which was due to better MOR kinetics of Pt_5Gd at high potentials. Even though Pt_5Gd is poisoned more by methanol than Pt, it also has a much higher initial activity than Pt. Comparing the activity of Pt_5Gd and Pt after methanol poisoning, Pt_5Gd retain a 2-3x activity enhancement over Pt with 10 mM methanol. That makes Pt_5Gd a potential replacement for Pt as DMFC cathode.

5

Possible routes for the synthesis of Pt_xM alloy nanoparticles

In the previous chapters it has been established that Pt_xM alloys (where M are early transition metals or lanthanides), and in particular Pt_2Gd, Pt5Tb and Pt_3Y alloys, are much more active (up to 5-6 fold increase) than Pt for the oxygen reduction reaction [48, 75, 76]. Additionally, in the presence of methanol the Pt_2Gd alloy retains the activity enhancement over Pt, making it an ideal candidate for a DMFC cathode catalyst. So far, the work on Pt_xM alloys has been studied in model systems, i.e. Ar-sputter-clean polycrystalline electrodes, sputter-deposited thin-films and mass-selected nanoparticles. However, in order to use these promising materials in a DMFC, the catalyst must be produced in nanoparticulate form, which is more technologically relevant. Pt_xY and Pt_xGd nanoparticles [78, 79] prepared on a small scale (80 – 270 ng) using physical synthesis methods in ultra high vacuum (UHV), have shown high activity and stability. However it is not economically viable to scale up these methods for fuel cell production. Instead, a chemical synthesis route must be found. As discussed in Section 1.4 the chemical synthesis is difficult because of the very different standard reduction potential of Pt and M precursors. Several routes of chemical synthesis of Pt_xM alloy nanoparticles were explained in Section 1.4. In this work I have chosen to focus on the solvothermal/supercritical fluid and high temperature annealing. This chapter will provide a brief description of the experimental setups, followed by a presentation of the results of the different synthesises.

5.1 Experimental description of synthesis techniques

Three setups were used for the synthesis experiments. First, a supercritical fluid flow reactor located at DTI; second, a supercritical fluid pulse reactor located

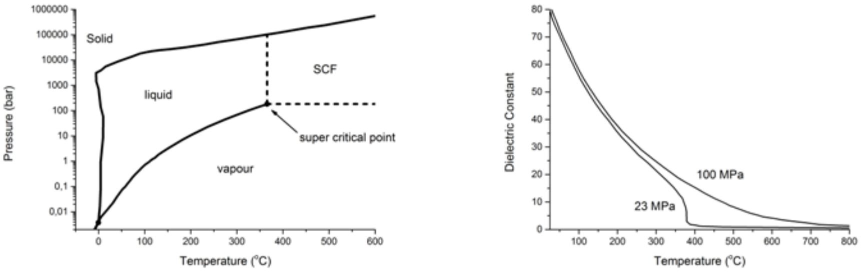

(a) Phase diagram of water [155] **(b)** Dielectric constant for water [158, 159]

Figure 5.1: Phase diagram of water adapted from [155]. b) Dielectric constant for water shown for different pressures and temperatures. It is seen that the dielectric constant changes more rapidly around the super critical point of water (217.8 bar, 374 °C). Figure was adapted from [158, 159]

at Aarhus University; and third high temperature reduction performed at CINF, DTU. In this section, the concept of supercritical fluid synthesis will be explained, followed by a description of each experimental setup. The experimental setups where used for the synthesis described in Section 5.2-5.3 and Chapter 6.

5.1.1 Supercritical fluid synthesis

Synthesis with supercritical fluids (SCF) takes advantage of the special properties of fluids above the supercritical point. The phase diagram of water is shown in Figure 5.1a, which was adapted from [155]. It can be seen that the supercritical point is at 374 °C and 217.8 bar. Above the supercritical point the interface between liquid and vapour phases disappears, thus resulting in a fluid with properties (density, viscosity and diffusivity) in between that of the liquid and vapour phase [156, 157]. The polarity of solvents depends on the dielectric constant of the solvent, and the dielectric constant changes with temperature and pressure. Approaching the supercritical point, the dielectric constant can dramatically; this can change the polarity of a solvent from polar to non-polar. This is shown in Figure 5.1b where the dielectric constant is plotted versus temperature for two different pressures. The figure was adapted from [158, 159]. In a polar liquid, such as water, inorganic salts are soluble. For supercritical water, however, the polarity decreases to the level of non-polar solvents thus making inorganic salts insoluble, which results in a supersaturation of the salts, causing crystallization [156, 157, 159]. This process can be utilized to form nanoparticles which have been demonstrated for both metals and metal oxides [160].

5.1.2 Supercritical flow synthesis of Pt_xM nanoparticles

Solvothermal synthesis using SCF has been performed in autoclaves until Adschiri et al [161] demonstrated SCF flow synthesis. Their apparatus consisted of two containers with precursor solution and pure solvent respectively. The content of the containers was pumped into pressurised tubes in different streams. The pure solvent was heated in its stream and then mixed with the cold precursor solution. The combined stream continues into the heated reactor after which the stream is cooled and then passes through a back pressure regulator. The idea was to initiate the reduction of the precursors at the mixing point with the hot solvent, because of the rapid heating and the change to supercritical phase. The particles were then formed inside the heated reactor, subsequently the particle solution could be collected after the solution exit through the back pressure regulator. Adschiri et al have demonstrated [159, 161] that the morphology and size of the particles could be controlled by choosing the right temperature, concentration and reaction time.

Supercritical flow system used for the synthesis was based on the same concept as Adschiri et al [161]. The setup was developed at the DTI and is similar to the machine designed at Aarhus University by Hald and others [162, 163]. A basic diagram of the machine is shown in Figure 5.2. The machine has four inlets where the two in the top are used for precursor solution and support material; the third is used for pumping preheated solvent; and the fourth is not used for this synthesis. The flows of precursor and support materials are mixed first. The loading on the support particles can be controlled by the solution concentration or ratio between the flows. The material flow is then rapidly heated by mixing it with preheated solvent prior to entering the reactor. The temperature of the combined flow is called the mixing temperature (T_{mix}) and is controlled by the temperature of the preheated solvent and the solvent flow to precursor/support flow ratio. The hot mixture then continues through the heated reactor tube with temperature T_{reactor}. The nanoparticles are formed in the hot reactor tube which is kept at supercritical fluid conditions. It has been observed that the average particle size increases with increasing reactor temperature [164, 165]. After leaving the reactor, the flow is passed through a cooler to reach room temperature. Finally, the product liquid leaves the system by passing through a pressure regulator that keeps the system at a constant pressure. The product which consists of suspended nanoparticles in solvent, is ultimately collected. The synthesis experiment at DTI was performed together with Christian Kallesøe from DTI.

5.1.3 Synthesis of Pt_xGd and Pt_xY nanoparticles in a supercritical pulse reactor

The disadvantage of the formally described SCF flow system design is that the reaction time inside the reactor is dependent on the flow rate and length/diameter of the reactor tube. In addition, the mixing temperature is dependent on the flow rate and, as result the reaction time can therefore only be changed in a small interval without changing the reactor. To enable, a longer reaction time, another

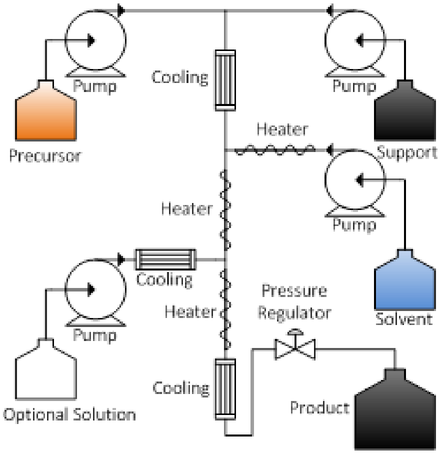

Figure 5.2: Schematics of the SCF flow system at DTI.

type of SCF reactor was used. This type of reactor is called a pulse reactor and was developed and build by Eltzholtz et al at Aarhus University [166]. A diagram of the pulse reactor is shown in Figure 5.3b. The reactor works by sending a pulse of precursor solution into the heated reactor for a specified duration. The volume of the reactor is so small compared to the heater that the solvent is rapidly heated this achieving a shock heating [166]. A second pulse of pure solvent is sent into the reactor to push the formed nanoparticles out. Hereafter the process is repeated as many time as required for making the desired amount of product. The advantage of this system is that any reaction time can be selected; however, consequently stalling the synthesis is slow due to the long reaction time and small volume of the reactor. The volume of the reactor is kept small to ensure rapid heating of the precursors. The pulse reactor synthesis experiments were performed at Aarhus University with the help of Muhamed Aref Hasen Mamakhel from Aarhus University.

5.1.4 High temperature reduction of Pt with YCl_3 or $Y(C_5H_5)_3$

At CINF it has been demonstrated that it is possible to form Pt5M alloys by depositing metallic Y on top of a Pt substrate in a UHV setup and then anneal it at a high temperature [167]. The alloy formation starts at 400-500 °C [168]. Extensive work has also been done using labile Y organometallic precursors with Pt nanoparticles to form Pt_xY alloy nanoparticles. The idea is to let the precursor thermally decompose on the nanoparticles surface and then anneal them at high temperature (above 400-500°) to form the alloy [169]. An alternative to an organometallic precursor is to use halides or oxides, given that it has been reported that Pt_xM alloys can be formed above 1200 °C in a very pure hydrogen atmosphere when fluorides and oxides are used as precursors [117–119]. However,

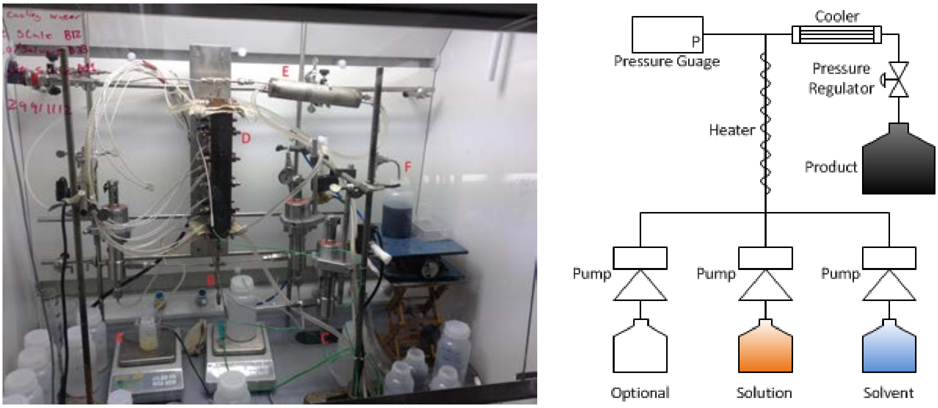

(a) Pulse reactor at Aarhus University **(b)** Schematics of Pulse Reactor

Figure 5.3: Image of the pulse reactor setup at Aarhus University a) and schematics of setup b). The setup consists of three pneumatic pumps each connected to an inlet container A-C. The pumps inject a pulse of precursor solution into the reactor D, where the reaction takes place over a selected period, and then solvent is pumped to move the product out of the reactor through a cooler E and then through the back pressure regulator F.

fluorides are significantly more difficult to reduce than other halides, which could indicate that the reduction/alloying can be performed with chlorides at a lower temperature. The thermodynamics of this will be derived in Section 6.1. Two experiments were designed and performed with Brian Peter Knudsen, CINF, one with an organometallic precursor Tris(cyclopentadienyl)yttrium(III) $Y(C_5H_5)$ and one with anhydrous YCl_3. Precursors were mixed with pre-dried/reduced (200 °C in H_2) unsupported Pt particles (HiSPEC 1000) in a 3:1 weight ratio inside a glovebox. The powder mixture was then put in a crystal glass reactor, sealed, and connected to the synthesis setup which is shown in Figure 5.4a and 5.4 b.

The setup consists of two instrument 5.0 gas bottles with H_2 and Ar gases from Linde Gas. The gas flow is controlled by a reduction valve on each of the gas bottles. The gas line from each gas bottle is split in two lines connected to two three-way valves that enable changing between Ar and H_2 gas. One of the two valves is connected directly to the reactor, and the other through a Schlenk line. The Schlenk has four ports, which can change between vacuum and gas. One port is used for the reactor and one is used as exhaust through an oil trap to avoid back diffusion of air and moisture. The last two ports are not used for this synthesis.

Before opening the ports on the reactor, the gas lines are flushed with both Ar and H_2. During the synthesis a constant flow of H_2 is flowing through the reactor. The reactor is heated inside a temperature controlled tube furnace that was programmed to heat the reactor to 900 °C in 90 minutes and then hold at 900 °C for 360 minutes before shutting off. The atmosphere inside the reactor was changed to Ar after the reactor had cooled down. Next, the reactor was disconnected from the setup and one of the ports was opened, allowing air slowly

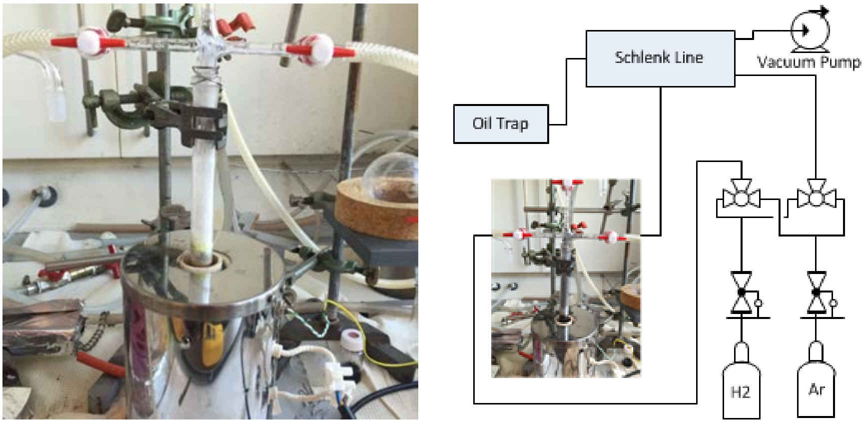

(a) Setup **(b)** Schematics of setup

Figure 5.4: a) Picture of setup, which consisted of a sealed glass reactor, placed inside a tube furnace, connected to a pure H_2 flow, and an exhaust through an oil trap. A yellow product is observed just above the furnace inside the reactor tube, corresponding to the organometallic precursors that sublimates and then condenses on the glass. b) Schematics of setup, which is explained in the text.

to diffuse into the reactor and passivate the nanoparticles. During the synthesis with the organometallic precursor a yellow deposit was observed inside the glass reactor just above the furnace as seen in Figure 5.4b. This is due to sublimation of the precursor that condenses on the glass wall outside the furnace. To maintain the amount of precursor in the reactor a gently tapping on the glass wall was performed in order to cause the deposit to fall to the bottom of the reactor where it melted.

The experimental procedures and synthesis setup were presented in this section. In the following sections the results of these synthesise will be presented.

5.2 Synthesis of Pt_xM nanoparticles using solvothermal techniques

The SCF synthesis of Pt_xM nanoparticles was inspired by the work of Dipankar et al [116], who reported that Pt_3Gd intermetallic compound could be synthesized under similar synthesis conditions as in the SCF reactors. They enclosed, an ethanol solution containing 0.5 M of $H_2PtCl_6 \cdot 3\,H_2O$ and $GdCl_3 \cdot H_2O$ in a special designed reactor for in-situ synchrotron experiments. While performing X-ray scattering experiments the reactor was pressurised to 250 bar, the temperature raised to 250 °C, and x-ray scattering measurements were performed in-situ. From the scatter data an atomic pair distribution function (PDF) was calculated, which describes the probability of finding two atoms with certain spacing and can be

T_{mix}	T_{reactor}	Precursor Flow	Support Flow	Pressure
257 °C	450 °C	10 mL/min	10 mL/min	300 bar
300 °C	450 °C	10 mL/min	10 mL/min	300 bar
350 °C	450 °C	10 mL/min	10 mL/min	300 bar
385 °C	450 °C	5 mL/min	5 mL/min	300 bar

Table 5.1: Experimental settings on the SCFS machine for the syntheses. The solvent temperature was kept at 500 °C throughout the experiments and the solvent flow was adjusted to maintain the mixing temperature.

used to identify both crystalline and non-crystalline substances. From the PDF analysis, they could observe the formation of particles that could be fitted to a Pt_3Gd structure. Given that similar conditions are possible to reproduce with the SCF systems, we aimed to imitate the literature results in both the SCF flow system and the pulse reactor.

5.2.1 Supercritical flow synthesis of Pt_xY/C nanoparticles

As mentioned in the beginning in Section 1.4, one of the major challenges in synthesising Pt_xM alloys is the large difference in reduction potential between Pt precursors and M precursors. As a consequence, the early reduction of the Pt precursor is highly favoured in any synthesis aiming to co-reduce Pt and M, especially when the synthesis takes places at elevated temperatures. The highly favoured early reduction of Pt precursor thus, becomes one of the major issues to avoid. Given that the reactor heating rate is restricted, Pt reduction would start at lower temperatures before the reduction of M takes place, resulting in pure Pt nanoparticles. The M metal would be reduced on the surface of the Pt, leading to a non-stable configuration since the M metal would be oxidized as soon it comes in contact with water or air. Alternatively, the SCF flow systems rapid heating of the precursors might be a big advantage for this synthesis since its configuration favours the co-reduction. In any case, we anticipated that high temperatures are needed to reduce the YCl_3 precursor. Therefore, to favour reduction the rector temperature was set to 450 °C, which was the maximum temperature possible at the time. To heat the precursor solution more rapidly the mixing temperature was increased gradually from 257°C, which is just above the supercritical point for ethanol, to 385 °C, which was the maximum achievable mixing temperature for the experiment. The mixing temperature was determined by the ratio between precursor flow and solvent flow. To reach the highest mixing temperature the precursor flow was reduced and the solvent flow set to maximum. In all of the experiments the solvent temperature was set to 500 °C. The experimental settings are shown in Table 5.1.

Ideally, the experiments should have been carried out using the same precursor concentration as [116]. However, to reduce corrosion of the supercritical reactors from chloride salts, the precursor solution concentration was reduced one order

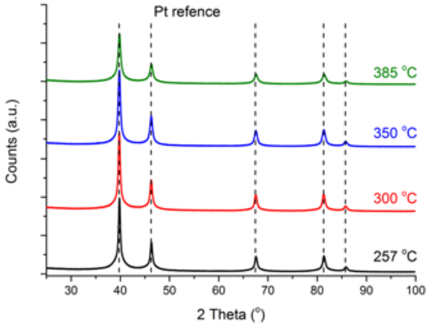

(a) PXRD spectra of temperature series

T_{mix} [°C]	Size #1 [nm]	Size #2 [nm]
257	3.0	22.7
300	2.8	20.4
350	2.6	17.6
385	2.6	15.3

(b) Crystallite size from Rietveld refinement

Figure 5.5: Figure 5.5 – PXRD spectra of attempted Pt_xY synthesis with different vertical temperatures. The peak positions fits to pure Pt phase. No alloy phase is observed. The PXRD measurements were performed by Patricia Hernandez-Fernandez, DTI

of magnitude. As a result, the concentration of $H_2PtCl_6 \cdot 6\,H_2O$ and $YCl_3 \cdot 6\,H_2O$ was 0.0138 M, whereas Dipankar et al [116] used 0.5M.

5.2.1.1 Characterisation of synthesised Pt_xY/C nanoparticles

The synthesized particles were washed similar as the synthesized Pt/C particles. After being washed and dried, the particles were subjected to PXRD analysis. The XRD spectra for the temperatures series are shown in Figure 5.5a where only peaks attributed to the Pt phase are observed. Rietveld refinement of the data shows a broad size distribution where two Pt phases with different crystallite size were required to describe the XRD pattern as explained in Section 2.2.2.2. From the refinement the ratio between the two sizes is observed to be around 1:1. The crystallite sizes seen in Figure 5.6b show an inverse relation with the mixing temperature. This seems counterintuitive, but could be tentatively explained by the fact that the reaction time in the reactor is correlated to the mixing temperature by the solvent flow. To reach the high mixing temperatures the solvent flow needs to be doubled, which corresponds to an overall flow rate increase of about 50%, which causes the reduction of the reaction time by a factor of two. Given that the particle size is dependent on both the reactor temperature and the reaction time, the increase in mixing temperature causes the reaction time to decrease as does the particle size. The XRD refinement also suggests that a considerable fraction of particles are rather small (3nm), which is too small for active alloy nanoparticles reported in [78].

The synthesised particles were also measured using XPS to evaluate if any yttrium were present in the surface layers and if the element was in metallic state, suggesting alloying with Pt. The XPS spectrum of the Y3d peak is shown in

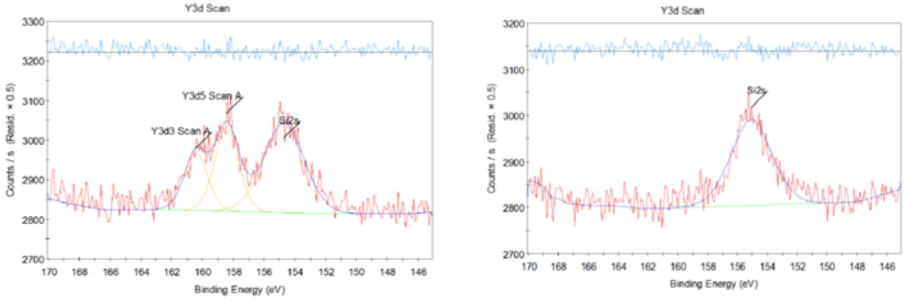

(a) As prepared

(b) After acid wash

Figure 5.6: XPS spectra of the product of the flow synthesis performed at 385 °C after water wash a) and b) after acid wash. Only Y3d peaks attributable to oxidized Y can be observed in a). The blue curve in the top is the residue from the fitting. XPS measurements were performed by Kenneth Brian Haugshøj, DTI.

Figure 5.6a, where Y3d$_{3/2}$, Y3d$_{5/2}$ and Si2s peaks are observed. The Si contamination could originate from the glassware used for preparing the precursors or the glassware used to clean the product. The binding energy of Y3d$_{5/2}$ in metallic state has been measured at CINF and is 156 ± 0.2 eV for both sputter cleaned polycrystalline alloy disks and UHV prepared nanoparticles [74,78], which is 2 eV lower than seen in Figure 5.6a The high binding energy of Y could be caused by the presence of oxidized yttrium in the electrocatalyst, namely as oxide, hydroxide or chloride, and suggests that the alloy was not formed. To verify if the alloys was actually formed, we acid-treated the nanoparticles since yttrium oxides/hydroxides/chlorides are dissolved at low pH. Thus, the particles were acid treated in 0.1 M $HClO_4$ for 10 minutes and then diluted in water and centrifuged to recover the acid-treated particles. The XPS spectrum of the acid-treated sample is shown in Figure 5.6b, showing no yttrium signals. Only the Si2s peak, also detected in Figure 5.6a, was present in the acid-leached catalyst.

In conclusion, the SCFS synthesis of Pt_xY alloy nanoparticles was not successful. Two hypotheses can be proposed to explain the negative results. First, yttrium oxide has a huge heat of formation (-1800 kJ/mol) whereas the alloy has -386 kJ/mol, and it is therefore more thermodynamically favourable to form the corresponding oxide when oxygen or water is present. Also, synthesises were performed with absolute alcohol (99.8%), which contains 0.2% water and hydrated chloride salts. From thermodynamics considerations, it is very difficult to reduce the yttrium chloride instead of oxidizing it. However Dipankar et al [116] measured a Pt_3Gd alloy structure using also absolute ethanol and hydrated chloride salts. The authors reported that the alloy formation was clearly detected after 40s and the complete conversion happened after 60s. We note that the reaction time for the flow reactor is 5 s for the lowest mixing temperature and the reaction time decreases at the mixing temperature increases. Consequently, we proposed as second hypothesis that the reaction time in the reactor was too short to facilitate

$H_2PtCl_6 \cdot 6\,H_2O$	$YCl_3 \cdot 6\,H_2O$	$GdCl_3 \cdot 6\,H_2O$
5.2 mM	6 mM	
5.2 mM	12 mM	
5.2 mM	60 mM	
5.2 mM	120 mM	
5.2 mM		60 mM

Table 5.2: Concentration of precursor solutions for hydrated synthesis in pulse reactor

alloy formation.

5.2.2 Pulse reactor

The pulse reactor experiments were divided into two sections, depending on whether hydrated or anhydrous solvents and precursors were used.

5.2.2.1 Synthesis with hydrated precursors

The experiments focused mainly on Pt_xY, but a single Pt_xGd synthesis was also attempted to examine if any difference between the two used precursors, $YCl_3 \cdot 6\,H_2O$ and $GdCl_3 \cdot 6\,H_2O$ could be observed. All experiments were performed with a reactor temperature of 250 °C and a pressure of 300 bar. The reaction time, 60 s, was selected based on the results from the in-situ study [116] and also as a compromise with the total synthesis time, since only a tiny volume (1.5 mL) is introduced in the reactor at each pulse/cycle. The experiments were performed for different $H_2PtCl_6 \cdot 6\,H_2O/YCl_3 \cdot 6\,H_2O$ ratios. We anticipated that only a fraction of the $YCl_3 \cdot 6\,H_2O$ could react and thus an excess of such precursor was added. The precursors were mixed in absolute ethanol and the same solvent was used in the solvent pump. The precursor concentrations are listed in Table 5.2.

The products from the synthesis were measured with PXRD to determine if any Pt_xM alloy phases were formed. The measurements are shown together in Figure 5.7b for the purpose of comparison. The four synthesises using the yttrium precursor does not show any other peaks than those associated with pure Pt in a FCC structure. Likewise the experiment with gadolinium precursor exhibited the Pt FCC peaks but also additional peaks from a second phase, which matches the structure of Gadolinium bis(hydroxo)chloride $Gd(OH)_2Cl$. This suggests that the gadolinium precursor was partially oxidized, which could be expected since hydrated lanthanide chlorides upon continuous heating losses some water molecules, followed by formation of hydroxochlorides and oxychlorides, and finally formation of oxides [170–172]. This behaviour severely hinders the reduction with hydrated precursors. As a plausible solution, the experiments were repeated with anhydrous precursors ($PtCl_4$, YCl_3 and $GdCl_3$) and anhydrous ethanol (30 ppm water).

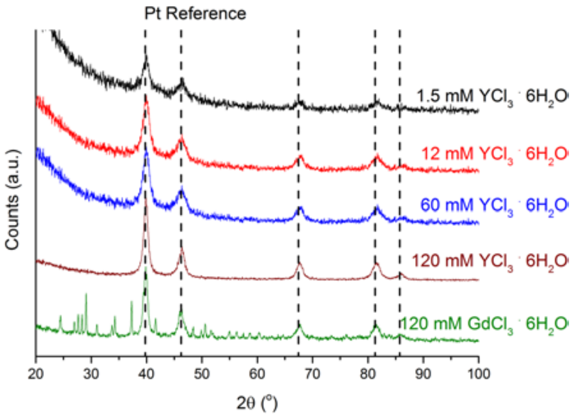

Figure 5.7: PXRD pattern of the different synthesises carried out using the pulse reactor. The platinic acid amount is kept constant while the hydrous YCl_3 and $GdCl_3$ amount are varied as seen on the plot. A Pt phase is the only crystallographic structure present in all spectra, whereas diffraction peaks attributable to Gadolinium bis(hydroxo)chloride are observed when Gd-precursor is used.

$PtCl_4$	YCl_3	$GdCl_3$
4.9 mM	5.9 mM	
2.4 mM	11.9 mM	
5.1 mM	118.8 mM	
5.1 mM		120.2 mM

Table 5.3: Concentrations of precursor solutions used for anhydrous pulse reactor experiments

5.2.2.2 Synthesis with anhydrous precursors and solvent

The precursor solution was prepared by weighing and mixing the salts inside a glovebox with Ar atmosphere. The salts were then put in sealed containers and the anhydrous ethanol was added outside the glovebox using a syringe. The bottles with precursor solution and solvent were connected to the pulse reactor setup. However, since the pumps were not powerful enough to pump the solution through a syringe tube, the containers were not completely sealed. N_2 was therefore flowed into the containers to keep them water/air free. The exact concentrations of precursors in the different synthesises are listed in Table 5.3.

The synthesis products were measured using PXRD and is plotted in Figure 5.8. The main peaks can be explained by a Pt FCC phase. We noted that in the XRD pattern of the second synthesis sample (red line in the middle) there are additional peaks, albeit very small. The weak signal makes it impossible to identify which phase the peaks are associated with. Since the additional peaks only appear in one of the samples it is most likely that these peaks correspond to

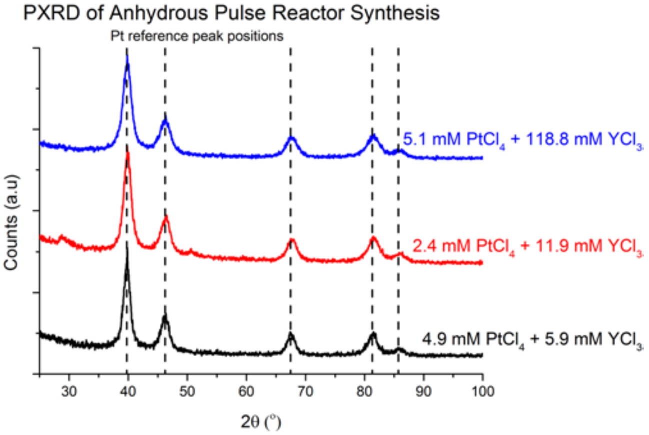

Figure 5.8: PXRD spectra for the synthesis performed in the pulse reactor with anhydrous precursors and ethanol. All the peaks in the different spectra can be attributed to a single Pt phase.

a contamination. The PXRD measurements of the $GdCl_3$ synthesis (not shown) also reveal the presence of a pure Pt phase as only crystallographic structure in the catalyst.

In conclusion, none of the supercritical fluid synthesis methods were successful in synthesising Pt_xGd or Pt_xY alloy nanoparticles. This is puzzling since a successful synthesis of Pt_3Gd nanoparticles was reported using very similar conditions [116]. Anhydrous conditions did not change the outcome of the experiment, but from the reported experiment, anhydrous conditions should not be necessary. A possibility is that the product is not stable enough to survive outside the reactor and thus cannot be measured ex-situ. Without understanding how it was possible to form Pt_3Gd nanoparticles in the in-situ experiments, it is difficult to reproduce the conditions ex-situ.

5.3 Pt_3Y nanoparticles synthesised by high temperature reduction

The high temperature reduction synthesis was partly based on the work by Erdmann et al [117, 118] and Bronger [119], who showed that Pt_xM alloys could be formed from Pt and M oxides or fluorides reduced in H_2 or NH_3 at high temperatures as described in Section 1.4. Their work, and thermodynamic considerations, explained in Section 6.1, led us to attempt the Pt_xY synthesis using unsupported Pt and YCl_3. In addition to the chlorides, prior work by Brian Peter Knudsen, CINF, [169] suggested that Pt_xY also could be synthesised using a organometallic precursor, $Y(C_5H_5)_3$, Tris(cyclopentadienyl)yttrium(III) (YCp3). In this section the results of the synthesis with unsupported Pt, and YCl_3 and YCp3 respectively,

(a) Product from synthesis **(b)** Lumps found in product

Figure 5.9: a) Product from the organometallic synthesis, which is a crude black powder with some small shining particles in it. b) Small lumps found amongst the product powder of the organometallic synthesis.

will be presented. The experimental procedure was explained in Section 5.1.4 The synthesis with unsupported Pt nanoparticles and YCp3 resulted mainly in a powder (Figure 5.9a) with some small lumps Figure (5.9b). The lumps were examined with XPS and consisted mainly of C and Y and we thus suspect they are yttrium carbide, which will be shown in the characterisation in Section (5.3.2). The synthesis with unsupported Pt and YCl_3 resulted in a grey powder, not shown. Characterisation of the two synthesis is presented in the next sections.

5.3.1 PXRD characterisation of product

The product powder was crushed and measured using PXRD. The XRD spectra of the synthesized nanoparticles are plotted together with the spectra of the as-received unsupported Pt and the XRD measurement of the polycrystalline Pt_3Y alloy disk used in the electrochemical experiments [48, 74] in Figure 5.10. The peaks of the synthesized nanoparticles samples are shifted compared to the Pt nanoparticles, and the width of the peaks has decreased significantly, which suggest that the Pt particles have alloyed with Y and grown in size. To identify the alloy phase, the XRD spectra were compared with the spectra of different Pt_xY alloys measured at CINF Pt5Y, Pt_3Y and Pt_2Y. The best match was the Pt_3Y alloy whose spectrum is plotted in the figure (green line). The main features of Pt_3Y polycrystalline are present in both synthesized samples. The spectrum of poly Pt_3Y also contains a number of lines that are not attributable to the Pt_3Y phase (blue dashed lines) and interestingly several of these can also be observed in the sample synthesized with the organometallic precursor. The most likely phase for the peaks is the Pt_2Y phase. It is not possible to confirm if the product of the

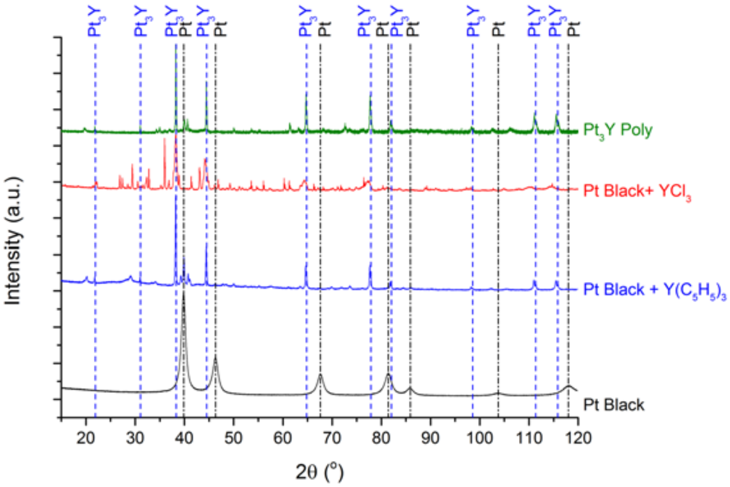

Figure 5.10: XRD spectrum of the product of the syntheses with YCl_3 and $Y(C_5H_5)_3$ as well as the Pt black precursor. The spectrum of the Pt_3Y phase from [48, 74] is used as reference. The peak position of the most pronounced peaks are also shown for Pt (ICSD: 64923) and Pt_3Y (ICSD: 649857) [118]. The Pt peaks are only visible in the Pt black spectrum whereas Pt_3Y peaks are visible in the three other spectra.

synthesis with chlorides (red line) also contains the Pt_2Y phase, since it shows so many other lines that can be explained by yttrium chlorides, oxychlorides; platinum and yttrium silicides. Three phases describes most of the peaks: Pt_3Y (ICSD: 649852 [120], YOCl (ICSD: 60586 [173]) and Pt_4Si_4 (COD: 9008940 [174]). The crystallite sizes were determined from Rietveld refinement. The size of the unsupported Pt was 6.9 nm whereas the crystallite size in the synthesized particles from organometallic precursor was 67 nm. It was not possible to make a good Rietveld refinement for the YCl_3 synthesis but from the peak broadening it appear to have grown significantly.

5.3.2 XPS characterisation of samples

The samples were acid washed in 0.1 M HClO4 to remove leftover precursor and oxides, which makes easier to detect metallic Y inside of the nanoparticles using XPS, as expected from the creation of a Pt-skeleton structure [78]. The two samples were measured with XPS by Paolo Malacrida, CINF and from survey scans the most interesting features were the Pt4f, Y3d, C1s and O1s peaks. The Pt4f and Y3d peaks from organometallic synthesis are plotted in Figure 5.11a.

The shapes of the peaks suggest that there could be two species of Pt: a metallic Pt species (A, marked in grey) with a $Pt4f_{7/2}$ of 71.2 eV, within the range of 70.6-71.3 eV reported values in the NIST XPS database [175]; and a second Pt species (B, marked in red), most likely PtO, albeit the corresponding binding energy (72.1 eV) is a bit lower than the range reported in the NIST XPS database (72.4-74.6 eV).

The Y3d peak are plotted in Figure 5.11b and to achieve a good fit three doublets were fitted. The doublet with the lowest binding energy (Y3d A, blue), has a Y3d$_{5/2}$ peak position of 155.3 eV, which is significantly lower than the average values for metallic yttrium found in the NIST XPS database [175]; and measured at CINF using Pt$_x$Y model samples [74, 78] (155.7 eV and 156±0.2 eV, respectively). The XRD measurements of the polycrystalline Pt$_3$Y disk and the synthesised nanoparticles are quite similar and thus the downshift of the Y3d peak could be related to the Pt$_3$Y phase.

The Y3d B doublet in Figure 5.11b (red) is attributed to an Y oxide since the peak position of Y3d$_{5/2}$ 156.6 eV is within the range of reported binding energy of yttrium oxide 156.4-158.6 eV, according to the NIST XPS database [175]. As previously stated the product of the organometallic synthesis consisted of a powder (Figure 5.9a) and small lumps (Figure 5.9b). The small lumps were also measured by XPS and the main composition was Y, O and C . The position of the Y3d peak (Figure 5.11b insert) coincides with the position of the Y3d C doublet (grey) in Figure 5.11b and it is thus likely that this peak is related to yttrium carbide.

The XPS measurements of the sample prepared in the synthesis using YCl$_3$ are shown in Figure 5.11c and 5.11d. The Pt4f peak shown in Figure 5.11c is broader than the obtained in the organometallic synthesis shown in Figure 5.11a. The peak is described by three doublets: metallic Pt (A, grey); a second one, shifted up in binding energy (B, red); and a third, one shifted down in binding energy (C, blue). The corresponding Y3d spectrum is plotted in Figure 5.11d show that Y3d doublets alone cannot explain the obtained signal Therefore two Si2s peaks were added to describe the measurement. The presence of Si in the sample is likely because the peaks necessary for the fitting are located at 151.6 eV and 153.9 eV, which are close to the position of Si 150.6±0.1 eV and SiO2 154.7±0.5 eV [175]. Additionally, the existence of a PtSi phase fits with the XRD results shown in Figure 5.10. Permyakova [176] studied several Pt-Si alloys prepared by arc-melting and observed a similar Si2s peak 154 eV for Pi0.5Si0.5 and 153-154 eV for Pt0.8Si0.2 (see Figure 4.6 in [176]). Based on this it is likely that a PtSi alloy was formed in the synthesis with YCl$_3$. Given that no Pt-Si alloys were observed in the product of the organometallic synthesis, it is assumed that the Pt-Si alloying is made possible by a reaction between the YCl$_3$ and the SiO2 that the reactor is made of. Besides the two Si2s peaks, Figure 5.11d depicts two Y3d doubles in the XPS spectrum. The first doublet (Y3d A, green) is likely metallic Y since the Y3d$_{5/2}$ peak is at 155.6 eV. The second doublet (Y3d B, purple) could be yttrium oxide, yttrium chloride or yttrium oxo-chloride. The Y3d$_{5/2}$ peak position of 158.7 eV is in between what is reported for oxides (156.4 – 158.6 eV) and halides (158.3-159.1 eV) in [175]. The fitted XPS peak position are summarised in Table 5.4.

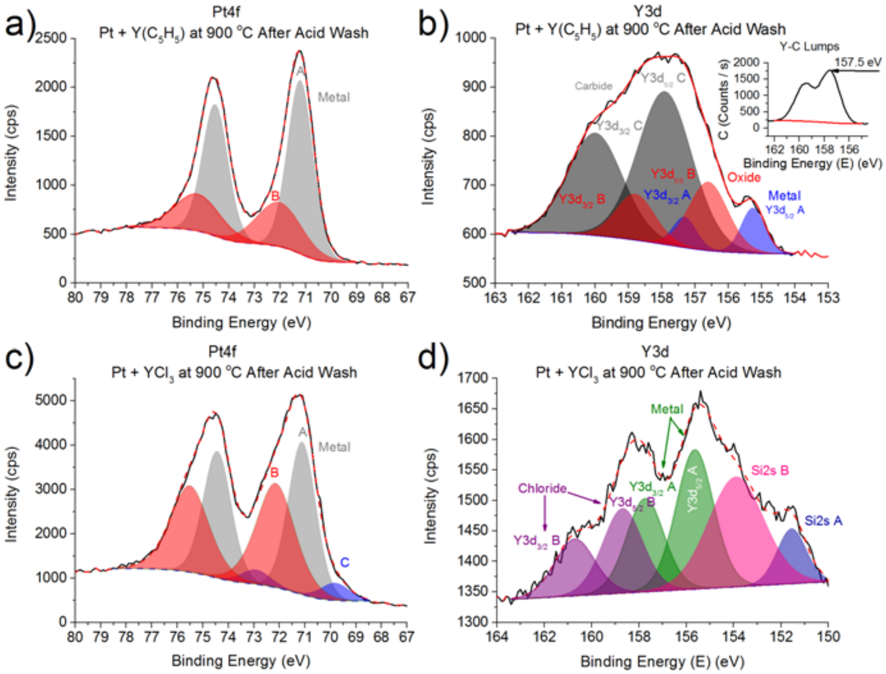

Figure 5.11: Detailed XPS scan of the Pt4f peak a) and Y3d peak b) of the catalyst obtained in the synthesis using $Y(C_5H_5)_3$, and the Pt4f peak c) and Y3d peak d) of the synthesized product when using YCl_3. In a) the Pt4f peak have been fitted with two doublets where the A doublet (grey) fits metallic Pt and the B doublet (red) is another chemical state. In b) the Y3d peak was fitted using three doublets to achieve a good fit. Doublet Y3d A is attributed to metallic Y; doublet Y3d B is likely an oxide; and doublet Y3d C is attributed to yttrium carbide. In c) the Pt4f peak is broader compared to a) and is described by three doublets where one shifted up in binding energy (B red) and one is shifted down in binding energy (C blue) compared to metallic Pt (A grey). In d) the Y3d peak is convoluted with what are likely Si2s peaks. The Y3d part of the peak is described by two doublets where one is metallic Y (Y3d A green) and the other (Y3d B purple) could be a yttrium chloride. Measurements were performed by Paolo Malacrida, CINF.

	Pt/C + YCp3 (900 °C)		**Pt/C + YCl$_3$ (900 °C)**	
	Pt4f$_{7/2}$	**Pt4f$_{5/2}$**	**Pt4f$_{7/2}$**	**Pt4f$_{5/2}$**
Pt4f A (Metal)	71.2	74.5	71.1	74.4
Pt4f B	72.1	75.2	72.1	75.5
Pt4f C			69.8	72.9
	Y3d$_{5/2}$	**Y3d$_{3/2}$**	**Y3d$_{5/2}$**	**Y3d$_{3/2}$**
Y3d A (Metal)	155.3	157.3	155.6	157.7
Y3d B (Oxide)	156.6	158.8		
Y3d C (Carbide)	157.9	159.0		
Y3d D (Chloride)			158.7	160.7
				Si2s
Si2s A				151.6
Si2s B				153.9

Table 5.4: Fitted peak positions in eV of the XPS spectra on Figure 5.11

5.3.3 SEM and EDX analysis of the synthesised samples prepared from YCp3

The XPS measurements of the catalysts synthesized using YCl$_3$ and the organometallic precursor confirmed that both methods were successful in making metallic yttrium in the form of Pt$_x$Y alloy. At the same time, it is also seen that by-products are formed in both syntheses, which remain on the nanoparticles surface. In order to gain insights into the distribution of the synthesis products in the catalyst, electron microscopy analyses were performed. The organometallic synthesis product was measured both as-prepared and after acid-wash using SEM and SEM-EDX by Erik Wisaeus, DTI. Characteristic SEM images of the as-prepared sample are shown in Figure 5.12a and 5.12b. As observed, the sample mainly consists of smooth spheres that from EDX consist of mainly Y and C. This suggests that the thermal decomposition of the Y(C$_5$H$_5$)$_3$ precursor creates yttrium carbides that form large spheres. Both the large (1-2 µm) and small (100-200 nm) spheres appear to be yttrium carbide. Interestingly, no Pt was detected when performing EDX on the as-prepared sample so it is assumed that the Pt$_3$Y alloy is completely covered with yttrium carbide.

Figures 5.12c-d show SEM images of the sample after acid wash, revealing a signal for Pt and Y, which supports the presence of a Pt-Y alloy since there is no carbide and yttrium and yttrium oxide is not stable in acid. It is observed from Figure 5.12c that the particles are rougher than the as-prepared in Figure 5.12a, which is likely to be a result of acid leaching. A SEM-EDX mapping was performed in the rectangular area highlighted in 5.12c. The signals from C K$_{\alpha1,2}$, O K$_{\alpha1}$, Y L$_{\alpha1}$ and Pt M$_{\alpha1}$ are also shown in Figure 5.12c. As a result, the carbon is concentrated on the left side of the area, and from the image it is possible to distinguish between the area with and without carbon. From Figure 5.12c and

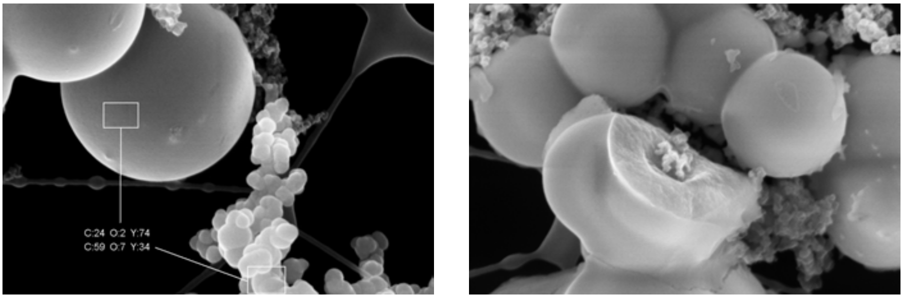

(a) SEM image of as prepared sample

(b) SEM image of as prepared sample

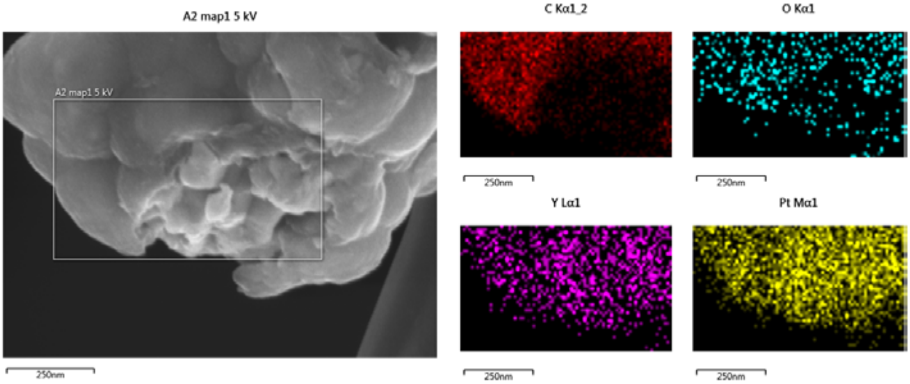

(c) SEM image and EDX mapping of acid washed sample. The EDX mapping was performed inside the marked box in the image

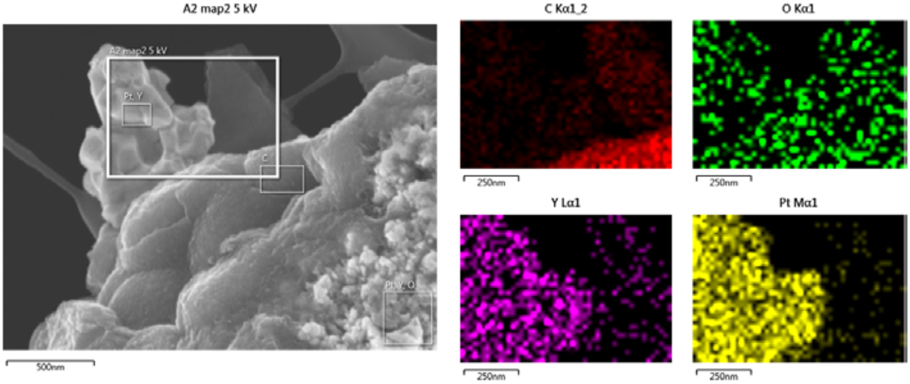

(d) SEM image and EDX mapping of acid washed sample. The EDX mapping was performed inside the marked box in the image

Figure 5.12: SEM images and EDX mapping of the organometallic synthesis product before acid wash a,b) and after acid wash c,d). Images are curtesy of Erik Wisaeus, DTI

5.12d it appears that the Pt_3Y alloy is covered with carbon species. Similarly, the examination of Figure 5.12d suggests that the Pt_3Y alloy is protruding from a carbon structure. From the images it is seen that the Pt_3Y alloy has grown into large agglomerates and that the precursor decomposes into large carbides that cover the alloys.

5.4 Summary

Pt_xY/C nanoparticles were attempted synthesized in a supercritical flow system in order to reproduce the solvothermal synthesis of Pt_3Gd reported in literature, but no alloy was detected, resulting in pure Pt catalysts. It was also investigated if Pt_xY or Pt_xGd could be synthesized in a supercritical pulse reactor under both hydrated and anhydrous conditions, as this reactor type offered longer reaction times which were closer to the reported synthesis. However, this synthesis procedure did not result in alloy formation either and therefore this type of synthesis was abandoned , leading to the quest of new techniques for carrying out this task. A high temperature reduction/annealing synthesis was attempted where Pt nanoparticles were mixed with either a organometallic precursor ($Y(C_5H_5)_3$) or a halide (YCl_3), subsequently reduced in H_2 at high temperatures (900 °C). Pt_3Y was formed using both precursors, but different by-products were also formed depending on the precursor used. When using YCl_3, YOCl and PtSi structures were formed as a biproduct. The YOCl could be removed with acid but the PtSi alloy stayed on the catalyst. XPS analysis confirmed that the Y was in a metallic state. In contrast, when using the organometallic precursor an almost pure Pt_3Y structure was formed and it was confirmed by XPS that the Y was metallic. However, a large fraction of the Y was also in another oxidation state, more likely as yttrium carbide, YC_2. This was checked with SEM analysis, which showed large spheres containing mainly Y and C according to SEM-EDX. The alloy was only visible in SEM-EDX after acid wash. It is speculated that in the case of the organometallic synthesis, the resulting particles grow and merge into huge agglomerates that are covered by YC_2 generated from the precursor decomposition, hindering their use for electrocatalysis purposes. In conclusion, we have developed synthesis methods that are capable of forming Pt_3Y alloys. However, the resulting nanoparticles are excessively large and the surface is covered with by-products that block Pt sites for the electrocatalysis, even after treatment in acid. Therefore, this method requires optimization to synthesize suitable active electrocatalysts. This is the topic of the next chapter.

6

High temperature synthesis of Pt_xM alloy nanoparticles

In Chapter 5 different synthesis routes for Pt_xM nanoparticles (where M is an early transition metal, alkali earth or lanthanide) were explored. The most promising was the formation of Pt_3Y particles from high temperature annealing of unsupported Pt nanoparticles with either $Y(C_5H_5)_3$ or YCl_3. In this chapter the high temperature annealing synthesis method will be studied in detail. The chapter is divided into five sections. First, I examine the thermodynamics of the high temperature reduction. Section 6.2 studies the effect of annealing on the Pt/C seed nanoparticles. Section 6.3 and 6.4 investigate the high temperature synthesis of Pt_xY/C from a commercial Pt/C mixed with either $Y(C_5H_5)_3$ or YCl_3 respectively. In addition the synthesis of other Pt_xM alloy nanoparticles like Pt_xGd/C and PtxTb/C is included in Section 6.4.2. The final section provides a summary, which additionally contains suggestions for an improved synthesis setup.

6.1 Thermodynamics of high temperature reduction in H_2

To better understand the conditions under which the synthesis of Pt_xM nanoparticles is possible, the thermodynamics of different reduction reactions were studied. It is well known that lanthanides and early transition metals form very stable oxides, which could drive the synthesis reaction towards oxide formation, and it is therefore interesting to study the sensitivity of these reactions towards oxygen and water. In Chapter 5 it was postulated that it is easier to form Pt_xM alloys from chlorides than fluorides and oxides, which was based on the reduction of M chlorides, fluorides and oxides into M metal. In this section it will be studied which halides are easiest to reduce in order to form Pt_xM alloys. Finally, the trends in reduction for the lanthanide series, Y and Ca will also be discussed.

Alloy	$T_{\text{Reduction}}$ [K]	ΔH [kJ/mol]	ΔS [J/(mol K)]	Range [K]	Ref
Pt_5Y	1200	-385.97	-5.4	1100-1600	[179, 180]
Pt_3Y	1350	-386.83	-19.6	1300-1700	[179, 180]
Pt_5Gd	1200	-438	-51	1073-1373	[179, 181]
Pt_2Gd	1400	-412	-60	1373-1673	[179, 181]
Pt_5Tb	1200	-442	-44	1073-1373	[179, 181]
Pt_3Tb	1300	-425	-46	1273-1573	[179, 181]
Pt_5Ca	1200	-231.5	-25.5	1200-2133	[178]

Table 6.1: Thermodynamic data for select Pt_xM alloys adapted from [117, 118, 178–181]

6.1.1 Thermodynamic data for Pt_xM alloys

The formation of Pt_xM alloys have been studied in literature for bulk systems both by mixing metals at high temperature [177, 178] and by reducing metal oxides [117, 179–181]. Table 6.1 lists reduction temperatures for select Pt_xM alloys from M-oxides in H_2 using data from [117, 178]. The formation enthalpy and entropy are also listed in Table 6.1 using data from [179–181]. The formation entropy/enthalpy was measured by reducing oxides at different temperatures and then determining the equilibrium constant from the partial pressure of water vapour, which were measured using Galvanic cells [179–181]. The enthalpy values for Pt_5Y and Pt_3Y (-385.97 kJ/mol and -386.83) are close to the values calculated using DFT (-356 kJ/mol and -380 kJ/mol) by Ulrik Grønbjerg Vej-Hansen at DTU Physics [182].

The program HCS Chemistry 6.1 was used to perform the thermodynamic calculations in this section. The program contains a large database of thermodynamic data for a large number of compounds. Unfortunately it does not contain the Pt_xM alloys. The values from Table 6.1 have therefore been used together with additional values from the literature [179]. The program calculates the Gibbs free energy of a compound at different temperatures, and by subtracting Gibbs free energy of the different reactants and products, the change in Gibbs free energy from the reaction can be calculated. To do this for a compound, the program needs the standard enthalpy and standard entropy of the material as well as a function describing the temperature dependent specific heat capacity. Table 6.1 list the change in enthalpy for alloys from its composing elements at standard conditions, which per definition is the standard enthalpy of the alloys. It is not obvious from the table data what the standard entropy and specific heat capacity function are, but that can be calculated as will be shown in the following. The main criteria for the missing parameters in the program, is that the change in Gibbs free energy that the program calculates should be the same as the experimental reported values. The data in Table 6.1 is based on experiments where Pt is mixed with oxides of the M metal (where M is an early transition metal or lanthanide). The mixture was heated under a very pure H_2 flow to form the following reaction [118, 180, 181]:

$$x\mathrm{Pt} + \frac{1}{2}\mathrm{M_2O_3} + \frac{3}{2}\mathrm{H_2(g)} = \mathrm{Pt}_x\mathrm{M} + \frac{3}{2}\mathrm{H_2O(g)} \tag{6.1}$$

The equilibrium constant, K, of the reaction can be determined from the ratio between partial pressure of product gas, $P_{\mathrm{H_2O}}$, (water vapour) and reaction gas, $P_{\mathrm{H_2}}$, (H_2) [180, 181]:

$$K = \left(\frac{P_{\mathrm{H_2O}}}{P_{\mathrm{H_2}}}\right)^{\frac{3}{2}}$$

The change in Gibbs free energy for the reaction, ΔG_{r}, is related to the equilibrium constant by the equation [11]:

$$K = e^{-\frac{\Delta G_{\mathrm{r}}}{RT}} \tag{6.2}$$

Where R is the gas constant and T is the temperature. The change in Gibbs free energy for the reaction is determined by the difference in Gibbs free energy between the reactants and products:

$$\Delta G_{\mathrm{r}} = G_{\mathrm{Pt_xM}} + \frac{3}{2}G_{\mathrm{H_2O}} - \left(xG_{\mathrm{Pt}} + \frac{1}{2}G_{\mathrm{M_2O_3}} + \frac{3}{2}G_{\mathrm{H_2}}\right) \tag{6.3}$$

The Gibbs free energy of the compounds in the reaction can also be described as the change in Gibbs free energy from the elemental substances to the compounds:

$$\begin{aligned}
\Delta G_{\mathrm{H_2O}} &= G_{\mathrm{H_2O}} - \left(G_{\mathrm{H_2}} + \frac{1}{2}G_{\mathrm{O_2}}\right)\\
\Delta G_{\mathrm{M_2O_3}} &= G_{\mathrm{M_2O_3}} - \left(2G_{\mathrm{M}} + \frac{3}{2}G_{\mathrm{O_2}}\right)\\
\Delta G_{\mathrm{Pt_xM}} &= G_{\mathrm{Pt_xM}} - (xG_{\mathrm{Pt}} + G_{\mathrm{M}})
\end{aligned} \tag{6.4}$$

By substituting these expressions into equation 6.3 the following expression is derived:

$$\begin{aligned}
\Delta G_{\mathrm{r}} = {}& \left(\Delta G_{\mathrm{Pt_xM}} + xG_{\mathrm{Pt}} + G_{\mathrm{M}}\right) + \frac{3}{2}\left(\Delta G_{\mathrm{H_2O}} + G_{\mathrm{H_2}} + \frac{1}{2}G_{\mathrm{O_2}}\right)\\
&+ \left(xG_{\mathrm{Pt}} + \frac{1}{2}\left(\Delta G_{\mathrm{Pt_xM}} + 2G_{\mathrm{M}} + \frac{3}{2}G_{\mathrm{O_2}}\right) + \frac{3}{2}G_{\mathrm{H_2}}\right)
\end{aligned}$$

Which can be reduced to:

$$\Delta G_{\mathrm{r}} = \Delta G_{\mathrm{Pt_xM}} + \frac{3}{2}\Delta G_{\mathrm{H_2O}} - \frac{1}{2}\Delta G_{\mathrm{M_2O_3}}$$

By looking up $\Delta G_{\mathrm{H_2O}}$ and $\Delta G_{\mathrm{M_2O_3}}$ in a thermodynamic data table, the change in Gibbs free energy for the alloy $\Delta G_{\mathrm{Pt_xM}}$ can be determined. This is what was done in the papers [179–181], which is the source of the data in Table 6.1.

$$\Delta G_{\mathrm{Pt_xM}} = \Delta G_{\mathrm{r}} - \frac{3}{2}\Delta G_{\mathrm{H_2O}} + \frac{1}{2}\Delta G_{\mathrm{M_2O_3}}$$

The ΔG_{r} was measured at several temperatures in [179–181] and a linear dependence on temperature is reported, suggesting a near constant enthalpy and entropy in the measured temperature range:

$$\Delta G_{\mathrm{Pt_xM}} = H_0 - TS_0$$

The Gibbs free energy for the alloy $G_{\mathrm{Pt_xM}}$ can then be determined by inserting $\Delta G_{\mathrm{Pt_xM}}$ in equation 6.4 and write out the expression with enthalpy and entropy terms:

$$H_0 - TS_0 = H_{\mathrm{Pt_xM}} - TS_{\mathrm{Pt_xM}} - xH_{\mathrm{Pt}} + TxS_{\mathrm{Pt}} - H_{\mathrm{M}} + TS_{\mathrm{M}}$$

This can be separated into an expression for enthalpy and entropy:

$$H_{\mathrm{Pt_xM}} = H_0 + xH_{\mathrm{Pt}} + H_{\mathrm{M}} \tag{6.5}$$

$$S_{\mathrm{Pt_xM}} = S_0 + xS_{\mathrm{Pt}} + S_{\mathrm{M}} \tag{6.6}$$

The enthalpy in equation 6.5 is temperature dependent, but the programme only needs the standard enthalpy, and since the standard enthalpies for Pt and M per definition is zero, the standard enthalpy is equal to H_0. The program also needs the standard entropy, which can be calculated from equation 6.6 where $S_{\mathrm{Pt}}(25\ ^\circ\mathrm{C})$ and $S_{\mathrm{M}}(25\ ^\circ\mathrm{C})$ is found in the programs database. The specific heat capacity, C_P, at constant pressure can be calculated from the following equation:

$$C_P(T) = T\left[\frac{dS}{dT}\right]_P \tag{6.7}$$

The program uses the function in equation 6.8 to describe the specific heat capacity using four constants. The constants can be determined by fitting the function in eq. 6.8 to the calculated specific heat capacity in eq. 6.7 using the entropy from 6.6 and the database values for $S_{\mathrm{Pt}}(T)$ and $S_{\mathrm{M}}(T)$.

$$C_P(T) = A + 10^{-3}BT + 10^{5}CT^{-2} + 10^{-6}DT^{2} \tag{6.8}$$

The calculated specific heat capacity for $\mathrm{Pt_5Y}$ is shown in Figure 6.1a together with the fitted parameters for function (6.16). The points marked with red were ignored in the fit, since these points cannot be described by the function (6.16). The fitted values were used in all calculations performed with the program. The values are listed in Appendix A. To check for self-consistency the fitted values were used to calculate the change in Gibbs free energy for creating $\mathrm{Pt_5Y}$ alloy from Pt and $\mathrm{Y_2O_3}$ in $\mathrm{H_2}$. The calculated change is shown in Figure 6.1b together with the experimental values [180], which the thermodynamic values were determined from. The figure shows a good overlap between the calculated line and the experimental points, and I will thus use this method to calculating changes in Gibbs free energy for all of the alloys.

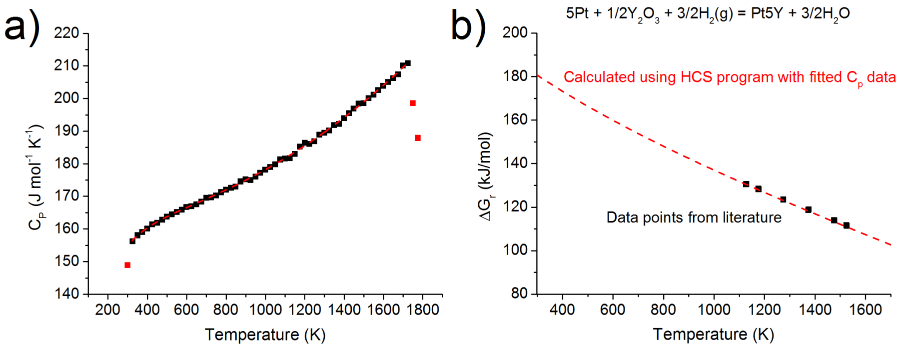

Figure 6.1: Specific heat capacity for Pt_5Y calculated using eq. 6.7 (black and red points). The dashed red line is fitted using eq. 6.8. Red points are ignored in the fit. b) Calculated change in Gibbs free energy from forming Pt_5Y from oxides (red line) calculated using the HCS 6.1 programme and the fitted data from a) and the measured experimental values from the experiment [180] (black squares).

6.1.2 PtxM alloys and M oxides

The most stable and common form of early transition metals and lanthanides is oxides. Therefore the reactions between the Pt_xM alloys and the corresponding M oxides will be studied first. Focus is on the Pt-Y system since the Pt_3Y alloy was formed using this synthesis method as shown in Section 5.3. By using the thermodynamic data shown in Table 6.1 and Appendix A, it was possible to calculate ΔG for forming Pt_5Y and Pt_3Y from oxides. This is depicted in Figure 6.2a and 6.2b where the reaction from Pt and Y_2O_3 to Pt_5Y is shown as a black line; the reaction from Pt and Y_2O_3 to Pt_3Y as a red line; the reaction from Pt_5Y and Y_2O_3 to Pt_3Y as a blue line. Evidently, all reactions have positive changes in ΔG within the temperature range displayed, which is wider than the practical range for making nanoparticles, as the nanoparticles agglomerate at elevated temperatures. The ΔG is normalised differently in Figure 6.2a compared to 6.2b, by moles alloy molecule and moles water molecule respectively. The normalisation is important as it changes which reaction is most favourable. In Figure 6.2a it seems that forming Pt_3Y is most favourable but only by forming Pt_5Y first. In Figure 6.2b on the other hand it is most favourable to form Pt_5Y. It is therefore not clear which normalisation that tells which reaction is most favourable. Rather, the reaction conditions that favour the different reactions can be calculated by using the equilibrium constant, which can be determined from eq. 6.2.

Reaction (6.1) is valid in the case of a M_2O_3 oxide, but not all oxides of the M metals of interest form a M_2O_3 oxide. Instead eq. (6.1) can be written more generally as:

$$x\mathrm{Pt} + \frac{1}{2}\mathrm{M}_y\mathrm{O}_z + \frac{z}{y}\mathrm{H}_2(\mathrm{g}) = \mathrm{Pt}_x\mathrm{M} + \frac{z}{y}\mathrm{H}_2\mathrm{O}(\mathrm{g}) \tag{6.9}$$

The gas phase equilibrium this reaction is:

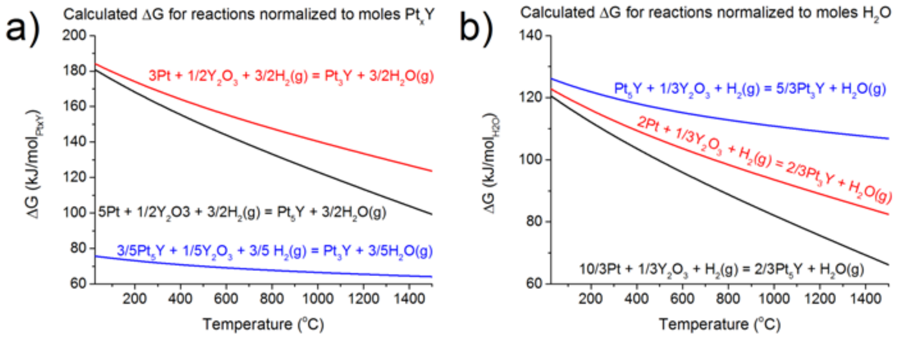

Figure 6.2: Calculated change in Gibbs free energy for forming; Pt_5Y from Pt and Y_2O_3 (black); Pt_3Y from Pt and Y_2O_3 (red); and Pt_3Y from Pt_5Y and Y_2O_3. The plots are either normalized per mole alloy molecule a) or per mole H_2O molecule b)

$$K = \left(\frac{P_{H_2O}}{P_{H_2}}\right)^{\frac{z}{y}} \Longleftrightarrow \frac{P_{H_2O}}{P_{H_2}} = K^{\frac{y}{z}} \tag{6.10}$$

The ratio between partial pressure of water vapour and hydrogen that allows reaction 6.9 to proceed can be seen from eq. 6.10. This is plotted in Figure 6.3b for the three reactions in Figure 6.2. Partial pressures of water higher than the limit from eq. 6.10 oxidise the alloys (white area), while partial pressures of water lower than the limit for the different reactions causes reduction and formation of the alloys. Therefore, according to Figure 6.3b, it is only possible to form the Pt_5Y alloy in the red area; in the blue area both Pt_5Y and Pt_3Y can form; and in the green area both Pt_5Y and Pt_3Y can be formed and it is also favourable to convert Pt_5Y into Pt_3Y. In other words, Figure 6.3b shows the tolerance for water in the different reactions. Furthermore, the figure exhibit trends similar to those in Figure 6.2b, meaning that the ΔG normalized to moles of water, shows which reaction is most favourable and thus have the largest water tolerance. This is also evident from eq. 6.10. The three reactions have a different alloy to oxide ratio and thus also a different alloy to water ratio. This is important for the reaction time, which will be described in the end of the section. The tolerance towards oxygen for the different reactions can also be extracted using the same procedure as for water. The reaction for oxidising the alloys with oxygen is:

$$\mathrm{Pt}_x\mathrm{M} + \frac{z}{y}\mathrm{O}_2(\mathrm{g}) = x\mathrm{Pt} + \frac{1}{y}\mathrm{M}_y\mathrm{O}_z \tag{6.11}$$

The gas equilibrium for the reaction is:

$$K_{O_2} = \left(\frac{1}{P_{O_2}}\right)^{\frac{z}{y}} \Longleftrightarrow P_{O_2} = K^{-\frac{y}{z}} \tag{6.12}$$

The partial pressure of oxygen limit from eq. 6.12 for the oxidation/reduction of Pt_5Y is plotted in Figure 6.3a. The area above the limit (white) favours oxidation

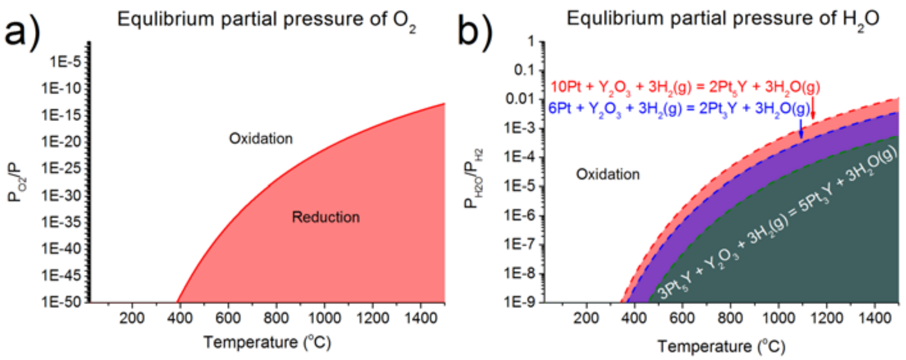

Figure 6.3: a) Oxygen tolerance of Pt_5Y at different temperatures. In the white area oxidation is favoured and in the red reduction is favoured. b) Shows the water tolerance for different reactions that forms Pt_xY alloys. In the white area all of the alloys are unfavourable. In the red area Pt_5Y can be formed. In the blue and the green region both Pt_5Y and Pt_3Y can be formed, but in the green region it is also favourable to convert Pt_5Y to Pt_3Y.

of the alloy, whereas the area below (red) favours the reduction of the alloy. From the plot it seems unlikely that the alloy would be stable under ambient conditions in air, but from experiments it is known that the alloy is stable in air except for a few monolayers that are oxidised. The likely explanation for this is that oxygen is kinetically limited by the surface oxide from diffusing into the alloy. Moreover, when the Pt overlayer is formed, it will too protect the alloy from oxidation. At elevated temperatures, diffusion increases in the Pt alloys, making oxidation possible. The onset of the oxidation of the alloys in O_2 was measured by Erdmann [117] for a number of Pt alloys with alkali earth, early transition metals and lanthanides. The onset was in the range 330-660 °C where Pt_3Sr had the lowest onset and Pt_3Mg the highest. The most relevant alloy in the study for this thesis was the Pt_5Tb with an onset temperature of 450 °C. This suggests that any oxygen present under synthesis conditions can oxidize the formed alloy.

The oxygen and water tolerance are related. This can be seen by calculating the equilibrium for the gas phase reaction of oxidizing hydrogen into water:

$$\mathrm{H_2(g)} + \frac{1}{2}\mathrm{O_2(g)} = \mathrm{H_2O(g)}$$

The gas phase equilibrium can then be written as:

$$K_{\mathrm{H_2O}} = \frac{P^2_{\mathrm{H_2O}}}{P^2_{\mathrm{H_2}} P_{\mathrm{O_2}}} \Longleftrightarrow \frac{P_{\mathrm{H_2O}}}{P_{\mathrm{H_2}}} = \sqrt{K_{\mathrm{H_2O}} P_{\mathrm{O_2}}} \tag{6.13}$$

The water tolerance is found by substituting 6.12 into 6.13. It is seen that the water tolerance is related to the oxygen tolerance by the gas phase equilibrium constant for oxidising hydrogen:

$$\frac{P_{H_2O}}{P_{H_2}} = \sqrt{K_{H_2O} K_{O_2}^{-\frac{y}{z}}} \tag{6.14}$$

It is clear that the water and oxygen concentrations are crucial for the success of the synthesis. The calculations so far have been performed for equilibrium conditions. However, it is not certain that equilibrium will be reached within the timescale of the synthesis. The synthesis is performed with a flowing H_2 gas with a known trace amount of O_2 and H_2O in it. Even assuming that all O_2 molecules will react with an alloy until the equilibrium is reached, the amount of oxidized alloy will depend on the flowrate of the gas and the time of the synthesis. The flux of O_2 can be calculated using the ideal gas equation:

$$n_{O_2} = \frac{P_{O_2} V(Q,t)}{RT} = \frac{P_{O_2} Qt}{RT}$$

Where n_{O_2} is moles of oxygen, P_{O_2} is the partial pressure of oxygen in the feed gas, $V(Q,t)$ is the volume, R is the gas constant, Q is the flow rate, and t is the time. The amount of converted alloy then becomes:

$$n_{\mathrm{ox}} = \frac{z}{2y} n_{O_2} = \frac{z}{2y}\left(\frac{P_{O_2} Qt}{RT} - \frac{P^{\circ}_{O_2} Qt}{RT}\right)$$

The equilibrium partial pressure of oxygen $P^{\circ}_{O_2}$ seen in Figure 6.3a is 10-20 orders of magnitude lower than the trace amounts of oxygen in the feed gas, which is in the ppb range for H_2 instrument 6.0 gases. Thus, the term with the equilibrium pressure may be disregarded. The ratio between alloy and oxidized alloy can then be written as:

$$\frac{n_{\mathrm{ox}}}{n_{\mathrm{Pt_xM}}} = \frac{\frac{z}{2y}\frac{P_{O_2} Qt}{RT}}{\frac{w_{\mathrm{Pt}}}{x m_{\mathrm{Pt}}}}$$

Where w_{Pt} is the Pt weight and m_{Pt} is the Pt atomic mass. The time it will take to completely oxidize the alloy can then be written as:

$$t = \frac{2y}{xz} \frac{w_{\mathrm{Pt}} RT}{m_{\mathrm{Pt}} P_{O_2} Q}$$

The oxidation time is plotted in Figure 6.4a for three different flow rates. The amount of Pt is 0.1 g and the flow rate is measured at 25 °C. Evidently, based on the chosen flow rates, it would take at least a week to completely oxidize all of the alloy material for O_2 concentrations of 2 ppm which is the concentration in a HiQ Hydrogen 5.0 from Linde Gas. The time scale of the synthesis shown in Section 5.3 is maximum 6-8 hours at high temperatures and thus far from the time it takes to oxidise the product. Therefore is instrument 5.0 gas pure enough for the synthesis of Pt_xY alloys.

The minimum time of synthesis from oxides can also be calculated using a similar approach as for O_2. If the reaction is not kinetically limited then the

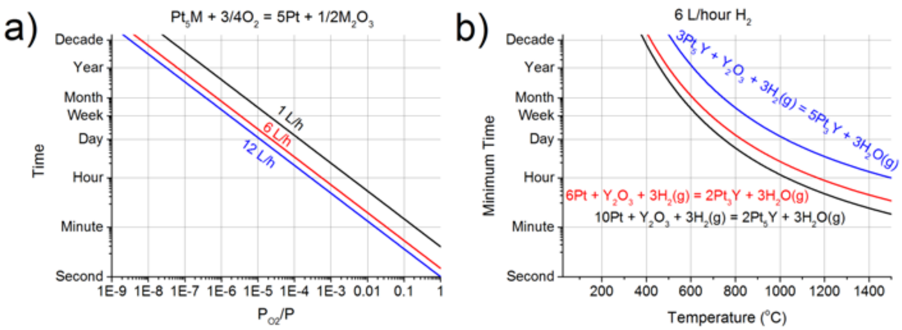

Figure 6.4: Time it would take to completely oxidize Pt_5M alloy made from 0.1 g Pt for different flow rates calculated at 25 °C. b) Minimum time it would take to make the alloy from 0.1 g Pt plus yttrium oxide in a hydrogen atmosphere at different temperatures. It is assumed that the reaction is only mass transport limited, where the maximum mass flux of product gas is calculated from equilibrium partial pressure of water and a H_2 flow rate of 6 L/hour (measured at 25 °C).

reaction rate will be limited by how fast the product gas can be removed. In Figure 6.3b the equilibrium partial pressure of water is calculated for different reduction reactions for making the alloy. In a mass transport limited situation the equilibrium pressure will also be the maximum partial pressure and the maximum reaction rate will depend on how much water can be removed at the maximum partial pressure. Thus the amount of product gas can be written as:

$$n_{\mathrm{H_2O}} = \frac{P_{\mathrm{H_2O}}V}{RT} = \frac{P_{\mathrm{H_2O}}Qt}{RT}$$

The amount of water can be related to the amount of alloy molecules formed:

$$\frac{w_{\mathrm{Pt}}}{x m_{\mathrm{Pt}}} = n_{\mathrm{Pt_xM}} = \frac{z}{y} n_{\mathrm{H_2O}} = \frac{z}{y}\left(\frac{P_{\mathrm{H_2O}}Qt}{RT}\right)$$

The minimum time can then be deduced:

$$t = \frac{y}{xz}\frac{w_{\mathrm{Pt}}RT}{m_{\mathrm{Pt}}P^{\circ}_{\mathrm{H_2O}}Q}$$

The minimum time is plotted in Figure 6.4b for three different reactions to form either Pt_5Y or Pt_3Y. The flow rate is 6 L/hour and calculated at 25 °C, and the amount of Pt used is 0.1 g. It can be seen that Pt_5Y reduction becomes practical around 1000 °C and Pt_3Y around 1200 °C. It should be noted that the minimum reduction time scales with Pt and the flow rate. If either is changed by for instance an order of magnitude, the minimum will also change by an order of magnitude. This means the minimum time can be reduced by increasing the flow rate although at some point the reaction will be kinetically limited and then increasing flow rate beyond this point will not matter.

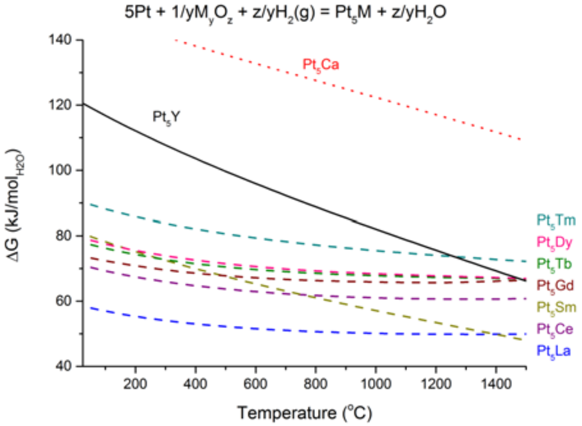

Figure 6.5: Comparison of ΔG for forming different Pt$_5$M alloys from Pt and M_yO_z in H_2. The ΔG has been normalized to moles of H_2O.

The focus has so far been on the Pt$_x$Y alloys, but the same methodology can also be applied on other Pt$_x$M alloys. In Figure 6.5 the ΔG is plotted for forming different Pt$_5$M alloys from Pt and M_yO_z alloys in H_2. The ΔG has been normalized to moles H_2O in the reaction to keep the same trend as would be seen for equilibrium partial pressure of H_2O in the reaction. Evidently, the alloy with an alkali metal has the highest ΔG making it the most difficult to reduce. It is also seen that all lanthanide alloys have a lower ΔG than for forming Pt$_5$Y making them easier to form. There is also a clear trend for the lanthanides, with early lanthanides being the easiest to form from oxides.

6.1.3 Halides

It is possible to form Pt$_x$M alloys from M oxides, but the reaction temperature is quite high (>1000 °C) and the process is slow. The alternative to oxides is to use halides, which was demonstrated in Section 5.3 where Pt$_3$Y was formed from Pt and YCl_3 in a H_2 flow at 900 °C. To learn more about the halide system, ΔG is calculated for the following reaction:

$$x\mathrm{Pt} + \mathrm{MHalide}_3 + \frac{3}{2}\mathrm{H}_2(\mathrm{g}) = \mathrm{Pt}_x\mathrm{M} + 3\,\mathrm{HHalide}(\mathrm{g})$$

The ΔG for forming Pt$_5$Gd from different halides is plotted in Figure 6.6a. It is seen that the alloy formation from halides in general has a lower ΔG, thus making it easier to form the alloys. There is also a general trend among the halides in which GdI3 is the easiest to reduce and GdF3 is the hardest. To determine how difficult it is to form the alloy from halides in a H_2 flow, the gas phase equilibrium equation for this reaction is used:

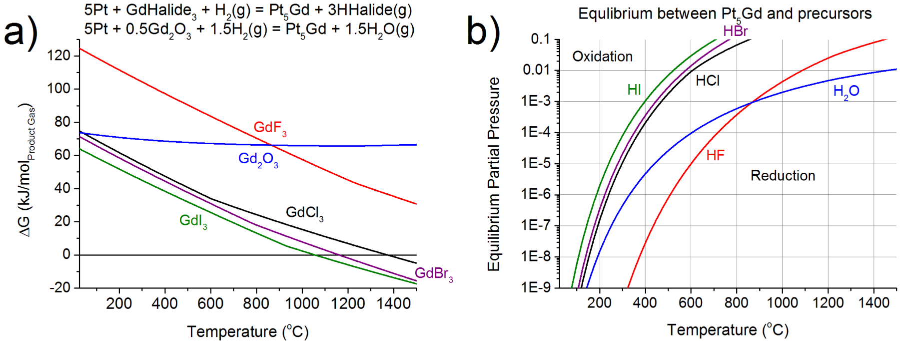

Figure 6.6: a) The ΔG for forming Pt_5Gd from different precursor normalized by moles gas phase product. It can be seen that the ΔG is smaller when forming the alloy from halides than oxides. b) Equilibrium partial pressure of the product gas involved in the reaction. The reaction with HCl, HBr and HI product gasses all have a very high equilibrium partial pressure at lower temperatures (500 °C – 900 °C) compared to HF and H_2O.

$$K_{\text{HCl}} = \frac{(P_{\text{HCl}}/P)^3}{(P_{\text{H}_2}/P)^{\frac{3}{2}}} \tag{6.15}$$

This expression is not easily solved, but since $P_{\text{H}_2} \approx P = 1$ bar for most relevant values of P_{HCl} eq. 6.15 can be approximated as:

$$K_{\text{HCl}} = P_{\text{HCl}}^3 \Longleftrightarrow P_{\text{HCl}} = \sqrt[3]{K_{\text{HCl}}} \tag{6.16}$$

The error of this approximation reaches 10% when the P_{HCl} increases beyond 0.0322 bar. The error becomes negligible for P_{HCl} below 0.01 bar. The approximated equilibrium partial pressure of different product gasses is plotted in Figure 6.6b. In general the halides have a much higher equilibrium partial pressure of the product gas than for the oxides meaning that it is easier to form Pt_5Gd alloy from halides than oxides, since the reaction can tolerate a much higher product gas concentration. There is also a trend in the halides in which GdF3 is the most difficult to reduce and then it becomes easier through the halide series. The temperature region of interest for this synthesis is 500-900 °C and in this region there is a negligible difference between using $GdCl_3$, GdBr3 and GdI3. All have a P_{HCl} in this temperature range so high that the approximation in 6.16 begins to break down. From a practical perspective, removing percentage or per mille level of HCl gas is relative easy, and the synthesis can thus be performed with halides at much lower temperatures than for oxides.

In the synthesis performed in Section 5.3, it was speculated that the precursor was in a liquid state, which facilitated transport of precursor to the Pt nanoparticles. It is therefore important to look at the melting temperature of the different precursors. In Table 6.2 the melting temperature of different gadolinium precursors is listed. $GdCl_3$ not only has the lowest melting point of the precursors on the list, it is also easy to reduce as seen in Figure 6.6b, and finally it is easy to

Precursor	Melting point
GdF3	1232 °C(1505 K [183])
Gd2O3	2425 °C(2698 K [184]
GdCl3	602 °C(875 K [185])
GdBr3	770 °C(1043 K [186])
GdI3	930 °C(1203 [184])

Table 6.2: Shows the melting point for different gadolinium precursors [183–186].

procure. Similar calculations have been performed for Pt$_x$Y and PtxTb alloys, which also found chlorides to be the best choice of precursor among halides and oxides.

Having found that chlorides are the best choice of halide precursor for this synthesis, the same analysis that was performed for the lanthanide oxides can be applied on the lanthanide chlorides. Figure 6.7a shows a comparison of equilibrium partial pressure of HCl gas for reactions forming Pt$_5$M alloys using different chlorides as precursors. In the plot the precursors with the highest equilibrium pressure of HCl at lowest temperature is easiest to reduce. It is clear that the easiest alloy to form is Pt5Dy from DyCl3. However, all of the lanthanide alloys have a sufficiently high equilibrium partial pressure (>1‰) of HCl in the relevant temperature range (500-900 °C), that it should be possible to synthesise all of them from chlorides. Pt5Ca is much more difficult to form from chlorides than the other alloys, which is similar behaviour as for oxides. It seems that Pt5Ca and likely other Pt alkali metal alloys are more difficult to form than the Pt lanthanide and early transition metal alloys.

Figure 6.7b shows the equilibrium partial pressure of HCl gas for different reactions between Pt$_x$Y alloys and chlorides. In the white region it is not favourable to form the alloy from chlorides. In the red region Pt$_5$Y can be formed; in the blue region both Pt$_5$Y and Pt$_3$Y be formed; and in the green region both Pt$_5$Y and Pt$_3$Y can be formed and it is also favourable to convert Pt$_5$Y into Pt$_3$Y. Because the equilibrium partial pressure of HCl is so high for all three reactions in the temperature region of interest (500-900 °C), it would be realistic to have a partial pressure of HCl where both Pt$_5$Y and Pt$_3$Y alloy particles can be formed at the same time. If the reaction was mass transport limited, the partial pressure would approach the highest allowed value, which would be the transition to Pt$_5$Y alloy. When Pt is fully converted into Pt$_5$Y, the reaction no longer takes place, which would force the partial pressure down to the equilibrium value for transforming Pt$_5$Y to Pt$_3$Y. Whether the reaction is mass transport limited or kinetic limited will determine if Pt$_5$Y and Pt$_3$Y are formed at the same time or Pt$_3$Y is formed after Pt$_5$Y is formed.

In summary, the thermodynamic calculations showed that although the synthesis is sensitive to O_2 and H_2O from a practical perspective, it should be possible to avoid oxidation when using instrument 5.0 gas or purer in the timescale of the

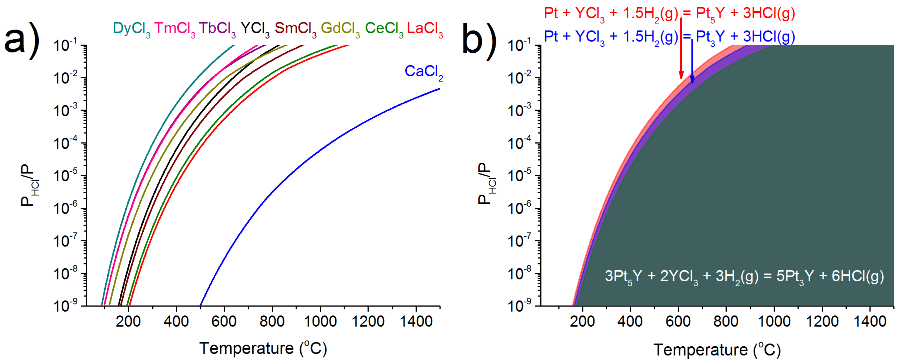

Figure 6.7: a) Equilibrium partial pressure of product HCl gas for reactions forming different Pt_5M alloys from chlorides. b) Equilibrium pressure of product HCl gas for reactions forming Pt_xY alloys. In the white area it is not favourable to form the alloy; in the red area only the Pt_5Y alloy is formed; in the blue area both the Pt_5Y and Pt_3Y are formed; and in the green area both alloy can be formed but it is also favourable to change Pt_5Y into Pt_3Y.

synthesis. It was also shown that precursors of M halides, namely chlorides, bromides and iodides can be reduced to form Pt_xM alloys in the 500 - 900 °C range of interest for the synthesis. Based on the thermodynamics of the reduction and melting temperature, YCl_3, $GdCl_3$ and $TbCl_3$ are the best precursors to form Pt_xY, Pt_xGd and PtxTb alloys respectively from halides, and these will therefore be used in section 6.4.

6.2 Annealing of Pt/C seed particles

As discussed in section 1.3.4.2 the particle size of the alloy is crucial to achieve the mass activity gains reported for cluster source fabricated nanoparticles [78,79]. Therefore the choice of Pt seed particles can determine the success of the synthesis. The size distribution of the synthesised alloy nanoparticles will depend on the size distribution of the carbon supported Pt (Pt/C) seed particles and the stability of these particles under high temperature annealing. We were able to procure commercial Pt/C nanoparticles with a specified size of 6.6 nm and 50% wt. loading Pt from Tanaka Kikinzoku Kogyo (TKK) and these were used for all the synthesis experiments in this chapter.

The Pt/C nanoparticles were characterised both as received and after annealing at 900 °C to see how the nanoparticles behave under similar conditions as the alloy synthesis. The annealing was performed with a H_2 flow and the sample was heated in a 25 min. ramp to 200 °C, held for 60 min. then ramped up to 900°C in 70 min., and finally held at 900 °C for 60 min. The sample was allowed to decrease in temperature to 500 °C for 50 min. where after the heating stopped, allowing the sample to cool down slowly. The as received and annealed samples were measured with PXRD, and the measurements and Rietveld refinements are

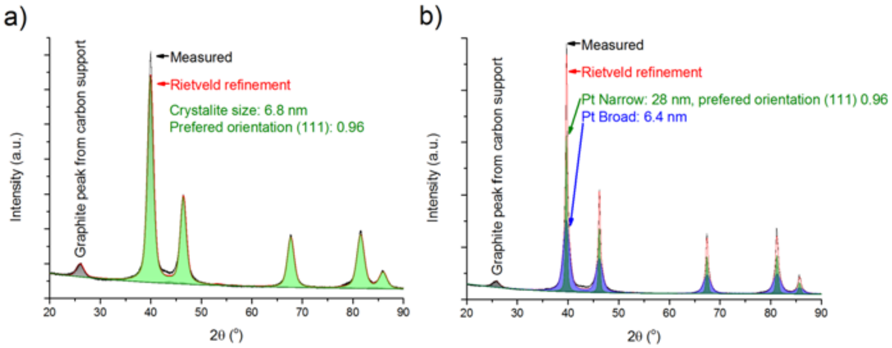

Figure 6.8: PXRD measurement and Rietveld refinement of a) as received Pt TKK 50% wt. Pt/C and b) same catalyst after being annealed for 60 minutes at 900 °C in H_2.

shown in Figure 6.8a and figure 6.8b for the two samples respectively. Besides the Pt phase, a graphite phase is also present, which stems from the support, suggesting that the support material is a graphitized carbon. The Rietveld refinement (red line) describes the measurement of the as received sample well, although some intensity is missing for the (111) reflection at 39-40 °. The extra intensity for the (111) peak could suggest some preferred direction for the crystallites in the (111) direction. This has been included in the fitting and the preferred orientation in the (111) direction was fitted to 0.96 where 1 is no preferred orientation and 0 is complete preferential growth. The crystallite size was determined to 6.8 nm from the peak broadening by assuming spherical particles and no micro strain. The Rietveld refinement for the annealed sample was more complicated since the peaks associated with Pt could not be described by a single phase. Instead, two phases were used with different peak broadenings. While this provided a better description, some intensity for the (111) peak was missing and a preferred orientation was thus added to the refinement. The preferred orientation did not give any meaningful value for the Pt phase with the broader peaks, but for the narrower Pt phase, the refinement gave the same value as for the as received sample. The sizes from the refinement of the annealed sample do not have a physical meaning since it is not known if the size distribution can be described by two sizes. The simple interpretation is that the size distribution is quite broad.

The size distribution of the Pt/C was investigated further by use of small angle x-ray scattering (SAXS). For the measurement a sample of the support material was prepared by taking some of the annealed Pt/C and dissolving the Pt in Aqua Regia solution (3:1 HCl 37% and HNO_3 65%). The solution was then diluted with distilled water and centrifuged to rinse the carbon support. The dried carbon support, as received Pt/C and Pt/C annealed at 900 °C were measured in powder form in the SAXS setup at DTI by Solveig Røgild Madsen. The signal from the carbon support was subtracted from the two other samples, and the size distribution calculated from the inverse Fourier transform. The calculated size distribution is shown in Figure 6.9a. There is a clear difference in size distribution between the two samples. The as received sample has a lower peak position than the annealed sample and also a more narrow distribution. For the annealed sample, most of the distribution lies at smaller radii, suggesting that many particles have not grown. The distribution does however continue to radii much larger (>30 nm) than for the as received sample (<10nm). The as received sample shows ripples and negative values in the size distribution for larger radius sizes, which is likely an artefact from the Fourier transform, also known as Fourier Ripples. The size distribution for the annealed sample also contains what could be ripples at larger radii (>10 nm), from the plot it is not possible to see if it is an artefact or not. The effect of Fourier Ripples can be avoided by changing the boundaries of the inverse Fourier transform, since the Fourier Ripples are dependent on the integration limits. The cumulative distribution in Figure 6.9b is constructed by integrating the distributions shown in Figure 6.9a. An indication of the uncertainty in the data and Fourier transform is found from changing the integration boundaries of the transform and observing changes in the cumulative distribution. The software used for the data treatment (EasySAXS) calculates the radii at 20%, 50% and 80% of the integral denoted $r_{20\%}$, $r_{50\%}$ and $r_{80\%}$ respectively. The $r_{20\%}$ and $r_{50\%}$ values (3.3 nm and 4.4 nm respectively) change very little whereas the $r_{80\%}$ is in the range 11 nm to 30 nm. This suggests that the cumulative distribution is stable for 0 to around 50% whereas the distribution around 80% is quite sensitive to the boundaries of the inverse Fourier transform. The cumulative distribution shows that 75% percent of the volume of the as received particles are in the range 6-12 nm diameter particles we are aiming for, and after annealing this number drops to 50%. Most of the distribution loss for the annealed particles is spread to larger particles, which may have the higher specific activity, but in turn a poor mass activity due to their size. Only 5% of the annealed Pt particles' volume is used for smaller particles that do not form as active alloy nanoparticles [78, 79]. The surface to volume ratio was calculated from the SAXS data, and was found to drop from 0.7181 to 0.5273 for as received to the annealed sample, which is a loss of 27% of the surface per mass.

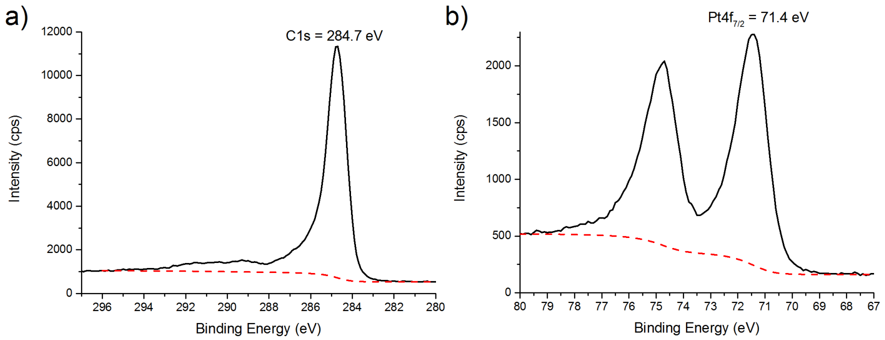

Figure 6.10: XPS measurement of the annealed (900 °C) Pt/C 50% wt. catalyst. The C1s peak is plotted in a) and the Pt4f peak in b).

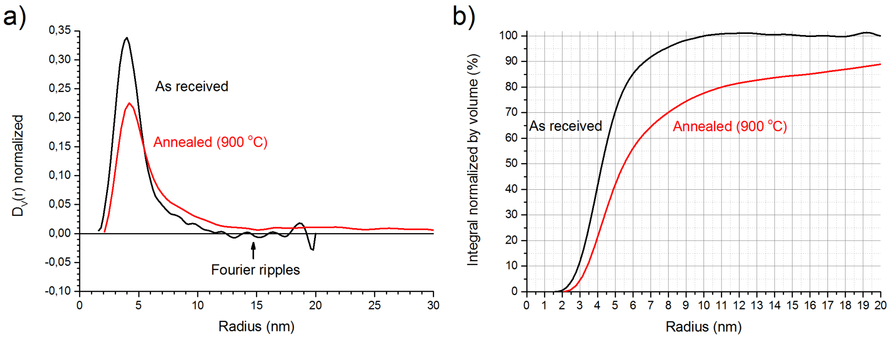

Figure 6.9: a) Fourier transformed SAXS measurements of TKK Pt/C 50% wt. as received and after annealing to 900 °C. b) Shows the cumulative distribution calculated by integrating a). Measurement performed by Solveig Røgild Madsen, DTI

The annealed Pt/C nanoparticles were also measured using XPS, thus creating a reference for the C1s and Pt4f peaks when measuring the alloy nanoparticles. The peaks are shown in Figure 5.10a and Figure 5.10b for the C1s and Pt4f peaks respectively. The Pt4f7/2 peak position is slightly higher (71.4 eV) than expected (71.1 eV) which could just be a small shift in the instrument. The C1s peak position was 284.7 eV.

The as received and annealed Pt/C was additionally characterized electrochemically. The average values are based on experiments performed by Amado Andres Velazquez-Palenzuela (CINF) and myself. The electrochemical surface area was determined by means of CO stripping to be 25±1.5 and 21±0.2 for the as received and annealed Pt/C respectively. This is a decrease of 16% which is lower than expected from the SAXS measurements. The specific activity (1.0±0.2 mA/cm2 and 1.32±0.09 mA/cm2) and mass activity (0.27±0.04 A/mgPt and 0.28±0.02 A/mgPt) were also measured for the as received and annealed samples respectively.

6.3 Pt_xY/C synthesis in quartz reactor using organometallic precursor

The synthesis using organometallic precursors was not treated thermodynamically in Section 6.1 since cyclopentadienyl Yttrium(III) (YCp3) decomposes easily, the reaction is thus not between Pt and YCp3 at the alloying temperature, but rather some species that YCp3 decomposes into. The thermodynamic data for YCp3 in literature [187], were determined from heat of combustion at low temperatures (<100 °C) and may not be valid in the alloying region (>500 °C). Section 5.3 demonstrated that Pt_3Y nanoparticles could be synthesised using YCp3 and it was also demonstrated that some Y-C compound, likely YC_2, was formed during the synthesis. It is not known if the Pt_3Y was formed from YC_2 or some other YC_xH_y species, and not knowing which reactions that take place, makes it impossible to construct a thermodynamic model. Instead, the experiments from Section 5.3 were repeated with a commercial Pt/C to see if electrochemical active Pt_xY/C nanoparticles could be formed.

The experimental conditions were kept the same as in Section 5.3. 200 mg of TKK Pt/C 50% wt. were mixed with YCp3 in a 1:3 Pt to YCp3 weight ratio inside a glovebox. The Pt/C was pre dried by heating it in H_2 at 200 °C for one hour. The mixture was put into a quartz reactor and sealed. The sealed reactor was taken from the glovebox and connected to the synthesis setup (reactor and setup are shown in Figure 5.4, Chapter 5). The gas lines were purged prior to connecting them to the reactor, and then a flow of H_2 was started through the reactor and a heating program started. The program consisted of three temperature levels; first the reactor was heated to 200 °C in 25 min. and held for one hour; then it was heated to 900 °C in 70 min. and then held for one hour; finally the temperature was lowered to 500 °C and held for 50 min after which the heating program ended.

6.3.1 Characterisation of Pt_xY/C nanoparticles made from YCp3 at 900 °C

The resulting powder was measured using PXRD both as prepared and after acid wash in 1M H_2SO_4. The PXRD measurements are shown in Figure 6.11 together with the PXRD measurement of the annealed Pt/C. The PXRD results are quite different from the results in Section 5.3 where mainly Pt_3Y was formed and no Pt peaks visible. In Figure 6.11 the Pt peaks (marked A) are also visible in the spectrum for the alloy nanoparticles (marked B), meaning that Pt had not been fully alloyed. The Pt_3Y phase is clearly present from the peaks (marked C), but another Pt_xY alloy phase is also present, which possibility could be the Pt_2Y phase that matches several of the peaks. Another interesting point is that the Pt_2Y phase have peaks around 20 ° marked E and F for the as prepared and acid washed sample respectively, and that the ratio between the E and D (graphite from the support), and F and D are different, which suggest that some of the Pt_2Y phase was removed during the acid wash. The latter also matches experiments performed with polycrystalline Pt_2Y which was found to be unstable during ORR measurements in acidic electrolyte [49, 74]. An unexpected peak is observed around 36 ° (marked G) in the as prepared sample, but almost disappears in the acid washed sample (marked H) which suggests that the phase is unstable in acid. From the elements that are present, the most likely phase that describes the peaks is Y18Pt50.56Si15.44 which means that the precursor is also reacting with the glassware.

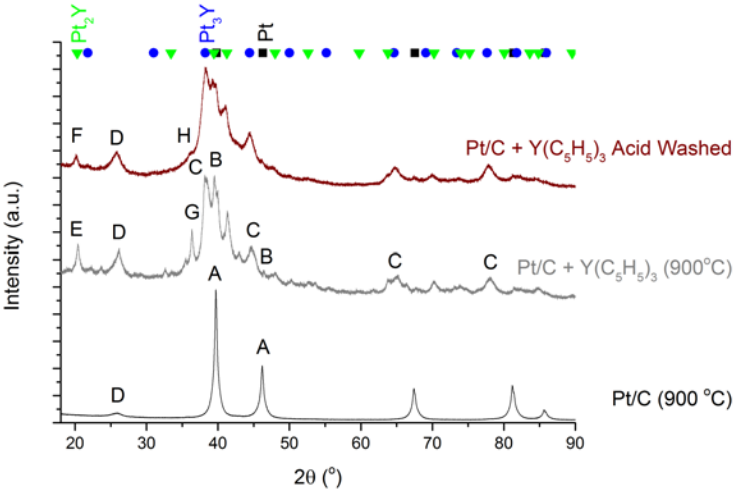

Figure 6.11: PXRD measurements of the annealed Pt/C seed particles as well as the synthesized Pt_xY/C particles using $Y(C_5H_5)_3$ shown both as prepared and after acid wash in 1M H_2SO_4. The reference peak positions for Pt (black square), Pt_3Y (blue circle) and Pt_2Y (green triangle) are shown at the top. A marks Pt's (111) and (002) reflections which are hardly visible in the synthesised sample at peak position B where the observed Peak matches the (113) reflection of either Pt_5Y or Pt_2Y. C marks the main Pt_3Y peaks. D is a reflection from the graphitised carbon support. The peak at position E could be either Pt_5Y or Pt_2Y. It is observed that the F peak decreases compared to the D peak after acid wash.

The synthesised samples were also measured using XPS as seen in Figure 6.12. The survey for the as prepared sample (Figure 6.12a) contains Pt, Y, C and O, which is as expected for a carbon supported Pt_xY measured on carbon tape. The C1s and Pt4f in Figure 6.12b and 6.12c respectively show little difference compared to the same peaks measured on the annealed Pt/C sample seen in Figure 6.10. The Pt4f7/2 peak have the same position (71.4 eV) as the annealed Pt/C and the C1s is only shifted -0.2 eV compared to the annealed Pt/C sample. The Y3d peaks for the as prepared sample are shown in Figure 6.12d, and from the spectrum, it can be seen that there is at least two Y3d doublets, one large and a smaller one at lower binding energies. The sample was measured again after being washed twice in 1 M H_2SO_4, referred to as "2x acid wash", once more leaving it in 1 M H_2SO_4 for five days, and then washing one last time in 1 M H_2SO_4 referred to as "4x acid wash". By comparing the three Y3d spectra, it is clear that there is at least four different species. The as prepared sample contains; a doublet likely related to Pt_3Y with an Y3d5/2 peak at 155.3 eV; a doublet with a Y3d5/2 peak at 157.6 eV which based on the results from Section 5.3 are likely to be yttrium carbide; a doublet with a Y3d5/2 peak at slightly lower binding energy 157 eV which is likely to be an oxide; and finally a fourth doublet that was added because it is present in the acid washed samples describing metallic Y with a Y3d5/2 peak at 156.4 eV. From the fitting it is clear that most of the Y3d peak stems from yttrium carbide and yttrium oxide. The acid wash did remove the oxide, but only some of the carbide and even after the additional acid wash there is still some yttrium carbide remaining as seen in Figure 6.12e. In Figure 6.12e depicts more than one metallic Y3d doublet where one has the usual Y3d5/2 peak at 156.4 eV and the other at 155.4 eV. This fits with the XRD results where other Pt_xY alloy phases were observed besides Pt_3Y. The fitted Y3d carbide peak normalized to the Pt4f peak is shown for all three samples in Figure 6.12f, and it is seen that the initial acid wash removes most of the carbide compared to the second, harsher acid treatment removes a little which suggest that the remaining yttrium carbide is stable in acid.

STEM measurements were performed by Brian Peter Knudsen, CINF on the acid washed sample. A general view is presented on Figure 6.13a, and to clean up the image a Fourier band-pass filter of 3-40 pixels was applied and the result is displayed in Figure 6.13b. The same filter was applied to Figure 6.13c and 6.13e, and the results are shown in Figure 6.13d and 6.13f respectively. The general view image shows many large nanoparticles with edged shapes. Taking a closer look at the particles in Figure 5.13d and 5.13f reveals a numerous tiny holes. It is not known whether these low intensity areas are actual holes in the particles or areas with lighter elements that causes a lower intensity in STEM. The intensity is proportional to the atomic mass squared so lighter elements like Y which weigh less than half of Pt will have ¼ the intensity of Pt, and thus the holes can be areas with a more Y or Si rich alloy.

6.3.2 Temperature series using organometallic precursor

The initial experiment with Pt/C and YCp3 at 900 °C showed in contrary to what was seen with unsupported Pt and YCp3 the formation of other Pt_xY phases than Pt_3Y and that Pt was not fully converted. XPS measurement showed formation of yttrium carbide which could not be completely removed with acid treatment. A good alloy electro catalyst should have only a single phases and no carbide on the surface. To achieve this, the YCp3 concentration was doubled to convert the remaining Pt as the shift from unsupported Pt to carbon supported Pt provides much more surface area to react with and more precursor is thus needed. To avoid the carbide formation and the more yttrium rich phases, a temperature series was performed, hypothesising that the carbide formation and alloy formation were

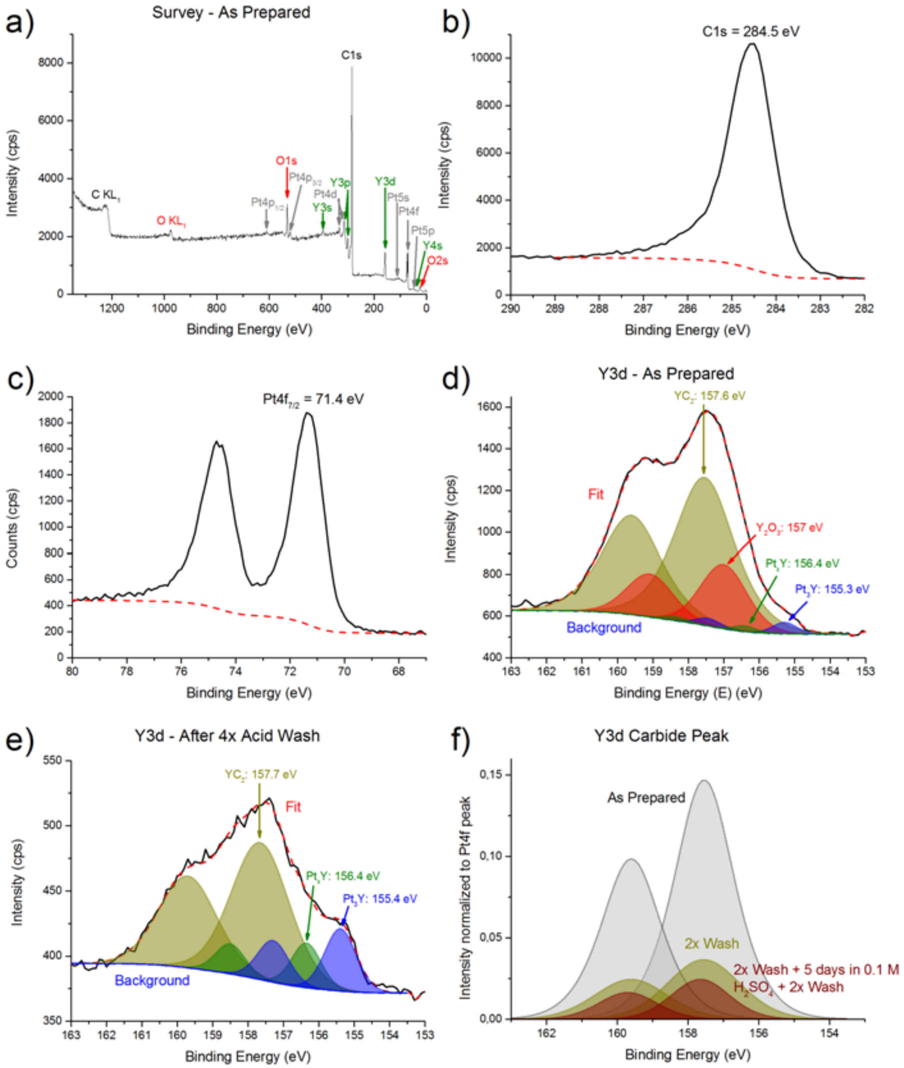

Figure 6.12: XPS measurements of synthesized particles from Pt/C and $Y(C_5H_5)_3$ at 900 °C. a) Survey scan for the as prepared sample. The C1s, Pt4f and Y3d peaks for the as prepared sample are plotted on b), c) and d) respectively. e) Shows the fitted Y3d peak after 4 times of acid wash. f) Fitted Y3d peaks assigned to yttrium carbide shown as prepared, after 2 and 4 times acid wash respectively. Measurements performed by Paolo Malacrida, CINF.

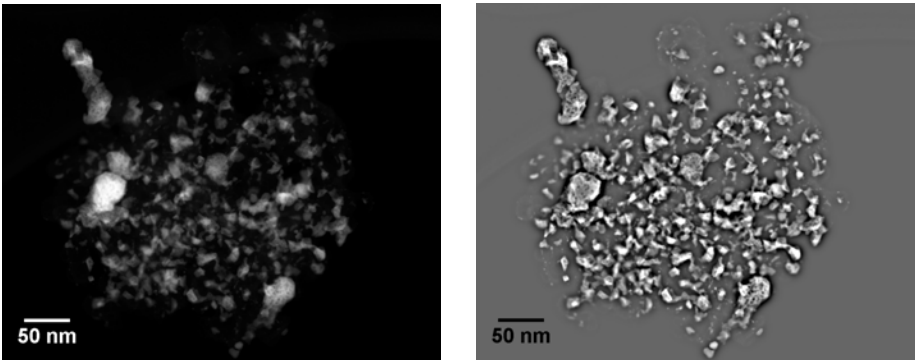

(a) Origninal **(b)** With bandpass filter

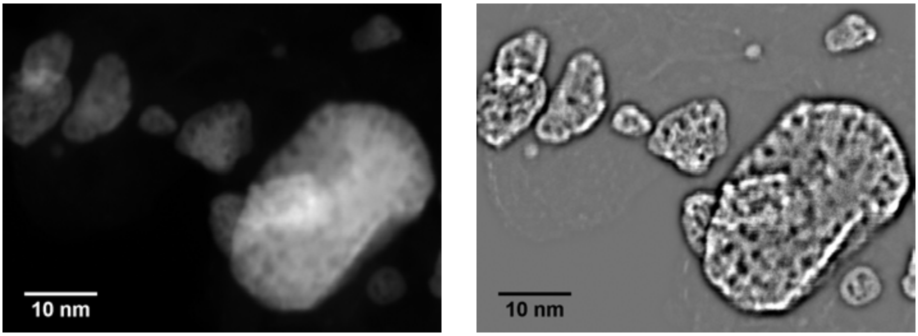

(c) Origninal **(d)** With bandpass filter

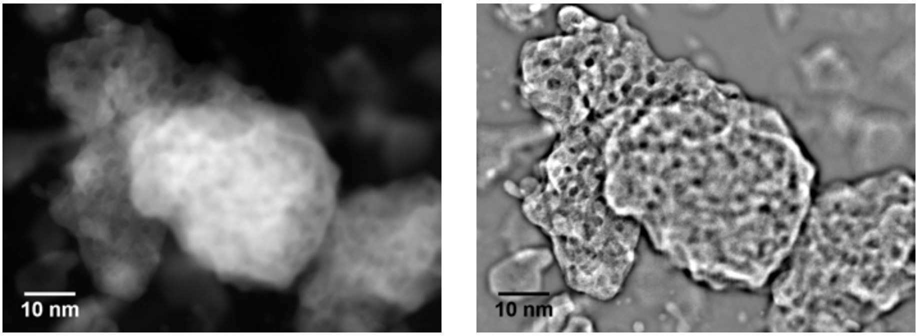

(e) Origninal **(f)** With bandpass filter

Figure 6.13: STEM images of Pt$_x$Y nanoparticles made from Pt/C and Y(C_5H_5)$_3$ at 900 °C. a),c),e) are the original images and b),d),f) are made by applying a band pass filter between 3-40 pixels to the originals. Measurement by Brian Peter Knudsen, CINF.

temperature dependent. The lowest temperature for alloy formation is around 500 °C since this is where the Pt becomes mobile, which have been observed in previous experiments performed at CINF [168]. The series was performed with doubled YCp3 amount from 900 °C to 500 °C in steps of 100 °C.

6.3.2.1 PXRD measurements of temperature series with organometallic precursors

The resulting products were measured with PXRD and is shown in Figure 6.14a and 6.14b for the as prepared sample and the sample after two times acid wash in 1 M H_2SO_4 respectively. The synthesis performed at 500 °C resulted mainly in Pt and some other phase that could be removed in the acid wash. The (022) reflection from Pt at 67.5 ° marked A in Figure 6.14a and F in Figure 6.14b can be seen for all temperatures except at 900 °C, meaning that for temperatures lower than 900 °C the Pt is not fully converted. Since no alloy was formed at 500 °C an extra step was added at 550 °C to see when the alloy formation is initiated. At 550 °C the Pt_3Y phase starts to appear, which can be seen from the peak marked B and C on the as prepared samples and G and H on the acid washed samples. The Pt_3Y phase peaks increases when raising the temperature from 550 °C to 600 °C, then decreases a bit at 700 °C to rise again at 800 °C. At 900 °C for the as prepared sample, the (111) reflection of Pt_3Y (marked B) is present, but the other reflections (marked C and H) are not seen and the peak seen at 38.2 ° could thus stem from another phase formed at 900 °C. Another peculiarity of the 900 °C sample is the presence of sharp, well defined peaks in the as prepared sample, which either disappear or broaden and convolute into large broad features after acid wash. One explanation could be that the phases formed at 900 °C are unstable, corrodes in the acid and their peaks thus broaden as the crystallites corrodes/shrinks. Besides the formation of Pt_3Y, at least one other phase is present too. Looking at the peaks around 39-46 ° for the samples prepared at 600° or higher, peaks are found that fits with either the cubic structure of Pt_2Y or Pt_5Y, whose peaks are quite close to each other. However since the peaks start appearing at higher temperatures than the Pt_3Y peaks, which can be seen by comparing peaks B with D, it seems more likely that is the more yttrium rich phase Pt_2Y. The Y18Pt50.56Si15.44 phase is also changing with temperature, and the phase scales down with temperature and is not visible below 700 °C. The phase is not stable in acid and comparing peaks E with peaks J it is seen that the peak intensity decreases after acid wash.

A general temperature trend for the different structures exists, in which alloying increases with temperature and the more yttrium rich phases become more favourable at higher temperatures, although the ratio in peak intensity between the Pt_3Y and Pt_2Y is different at 700 °C compared to at 600 °C and 800 °C, suggesting that temperature is not the only factor in the alloying process. Other factors could include the mixing of precursors, which is done in a mortar, potentially making it difficult to mix the same way each time. Additionally the YCp3 precursor was enclosed in 1g ampoules and since 500 mg was used for each ex-

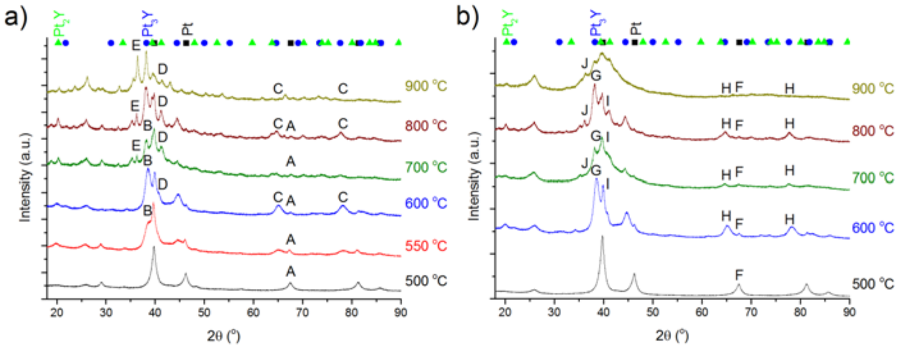

Figure 6.14: Shows PXRD measurements of synthesized Pt_xY/C nanoparticles prepared using Pt/C and $Y(C_5H_5)_3$ at different temperatures where a) shows the as prepared particles and b) after acid wash in 1M H_2SO_4. The points in the top mark the reference peak position of Pt (black square), Pt_3Y (blue circle) and Pt_2Y (green triangle). A and F mark the (022) Pt reflection on the as prepared and acid washed samples respectively. The peak intensity decreases with temperature, but is visible up till 900 °C. B, C, G and H marks Pt_3Y peak positions which are visible from 550 °C and up. D and I mark the position of Pt (111), Pt_5Y (113) and Pt_2Y (113) peak position. E and J show the position of the major peak for the $Y_{18}Pt_{50.56}Si_{15.44}$ phase.

periment, a new ampoule was opened for every second experiment. While the ampoules with YCp3 had the same batch number, it is unknown if there was a variation in the batch and as soon as the ampoules were opened any air/water leakage in the glovebox could potentially oxidize the precursor.

6.3.2.2 XPS measurements of temperature series with organometallic precursors

The samples were also measured with XPS and analysed in a similar manner to that for Figure 6.12. A comparison of the surface composition, excluding C and O is shown in Figure 6.15a for the acid washed samples, depicting more yttrium carbide than metallic yttrium for all temperatures. The yttrium carbide layer further makes it difficult to see the metallic yttrium inside the nanoparticles, especially at 900 °C where mostly carbide is measured. The fitted yttrium carbide peak normalised to the C1s peak is shown for different temperatures in Figure 6.15b. The carbide peak evidently decreases with temperature and shifts to higher binding energies, which could indicate that there is more than one carbide species present, formed at different temperatures. However, none of them could be completely removed in acid treatment.

6.3.2.3 Electrochemical characterisation of synthesis with organometallic precursors at 700 °C

Comparing the relative peak intensity of the different phases seen in the PXRD measurements in Figure 6.14, the sample prepared at 700 °C is the one with most

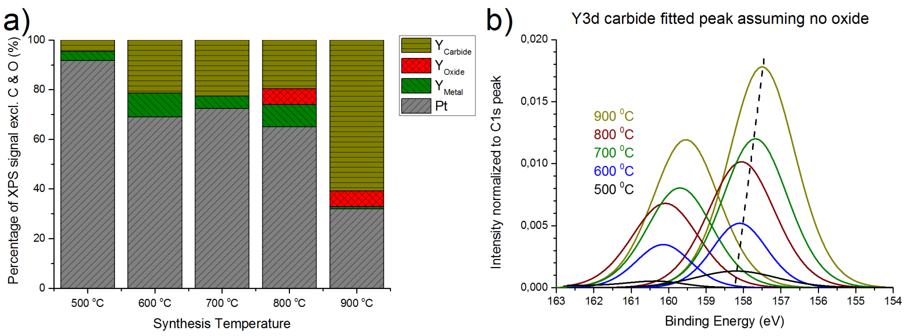

Figure 6.15: a) Composition of XPS signal (excl. O and C), calculated from fitted XPS peaks for the acid washes samples. b) Fitted Y3d doublet associated with yttrium carbide for the sample synthesised at different temperatures.

Pt_3Y phase compared to the Pt and Pt_2Y phases, thus making it the best candidate as an active electrocatalyst and thus this sample was tested electrochemically. The electrodes for the electrochemical measurements were prepared as discussed in Section 2.1.1.3. The CVs in N2 are shown in Figure 6.16a where the synthesised sample is plotted together with the as received Pt/C. The current is normalised to geometric area and the loading on the alloyed sample is higher (21 µg/cm2) than for the reference sample (15 µg/cm2). From the CVs it seems that the alloyed sample has the same H adsorption/desorption peaks although supressed. Since the loading is higher, but the H adsorption and desorption smaller, it is clear that the alloyed sample has less electrochemical active surface area (ECSA), which is also confirmed by the CO stripping shown in Figure 6.16b. The ECSA was determined to 7.5 ± 0.35 m^2/g which is considerably lower than the as received Pt/C (25 ± 1.5 m^2/g) and annealed Pt/C (21 ± 0.2 m^2/g), suggesting that the loss of surface area is due to surface blocking and not particle agglomeration and this is also consistent with the XPS measurements showing yttrium carbide on the surface. The ORR activity was measured in O_2 saturated 0.1 M $HClO_4$ at 1600 rpm and 50 mV/s. The specific activities of the Pt_xY/C and the as received Pt/C are plotted in Figure 6.16c where some gain in specific activity can be observed. The gain in specific activity is within the error of the measurements of both the as received Pt/C and annealed Pt/C as seen in Figure 6.16d. However, the mass activity of the alloyed sample is significant lower than the Pt/C reference, which is due to the large loss of surface area.

In summary Pt_xY alloys can easily be formed from the YCp3 precursor. However, the current method provides little control as to which Pt_xY phases are formed, and in addition corrosion resistant yttrium carbide is formed on the surface, blocking a large part of the surface. The alloys showed some activity enhancements but far from the expected gains of the alloys. As no further routes were available for continuing the synthesis with YCp3, the focus was shifted to chlorides instead, which is the topic of the next section.

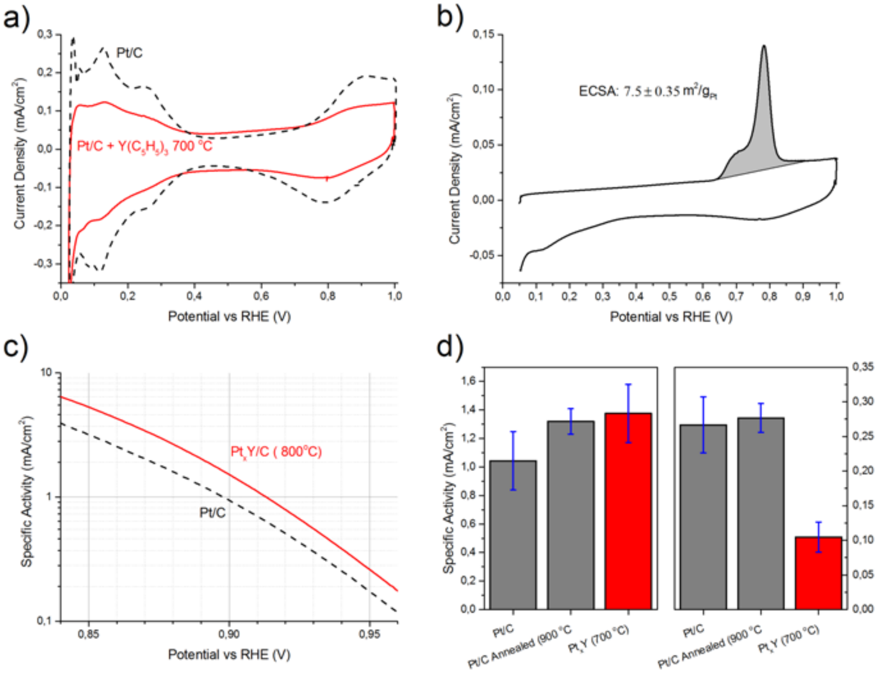

Figure 6.16: a) Pt_xY/C sample prepared with Pt/C and $Y(C_5H_5)_3$ at (700 °C) in N2 saturated 0.1 M $HClO_4$ at 50 mV/s. b) CO stripping cycle measured on the sample where the grey area is the integrated CO stripping charge used in the calculation of electrochemical surface area (ECSA). c) Mass transport, ohmic drop and capacitance corrected specific activity of the sample compared to the as received Pt/C catalyst. The measurement was performed in O_2 saturated 0.1 M $HClO_4$ at 1600 rpm and 50 mV/s. d) Comparison between the specific and mass activity of the sample compared to the as received Pt/C and the Pt/C annealed to 900 °C in H_2.

6.4 Pt$_x$M/C synthesis with MCl$_3$ in quartz reactor

Alternatively to using organometallic precursors for making Pt$_x$M alloys, chlorides and other halides can also be used as seen in section 5.3 and 6.1. The advantage of using halides as precursors are that they are much cheaper and that left-over precursor can be easily removed with either water or acid, thus overcoming the problem of surface blocking seen when using organometallic precursors. Therefore, the experiment seen in Section 5.3 with unsupported Pt and anhydrous YCl$_3$ was repeated, though using Pt/C instead of unsupported Pt, keeping all other parameters the same. The dry powders were mixed with a mortar inside a glovebox and thereafter placed in a quartz reactor. The reactor was placed in a tube furnace and hydrogen was flowed through the reactor throughout the synthesis. The temperature program consisted of a 90 min. heating ramp to 900 °C and then kept at 900 °C for six hours. Following the synthesis the reactor was allowed to cool down slowly. Close to room temperature, the gas lines were closed and the reactor slightly opened, to allow slow diffusion of air into the reactor to passivate the nanoparticles.

6.4.1 Characterisation of synthesis with MCl$_3$ prepared at 900 °C

The resulting powder was measured with PXRD both as prepared and after double acid treatment in 1 M H$_2$SO$_4$. The spectrums are shown in Figure 6.17 together with the spectrum of annealed Pt/C. The as prepared sample contains mainly YOCl and PtSi but after acid wash the Pt$_x$Y phases becomes visible. Most of the intensity in the acid washed sample stem from the PtSi phase, but Pt$_3$Y and Pt$_2$Y phases can also be seen. Small peaks from a Pt phase is also present, meaning that Pt was not fully converted. This was also observed when using the organometallic precursors, which suggest that it is a recurring problem when using the carbon supported Pt and the additional surface area and volume available.

The synthesised sample was also analysed using XPS, and a survey of the as prepared sample is shown in Figure 6.18a, showing the presence of Pt, Y, C, O and Cl on the surface. After the acid wash (Figure 6.18b) the Cl peaks disappear and the Y3d peaks diminishes, which means that there was plenty of YCl$_3$ left after the synthesis and this could be removed in the acid wash. The Pt4f peak is plotted before (Figure 6.18c) and after acid wash (Figure 6.18d), and both are quite broadened compared to the Pt/C in Figure 6.10b and the Pt$_x$Y from organometallic precursors in Figure 6.12c. Each of the Pt4f peaks are fitted as two doublets where the lower binding energy doublet is metallic Pt with a Pt4f7/2 binding energy of 71.3 eV and 71.4 eV for the as prepared sample and acid washed respectively. The higher binding energy doublet is shifted 1.1 eV and 0.6 eV for the as prepared and acid washed samples respectively. Pt oxides are in average shifted 2.9 eV [175], which make PtO unlikely. There is few reports on PtxSi, but

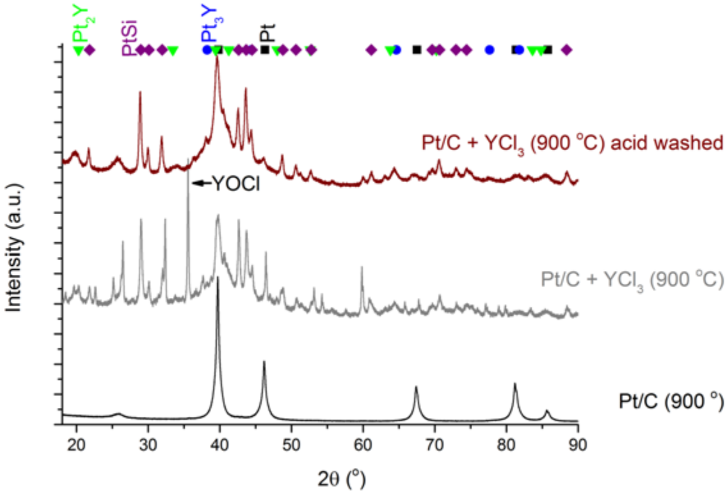

Figure 6.17: PXRD measurements of the synthesised sample with YCl_3 prepared at 900 °C both as prepared and after acid wash in 1 M H_2SO_4. The sample is compared to the annealed Pt/C at 900 °C. The reference peak positions for Pt (black squares), Pt_3Y (blue circles), Pt_2Y (green triangle) and PtSi (purple diamonds) are shown at the top. Only reference peaks with a relative intensity larger than 10% are shown. The as prepared sample has more peaks than after acid wash. These have been identified as mainly YOCl.

one report state an 1.3 eV upshift of Pt4f for Pt2Si and 1.6 eV shift for PtSi [188]. It is possible the higher binding energy Pt4f is related to the PtSi alloy although the shift is smaller than that reported in literature [188]. In Figure 6.18e, the Y3d peak of the as prepared sample is plotted and fitted using two Y3d doublets and one Si2s singlet. The main peaks are likely yttrium chloride or yttrium oxochloride since the binding energy of the Y3d5/2 peak 158.5 eV is in the range of what is reported for yttrium halides (YI3: 158.3 eV, YF3: 159.1 eV) [175] and yttrium oxides 156.4-158.6 eV [175]. The most intense phase in the PXRD measurement was YOCl. The figure also shows a lower binding energy Y3d peak, but since it is in the tail of the other peak its binding energy cannot be accurately determined. Finally, there is also a signal at lower binding energies, which is likely one or more Si2s peaks. The Y3d peak for the acid washed sample is shown in Figure 6.18f where most of the peak at higher binding energy has disappeared. The peak is fitted with three Y3d doublets and two Si2s singlets. The Y3d B doublet (green) and Y3d C doublet (purple) are quite visible in the spectrum, whereas the Y3d A peak was added because of the small jump in intensity around 155 eV which could be a Y3d peak or noise. The peak position of the Y3d5/2 peak, in the Y3d A and Y3d B peaks suggest that peaks are related to metallic Y. The two Si2s peak are similar to what was observed in Section 5.3.

The acid washed sample was also measured using STEM by Brian Peter Knudsen, CINF. A general view is presented in Figure 6.19a, where both small particles

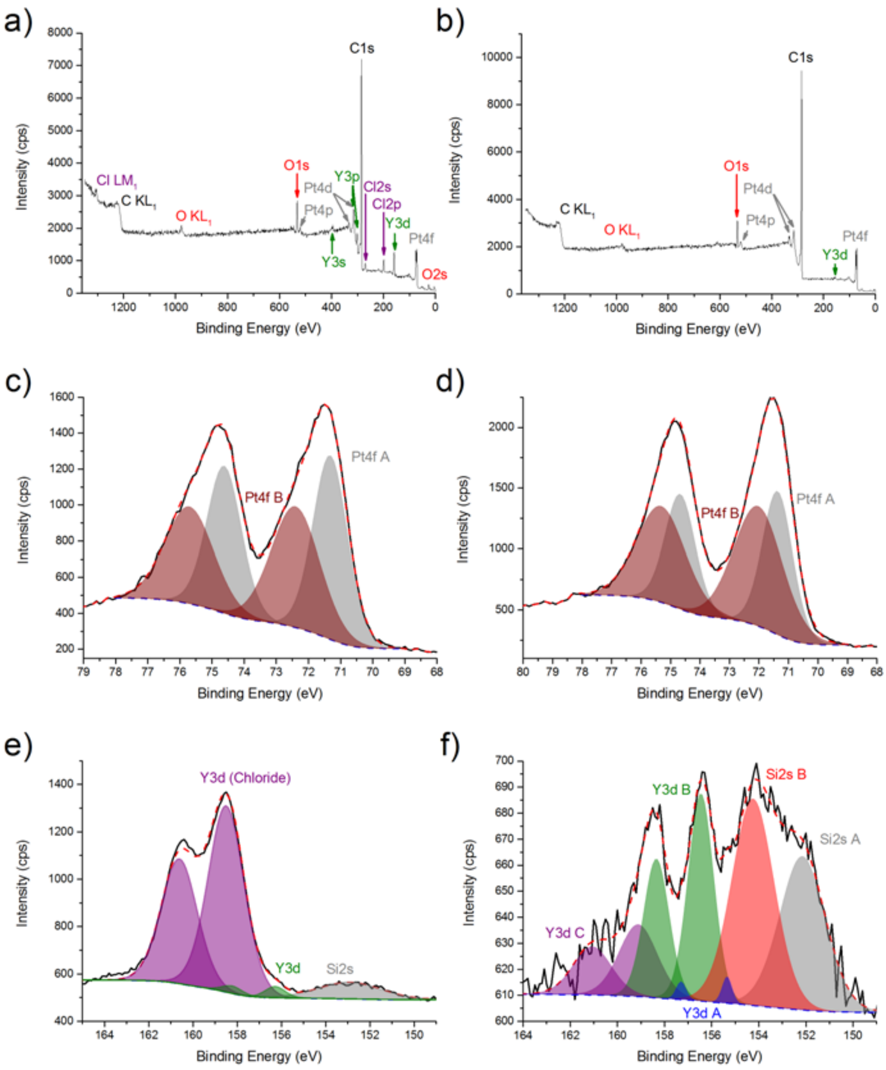

Figure 6.18: XPS measurement of Pt$_x$Y/C sample made from Pt/C and YCl$_3$ at 900 °C both as prepared a), c), e) and after acid wash in 1 M H$_2$SO$_4$ b), d), f). Survey scans are shown in a) for the as prepared sample and b) after acid wash. The Pt4f peaks are shown for the as prepared sample c) and acid washed d). The Pt4f peaks were fitted using two doublets where Pt4f A (grey) is metallic Pt and Ptf4 B (brown) is another species. The Y3d peaks are plotted before e) and after f) acid wash, and besides the Y3d peak signals from Si2s peaks are also observed. Measured by Paolo Malacrida, CINF

and large agglomerates are seen. Figure 6.19b shows two nanoparticles on the original image and after applying a band pass filter between 3-40 pixels. Both particles have a crystalline core, although different, or different planes. The shells of the two particles also appear crystalline, but with a different crystal structure/-plane than seen in the core. The shell thickness is approximately 0.7 nm for the small particle and 2.7 nm for the large particle. A different crystal structure is likewise seen on the particles in Figure 6.19c. The structure appears to be full of holes, presumably lighter elements than in the surrounding atoms. Comparing this structure with different planes in Pt_xY structures, the most similar was the (111) plane in the Pt_3Y structure, shown in Figure 6.19d. Other structures were also observed as seen in Figure 6.19e and 6.19f. The particle in the middle in Figure 6.19e does not appear to have a shell since the crystal structure appears to continue to the edge of the particle. Several of the particles appear to have "holes" similar to those observed for the nanoparticles prepared with YCp3, seen in Figure 6.13d and 6.13f.

6.4.2 Temperature series with Pt/C and YCl_3

The temperature effect of reducing YCl_3 on Pt/C was also studied. The temperature was reduced from 900 °C in steps of 100 °C per experiment to determine the lower limit for the reduction temperature. The precursor amount was also increased to 1:10 Pt:YCl3 weight ratio in order to increase the Pt conversion.

6.4.2.1 PXRD measurements of temperature series with Pt/C and YCl_3

The resulting powder was measured with PXRD as seen in Figure 6.20a and 6.20b for the as prepared sample and the sample after double acid wash in 1 M H_2SO_4. The series was stopped at 700 °C since only a minor part of the Pt was converted into alloy, and an extra temperature point was added at 750 °C, which it is above the melting point of YCl_3 (721 °C [189]). There does not seem to be any difference in crystal phases measured for the samples prepared at 700 °C and 750 °C after acid wash as seen in Figure 6.20b. Looking at the measurements of the as prepared samples in Figure 6.20a, most of the peaks are associated with either yttrium oxychlorides or platinum silicide. The relative intensity of the phases changes with temperature, which can be seen from the main peaks of the three phases marked peak A, B and C. At 700 °C the most prominent phase is the YOCl (C) phase but as temperature increases, the $Y_2Cl_6O_{12}$ phase increases relative to the YOCl phase and dominates at 900 °C. The PtSi phase intensity increases with temperature too. The yttrium oxychlorides are removed in the acid wash and not seen in Figure 5.20b. At 800 °C in the acid washed sample the Pt_3Y appears (peak D), but there is still some Pt not alloyed (peak E). In the acid washed sample prepared at 900 °C there is mostly PtSi.

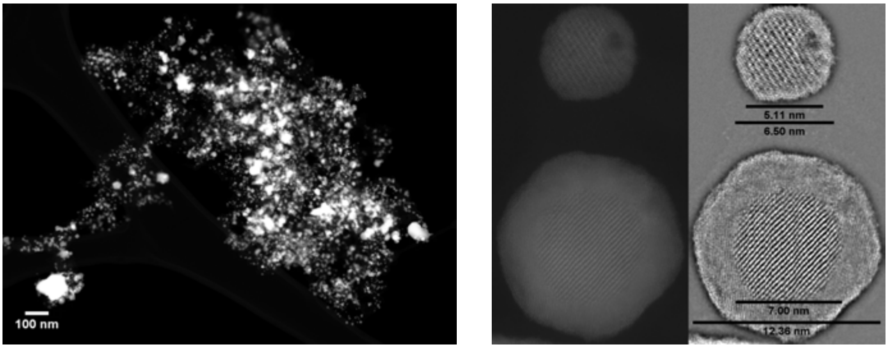

(a) Oveview **(b)** Core/Shell particles

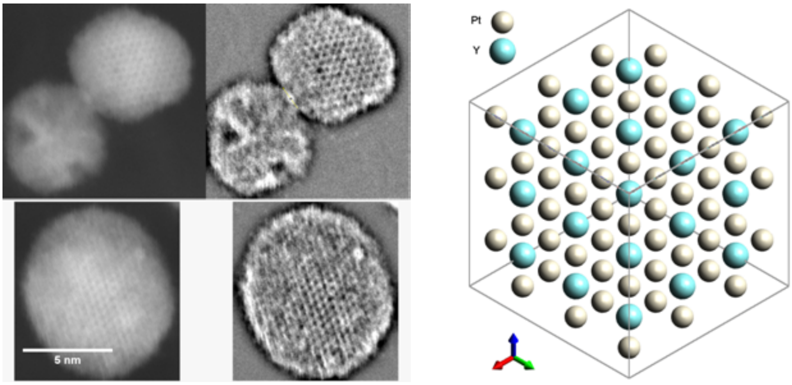

(c) Alloy nanoparticles **(d)** Pt$_3$Y(111) plane

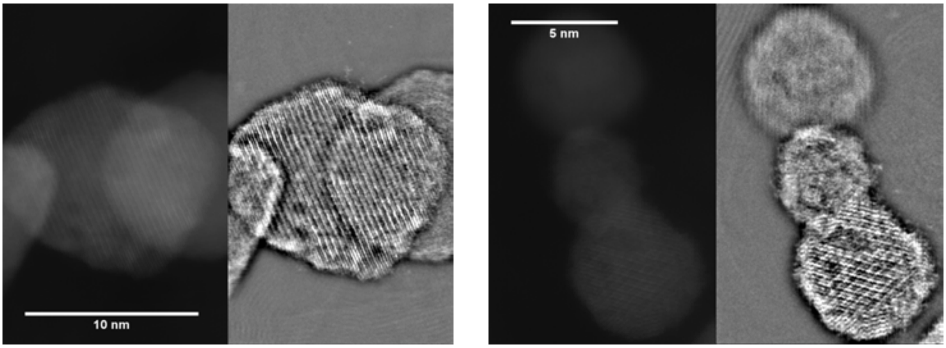

(e) Other particles **(f)** Another alloy structure

Figure 6.19: STEM images of Pt$_x$Y/C particles prepared with Pt/C and YCl$_3$ at 900 °C after acid wash. a) Shows an overview. b) Shows particles with a core shell structure and widely different shell thicknesses. c) Shows particles with a periodic "hole" structur,e which could be a lighter element such as Y, and the structure looks similar to the (111) plane of Pt$_3$Y seen in d). e) and f) Particles with structures different from Pt and are thus likely alloy particles. Measured by Brian Peter Knudsen, CINF

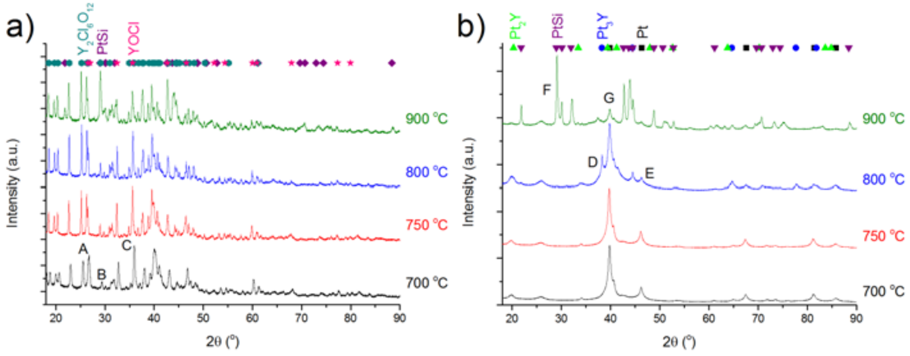

Figure 6.20: PXRD on samples synthesises from Pt/C and YCl_3 at different temperatures. The as prepared samples are shown in a) and b) is after acid wash in 1 M H_2SO_4. Reference peak positions for Pt (black square), Pt_3Y (blue circle), Pt_2Y (green triangle), PtSi (purple diamond), $Y_2Cl_6O_{12}$ (dark cyan hexagon) and YOCl (pink stars) are shown at the top. Only reference peak positions with relative peak intensity larger than 10% are shown. A, B and C mark the position of the main peak of the $Y_2Cl_6O_{12}$, PtSi and YOCl phases respectively. Their relative intensities changes with temperatures where $Y_2Cl_6O_{12}$ becomes stronger than YOCl at higher temperatures and PtSi becoming clearly visible at 900 °C. D shows the main Pt_3Y peak visible at 800 °C after acid wash. However, Pt peaks are still visible, which can be most easily seen from peak E. At 900 °C after acid wash b) the PtSi phase F is much more intense than the Pt and Pt_xY phases G.

6.4.2.2 XPS and EDX measurements of temperature series with Pt/C and YCl_3

The surface of the acid wash samples was examined using XPS and analysed in similar manner to that used in Figure 6.18. The data is summarised in Figure 6.21a where surface composition from XPS, excluding C and O of the different samples is plotted. At 900 °C most of the XPS signal (72%) is Si, which is not observed elsewhere in the XPS spectra for the lower temperature samples. The sample prepared at 800 °C has the most metallic Y and a Pt:Y ratio of 14.6. Comparing this value to the particles prepared by cluster source deposition, which had a Pt:Y ratio of 3-5 as prepared, 14-15 after ORR measurements and 16-17 after stability test [78], the ratio of the acid treated sample is identical to that of the electrochemical tested cluster source particles. It is expected that the as prepared Pt_xY/C nanoparticles form a Pt overlayer when exposed to acid, but it is not known if that overlayer is identical to the one formed during cycling in an electrochemical experiment. The samples prepared at 700 °C and 750 °C have a Pt:Y ratio of over 21 which is significantly higher than the ORR and stability tested nanoparticles prepared by magnetron sputtering in a cluster source [78] and they were thus expected to be as active. The bulk composition of the samples after acid wash was also measured using SEM-EDX, and the composition excluding C and O is plotted in Figure 6.21b. The sample prepared at 900 °C is mainly composted of Si, while the sample prepared at 800 °C still has Si present although it was not observed with PXRD or XPS for the acid washed sample. The sample prepared at

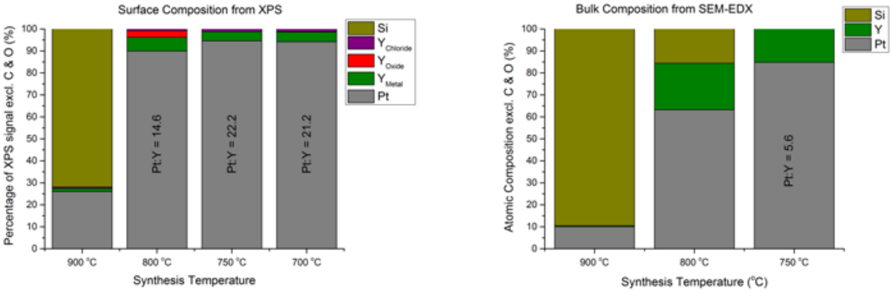

(a) XPS

(b) EDX

Figure 6.21: Surface composition of the acid washed samples from XPS excluding the signal from C and O. The Pt to metallic Y ratio is written on the columns. b) Bulk composition excluding C and O measured with SEM-EDX by Erik Wisaeus, DTI.

750 °C does not contain any Si; however, there is not enough Y for a Pt_5Y phase, which was also seen in the PXRD measurement in Figure 6.20.

6.4.2.3 Electrochemical measurements of Pt_xY/C sample prepared from YCl_3 at 800 °C

From the PXRD, XPS and SEM-EDX measurements, the sample prepared at 800 °C was the most promising and thus chosen for electrochemically testing. The CV of the measured sample is shown in Figure 6.22a (green solid line) together with the as received Pt/C (black dashed line) and the Pt_xY/C made from YCp3 (red dashed). The Pt loading was 13.5 µg/cm2, which is slightly lower than the others in the figure. The sample exhibits the same features (H and OH adsorption/desorption) as the Pt/C electrode although supressed. The electrochemical surface area (ECSA) was determined from CO stripping to be 19 ± 4 m^2/g, which is similar to that of annealed Pt/C (21 ± 0.2 m^2/g). The specific activity, plotted in Figure 6.22c, is slightly higher than the Pt_xY/C synthesised using YCp3 and the as received Pt/C. The average specific activity plotted in Figure 6.22d is likewise higher for the sample synthesis using YCp3 though the large standard deviation makes it impossible to determine whether it statistically has a higher specific activity than the other samples. However, for the mass activity a noticeable difference exists between the Pt_xY/C synthesises from YCp and YCl_3. Because the synthesised alloy has a larger electrochemical surface area when using YCl_3, the mass activity is several times higher than when using the YCp3. Unfortunately the improvement in mass activity over Pt/C and annealed Pt/C are within the standard deviation.

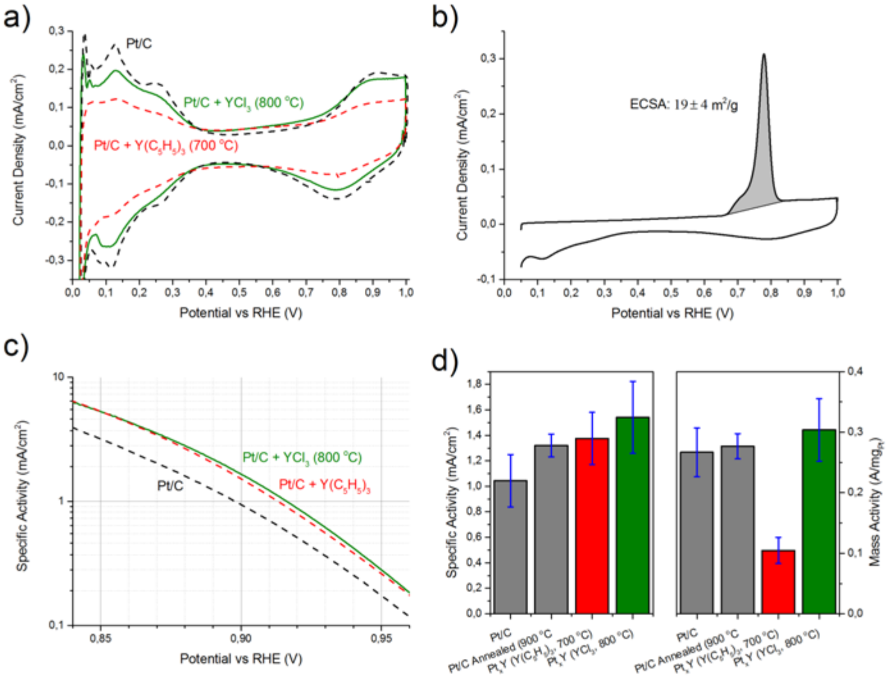

Figure 6.22: Electrochemical characterisation of synthesised sample from Pt/C and YCl$_3$ prepared at 800 °C. a) CV in N2 saturated 0.1 M HClO$_4$ at 50 mV/s. b) CO stripping cycle (10 mV/s). c) ;ass transport, ohmic drop and capacitance corrected specific activity of the sample (green), Pt/C as received (black) and synthesises nanoparticles using organometallic precursor (red). d) Comparison of the average specific and mass activities of the different samples.

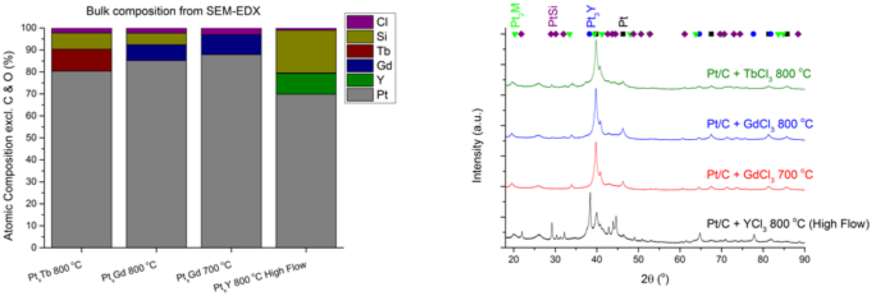

(a) XPS

(b) EDX

Figure 6.23: Figure 6.24 – a) Bulk composition excl. C and O from SEM-EDX. The SEM-EDX measurements were performed by Erik Wisaeus, DTI. b) PXRD measurements of synthesised samples from YCl_3, $GdCl_3$ and $TbCl_3$. (High Flow) designates the sample with increased H_2 (x8) during synthesis. The reference peak positions of Pt_2M (green triangle), PtSi (purple diamond), Pt_3Y (blue circle) and Pt (black square) are shown at the top. Only peaks with relative peak intensity larger than 10% are shown. The Pt_2M phase is calculated from Pt_2Y, but since Pt_2Gd and Pt_2Tb have the same structure and their lattice parameters only differs slightly the peaks position should be close to each other.

6.4.3 Synthesis of other Pt$_x$M alloys and the effect of flow rate

To analyse the importance of the melting point, the YCl_3 was replaced with $GdCl_3$ and $TbCl_3$, both having a lower melting point (602 °C [185] and 582 °C [189]) than YCl_3. They should accordingly to the thermodynamic calculations, be just as easily reduced to Pt_5M alloys as YCl_3. Another important parameter is the flow rate, since if the reaction is mass transport limited, by removal of product gas, increasing the flow rate would increase the reaction rate as seen in Figure 6.4a. Therefore the flow rate was increased for the Pt/C + YCl_3 by about a factor of eight, approximated by counting the number of bobbles formed per time in the oil trap, through which the exhaust gases exits. The products were acid washed twice in 1 M H_2SO_4 and then measured with SEM-EDX and PXRD. The SEM-EDX results are shown in Figure 6.24a where the bulk composition excluding C and O is plotted for the different samples. Evidently, all samples prepared at 800 ° contains a Si amount comparable to the Gd and Tb content. Moreover the Pt$_x$Y/C sample prepared at eighth times higher H_2 flow than the other synthesises, have much more Si than Y. This is also seen from the PXRD measurements in Figure 5.24b where the PtSi structure is seen for the high flow sample. Besides the PtSi phase, the Pt$_x$Y phases and specifically the Pt_3Y phase, have higher intensities than the sample prepared with a lower flow rate as seen in Figure 6.20b. Another interesting point is that the same Pt$_x$Gd/C amount seems to be present in the two samples prepared at 700 °C and 800 °C. Finally, all the Pt$_x$Gd and PtxTb samples contain a Pt phase, meaning that none of them were completely alloyed.

In conclusion, the Y, Gd and Tb precursors are too reactive to be used in the quartz reactor. In most of the synthesised samples platinum and/or yttrium platinum silicides were observed. Even at lower temperatures where no or little silicides were observed, silicides could be formed by increasing the H_2 flow rate. At the same time, it was not possible to completely convert Pt without also forming silicides. This is contrary to the experiment performed in section 5.3 for unsupported Pt, where Pt_3Y was formed without silicides or remaining Pt phases. This suggests that a balance exist where the alloy can be formed without forming silicides although this balance have proven difficult to find when using carbon supported Pt. The obvious solution is to replace quartz.

6.5 Summary and outlook

In this chapter a thermodynamic model was made for the synthesis of Pt_xM alloys. The model was used to predict the reduction of M_2O_3 oxides to Pt_xM alloys. It showed that the formation of oxides is favourable at all practical temperatures and partial pressures of oxygen for this synthesis. However, based on the time it would take to oxidise all of the alloy material in the reactor, it was found that instrument 5.0 purity gas could be used. The gas contains 2 ppm of O_2 and with that concentration it would take a week to completely oxidise all of the alloy material and as the synthesis takes 6-8 hours, instrument 5.0 gases is sufficient for the synthesis. The water tolerance is better than for oxygen and is in range of 1-1000 ppm in the temperature range of interest. The model showed that it was possible to make Pt_xM alloys from M_2O_3 oxides and Pt by reducing it in H_2. However, for the synthesis to practical, it has to be done in a matter of hours. Achieving that with the oxides requires the synthesis to be performed at 1000 and 1200 °C for the Pt_5Y and Pt_3Y respectively. Increasing the flow rate of H_2 could reduce the synthesis time, though only to the point where the reaction becomes kinetically limited and that point is unknown. Finally, the model showed that lanthanide oxides are easier to reduce than yttrium oxide and that synthesis with calcium oxide is less tolerant to water and oxygen.

Chapter 5 proved that Pt_3Y could be made from YCl_3, and the model was also applied on halides. The result found that halides are easier to reduce in case of chlorides, bromides and iodides, while fluorides are just as or even more difficult than oxides to reduce. In case of gadolinium halides, the iodide followed by bromide and chloride, was the easiest to reduce. All three of them were able to tolerate per mile or higher levels of product gas in the 500 °C – 900 °C range. However, $GdCl_3$ has the lowest melting point, which might be practical for the synthesis, making it more mobile. $GdCl_3$ is in addition more widely available which makes it a better choice for the synthesis. Comparing the different lanthanide chlorides, all were as easy to reduce as $GdCl_3$, and YCl_3 was similar to the lanthanide chlorides. The model predicts that $CaCl_2$ cannot be reduced in a reasonable time ($<$ 24 hours) below 1000 °C, and so this synthesis is not suited for making Pt5Ca alloys.

The choice of Pt seed particles for the high temperature synthesis is important since the alloy particles needs to be at least 6-8 nm in order for big activity enhancements to be seen. The best candidate was found to be a commercial Pt/C catalyst from Tanaka, and the particles size of this candidate was determined from PXRD before after annealing to 900 °C. The as received particles were found to be 6.8 nm in average, while the annealing caused a particle size distribution that too broad for the size to be determined from PXRD. Therefore, the particles were also measured using SAXS, which showed that 75% of the as received particles were in the desired 6-12 nm range, but after annealing that number dropped to 50%. However, only 5% of the particles were less than 6 nm after annealing, meaning that the rest were large agglomerates, positively enhancing the specific activity although causing the mass activity to suffer. SAXS showed that the surface to volume ratio decreased by 27% after annealing. The particles were also tested electrochemically and had an ECSA of 25±1.5 and 21±0.2 m^2/g before and after annealing respectively. The specific activity for the as received and annealed sample was 1.0±0.2 mA/cm2 and 1.32±0.09 mA/cm2 respectively, and the mass activity was 0.27±0.04 A/mgPt and 0.28±0.02 A/mgPt respectively. These were the benchmark values that the synthesised nanoparticles were compared to.

The synthesis using the organometallic precursor Tris(cyclopentadienyl)yttrium(III), that resulted in a Pt_3Y alloy in Chapter 5, was repeated with carbon supported Pt instead of unsupported Pt, to make catalytic active nanoparticles. The synthesis was done using the same experimental conditions as in Chapter 5 but the results came out different. Instead of a single Pt_3Y phase, the synthesis resulted in a mix of different Pt_xY, Pt and Y18Pt50.56Si15.44 phases. The Y18Pt50.56Si15.44 was not visible in the PXRD spectrum after acid wash. XPS showed metallic yttrium, but the dominant yttrium species was yttrium carbide, which could only partly be removed with acids. A temperature series was performed and the alloy phases were visible in the PXRD spectra down to 550 °C. Judging from the PXRD spectra synthesises performed at 600-700 °C had the purest Pt_3Y phase. All of the synthesises had a Pt phase, showing that Pt was not fully alloyed. The amount of Y18Pt50.56Si15.44 phase decreased with temperature and was not visible below 700 °C. XPS measurements showed that all samples prepared above 500 °C had a carbide signal, and that the carbide signal was larger than that of metallic yttrium. The sample prepared at 700 °C was measured electrochemically and had an ECSA of 7.5 m^2/g, which suggest that most of the surface is not accessible. The specific activity was in average larger than that of the as received and annealed Pt/C, however within the statistical error. The mass activity was significantly lower than for the Pt/C, which is due to less surface area. It seems that an yttrium carbide layer is covering the alloy nanoparticles and that this layer is difficult to remove. The synthesis with organometallic precursor therefore does not seem promising.

Chapter 5 demonstrated that Pt_3Y could be made from YCl_3 and unsupported Pt. This was repeated in this chapter with the carbon supported Pt. The synthesis resulted in mainly three phases: YOCl, $Y_2Cl_6O_{12}$, and PtSi, where YOCl and $Y_2Cl_6O_{12}$ could be removed in acid wash. After acid wash PtSi and different Pt_xY phases were observed in the PXRD spectra. XPS showed yttrium chloride, silicon, but also metallic yttrium. The sample was measured using STEM and the images showed crystalline particles, some of them clearly being alloys, which was seen from the mixture of heavier and lighter atoms. One of the structures could be Pt_3Y, but it was not possible to positively identify it. A temperature series was performed, and while little alloy was formed below 800 °C; all of the samples had a Pt phase. XPS showed only Si on the surface of the 900 °C sample whereas EDX showed Si in both the 900 °C and 800 °C sample. The 800 °C sample was measured electrochemically and the surface area was within the error of the annealed Pt/C. The specific average activity was higher than the Pt/C and Pt_xY/C prepared with organometallic precursor, although within the statistical error. The average mass activity was also higher than for the other samples, but still within the statistical error. The large spread in activity measurements was due to the Pt/C being more difficult to work with compared to other commerical Pt/C nanoparticles we have in our lab. The variance could likely be decreased if the ink formulation for the catalyst was optimised. Since $GdCl_3$ and $TbCl_3$ have a lower melting point than YCl_3, the synthesis was performed with these thus making it possible to lower the synthesis temperature to 700 °C. The thermodynamic model showed that the synthesis could be slowed down by a low gas flow, and the gas flow was therefore increased by a factor of eight at 800 °, which resulted in more alloy but also the formation of PtSi.

The synthesis works when using chlorides but the reactor setup needs to be optimised. The quartz reactor setup has several drawbacks besides the reactivity with the precursors. One is that rubber tubing is used for the gas lines and since the tubing is not impermeable to air and moisture, the background level of O_2 and H_2O becomes higher than specified for the gas bottle. The same problem exists with the glass-to-glass sealing of the reactor, which isn't completely leek tight either. This makes the concentration of O_2 and H_2O uncontrolled. Another material than glass, is needed for the reactor, as the chlorides clearly react with the glass. Steal reactors are not much better since Pt could form alloys with the 3d metal and the chlorides will also likely attack the reactor. The reactor material should be inert for the reaction. One option could be yttria as yttria is more stable than yttrium chloride and Pt will only react very slowly with yttria, when the temperature is below 1000 °C. Another alternative reactor material is carbon as it does not seem that the Pt nor YCl_3 have reacted with the carbon support of the Pt. This synthesis is very promising but will need some optimisation in order to make the very active Pt_xM nanoparticles.

7

Conclusion and Outlook

The µ-DMFC for hearing aids seems to be a promising technology that has a chance of being realised in commercial products and possibly pave the way for using DMFCs in other products. The success of this technology requires more power dense DMFC and possibly lower catalyst loading, if it is to be scaled up for more power demanding electronics. This thesis tries to aid by furthering the understanding of the electrochemical processes in the DMFC, how the catalysts work, how to make improve on these for the DMFC, and finally how to produce the catalyst in the quantities needed for fuel cell production.

7.1 The µ-DMFC and its electrochemistry

To determine the losses in the DMFC, a µ-DMFC with build-in reference electrodes was constructed and measured. The two major losses were the anode and cathode kinetics, which even with high catalyst metal loading of 14.6 and 3.53 mg/cm^2, lost 56% of the potential to kinetics. Only about 1% and 2% of the potential went to ohmic drop and methanol crossover for the fully working cell. The µ-DMFCs were limited by mass transport on the anode, which limited the maximum steady state current density to 30-32 mA/cm^2. This is lower than for a standard cell without reference electrode and thus the reference electrode might change the cell behaviour. To better understand the kinetics of the DMFC, a method was developed to measure DMFC electrodes outside of the DMFC. By placing the electrode in a so-called H-cell it was possible to measure the activity in a liquid half-cell. This was demonstrated for the methanol oxidation reaction. The measured kinetics had a Tafel slope of 118 mV/dec, suggesting a transfer coefficient α of 0.5.

The oxygen reduction reaction (ORR) was studied in a rotating disk electrode (RDE) setup to determine which parameters affect the activity measurement. The measurement was performed both on polycrystalline Pt extended surfaces and on carbon supported Pt nanoparticles. The effect of scan rate was observed for both type of samples, if the measurements were corrected for ohmic drop and possible background capacitive currents. The activity increased drastically by 75% when changing the scan rate from 5 to 100 mV/s. The scan rate and corrections are important, since papers about ORR catalyst, report measurements performed at various scan rate and not always with corrections, which makes it very difficult to compare results.

The ORR was also studied in the RDE setup in the presence of methanol to test which experimental parameters affected the results. The poisoning effect was found to be very depended on experimental parameters such as methanol concentration, electrode surface area and temperature. It was not possible to get meaningful results if either of these parameters were too high. The consequence of this is that methanol poisoning cannot be measured quantitatively in a RDE setup, but only used for qualitatively comparison of catalysts if the experimental conditions are identical. The methanol poisoning on polycrystalline Pt and Pt_5Gd was compared and Pt_5Gd was found to have a larger potential shift from methanol poisoning. This could be explained by better MOR kinetics at high potentials. However, the more important comparison examines which catalyst is more active in the presences of methanol. Evidently, the activity Pt_5Gd decreased more than the activity of Pt in the presence of methanol, but still retained an activity enhancement of 2-3x over Pt at the same methanol concentration. This makes Pt_5Gd a possible replacement for Pt as a DMFC cathode catalyst.

7.2 Synthesis of Pt_xM alloys

To use Pt_5Gd as a DMFC cathode, the alloy must be chemically synthesised as nanoparticles. This thesis list several possible routes, emphasising two of these. The first route was a solvo-thermal synthesis of Pt_3Gd, which was attempted for the synthesis of Pt_5Y/C and Pt_5Gd/C. The method was to rapidly heat Pt and Y chloride salts in ethanol under pressure. The method was attempted in a supercritical fluid flow system but resulted in only Pt nanoparticles. The flow reactor had a very short reaction time of <5s, which might have been too short for the reaction. The synthesis was therefore repeated in a pulse reactor, which was not limited by a short reaction time. Attempts with the same precursors, solvent, temperatures, pressure and time as reported in the litterature, did not yield any alloy nanoparticles. Finally, the synthesis was attempted with anhydrous solvents and precursors, which did not produce any alloy either. It was surprising that the method did not work as the reported experimental conditions were accurately reproduced. As another more promising method was found the solvo-thermal synthesis was abandoned.

The other method was the high temperature reduction and annealing of Pt nanoparticles with either an organometallic precursor, Tris(cyclopentadienyl) yttrium(III), or a chloride in a pure H_2 flow. Experiments with unsupported Pt with either precursor yielded Pt_3Y nanoparticles. The crystallite size was 60-70 nm, SEM images revealed that the product was large agglomerates in the hundreds of nm range. XPS measurements showed metallic yttrium and yttrium carbide for the organometallic synthesis, and yttrium chloride, metallic yttrium and silicon for the chloride synthesis. Although, the synthesis was successful in making metallic Pt_3Y, the particles were not suitable as an electro-catalyst, since the particles were too large and covered with either carbide or silicon oxide.

To synthesise a more suitable electro-catalyst, the syntheses were repeated with carbon supported nanoparticles but with a different result. Rather than a single Pt_3Y phase, a mixture of Pt, Pt_xY and platinum yttrium silicides phases were observed. XPS measurements showed that the nanoparticles were covered with a yttrium carbide that could not be removed in acid wash. This was also evident from electrochemical experiments where the measured surface area 7.5 m^2/g was much lower than the expected value of 21 m^2/g. The alloy nanoparticles showed a higher average specific activity than the as received Pt/C, although within the statistical error; however, the mass activity was significantly lower than for the Pt/C, which is likely because of the lower surface area. It seems unlikely that the organometallic synthesis can be used to form active electro catalysts without a way to remove the carbide covering the surface.

A thermodynamic model was developed to explain the synthesis. It showed that yttrium/lanthanide halides except for fluorides can be reduced in H_2 to form Pt_xM alloys from about 500 °C. Although other halides could be used, chlorides were chosen due to their lower melting point and since they are more widely available. The chloride based synthesis was also attempted with carbon supported nanoparticles and resulted in a mixture of Pt_xY, Pt, YOCl, $Y_2Cl_6O_{12}$, PtSi phases, where YOCl and $Y_2Cl_6O_{12}$ could be removed in acid wash and PtSi could not. A temperature series showed that silicides are less likely to form at lower temperatures and that the lowest temperature for forming alloys from the chloride precursor was at 800 °C. The chloride based alloy catalyst had a surface area close to the annealed Pt/C and an average specific activity higher than Pt/C and organometallic based Pt_xY/C although still within the statistical error. Synthesis with $GdCl_3$ and $TbCl_3$ were attempted to but also resulted in a mixture of phases. The limitation seems to be the reactor and the mixing of precursors. The glass reactor reacts with precursor and thus must be replaced. The poor mixing of precursor requires a much higher amount of yttrium precursor than stoichiometric, which is why more yttrium rich phases can be formed while the Pt is not fully alloyed. The synthesis is very promising but a new setup must be built in order to successfully make the very active alloy nanoparticles.

7.3 Outlook

The µ-DMFC with reference electrode measurements could be improved if the reference electrode setup could be made with less intrusion than the current version, which has a membrane flap protruding from the cathode plate. The current version is not capable of producing current densities as high as an unmodified cell, which is likely related to the reference electrode design. One alternative could be to use a µ-reference electrode, which are commercially available with diameters as small as 500 µm, and by using these it might be possible to connect a reference electrode to the cell without changing the water balance inside the cell. The cell measurements did also produce a lot of impedance, which if fitted to a physical model, could provide some insight into the functionality of the cell components.

The methanol poisoning experiments in a RDE setup was not able to quantitatively determine the methanol poisoning, due to the mass transport limitations in the RDE setup. An alternative could be to measure the ORR activity in an H-Cell like setup, where the O_2 is supplied through the gas diffusion layer, thus the measurement can be made without transport limitation of O_2. This would show the actual methanol poisoning of the electrode. In general the H-Cell setup could be used to provide a link between the fuel cell measurements and the RDE measurements. However, the H-cell must be redesigned to place the reference electrode very close to the working electrode, to avoid the very high ohmic drop reported in this thesis.

The reactor for the synthesis can be improved in several ways where the most important is to replace the glass with an inert material for the reactions. This is difficult since yttrium and yttrium chloride will react with most materials when heated. One option could be to use yttrium oxide as this is a more stable form of yttrium than yttrium chloride. and therefore should be stable. Alternatively, carbon could be used since the yttrium chloride does not seem to react with the carbon support of the Pt nanoparticle. It is also important to devise a better mixing of the precursors as the melted yttrium chloride does not seem to distribute evenly on the high surface area carbon supported Pt particles. If the mixing procedure could be improved, the precursor amount could be reduced, which should also help avoid the more yttrium rich phases.

Bibliography

[1] J. Hales, C. Kallesøe, T. Lund-Olesen, A.-C. Johansson, H. Fanøe, Y. Yu, P. Lund, A. Vig, O. Tynelius, and L. Christensen, "Micro fuel cells power the hearing aids of the future," *Fuel Cells Bulletin*, vol. 2012, pp. 12–16, dec 2012.

[2] H. A. Gasteiger and J. Garche, "Fuel Cells," in *Handbook of Heterogeneous Catalysis* (G. Ertl, H. Knözinger, F. Schüth, and J. Weitkamp, eds.), Weinheim, Germany: Wiley-VCH Verlag GmbH & Co. KGaA, mar 2008.

[3] F. T. Wagner, B. Lakshmanan, and M. F. Mathias, "Electrochemistry and the Future of the Automobile," *The Journal of Physical Chemistry Letters*, vol. 1, pp. 2204–2219, jul 2010.

[4] A. J. Bard and L. R. Faulkner, *Electrochemical Methods: Fundamentals and Applications, 2nd Edition.* John Wiley & Sons, Ltd, 2001.

[5] K. C. Neyerlin, W. Gu, J. Jorne, and H. a. Gasteiger, "Determination of Catalyst Unique Parameters for the Oxygen Reduction Reaction in a PEMFC," *Journal of The Electrochemical Society*, vol. 153, p. A1955, 2006.

[6] K. C. Neyerlin, W. Gu, J. Jorne, and H. A. Gasteiger, "Study of the Exchange Current Density for the Hydrogen Oxidation and Evolution Reactions," *Journal of The Electrochemical Society*, vol. 154, no. 7, p. B631, 2007.

[7] T. Iwasita, "Methanol and CO electrooxidation," in *Handbook of fuel cells* (W. Vielstich, A. Lamm, H. A. Gasteiger, and H. Yokokawa, eds.), Chichester, UK: John Wiley & Sons, Ltd, dec 2010.

[8] S. C. Thomas, X. Ren, S. Gottesfeld 2, and P. Zelenay, “Direct methanol fuel cells: progress in cell performance and cathode research,” *Electrochimica Acta*, vol. 47, pp. 3741–3748, aug 2002.

[9] C. E. Shaffer and C. Y. Wang, “Performance modeling and cell design for high concentration methanol fuel cells,” in *Handbook of Fuel Cells*, pp. 1–13, 2010.

[10] C. Xu, A. Faghri, and X. L. Li, “Development of a High Performance Passive Vapor-Feed DMFC Fed with Neat Methanol,” *Journal of the Electrochemical Society*, vol. 157, no. 8, pp. B1109–B1117, 2010.

[11] I. Chorkendorff and J. W. Niemantsverdriet, *Concepts of Modern Catalysis and Kinetics.* Wiley-VCH Verlag GmbH & Co. KGaA, 2011.

[12] H.-F. Oetjen, V. M. Schmidt, U. Stimming, and F. Trila, “Performance Data of a Proton Exchange Membrane Fuel Cell Using H2/CO as Fuel Gas,” *Journal of The Electrochemical Society*, vol. 143, no. 12, p. 3838, 1996.

[13] T. E. Springer, T. Rockward, T. A. Zawodzinski, and S. Gottesfeld, “Model for Polymer Electrolyte Fuel Cell Operation on Reformate Feed: Effects of CO, H2 Dilution, and High Fuel Utilization,” *Journal of The Electrochemical Society*, vol. 148, no. 1, p. A11, 2001.

[14] S. Gottesfeld, “A New Approach to the Problem of Carbon Monoxide Poisoning in Fuel Cells Operating at Low Temperatures,” *Journal of The Electrochemical Society*, vol. 135, no. 10, p. 2651, 1988.

[15] Z. Jusys and R. J. Behm, “Simulated "Air Bleed" Oxidation of Adsorbed CO on Carbon Supported Pt. Part 2. Electrochemical Measurements of Hydrogen Peroxide Formation during O 2 Reduction in a Double-Disk Electrode Dual Thin-Layer Flow Cell,” *The Journal of Physical Chemistry B*, vol. 108, pp. 7893–7901, jun 2004.

[16] H. A. Gasteiger, N. M. Markovic, and P. N. Ross, “H2 and CO Electrooxidation on Well-Characterized Pt , Ru , and Pt-Ru . 2 . Rotating Disk Electrode Studies of CO / H2 Mixtures at 62 C,” *Journal of Physical Chemistry*, vol. 99, pp. 16757–16767, 1995.

[17] T. J. Schmidt, M. Noeske, H. A. Gasteiger, R. J. Behm, P. Britz, and H. Bönnemann, “PtRu Alloy Colloids as Precursors for Fuel Cell Catalysts: A combined XPS, AFM, HRTEM, and RDE study,” *Journal of The Electrochemical Society*, vol. 145, p. 925, oct 1998.

[18] P. Liu, a. Logadottir, and J. Nørskov, “Modeling the electro-oxidation of CO and H2/CO on Pt, Ru, PtRu and Pt3Sn,” *Electrochimica Acta*, vol. 48, pp. 3731–3742, nov 2003.

[19] M. Arenz, V. Stamenkovic, B. Blizanac, K. Mayrhofer, N. Markovic, and P. Ross, “Carbon-supported Pt-Sn electrocatalysts for the anodic oxidation of H2, CO, and H2/CO mixtures.Part II: The structure-activity relationship,” *Journal of Catalysis*, vol. 232, pp. 402–410, jun 2005.

[20] B. N. Grgur, N. M. Markovic, and P. N. Ross, “Electrooxidation of H2 , CO, and H2/CO Mixtures on a Well-Characterized Pt70Mo30 Bulk Alloy Electrode,” *The Journal of Physical Chemistry B*, vol. 102, pp. 2494–2501, apr 1998.

[21] B. N. Grgur, N. M. Markovic, and P. N. Ross, “The Electro-oxidation of H2 and H2/CO Mixtures on Carbon-Supported PtxMy Alloy Catalysts,” *Journal of The Electrochemical Society*, vol. 146, no. 5, pp. 1613–1619, 1999.

[22] M. Watanabe, “New CO-tolerant catalyst concepts,” in *Handbook of Fuel Cells*, pp. 1–8, 2010.

[23] H. Igarashi, T. Fujino, Y. Zhu, H. Uchida, and M. Watanabe, “CO Tolerance of Pt alloy electrocatalysts for polymer electrolyte fuel cells and the detoxification mechanism,” *Physical Chemistry Chemical Physics*, vol. 3, no. 3, pp. 306–314, 2001.

[24] T. Iwasita and X. Xia, “Electrocatalysis of organic oxidations: influence of water adsorption on the rate of reaction,” *The Journal of Physical . . .*, vol. 5647, no. 97, pp. 7542–7547, 1997.

[25] M. Watanabe and S. Motoo, “Electrocatalysis by ad-atoms: Part III. Enhancement of the oxidation of carbon monoxide on platinum by ruthenium ad-atoms,” *Journal of Electroanalytical Chemistry and Interfacial Electrochemistry*, vol. 60, pp. 275–283, apr 1975.

[26] H. A. Gasteiger, N. Markovic, P. N. Ross, and E. J. Cairns, “CO Electrooxidation on Well-Characterized Pt-Ru Alloys,” *Journal of Physical Chemistry*, vol. 98, pp. 617–625, 1994.

[27] N. M. Marković, “The hydrogen electrode reaction and the electrooxidation of CO and H2/CO mixtures on well-characterized Pt and Pt-bimetallic surfaces,” in *Handbook of Fuel Cells* (W. Vielstich, A. Lamm, H. A. Gasteiger, and H. Yokokawa, eds.), vol. 3, Chichester, UK: John Wiley & Sons, Ltd, dec 2010.

[28] P. Piela, C. Eickes, E. Brosha, F. Garzon, and P. Zelenay, “Ruthenium Crossover in Direct Methanol Fuel Cell with Pt-Ru Black Anode,” *Journal of The Electrochemical Society*, vol. 151, p. A2053, jan 2004.

[29] T. T. H. Cheng, N. Jia, and P. He, “Characterization of the Degree of Ru Crossover and Its Performance Implications in Polymer Electrolyte Membrane Fuel Cells,” *Journal of The Electrochemical Society*, vol. 157, no. 5, p. B714, 2010.

[30] P. He, T. Cheng, R. Bashyam, A. P. Young, and S. Knights, “Relative Humidity Effect on Anode Durability in PEMFC Startup/Shutdown Processes,” in *ECS Transactions*, vol. 33, pp. 1273–1279, 2010.

[31] P. Ferrin, A. U. Nilekar, J. Greeley, M. Mavrikakis, and J. Rossmeisl, “Reactivity descriptors for direct methanol fuel cell anode catalysts,” *Surface Science*, vol. 602, pp. 3424–3431, nov 2008.

[32] H. A. Gasteiger, N. Marković, P. N. Ross, and E. J. Cairns, “Temperature Dependent Methanol Electro-Oxidation on Well Characterized Pt-Ru Alloys,” *Journal of The Electrochemical Society*, vol. 141, pp. 1795–1803, jan 1994.

[33] M. Watanabe and S. Motoo, “Electrocatalysis by ad-atoms: Part II. Enhancement of the oxidation of methanol on platinum by ruthenium adatoms,” *Journal of Electroanalytical Chemistry and Interfacial Electrochemistry*, vol. 60, pp. 267–273, apr 1975.

[34] T. Iwasita, H. Hoster, and A. John-Anacker, “Methanol oxidation on PtRu electrodes. Influence of surface structure and Pt-Ru atom distribution,” *Langmuir*, no. 20, pp. 711–718, 2000.

[35] A. Tripković, K. Popović, B. Grgur, B. Blizanac, P. Ross, and N. Marković, “Methanol electrooxidation on supported Pt and PtRu catalysts in acid and alkaline solutions,” *Electrochimica Acta*, vol. 47, pp. 3707–3714, aug 2002.

[36] K. Sasaki and R. R. Adzic, “Monolayer-Level Ru- and NbO[sub 2]-Supported Platinum Electrocatalysts for Methanol Oxidation,” *Journal of The Electrochemical Society*, vol. 155, no. 2, p. B180, 2008.

[37] J. Suntivich, Z. Xu, C. E. Carlton, J. Kim, B. Han, S. W. Lee, N. Bonnet, N. Marzari, L. F. Allard, H. a. Gasteiger, K. Hamad-Schifferli, and Y. Shao-Horn, “Surface Composition Tuning of Au-Pt Bimetallic Nanoparticles for Enhanced Carbon Monoxide and Methanol Electro-oxidation.,” *Journal of the American Chemical Society*, vol. 135, pp. 7985–7991, may 2013.

[38] T. H. M. Housmans and M. T. M. Koper, “Methanol Oxidation on Stepped Pt[n (111) × (110)] Electrodes: A Chronoamperometric Study,” *The Journal of Physical Chemistry B*, vol. 107, pp. 8557–8567, aug 2003.

[39] A. O. Neto, A. Y. Watanabe, M. Brandalise, M. M. Tusi, R. M. de S. Rodrigues, M. Linardi, E. V. Spinacé, and C. A. Forbicini, “Preparation and characterization of Pt–Rare Earth/C electrocatalysts using an alcohol reduction process for methanol electro-oxidation,” *Journal of Alloys and Compounds*, vol. 476, pp. 288–291, may 2009.

[40] T. Hyeon, S. Han, Y.-E. Sung, K.-W. Park, and Y.-W. Kim, “High-performance direct methanol fuel cell electrodes using solid-phase-synthesized carbon nanocoils.,” *Angewandte Chemie (International ed. in English)*, vol. 42, no. 36, pp. 4352–4356, 2003.

[41] H. A. Gasteiger, N. Markovic, P. N. Ross, and E. J. Cairns, “Methanol electrooxidation on well-characterized platinum-ruthenium bulk alloys,” *The Journal of Physical Chemistry*, vol. 97, pp. 12020–12029, nov 1993.

[42] N. M. Marković, H. A. Gasteiger, P. N. Ross Jr, X. Jiang, I. Villegas, and M. J. Weaver, “Electro-oxidation mechanisms of methanol and formic acid on Pt-Ru alloy surfaces,” *Electrochimica Acta*, vol. 40, pp. 91–98, jan 1995.

[43] T. Schmidt, H. Gasteiger, and R. Behm, “Methanol electrooxidation on a colloidal PtRu-alloy fuel-cell catalyst,” *Electrochemistry Communications*, vol. 1, pp. 1–4, jan 1999.

[44] A. M. Hofstead-Duffy, D.-J. Chen, S.-G. Sun, and Y. J. Tong, “Origin of the current peak of negative scan in the cyclic voltammetry of methanol electro-oxidation on Pt-based electrocatalysts: a revisit to the current ratio criterion,” *Journal of Materials Chemistry*, vol. 22, no. 11, p. 5205, 2012.

[45] P. Hernandez-Fernandez, P. B. Lund, C. Kallesøe, H. F. Clausen, and L. H. Christensen, “Supported Pt-based nanoparticulate catalysts for the electro-oxidation of methanol : An experimental protocol for quantifying its activity,” *International Journal of Hydrogen Energy*, vol. 40, no. 1, pp. 284–291, 2015.

[46] J. K. Nørskov, J. Rossmeisl, A. Logadottir, L. Lindqvist, J. R. Kitchin, T. Bligaard, and H. Jónsson, “Origin of the Overpotential for Oxygen Reduction at a Fuel-Cell Cathode,” *The Journal of Physical Chemistry B*, vol. 108, pp. 17886–17892, nov 2004.

[47] J. Rossmeisl, G. S. Karlberg, T. Jaramillo, and J. K. Nørskov, “Steady state oxygen reduction and cyclic voltammetry,” *Faraday Discussions*, vol. 140, pp. 337–346, oct 2008.

[48] J. Greeley, I. E. L. Stephens, A. S. Bondarenko, T. P. Johansson, H. A. Hansen, T. F. Jaramillo, J. Rossmeisl, I. Chorkendorff, and J. K. Nørskov, “Alloys of platinum and early transition metals as oxygen reduction electrocatalysts,” *Nature Chemistry*, vol. 1, no. 7, pp. 552–556, 2009.

[49] I. E. L. Stephens, A. S. Bondarenko, U. Grønbjerg, J. Rossmeisl, and I. Chorkendorff, “Understanding the electrocatalysis of oxygen reduction on platinum and its alloys,” *Energy & Environmental Science*, vol. 5, no. 5, p. 6744, 2012.

[50] J. Rossmeisl, A. Logadottir, and J. Nørskov, “Electrolysis of water on (oxidized) metal surfaces,” *Chemical Physics*, vol. 319, pp. 178–184, dec 2005.

[51] J. Greeley, J. Rossmeisl, A. Hellmann, and J. K. Norskov, “Theoretical Trends in Particle Size Effects for the Oxygen Reduction Reaction,” *Zeitschrift für Physikalische Chemie*, vol. 221, pp. 1209–1220, oct 2007.

[52] V. Stamenkovic, B. S. Mun, K. J. J. Mayrhofer, P. N. Ross, N. M. Markovic, J. Rossmeisl, J. Greeley, and J. K. Nørskov, “Changing the Activity of Electrocatalysts for Oxygen Reduction by Tuning the Surface Electronic Structure,” *Angewandte Chemie International Edition*, vol. 45, no. 18, pp. 2897–2901, 2006.

[53] V. R. Stamenkovic, B. Fowler, B. S. Mun, G. Wang, P. N. Ross, C. A. Lucas, and N. M. Marković, “Improved Oxygen Reduction Activity on Pt3Ni(111) via Increased Surface Site Availability,” *Science*, vol. 315, pp. 493–497, jan 2007.

[54] J. Zhang, M. B. Vukmirovic, Y. Xu, M. Mavrikakis, and R. R. Adzic, “Controlling the catalytic activity of platinum-monolayer electrocatalysts for oxygen reduction with different substrates.,” *Angewandte Chemie (International ed. in English)*, vol. 44, pp. 2132–5, mar 2005.

[55] W. P. Zhou, X. Yang, M. B. Vukmirovic, B. E. Koel, J. Jiao, G. Peng, M. Mavrikakis, and R. R. Adzic, “Improving electrocatalysts for O2 reduction by fine-tuning the Pt-support interaction: Pt monolayer on the surfaces of a Pd3Fe(111) single-crystal alloy,” *Journal of the American Chemical Society*, vol. 131, no. 35, pp. 12755–12762, 2009.

[56] S.-i. Choi, S. Xie, M. Shao, J. H. Odell, N. Lu, H.-c. Peng, L. Protsailo, S. Guerrero, J. Park, X. Xia, J. Wang, M. J. Kim, and Y. Xia, “Synthesis and characterization of 9 nm Pt-Ni octahedra with a record high activity of 3.3 A/mg(Pt) for the oxygen reduction reaction.,” *Nano letters*, vol. 13, pp. 3420–5, jul 2013.

[57] S.-I. Choi, M. Shao, N. Lu, A. Ruditskiy, H.-C. Peng, J. Park, S. Guerrero, J. Wang, M. J. Kim, and Y. Xia, “Synthesis and Characterization of Pd@Pt-Ni Core-Shell Octahedra with High Activity toward Oxygen Reduction.,” *ACS nano*, vol. 8, pp. 10363–71, oct 2014.

[58] X. Huang, Z. Zhao, L. Cao, Y. Chen, E. Zhu, Z. Lin, M. Li, A. Yan, A. Zettl, Y. M. Wang, X. Duan, T. Mueller, and Y. Huang, “High-performance transition metal-doped Pt3Ni octahedra for oxygen reduction reaction,” *Science*, vol. 348, no. 6240, pp. 1230–1234, 2015.

[59] T. Toda, H. Igarashi, H. Uchida, and M. Watanabe, “Enhancement of the electroreduction of Oxygen on Pt alloys with Fe, Ni, and Co,” *Journal of the Electrochemical Society*, vol. 146, no. 10, pp. 3750–3756, 1999.

[60] D. Wang, H. L. Xin, R. Hovden, H. Wang, Y. Yu, D. a. Muller, F. J. DiSalvo, and H. D. Abruña, “Structurally ordered intermetallic platinum-cobalt core-shell nanoparticles with enhanced activity and stability as oxygen reduction electrocatalysts.,” *Nature materials*, vol. 12, pp. 81–7, jan 2013.

[61] V. R. Stamenkovic and N. M. Markovic, “Oxygen reduction on platinum bimetallic alloy catalysts,” in *Handbook of Fuel Cells*, 2010.

[62] S. Guo, D. Li, H. Zhu, S. Zhang, N. M. Markovic, V. R. Stamenkovic, and S. Sun, “FePt and CoPt nanowires as efficient catalysts for the oxygen reduction reaction.,” *Angewandte Chemie (International ed. in English)*, vol. 52, pp. 3465–8, mar 2013.

[63] V. R. Stamenkovic, B. S. Mun, M. Arenz, K. J. J. Mayrhofer, C. A. Lucas, G. Wang, P. N. Ross, and N. M. Markovic, “Trends in electrocatalysis on extended and nanoscale Pt-bimetallic alloy surfaces,” *Nature Materials*, vol. 6, no. 3, pp. 241–247, 2007.

[64] J. Wu and H. Yang, “Study of the Durability of Faceted Pt 3 Ni Oxygen-Reduction Electrocatalysts,” *ChemCatChem*, vol. 4, no. 10, pp. 1572–1577, 2012.

[65] F. Hasché, M. Oezaslan, and P. Strasser, “Activity, Stability, and Degradation Mechanisms of Dealloyed PtCu3 and PtCo3 Nanoparticle Fuel Cell Catalysts,” *ChemCatChem*, pp. n/a–n/a, 2011.

[66] L. Dubau, J. Durst, F. Maillard, L. Guétaz, M. Chatenet, J. André, and E. Rossinot, “Further insights into the durability of Pt3Co/C electrocatalysts: Formation of "hollow" Pt nanoparticles induced by the Kirkendall effect,” *Electrochimica Acta*, vol. 56, no. 28, pp. 10658–10667, 2011.

[67] D. P. Wilkinson and J. St-Pierre, “Durability,” in *Handbook of Fuel Cells*, Chichester, UK: John Wiley & Sons, Ltd, dec 2010.

[68] C. Cui, L. Gan, M. Heggen, S. Rudi, and P. Strasser, “Compositional segregation in shaped Pt alloy nanoparticles and their structural behaviour during electrocatalysis,” *Nature Materials*, vol. 12, pp. 1–7, jun 2013.

[69] P. Strasser, S. Koh, T. Anniyev, J. Greeley, K. More, C. Yu, Z. Liu, S. Kaya, D. Nordlund, H. Ogasawara, M. F. Toney, and A. Nilsson, “Lattice-strain control of the activity in dealloyed core–shell fuel cell catalysts,” *Nature Chemistry*, vol. 2, no. 6, pp. 454–460, 2010.

[70] L. Dubau, T. Asset, R. Chattot, C. Bonnaud, V. Vanpeene, J. Nelayah, and F. Maillard, “Tuning the Performance and the Stability of Porous Hollow PtNi/C Nanostructures for the Oxygen Reduction Reaction,” *ACS Catalysis*, vol. 5, no. 9, pp. 5333–5341, 2015.

[71] J. X. Wang, C. Ma, Y. Choi, D. Su, Y. Zhu, P. Liu, R. Si, M. B. Vukmirovic, Y. Zhang, and R. R. Adzic, “Kirkendall effect and lattice contraction in nanocatalysts: a new strategy to enhance sustainable activity.,” *Journal of the American Chemical Society*, vol. 133, pp. 13551–7, aug 2011.

[72] C. Chen, Y. Kang, Z. Huo, Z. Zhu, W. Huang, H. L. Xin, J. D. Snyder, D. Li, J. a. Herron, M. Mavrikakis, M. Chi, K. L. More, Y. Li, N. M. Markovic, G. a. Somorjai, P. Yang, and V. R. Stamenkovic, “Highly crystalline multimetallic

nanoframes with three-dimensional electrocatalytic surfaces.," *Science (New York, N.Y.)*, vol. 343, pp. 1339–43, mar 2014.

[73] U. G. Vej-Hansen, J. Rosmeisl, I. Stephens, and J. Schiøtz, "Correlation between diffusion barriers and alloying energy in binary alloys," *Phys. Chem. Chem. Phys.*, 2015.

[74] I. E. L. Stephens, A. S. Bondarenko, L. Bech, and I. Chorkendorff, "Oxygen Electroreduction Activity and X-Ray Photoelectron Spectroscopy of Platinum and Early Transition Metal Alloys," *ChemCatChem*, vol. 4, pp. 341–349, mar 2012.

[75] M. Escudero-Escribano, A. Verdaguer-Casadevall, P. Malacrida, U. Grønbjerg, B. P. Knudsen, A. K. Jepsen, J. Rossmeisl, I. E. L. Stephens, and I. Chorkendorff, "Pt5Gd as a Highly Active and Stable Catalyst for Oxygen Electroreduction," *Journal of the American Chemical Society*, vol. 134, pp. 16476–16479, oct 2012.

[76] M. Escudero-Escribano, P. Malacrida, M. Hansen, U. Vej-Hansen, A. Velázquez-Palenzuela, V. Tripkovic, J. Schiøtz, J. Rossmeisl, I. Stephens, and I. Chorkendorff, "Tuning the activity of Pt alloy electrocatalysts by means of the lanthanide contraction," *Submitted*, 2015.

[77] F. J. Perez-Alonso, D. N. McCarthy, A. Nierhoff, P. Hernandez-Fernandez, C. Strebel, I. E. L. Stephens, J. H. Nielsen, and I. Chorkendorff, "The Effect of Size on the Oxygen Electroreduction Activity of Mass-Selected Platinum Nanoparticles," *Angewandte Chemie International Edition*, vol. 51, no. 19, pp. 4641–4643, 2012.

[78] P. Hernandez-Fernandez, F. Masini, D. N. McCarthy, C. E. Strebel, D. Friebel, D. Deiana, P. Malacrida, A. Nierhoff, A. Bodin, A. M. Wise, J. H. Nielsen, T. W. Hansen, A. Nilsson, I. E. L. Stephens, and I. Chorkendorff, "Mass-selected nanoparticles of PtxY as model catalysts for oxygen electroreduction," *Nature Chemistry*, vol. 6, no. July, pp. 732–738, 2014.

[79] A. Velázquez-Palenzuela, F. Masini, A. F. Pedersen, M. Escudero-Escribano, D. Deiana, P. Malacrida, T. W. Hansen, D. Friebel, A. Nilsson, I. E. Stephens, and I. Chorkendorff, "The enhanced activity of mass-selected PtxGd nanoparticles for oxygen electroreduction," *Journal of Catalysis*, vol. 328, pp. 297–307, aug 2015.

[80] T. J. Schmidt, H. A. Gasteiger, G. D. Stäb, P. M. Urban, D. M. Kolb, and R. J. Behm, "Characterization of High-Surface-Area Electrocatalysts Using a Rotating Disk Electrode Configuration," *Journal of The Electrochemical Society*, vol. 145, no. 7, p. 2354, 1998.

[81] U. Paulus, T. Schmidt, H. A. Gasteiger, and R. J. Behm, "Oxygen reduction on a high-surface area Pt/Vulcan carbon catalyst: a thin-film rotating

ring-disk electrode study," *Journal of Electroanalytical Chemistry*, vol. 495, pp. 134–145, jan 2001.

[82] H. A. Gasteiger, S. S. Kocha, B. Sompalli, and F. T. Wagner, "Activity benchmarks and requirements for Pt, Pt-alloy, and non-Pt oxygen reduction catalysts for PEMFCs," *Applied Catalysis B: Environmental*, vol. 56, pp. 9–35, mar 2005.

[83] K. Mayrhofer, D. Strmcnik, B. Blizanac, V. Stamenkovic, M. Arenz, and N. Markovic, "Measurement of oxygen reduction activities via the rotating disc electrode method: From Pt model surfaces to carbon-supported high surface area catalysts," *Electrochimica Acta*, vol. 53, pp. 3181–3188, feb 2008.

[84] Y. Garsany, O. A. Baturina, K. E. Swider-Lyons, and S. S. Kocha, "Experimental Methods for Quantifying the Activity of Platinum Electrocatalysts for the Oxygen Reduction Reaction," *Analytical Chemistry*, vol. 82, pp. 6321–6328, aug 2010.

[85] Y. Garsany, I. L. Singer, and K. E. Swider-Lyons, "Impact of film drying procedures on RDE characterization of Pt/VC electrocatalysts," *Journal of Electroanalytical Chemistry*, vol. 662, pp. 396–406, nov 2011.

[86] S. Kocha, "Best Practices and Benchmark Activities for ORR Measurements by the Rotating Disk Electrode Technique. 2014 DOE Hydrogen and Fuel Cells Program Review," tech. rep., NREL, 2014.

[87] S. Rudi, C. Cui, L. Gan, and P. Strasser, "Comparative Study of the Electrocatalytically Active Surface Areas (ECSAs) of Pt Alloy Nanoparticles Evaluated by Hupd and CO-stripping voltammetry," *Electrocatalysis*, vol. 5, pp. 408–418, jun 2014.

[88] A. Bonakdarpour, K. Stevens, G. D. Vernstrom, R. Atanasoski, A. K. Schmoeckel, M. K. Debe, and J. R. Dahn, "Oxygen reduction activity of Pt and Pt-Mn-Co electrocatalysts sputtered on nano-structured thin film support," *Electrochimica Acta*, vol. 53, pp. 688–694, dec 2007.

[89] K. Sasaki, H. Naohara, Y. Cai, Y. M. Choi, P. Liu, M. B. Vukmirovic, J. X. Wang, and R. R. Adzic, "Core-protected platinum monolayer shell high-stability electrocatalysts for fuel-cell cathodes.," *Angewandte Chemie (International ed. in English)*, vol. 49, pp. 8602–7, nov 2010.

[90] C. Wang, M. Chi, D. Li, D. Strmcnik, D. van der Vliet, G. Wang, V. Komanicky, K.-c. Chang, A. P. Paulikas, D. Tripkovic, J. Pearson, K. L. More, N. M. Markovic, and V. R. Stamenkovic, "Design and synthesis of bimetallic electrocatalyst with multilayered Pt-skin surfaces.," *Journal of the American Chemical Society*, vol. 133, pp. 14396–403, sep 2011.

[91] C. Wang, D. van der Vliet, K. L. More, N. J. Zaluzec, S. Peng, S. Sun, H. Daimon, G. Wang, J. Greeley, J. Pearson, A. P. Paulikas, G. Karapetrov, D. Strmcnik, N. M. Markovic, and V. R. Stamenkovic, "Multimetallic Au/FePt3 nanoparticles as highly durable electrocatalyst.," *Nano letters*, vol. 11, pp. 919–26, mar 2011.

[92] W. Liu, P. Rodriguez, L. Borchardt, A. Foelske, J. Yuan, A.-K. Herrmann, D. Geiger, Z. Zheng, S. Kaskel, N. Gaponik, R. Kötz, T. J. Schmidt, and A. Eychmüller, "Bimetallic aerogels: high-performance electrocatalysts for the oxygen reduction reaction.," *Angewandte Chemie (International ed. in English)*, vol. 52, pp. 9849–52, sep 2013.

[93] C. Baldizzone, S. Mezzavilla, H. W. P. Carvalho, J. C. Meier, A. K. Schuppert, M. Heggen, C. Galeano, J.-D. Grunwaldt, F. Schüth, and K. J. J. Mayrhofer, "Confined-Space Alloying of Nanoparticles for the Synthesis of Efficient PtNi Fuel-Cell Catalysts.," *Angewandte Chemie (International ed. in English)*, pp. 14250–14254, oct 2014.

[94] C. M. Pedersen, M. Escudero-Escribano, A. Velázquez-Palenzuela, L. H. Christensen, I. Chorkendorff, and I. E. Stephens, "Benchmarking Pt-based electrocatalysts for low temperature fuel cell reactions with the rotating disk electrode: oxygen reduction and hydrogen oxidation in the presence of CO (review article)," *Electrochimica Acta*, vol. 179, pp. 647–657, 2015.

[95] U. A. Paulus, T. J. Schmidt, and H. A. Gasteiger, "Poisons for the O2 reduction reaction," in *Handbook of Fuel Cells*, vol. 3, 2010.

[96] N. Alonso-Vante, "Chevrel phases and chalcogenides," in *Handbook of fuel cells*, pp. 1–10, 2010.

[97] T. J. Schmidt, U. A. Paulus, H. A. Gasteiger, N. Alonso-Vante, and R. J. Behm, "Oxygen Reduction on Ru[sub 1.92]Mo[sub 0.08]SeO[sub 4], Ru/-Carbon, and Pt/Carbon in Pure and Methanol-Containing Electrolytes," *Journal of The Electrochemical Society*, vol. 147, p. 2620, jul 2000.

[98] D. Cao, A. Wieckowski, J. Inukai, and N. Alonso-Vante, "Oxygen Reduction Reaction on Ruthenium and Rhodium Nanoparticles Modified with Selenium and Sulfur," *Journal of The Electrochemical Society*, vol. 153, no. 5, p. A869, 2006.

[99] L. Timperman, A. S. Gago, and N. Alonso-Vante, "Oxygen reduction reaction increased tolerance and fuel cell performance of Pt and RuxSey onto oxide–carbon composites," *Journal of Power Sources*, vol. 196, pp. 4290–4297, may 2011.

[100] E. Antolini, J. R. C. Salgado, a. M. dos Santos, and E. R. Gonzalez, "Carbon-Supported Pt-Ni Alloys Prepared by the Borohydride Method as Electrocatalysts for DMFCs," *Electrochemical and Solid-State Letters*, vol. 8, no. 4, p. A226, 2005.

[101] H. Yang, C. Coutanceau, J.-M. Léger, N. Alonso-Vante, and Claude-Lamy, “Methanol tolerant oxygen reduction on carbon-supported Pt–Ni alloy nanoparticles,” *Journal of Electroanalytical Chemistry*, vol. 576, pp. 305–313, mar 2005.

[102] J. R. C. Salgado, E. Antolini, and E. R. Gonzalez, “Carbon supported Pt–Co alloys as methanol-resistant oxygen-reduction electrocatalysts for direct methanol fuel cells,” *Applied Catalysis B: Environmental*, vol. 57, pp. 283–290, may 2005.

[103] J. T. Mueller and P. M. Urban, “Characterization of direct methanol fuel cells by ac impedance spectroscopy,” *Journal of Power Sources*, vol. 75, no. 1, pp. 139–143, 1998.

[104] S. H. Jensen, J. Hjelm, a. Hagen, and M. Mogensen, “Electrochemical impedance spectroscopy as diagnostic tool,” *Handbook of Fuel Cells*, vol. 6, 2010.

[105] a. Weber, H. Schichlein, and E. Ivers-Tiffée, “Electrochemical impedance spectroscopy,” *Handbook of Fuel Cells*, pp. 1–16, 2010.

[106] G. Hinds and E. Brightman, “In situ mapping of electrode potential in a PEM fuel cell,” *Electrochemistry Communications*, vol. 17, pp. 26–29, apr 2012.

[107] B. A. Averill and P. Eldredge, *Principles of General Chemistry v. 1.0.* 2012.

[108] M. Boutonnet, J. Kizling, P. Stenius, and G. Maire, “The preparation of monodisperse colloidal metal particles from microemulsions,” *Colloids and Surfaces*, vol. 5, no. 3, pp. 209–225, 1982.

[109] C. Coutanceau, S. Brimaud, C. Lamy, J.-M. Léger, L. Dubau, S. Rousseau, and F. Vigier, “Review of different methods for developing nanoelectrocatalysts for the oxidation of organic compounds,” *Electrochimica Acta*, vol. 53, pp. 6865–6880, oct 2008.

[110] Y. Luo, A. Habrioux, L. Calvillo, G. Granozzi, and N. Alonso-Vante, “Yttrium oxide/gadolinium oxide-modified platinum nanoparticles as cathodes for the oxygen reduction reaction,” *ChemPhysChem*, vol. 15, pp. 2136–2144, 2014.

[111] K. W. Lux and E. J. Cairns, “Lanthanide–Platinum Intermetallic Compounds as Anode Electrocatalysts for Direct Ethanol PEM Fuel Cells I. Synthesis and Characterization of Nanopowders,” *Journal of The Electrochemical Society*, vol. 153, pp. A1132–A1138, jan 2006.

[112] K. W. Lux and E. J. Cairns, “Lanthanide–Platinum Intermetallic Compounds as Anode Electrocatalysts for Direct Ethanol PEM Fuel Cells II. Performance of Nanopowders in an Operating PEM Fuel Cell,” *Journal of The Electrochemical Society*, vol. 153, pp. A1139–A1147, jan 2006.

[113] C. Yan and M. J. Wagner, “Air- and Water-Stable Gold-Coated Gadolinium Metal Nanocrystals.,” *Nano letters*, may 2013.

[114] J. a. Nelson, L. H. Bennett, and M. J. Wagner, “Solution synthesis of gadolinium nanoparticles.,” *Journal of the American Chemical Society*, vol. 124, pp. 2979–83, mar 2002.

[115] J. a. Nelson, L. H. Bennett, and M. J. Wagner, “Dysprosium nanoparticles synthesized by alkalide reduction,” *Journal of Materials Chemistry*, vol. 13, pp. 857–860, mar 2003.

[116] D. Saha, E. D. Bøjesen, K. M. Ø. Jensen, A.-C. Dippel, and B. B. Iversen, “Formation Mechanisms of Pt and Pt 3 Gd Nanoparticles under Solvothermal Conditions: An in Situ Total X-ray Scattering Study,” *The Journal of Physical Chemistry C*, vol. 119, no. 23, pp. 13357–13362, 2015.

[117] B. Erdmann, “Darstellung von Actiniden-Lanthaniden-Edelmetall (Pt, Pd, Ir, Rh)-Legierungsphasen durch gekoppelte Reduktion,” *Kernforschungszentrum Karlsruhe Report*, 1971.

[118] B. Erdmann and C. Keller, “Actinide(lanthanide)-noble metal alloy phases, preparation and properties,” *Journal of Solid State Chemistry*, vol. 7, no. 1, pp. 40–48, 1973.

[119] W. Bronger, “Preparation and X-ray investigation of platinum alloys with the rare-earth metals (Pt 5 Ln and Pt 3 Ln phases),” *Journal of the Less Common Metals*, vol. 12, pp. 63–68, 1967.

[120] N. Krikorian, “The reaction of selected lanthanide carbides with platinum and iridium,” *Journal of the Less Common Metals*, vol. 23, pp. 271–279, 1971.

[121] a. E. Dwight, J. W. Downey, and R. a. Conner Jnr, “Some AB3 compounds of the transitiom metals,” *Acta Crystallographica*, vol. 14, no. 1, pp. 75–76, 1961.

[122] T. Geballe, B. Matthias, V. Compton, E. Corenzwit, G. Hull, and L. Longinotti, “Superconductivity in Binary Alloy Systems of the Rare Earths and of Thorium with Pt-Group Metals,” *Physical Review*, vol. 137, no. 1962, pp. A119–A127, 1965.

[123] G. C. Messina, P. Wagener, R. Streubel, A. De Giacomo, A. Santagata, G. Compagnini, and S. Barcikowski, “Pulsed laser ablation of a continuously-fed wire in liquid flow for high-yield production of silver nanoparticles,” *Phys. Chem. Chem. Phys.*, vol. 15, no. 9, pp. 3093–3098, 2013.

[124] R. Intartaglia, G. Das, K. Bagga, A. Gopalakrishnan, A. Genovese, M. Povia, E. Di Fabrizio, R. Cingolani, A. Diaspro, and F. Brandi, “Laser synthesis of ligand-free bimetallic nanoparticles for plasmonic applications,” *Phys. Chem. Chem. Phys.*, vol. 15, no. 9, pp. 3075–3082, 2013.

[125] A. I. Yanson, P. Rodriguez, N. Garcia-Araez, R. V. Mom, F. D. Tichelaar, and M. T. M. Koper, “Cathodic corrosion: a quick, clean, and versatile method for the synthesis of metallic nanoparticles.,” *Angewandte Chemie (International ed. in English)*, vol. 50, pp. 6346–50, jul 2011.

[126] P. Rodriguez, F. D. Tichelaar, M. T. M. Koper, and A. I. Yanson, “Cathodic Corrosion as a Facile and Effective Method To Prepare Clean Metal Alloy Nanoparticles,” *Journal of the American Chemical Society*, vol. 133, pp. 17626–17629, nov 2011.

[127] D. Brandon and W. D. Kaplan, *Microstructual Characterization of Materials.* Wiley, 2nd editio ed., 2008.

[128] PANalytical, “HighScore Plus 4.0 Manual.”

[129] G. Williamson and W. Hall, “X-ray line broadening from filed aluminium and wolfram,” *Acta Metallurgica*, vol. 1, no. 1, pp. 22–31, 1953.

[130] L. W. Finger, D. E. Cox, and a. P. Jephcoat, “Correction for powder diffraction peak asymmetry due to axial divergence,” *Journal of Applied Crystallography*, vol. 27, no. pt 6, pp. 892–900, 1994.

[131] G. Caglioti, A. Paoletti, and F. Ricci, “Choice of collimators for a crystal spectrometer for neutron diffraction,” *Nuclear Instruments*, vol. 3, no. 4, pp. 223–228, 1958.

[132] J. Bolze, D. Beckers, and V. Kogan, “Size Distribution Determination of Nanoparticles and Nanosized Pores by Small-Angle X-Ray Scattering (SAXS) on a Multi-Purpose X-Ray Diffractometer.”

[133] H. Schnablegger and Yashveer Singh, *The SAXS Guide.* Graz: Anton Paar GmbH, 2013.

[134] P. Malacrida, M. Escudero-Escribano, A. Verdaguer-Casadevall, I. E. L. Stephens, and I. Chorkendorff, “Enhanced activity and stability of Pt–La and Pt–Ce alloys for oxygen electroreduction: the elucidation of the active surface phase,” *Journal of Materials Chemistry A*, vol. 2, no. 12, p. 4234, 2014.

[135] F. Maillard, E. R. Savinova, and U. Stimming, “CO monolayer oxidation on Pt nanoparticles: Further insights into the particle size effects,” *Journal of Electroanalytical Chemistry*, vol. 599, pp. 221–232, jan 2007.

[136] C.-M. Lai, J.-C. Lin, K.-L. Hsueh, C.-P. Hwang, K.-C. Tsay, L.-D. Tsai, and Y.-M. Peng, “On the Accelerating Degradation of DMFC at Highly Anodic Potential,” *Journal of The Electrochemical Society*, vol. 155, no. 8, p. B843, 2008.

[137] C. Lai, J. Lin, K. Hsueh, C. Hwang, K. Tsay, L. Tsai, and Y. Peng, "On the electrochemical impedance spectroscopy of direct methanol fuel cell," *International Journal of Hydrogen Energy*, vol. 32, pp. 4381–4388, 2007.

[138] F. Bresciani, A. Casalegno, M. Zago, and R. Marchesi, "A Parametric Analysis on DMFC Anode Degradation," *Fuel Cells*, vol. 14, no. 3, pp. 386–394, 2014.

[139] J. T. Müller, P. M. Urban, and W. F. Hölderich, "Impedance studies on direct methanol fuel cell anodes," *Journal of Power Sources*, vol. 84, pp. 157–160, 1999.

[140] D. Chakraborty, I. Chorkendorff, and T. Johannessen, "Electrochemical impedance spectroscopy study of methanol oxidation on nanoparticulate PtRu direct methanol fuel cell anodes: Kinetics and performance evaluation," *Journal of Power Sources*, vol. 162, no. 2 SPEC. ISS., pp. 1010–1022, 2006.

[141] M. Zago and a. Casalegno, "A physical model of Direct Methanol Fuel Cell anode impedance," *Journal of Power Sources*, vol. 248, pp. 1181–1190, 2014.

[142] S. Trasatti, "Reaction mechanism and rate determining steps," *Handbook of Fuel Cells Vol. 2*, no. 3, pp. 79–87, 2003.

[143] A. Velázquez-Palenzuela, E. Brillas, C. Arias, F. Centellas, J. A. Garrido, R. M. Rodríguez, and P.-L. Cabot, "Carbon monoxide, methanol and ethanol electro-oxidation on Ru-decorated carbon-supported Pt nanoparticles prepared by spontaneous deposition," *Journal of Power Sources*, vol. 225, pp. 163–171, mar 2013.

[144] S. Srinivasan, *Fuel Cells: From Fundamentals to Applications.* Springer, 2006.

[145] S. Gojković, T. Vidaković, and D. Durović, "Kinetic study of methanol oxidation on carbon-supported PtRu electrocatalyst," *Electrochimica Acta*, vol. 48, pp. 3607–3614, oct 2003.

[146] M. T. M. Koper, T. E. Shubina, and R. A. van Santen, "Periodic Density Functional Study of CO and OH Adsorption on Pt-Ru Alloy Surfaces: Implications for CO Tolerant Fuel Cell Catalysts," *The Journal of Physical Chemistry B*, vol. 106, pp. 686–692, jan 2002.

[147] T. Iwasita, F. C. Nart, and W. Vielstich, "An FTIR Study of the Catalytic Activity of a 85:15 Pt:Ru Alloy for Methanol Oxidation," *Berichte der Bunsengesellschaft für physikalische Chemie*, vol. 94, pp. 1030–1034, sep 1990.

[148] J. C. Davies, J. Bonde, Á. Logadóttir, J. K. Nørskov, and I. Chorkendorff, "The Ligand Effect: CO Desorption from Pt/Ru Catalysts," *Fuel Cells*, vol. 5, pp. 429–435, dec 2005.

[149] J. McBreen and S. Mukerjee, "In Situ X-Ray Absorption Studies of a Pt-Ru Electrocatalyst," *Journal of The Electrochemical Society*, vol. 142, no. 10, p. 3399, 1995.

[150] T. J. Schmidt, H. A. Gasteiger, and R. J. Behm, "Rotating Disk Electrode Measurements on the CO Tolerance of a High-Surface Area Pt/Vulcan Carbon Fuel Cell Catalyst," *Journal of The Electrochemical Society*, vol. 146, no. 4, p. 1296, 1999.

[151] H. A. Gasteiger, N. M. Markovic, and P. N. Ross, "H2 and CO Electrooxidation on Well-Characterized Pt , Ru , and Pt-Ru . 1. Rotating Disk Studies of the Pure Gases Including Temperature Effects," *Journal of Physical Chemistry*, vol. 99, pp. 8290–8301, 1995.

[152] J. X. Wang, N. M. Markovic, and R. R. Adzic, "Kinetic Analysis of Oxygen Reduction on Pt(111) in Acid Solutions: Intrinsic Kinetic Parameters and Anion Adsorption Effects," *The Journal of Physical Chemistry B*, vol. 108, pp. 4127–4133, apr 2004.

[153] M. Nesselberger, S. Ashton, J. C. Meier, I. Katsounaros, K. J. J. Mayrhofer, and M. Arenz, "The Particle Size Effect on the Oxygen Reduction Reaction Activity of Pt Catalysts: Influence of Electrolyte and Relation to Single Crystal Models," *Journal of the American Chemical Society*, vol. 133, pp. 17428–17433, nov 2011.

[154] N. Wakabayashi, H. Uchida, and M. Watanabe, "Temperature-Dependence of Methanol Oxidation Rates at PtRu and Pt Electrodes," *Electrochemical and Solid-State Letters*, vol. 5, pp. E62–E65, jan 2002.

[155] G. Beggerow, "Ag2CrO4 - H2O," in *High-Pressure Properties of Matter*, pp. 4–18, Berlin/Heidelberg: Springer-Verlag, 2000.

[156] P. G. Jessop and W. Leitner, "Supercritical Fluids as Media for Chemical Reactions," in *Chemical Synthesis Using Supercritical Fluids*, ch. 1, pp. 1–36, Weinheim, Germany: Wiley-VCH Verlag GmbH, dec 2007.

[157] F. P. Lucien and N. R. Foster, "Phase Behavior and Solubility," in *Chemical Synthesis Using Supercritical Fluids*, ch. 2, pp. 37–53, Weinheim, Germany: Wiley-VCH Verlag GmbH, dec 2007.

[158] J. W. Johnson and D. Norton, "Critical phenomena in hydrothermal systems; state, thermodynamic, electrostatic, and transport properties of H 2 O in the critical region," *American Journal of Science*, vol. 291, pp. 541–648, jun 1991.

[159] T. Adschiri, Y. Hakuta, K. Sue, and K. Arai, "Hydrothermal synthesis of metal oxide nanoparticles at supercritical conditions," *Journal of Nanoparticle Research*, vol. 3, pp. 227–235, 2001.

[160] T. Adschiri, Y.-W. Lee, M. Goto, and S. Takami, “Green materials synthesis with supercritical water,” *Green Chemistry*, vol. 13, no. 6, p. 1380, 2011.

[161] T. Adschiri, K. Kanazawa, and K. Arai, “Rapid and Continuous Hydrothermal Synthesis of Boehmite Particles in Subcritical and Supercritical Water,” *Journal of the American Ceramic Society*, vol. 75, no. 9, pp. 2615–2618, 1992.

[162] P. Hald, *Supercritical synthesis of complex nano materials.* PhD thesis, Aarhus University, 2009.

[163] P. Hald, J. Becker, M. Bremholm, J. S. Pedersen, J. Chevallier, S. B. Iversen, and B. B. Iversen, “Supercritical Propanol–Water Synthesis and Comprehensive Size Characterisation of Highly Crystalline anatase TiO2 Nanoparticles,” *Journal of Solid State Chemistry*, vol. 179, pp. 2674–2680, aug 2006.

[164] C. Kallesøe, H. F. Clausen, L. H. Christensen, T. Lund-Olsen, M. A. HASEN MAMAKHEL, B. B. IVERSEN, J. BECKER-CHRISTENSEN, D. F. AARUP, and J. HALES, “Method of preparing a catalytic structure,” 2014.

[165] J.-L. Mi, H. F. Clausen, M. Bremholm, M. S. Schmøkel, P. Hernández-Fernández, J. Becker, and B. B. Iversen, “Pulsed-Flow Near-Critical and Supercritical Synthesis of Carbon-Supported Platinum Nanoparticles and In Situ X-ray Diffraction Study of Their Formation and Growth,” *Chemistry of Materials*, vol. 27, pp. 450–456, 2015.

[166] J. R. Eltzholtz and B. B. Iversen, “High-temperature and high-pressure pulsed synthesis apparatus for supercritical production of nanoparticles.,” *The Review of scientific instruments*, vol. 82, p. 084102, aug 2011.

[167] T. P. Johansson, E. T. Ulrikkeholm, P. Hernandez-Fernandez, M. Escudero-Escribano, P. Malacrida, I. E. L. Stephens, and I. Chorkendorff, “Towards the elucidation of the high oxygen electroreduction activity of PtxY: surface science and electrochemical studies of Y/Pt(111).,” *Physical chemistry chemical physics : PCCP*, vol. 16, no. 27, pp. 13718–25, 2014.

[168] E. T. Ulrikkeholm, *Singly crystal studies of platinum alloys for oxygen reduction electrodes.* PhD thesis, DTU, 2014.

[169] B. P. Knudsen, *Synthesis and test af new platinum-alloy based electrocatalysts.* Master thesis, Technical University of Denmark, 2012.

[170] *A LANTHANIDE LANTHOLOGY Part 1, A - L.* No. reprinted, Molycorp, Inc. Mountain Pass, CA, U.S.A, 1997.

[171] L. Sokolova, A. Lapitskaya, A. Bol’shakov, S. Pirkes, and B. Abalduev, “Thermographic and thermogravimetric investigation into crystallohydrates of rare earth and yttrium chlorides,” *Zhurnal Neorganicheskoj Khimii*, vol. 26, no. 7, pp. 1736–1741, 1981.

[172] G. J. Kipouros and R. A. Sharma, “Characterization of neodymium trichloride hydrates and neodymium hydroxychloride,” *Journal of the Less Common Metals*, vol. 160, pp. 85–99, apr 1990.

[173] G. Meyer and T. Staffel, “Die Tieftemperatur-Synthese von Oxidhalogeniden, YOX (X = Cl, Br, I), als Quelle der Verunreinigung von Yttriumtrihalogeniden, YX3, bei der Gewinnung nach der Ammoniumhalogenid-Methode. Die Analogie von YOCl und YSCl,” *Zeitschrift für anorganische und allgemeine Chemie*, vol. 532, pp. 31–36, jan 1986.

[174] R. W. G. Wyckoff, *Crystal Structures 1.* Wiley, 1963.

[175] “NIST X-ray Photoelectron Spectroscopy Database.”

[176] A. A. Permyakova, *Electrocatalysts and their Supporting Materials for Proton Exchange Membrane Fuel Cells: Activity and Durability Studies.* Ph.d. thesis, DTU, 2013.

[177] Q. Guo and O. J. Kleppa, “The standard enthalpies of formation of the compounds of early transition metals with late transition metals and with noble metals as determined by Kleppa and co-workers at the University of Chicago - A review,” *Journal of Alloys and Compounds*, vol. 321, no. 2, pp. 169–182, 2001.

[178] M. Mangelmann, “KFK 2107: Untersuchungen zur Stabilität von Erdalkali-/Lanthaniden-Edelmetallegierungen,” tech. rep., Kerforschung Karlsruhe, 1975.

[179] H. Kleykamp, “Thermodynamics of the systems of the platinum metals with other transition metals: I. Integral data,” 1993.

[180] L. Hellwig, *Thermodynamische Untersuchungen an den Systemen Yttrium-Platin und Neptunium-Platin durch EMK-Messungen mit galvanischen Festkörperketten.* No. November, Kernforscungszentrum Karlsruhe, 1978.

[181] G. Kemmler, *Untersuchungen zur Stabilität von Lanthaniden-Platin Verbindungen.* Kernforscungszentrum Karlsruhe, 1977.

[182] U. G. Vej-Hansen, *Structure, activity, and stability of platinum alloys as catalysts for the oxygen reduction reaction.* PhD thesis, Technical University of Denmark, 2015.

[183] “Thermodynamic Properties of Compounds, VF2 to ScF3,” in *Pure Substances. Part 3 _ Compounds from CoCl3_g to Ge3N4*, pp. 275–300, Berlin/Heidelberg: Springer-Verlag.

[184] “Thermodynamic Properties of Compounds, Fe2I6 to GeI4,” in *Pure Substances. Part 3 _ Compounds from CoCl3_g to Ge3N4*, pp. 375–400, Berlin/Heidelberg: Springer-Verlag.

[185] “Thermodynamic Properties of Compounds, CoCl3 to NpCl3,” in *Pure Substances. Part 3 _ Compounds from CoCl3_g to Ge3N4*, pp. 1–24, Berlin/Heidelberg: Springer-Verlag.

[186] K. Gschneidner, J.-C. G. Bünzli, and V. K. Pecharsky, *Handbook on the Physics and Chemistry of Rare Earths, Bind 33.* Elsevier, 2003.

[187] I. B. Rabinovish, V. P. Nistratov, V. I. Telnoy, and M. S. Sheiman, *Thermochemical and thermodynamic properties of organometallic compounds.* New York: Begell House, 1999.

[188] P. J. Grunthaner, F. J. Grunthaner, and A. Madhukar, “Chemical bonding and charge redistribution - Valence band and core level correlations for the Ni/Si, Pd/Si, and Pt/Si systems,” *Journal of Vacuum Science & Technology*, vol. 20, no. 3, pp. 680–683, 1982.

[189] Landolt-Börnstein, “Thermodynamic Properties of Compounds, PCl3O to Co2Cl4,” in *Pure Substances. Part 3 _ Compounds from CoCl3_g to Ge3N4*, pp. 25–50, 19 a3 ed.

A

Appendix A - Fitted thermodyanamics data for Pt_xM alloys

Table A.1 shows the fitted values used in thermodynamic calculations in Section 6.1. The values were calculated using equation 6.5-6.8 from litterature data [178–181].

	H_0 [kJ/mol]	S_0 [J/(mol K)]	A [J/(mol K)]	B	C	D
Pt_5Y	-386	247.5	164.8	-3.03	-9.66	17.38
Pt_5La	-437	217.1	158.1	13.83	-8.88	9.58
Pt_5Ce	-426	232.2	156.4	24.30	-10.08	5.92
Pt_5Pr	-444	230.1	148.2	33.75	0.63	4.54
Pt_5Nd	-435	229.2	144.9	41.06	2.69	2.35
Pt_5Sm	-414	246.7	175.1	7.70	-22.25	13.87
Pt_5Eu	-333	236.0	142.8	40.76	5.56	0.09
Pt_5Gd	-438	225.2	145.6	22.93	11.34	9.74
Pt_5Tb	-442	237.5	154.0	16.52	-2.07	12.60
Pt_5Dy	-438	235.1	181.2	-40.22	-17.46	39.45
Pt_5Ho	-445	236.2	179.6	-37.12	-12.64	37.62
Pt_5Er	-444	237.6	168.8	-8.62	-9.84	20.70
Pt_5Tm	-433	235.2	164.3	-1.61	-10.71	16.98
Pt_5Ca	-232	224.2	137.1	56.19	7.70	-7.84
Pt_3Sc	-414	135.7	119.3	-22.20	-13.01	23.00
Pt_3Y	-387	150.1	108.5	1.17	-5.67	10.46
Pt_3Tb	-425	152.2	101.8	14.90	-2.37	7.74
Pt_3Dy	-424	148.9	122.9	-33.06	-11.64	31.38
Pt_3Ho	-442	143.9	123.4	-33.19	-8.80	30.80
Pt_3Er	-442	143.0	94.8	19.55	9.62	5.47
Pt_3Tm	-443	141.9	106.3	4.97	-5.03	9.19
Pt_3Yb	-414	127.7	99.8	19.64	2.25	4.30
Pt_2La	-384	88.2	70.5	24.70	-0.06	-2.51
Pt_2Ce	-394	93.3	68.5	35.53	-1.13	-6.31
Pt_2Pr	-396	96.4	60.7	30.08	17.57	-1.07
Pt_2Nd	-416	82.4	59.7	48.67	9.07	-8.64
Pt_2Eu	-296	108.1	58.2	47.29	11.59	-10.41
Pt_2Sm	-399	96.8	87.8	17.89	-13.58	2.08
Pt_2Gd	-412	91.4	65.7	23.05	12.50	1.46

Table A.1: Fitted thermodynamic parameters for different Pt_xM alloys used in thermodynamic calculations in HCS Chemistry 6.1

B

Appendix B - Paper 1

Electrochimica Acta 179 (2015) 647–657

Contents lists available at ScienceDirect

Electrochimica Acta

journal homepage: www.elsevier.com/locate/electacta

Benchmarking Pt-based electrocatalysts for low temperature fuel cell reactions with the rotating disk electrode: oxygen reduction and hydrogen oxidation in the presence of CO (review article)

Christoffer M. Pedersen [a,b], María Escudero-Escribano [b], Amado Velázquez-Palenzuela [b], Leif H. Christensen [a], Ib Chorkendorff [b], Ifan E.L. Stephens [b,*]

[a] Center for Nano- and Micro technology, Danish Technological Institute (DTI), Gregersenvej, DK-2630 Taastrup, Denmark
[b] Center for Individual Nanoparticle Functionality, Department of Physics, Building 312, Technical University of Denmark (DTU), DK-2800 Lyngby, Denmark

ARTICLE INFO

Article history:
Received 19 January 2015
Received in revised form 23 March 2015
Accepted 24 March 2015
Available online 31 March 2015

Keywords:
Fuel Cells
Electrocatalysis
Oxygen Reduction Reaction
Hydrogen Oxidation Reaction
CO Poisoning

ABSTRACT

We present up-to-date benchmarking methods for testing electrocatalysts for polymer exchange membrane fuel cells (PEMFC), using the rotating disk electrode (RDE) method. We focus on the oxygen reduction reaction (ORR) and the hydrogen oxidation reaction (HOR) in the presence of CO. We have chosen our experimental methods to provide the most optimal compromise between the ease of carrying out the measurements and for ensuring comparability with PEMFC conditions. For the ORR, the effect of temperature, scan rate, Ohmic drop correction and background subtraction on the catalyst activity is investigated, both on a polycrystalline Pt disk and two different commercial Pt/C catalysts. To benchmark the CO tolerance of HOR catalysts, cyclic voltammetry and chronoamperometry are used, on polycrystalline Pt and commercial catalysts consisting of Pt/C and PtRu/C. We recommend the optimal conditions for obtaining a benchmark of ORR activity and CO tolerance of HOR catalysts.

1. Introduction

Low-temperature fuel cells, in particular Proton Exchange Membrane Fuel Cells (PEMFCs) could take a pivotal role in a future society based on sustainable energy. They convert chemical energy efficiently into electricity; should the hydrogen be derived from splitting water, they would emit negligible CO_2 emissions. PEMFCs can be used complementary to batteries for powering zero CO_2 emission vehicles. One of the chief advantages of using PEMFCs in automobile applications, over batteries, is the high energy density. For long range vehicles (~500 km range) the PEMFC energy storage system can be made about six times lighter than for a similar advanced Li-ion battery system [1,2]. Analysis of zero emission vehicles suggest that fuel cell vehicles are more economically viable for the longer range vehicles whereas for urban transport (~160 km range) batteries are the better choice [1–3]. Another practical advantage is that it is much faster to refuel hydrogen than it to recharge a similar sized battery. However, the high cost of PEMFCs, together with their relative limited lifetime compared to competing technologies is hindering wide adaption of this technology [4]. Part of the high cost is due to the high Pt loading necessary at the cathode ($0.4\,mg_{Pt}/cm^2$), where the oxygen reduction reaction (ORR) takes place [4–7]. To reduce costs, the Pt loading should be reduced by increasing the activity of the ORR catalyst. Tremendous progress has been made in improving the activity for the ORR in the last decade [8–31].

Scalable Pt-alloy catalysts are now implemented in PEMFC's with activity and stability that exceed performance targets set by the DOE for 2020, listed in Table 1 [31]. However, even when the DOE targets are obtained, it would still only be possible to produce 17.4 million fuel cell vehicles a year (assuming 12.5 g per 100 kW, and using worldwide production of platinum in 2012: 218,000 kg [33]). In comparison, ~87.4 million vehicles were produced worldwide in 2013 [34]. Moreover, although state-of-the-art alloys often perform well in accelerated degradation tests [27,28,31], it is not clear how well they will perform over the long term in PEMFCs [35].

It is worth bearing in mind that should the Pt-loading in PEMFC's be decreased by an order of magnitude, they will reach a similar level to the amount currently used in advanced catalytic converters [3,6]. This means that a catalyst is required with a stable activity of around 1.6 A/mg *mass activity* at 0.9 V, when measured in a fuel cell. Fig. 1 shows the specific activity (a) and mass activity (b) of a selection of some of the most active ORR catalysts. We have

---

* Corresponding author.
E-mail address: ifan@fysik.dtu.dk (I.E.L. Stephens).

http://dx.doi.org/10.1016/j.electacta.2015.03.176
0013-4686/

Table 1
–Summary of DOE targets for catalyst in automotive applications from the Fuel Cell Technologies Office Multi-Year Research, Development, and Demonstration Plan [32].

	2020 Target
Pt group metal total content (both electrodes)	$0.125\,g\,kW^{-1}$
Pt group metal total loading	$0.125\,mg\,cm^{-2}$
Loss in initial catalytic activity (mass activity)	$<40\%$
Catalyst support stability (mass activity loss)	$<10\%$
Mass activity @ 0.9 V vs RHE	$0.44\,A\,mg_{Pt}^{-1}$

normalised the mass activity to the total mass of precious metal, as opposed to the total mass of Pt only (for example a metal like Au has a similar cost to Pt, and a metal like Pd may currently be cheaper, but has similar supply limitations to Pt). The comparison of these different data is sometimes challenging, especially as different experimental conditions have been applied, including (a) temperature (b) scan rate (c) correction of Ohmic losses (d) subtraction of background capacitive currents. Several articles have addressed some of these parameters, in order to develop more meaningful benchmarks [5,36–40]. However, given that this is a rather fast moving field, we take the view that there is a need for an updated overview of how these different parameters affect the measured catalyst activity.

The anode of low-temperature PEMFCs, where the oxidation of hydrogen takes place, can operate with much lower Pt loadings than the cathode (where the ORR occurs), when pure H_2 is used. Loadings as low as 0.05 mg/cm^2 can be used in a fuel cell and still drive currents on the order of A/cm^2 at negligible over potential [4,41]. Indeed, on Pt/C, due to the ultra-fast kinetics of hydrogen oxidation, in combination with the low solubility of H_2 in liquid electrolytes, rotating disk electrode (RDE) based techniques grossly underestimate the activity of the catalyst by orders of magnitude [42–47].

The majority of H_2 produced today is derived by reforming fossil fuels. This is because the high purity grade H_2 produced from electrolysis is expensive, due to the greater energy input required to produce it. Reformate hydrogen contains trace amounts of CO; the HOR activity of Pt is significantly degraded when CO concentrations as low as 10 ppm are present in the anode feed gas [4,48,49]. In automotive applications, the varying reformate gas flows due to varying power demands, makes it difficult to achieve CO content in the <10 ppm range [4] resulting in substantial performance losses induced from CO poisoning. One strategy to mitigate the effect of CO is to air-bleed the anode [50], by feeding the reformate H_2 with ~2% O_2; this oxygen oxidises the CO to CO_2 [4]. A major disadvantage of using air-bleed is the increased production of H_2O_2 which degrades the membrane [51]. Another solution to CO poisoning is to develop CO-tolerant HOR electro catalysts for low-temperature fuel cells that could be fed with impure hydrogen produced by reforming of hydrocarbons. This has been achieved by alloying Pt with other metals such as Ru [52–54], Sn [54,55], Mo [56,57], Fe, Co and Ni [58,59]. Pt–Ru exhibits the most superior performance of these catalysts due to its higher activity at low potentials 0–0.2 V vs RHE [60]. At more positive potentials, above 0.3–0.4 V vs RHE, i.e. in the *post-ignition* region, the CO-tolerance of this catalyst is by virtue of the bifunctional electrooxidation of CO to CO_2:Ru activates water and Pt activates CO [61–63]. However, for fuel cell applications, the activity below 0.3–0.4 V vs RHE, i.e. in the *pre-ignition* region, is of much greater relevance. Under such conditions, even Pt-Ru is unable to oxidise CO; on the other hand, the Pt-surface atoms will

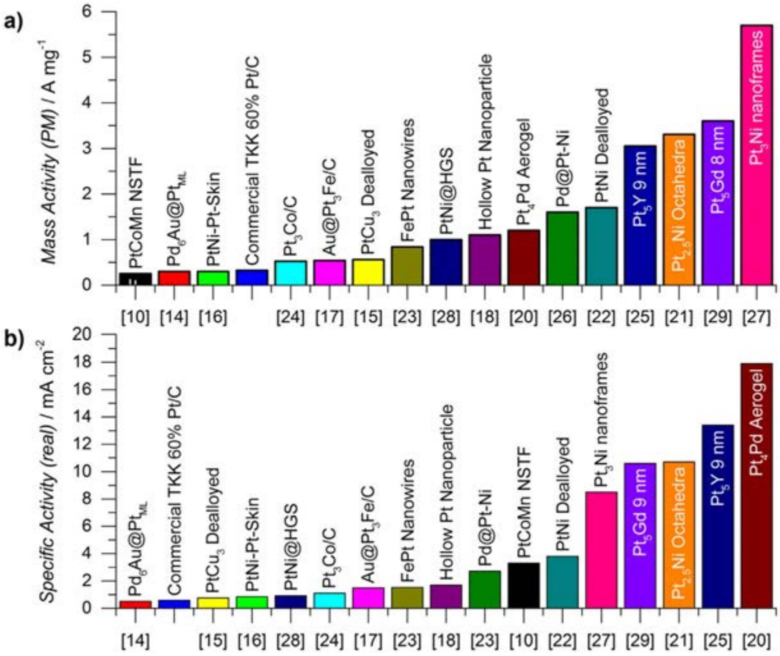

Fig. 1. Showing a) mass activity and b) specific activity at 0.9 V vs RHE for a selection of nanoparticulate catalysts reported in literature. Data adapted from [10,14–18,20–29]. In cases where either the mass activity or specific activity was specified directly at 0.9 V vs RHE it has either been found from digitized data in supporting information found in [20]; converting between mass activity and specific activity using specified electrochemical surface area [21,27]; or in the case of [14,16] using extrapolated data by Baldizzone et al. [28]. Note that the mass activity of $Pd_5Au@Pt_{ML}$ and $Au@Pt_3Fe/C$ have been normalized to Pt mass and not precious metal (PM) like the rest.

exhibit significantly weakened interaction with CO, resulting in lower coverages of CO at the surface of the catalyst [63–66]. In turn, hydrogen can adsorb onto the surface and hence be oxidised. It turns out that Pt–Ru tends to suffer from poor stability: the Ru crosses over to the cathode where it degrades the ORR performance [67–70]. Consequently, there is a need for a catalyst that is both more stable than Pt–Ru and is able to function in 50–100 ppm CO, without the need for air-bleeding. Testing the CO tolerance in a rotating disk electrode (RDE) setup is more appealing for catalyst development, both because the catalyst can be tested without the influence of the other components of the fuel cell, and because the electrode preparation is less complex and more easily reproducible. There are generally two main approaches to evaluate the CO poisoning using RDE experiments: (i) to measure the onset of the hydrogen oxidation reaction (HOR) when the electrode has been poisoned by CO beforehand [52,60], or (ii) to start with a CO-free electrode, hold it at an anode relevant potential and then poison it with CO during HOR [58,59].

Herein, we will assess the effects of different experimental parameters on the activity of commercial Pt/C catalysts, using the thin film rotating disk electrode method [71,72]. We will also show the effect of temperature, scan rate and Ohmic drop correction on flame-annealed polycrystalline Pt electrodes. In addition, we will study the HOR in the presence of CO, evaluating the methods described above, using extended surfaces of smooth polycrystalline Pt, as well as Pt/C and PtRu/C commercial nanoparticulate catalysts. All of the catalyst materials under investigation can be sourced easily from standard suppliers. In our discussion, we will make recommendations for key experimental parameters, with the aim of finding the best compromise between ensuring (a) that the experiments can be performed easily in a reproducible manner, over a relatively short time frame, and (b) that the measurements are relevant for fuel cell operating conditions.

2. Experimental

The experiments were performed in an electrochemical cell using the rotating disk electrode method [36,37,73,74]. All glassware, including the cell, were cleaned prior to experiments. The glassware were cleaned first in piranha (98% H_2SO_4 (Merck, Emsure) and 30% H_2O_2 (Merck, Emsure), 3:1 v/v) for at least 24 h and then cleaned several times in 18.2 MΩ cm Millipore water at 85–90 °C to remove possible traces of the cleaning solution. The electrochemical cell consisted of a working electrode which was mounted on a Pine Instruments rotator, a platinum wire (Chempur 99.9%, 0.5 mm diameter) to act as counter electrode, and an Hg/Hg_2SO_4/K_2SO_4 (0.6 M) reference electrode (Schott Instruments) connected to the cell via a Luggin capillary. The electrolytes, 0.1 M $HClO_4$ and 0.5 M H_2SO_4, were prepared from 70% $HClO_4$ Merck Suprapur and 96% H_2SO_4 Merck Suprapur respectively. The ORR experiments were performed in 0.1 M $HClO_4$ electrolyte whereas the HOR/CO tolerance experiments were performed in both 0.1 M $HClO_4$ and 0.5 M H_2SO_4. The samples; a 5 mm polycrystalline Pt disk, or glassy carbon disk, were mounted in a changeable rotating ring disk (RRDE) tip from Pine Instruments. Two tips were used: a standard one made of Teflon and one made of Polyether ether ketone (PEEK), which has a lower thermal expansion constant than Teflon. The PEEK RRDE tip was used only for the high temperature CO poisoning experiments, together with a gas purged wheel bearing assembly from Pine Instruments to prevent O_2 entering the cell. The electrochemical measurements were performed using a VMP2 multi-channel potentiostat (Bio-Logic Instruments) computer-controlled using EC-Lab software. The gasses used were supplied by AGA with Instrument 5.0 purity for Ar, N_2 and O_2 gasses; Instrument 4.5 for the H_2 gas; Instrument 3.7 for the CO gas; Instrument 100 ppm CO in H_2 gas and Instrument 2% CO in H_2 gas.

2.1. Preparation of Polycrystalline Pt Electrodes

A polished 5 mm polycrystalline 99.99% Pt disk from Pine Instruments was used to carry out the polycrystalline electrode experiments. In order to prepare the disk, the following treatment was performed: it was annealed in a butane flame (using a hand held burner typically used for grilling foods) for 5 minutes; within 1 second of the flame being removed, the disk was covered with a glass vessel, through which a stream of Ar was flown. After 3 minutes in this reducing atmosphere, by which time the electrode would have reached room temperature, the Pt electrode surface was then covered with a droplet of ultrapure water (18.2 MΩ cm), saturated with H_2. The disk was then placed face down on a piece of polypropylene film [75] from Chemplex; the film was cleaned beforehand by sonicating it in several washes of ultrapure water. The disk was subsequently mounted from the film onto a changeable Teflon RRDE tip from Pine Instruments. The prepared electrode was inserted into the electrolyte under potential control at 0.05 V vs reversible hydrogen electrode (RHE). The electrode was then cycled in a nitrogen-saturated 0.1 M $HClO_4$ solution from 0.05 to 1.0 V vs the RHE at 50 mV s^{-1} until the CV was stable, typically after 10–20 cycles.

2.2. Preparation of Carbon Supported Nanoparticle Electrodes

Three commercial carbon-supported catalysts were chosen for carrying out the ORR and the CO-tolerance benchmarking analyses: TEC10F60TPM from Tanaka Kikinzoku Kogyo (TKK) (Pt/C, average particle size 2.9 nm with a 58.2% wt. Pt loading); HiSPEC 13100 from Johnson Matthey (JM) (Pt/C, average particle size 4.6 nm with a 70% wt. Pt loading; and HiSPEC 10100 from JM (PtRu/C, average particle size 2.8 nm with 40% wt. Pt and 20% wt. Ru loading). The particle size and catalyst loading are as specified by the supplier. The electrodes was prepared similar to ref. [5,37,38] by ultrasonic dispersing catalyst into an ink consisting of mainly water and absolute ethanol (99.8%, Fluka, puriss. p.a., ACS Reagent), but also small amounts of polyvinylpyrrolidone (PVP) from Sigma–Aldrich was added to help disperse the nanoparticles in the ink and Nafion® perfluorinated resin solution (Sigma–Aldrich, 5% wt.% in mixture of lower aliphatic alcohols and water) was added to improve adhesion to the glassy carbon. The exact composition must be optimized for each catalyst. Nonetheless, in general we used 1:4 water to ethanol weight ratio for the Pt/C catalysts and 1:8 water to ethanol weight ratio for the PtRu/C catalyst. Each ink had the following composition: 4 mg catalyst, 7.5 mg PVP (2% in ethanol) and 20 mg Nafion solution. The concentration of catalyst in the ink corresponded to a loading of 14–30 (Pt) μg cm^{-2} on the glassy carbon when depositing 10 μL of ink. The glassy carbon disks were polished beforehand using Buehler MicroPolish™ 0.05 μm alumina particles on a Buehler MicroCloth PSA and then ultra-sonicated twice in both isopropanol and deionized water. The electrodes were prepared by first mounting the polished and cleaned glassy carbon disk in the tip, and then drop casting the ink on a glassy carbon disk, while measuring the mass of the droplet to accurately calculate the Pt mass on the electrode. We tried different procedures for depositing and drying the catalyst ink on the glassy carbon, including covering the as-prepared electrode with a glass beaker; rotating the electrodes [38]; and a mild heat treatment at 40–45 °C in air. The quality of the films was evaluated on the basis of (a) the visual criteria specified by Garsany et al. [37] (Fig. 2 in their paper); (b) by comparing the electrochemical active surface area (ECSA) determined from CO stripping to the ECSA specified by the supplier of

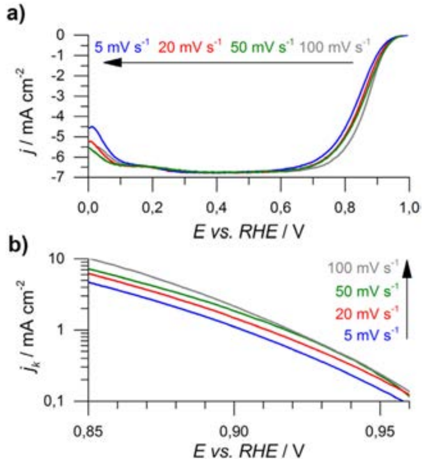

Fig. 2. a) Cyclic voltammogram in O_2-saturated 0.1 M $HClO_4$ at 23 °C on polycrystalline Pt, 1600 rpm at different scan speeds. b) Kinetic current density for the ORR for polycrystalline Pt measured in O_2 saturated 0.1 M HClO4 at 23 °C, 1600 rpm and different scan speeds. Only the anodic cycle has been plotted.

the catalyst; (c) finally from the CV in O_2, where we ensured that the film would reach the diffusion limited current density plateaux at 0.7 V vs RHE [37]. In our own experience, the rotation method resulted in the best films on the Teflon RDE tips [38]. In contrast, on the PEEK tips, it was challenging to confine the inks within the area of the disk, due to the lower hydrophobicity compared to the Teflon tip; consequently for the PEEK tips we used the stationary drop cast method. The as-prepared electrodes were cleaned with ultrapure water before being inserted into the electrolyte under potential control. Before the ORR and the H_2/CO oxidation experiments, the electrodes were pre-conditioned by cycling in N_2 at 100 mV/s until the CV was stable. For Pt/C catalysts, the potential never exceeded 1 V vs RHE to minimize corrosion of the support and roughening the surface [76] and for PtRu/C, it never exceeded 0.8 V vs RHE, to avoid dissolution or irreversible oxidation of Ru atoms [77,78].

2.3. RDE Measurements

Experiments were performed at both room temperature, i.e. 23 °C, and at 60 °C. Although fuel cells are often operated as high as 90 °C, [4] the maximum temperature we use in our experiments is 60 °C to avoid problems with electrolyte evaporation, as the vapour pressure of water increases drastically above this temperature [72]. The temperature of the electrochemical cell was controlled using a heated water jacket. For each experiment, the Ohmic resistance and RHE potential were measured at both temperatures. The Ohmic resistance was determined from the fitted high-frequency intercept measured using electrochemical impedance spectroscopy [79]. The measured Ohmic resistance in 0.1 M $HClO_4$ ranged from 24–33 Ω at 23 °C, and from 17 to 22 Ω at 60 °C. The measured Ohmic resistance in 0.5 M H_2SO_4 ranged from 7 to 8 Ω at 23 °C and from 4 to 5 Ω at 60 °C. The Ohmic drop compensation was done by either online Ohmic drop correction or in the post treatment of the data. In case of the online Ohmic drop correction, 85% correction was applied resulting in a residual uncompensated contribution of $<5\,\Omega$. The RHE potential was measured by bubbling H_2 over the Pt electrode in the electrolyte at 1600 rpm and measuring the mean of the intersection value whilst voltametrically cycling the electrode from −0.02 to 0.3 V vs RHE at 20 mV/s. In 0.1 M $HClO_4$, 0 V RHE ranged from −0.725 to −0.717 V at 23 °C and from −0.711 to −0.704 V at 60 °C, with respect to the Hg/Hg_2SO_4 reference electrode.

ORR measurements were performed by bubbling O_2 in the cell, while cycling between 0.0 and 1.0 V vs RHE at different scan rates, namely 5, 20, 50 and 100 mV s^{-1}, until a stable limiting current was obtained. In the case of the nanoparticulate catalysts, a CV was also recorded in N_2 using the same parameters to enable the subtraction of background capacitive currents at a later point.

The electrochemical active surface area (ECSA) was determined by the electrooxidation of a CO adlayer. CO was adsorbed on the surface by bubbling CO in the cell for 3–5 min, while holding the electrode at 0.05 V vs. RHE. Afterwards, the electrolyte was purged with Ar for 15 minutes while maintaining potential control. Finally the potential was scanned anodically between 0.05 V and 1.0 V vs RHE at 10 mV/s. The integral of the stripping peak was converted to electrode area using the value, 420 $\mu C/cm^2$ [80] which we chosen for the sake of consistency with our earlier works [25,29,81], although the exact value is somewhat arbitrary, as it could easily vary by up to 40%. We implicitly assume that the coverage of *CO is independent of surface structure and alloying. However, it turns out that *CO and *H coverage depends on both alloying and surface orientation [11,82–85]; in particular, on alloys the ECSA might be artificially lowered for alloys by this effect.

CO poisoning experiments were performed by bubbling a CO/H_2 mixture gas (either 100 ppm or 2% CO in pure H_2) in the cell. All CO poisoning experiments were performed at 60 °C while rotating at 2500 rpm. Prior to each experiment, the surface was pre-conditioned by first cycling at 100 mV s^{-1} between 0 and 0.8 V vs RHE for 21 cycles and then the potential was held at 0.8 V vs RHE for 30 s to electro-oxidize the CO adsorbed on the surface. After this pre-treatment, the experiments were carried out. We chose to study the CO poisoning behaviour of the Pt-based catalysts by performing two different types of experiments, namely potential staircase and cyclic voltammetry. In the case of the potential staircase experiments, this was accomplished by holding the potential at 0.1 V vs RHE while bubbling with the CO containing H_2 gas. The duration of poisoning at 0.1 V depends on the concentration of CO in the gas. For the 100 ppm CO, the potential was held for 30 min in the case of the polycrystalline Pt disk, and for at least one hour for the nanoparticulate catalysts. The long deposition time for the 100 ppm CO mixture is due to transport limitation of gaseous species in RDE in combination with only a very small fraction (100 ppm) of the gaseous species reaching the electrode are CO. Using the 2% CO, a constant time of 15 min was used for all of the samples. After the initial poisoning at 0.1 V, the potential was stepped by 0.05 V for 5 min at each step up to 0.8 V vs RHE. For the CO poisoning cyclic voltammetry measurements, first the surface was pre-treated as described earlier and then the potential was held at 0.1 V vs RHE for 5 min while bubbling the CO-containing gas. The potential was then cycled up to 0.8 V vs RHE at 1 mV s^{-1}.

3. Results and discussion

3.1. Oxygen Reduction Reaction

3.1.1. Oxygen Reduction Reaction on Polycrystalline Pt

Polycrystalline Pt provides a useful benchmark of oxygen reduction activity. It is often used as an activity reference for model surfaces [36,86,87]. It is simpler to prepare than a single crystal surface, but at the same time, its low roughness factor means that it is more sensitive to the presence of impurities than thin films of Pt/C. The attainment of the benchmark activity value of oxygen reduction on polycrystalline Pt is a clear sign that the cell and the electrolyte are clean, and that the electrochemical methods have been performed appropriately. Even so, the specific activity of

Table 2

–Shows the mean values for the specific activity and mass activity for ORR measured at 0.9 V vs RHE, at 1600 rpm, from the anodic sweep. The average was calculated from at least 2 measurements, and the error bars correspond to the standard deviation. All data have been corrected for both Ohmic drop resistance and capacitive currents.

Material	Temperature	Specific Activity (mA/cm^2) at				Mass Activity (A/mg$_{Pt}$) at			
		5 mV/s	20 mV/s	50 mV/S	100 mV/s	5 mV/s	20 mV/s	50 mV/s	100 mV/s
Pt Poly									
	23 °C	1.2 ± 0.2	1.7 ± 0.2	1.9 ± 0.2	2.1 ± 0.3				
	60 °C			2.0 ± 0.2					
TKK 60% Pt/C									
	23 °C	0.4 ± 0.02	0.51 ± 0.02	0.58 ± 0.01	0.61 ± 0.01	0.22 ± 0.01	0.28 ± 0.01	0.32 ± 0.01	0.34 ± 0.02
	60 °C			0.73 ± 0.02				0.41 ± 0.02	
HiSPEC 13100 Pt/C		0.26 ± 0.02	0.32 ± 0.02	0.35 ± 0.02	0.36 ± 0.03	0.16 ± 0.01	0.19 ± 0.01	0.21 ± 0.01	0.22 ± 0.02

polycrystalline Pt is dependent on both the correct preparation (in particular the annealing) of the surface and a number of experimental parameters such as scan rate, Ohmic drop correction etc. All ORR experiments have been performed in 0.1 M $HClO_4$, since perchlorate anions weakly adsorb, if at all on Pt surfaces. In contrast, in H_2SO_4 based electrolytes, sulphate anions adsorb strongly on the surface and interfere with the ORR [88–90]. For polycrystalline Pt in 0.05 M H_2SO_4 the activity is lowered by a factor of four compared to in 0.1 M $HClO_4$ [87] (Table 2).

The cyclic voltammograms in O_2 on polycrystalline Pt is shown on Fig. 2a for different scan speeds. The data shown have been corrected using Eq. (1) where $E_{WE\ vs\ REF}$ is the measured potential, E_{RHE} the measured potential of the reversible hydrogen electrode, I is the current and R is the Ohmic drop resistance.

$$E_{WE,Corrected} = E_{WEvsREF} - E_{RHE} - IR \tag{1}$$

From the voltammogram in oxygen, it is possible to compare extended surfaces with similar roughness and diffusion limited current density, j_d. However, a more universal comparison can be made from calculating the kinetic current density, j_k, by applying the mass-transport correction using the relation shown in Eq. (2) [91]. For rough surfaces and nanoparticulate catalysts, the current should be normalized to the active surface area instead of the geometric area. The polycrystalline Pt disk used in this experiment have been polished before experiments, as described above, and CO stripping experiments showed slightly lower stripping charge density 349 ± 9 μC/cm^2 than what reported in the literature [36,82,92], which suggest the surface is not rough. The data for the Pt disk have been normalized using the geometric area.

$$\frac{1}{j_k} = \frac{1}{j} - \frac{1}{j_d} \tag{2}$$

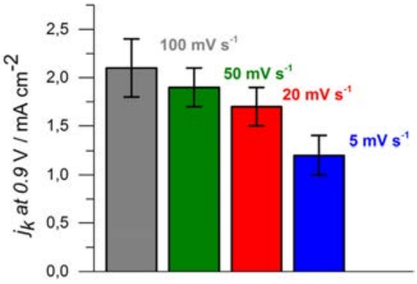

Fig. 3. Average kinetic current density based on four measurements for the ORR measured on polycrystalline Pt at 0.9 V vs RHE, at 1600 rpm, 23 °C and at different scan speeds. The error bars shows the standard deviation.

In the literature, there here is a large spread in used scan rate: 5 mV/s [5,15,22], 10 mV/s [18,20,21], 20 mV/s [5,8,11,12,27,36], 50 mV/s [19,25,87], 100 mV/s [93]. This makes it difficult to compare both data from different papers and to compare RDE experiments with fuel cell performance. Fig. 2b shows the kinetic current density for one experiment at different scan rates. The j values have been corrected by mass-transport effects, electrolyte resistance [94], converted to the RHE scale and normalized to the geometric surface area. Clearly, the specific activity increases with increasing scan rate. It is unclear whether this is due to sometime dependent reconstruction of the surface, possibly related to the adsorption of OH, O and other reaction intermediates, or due to contamination of the surface from impurities [5].

At low scan rates, the CV's in N_2 and O_2 become less reproducible and donot stabilize when the concentration of contamination in the electrolyte is high [5]. For the ORR activity reported here, with only the anodic cycle shown (by convention in these type of studies, the data are taken from the anodic cycle [72], although similar trends would be observed from the cathodic cycle). The mean values for the catalytic activity reported in Fig. 3 are in agreement with the literature [87], for experiments performed under the same nominal experimental conditions.

The effect of temperature was also measured by raising the temperature in the electrochemical cell to 60 °C, and calibrated using the RHE potential and Ohmic drop resistance as these changes with temperature. The resulting ORR activity can be seen on Table 2. The average activity increases but is still within the error of the measurement performed at 23 °C, in agreement with Vliet et al. experiments [94]. Notably, Gasteiger and co-workers reported similar observations [5] when measuring the ORR on Pt-based catalysts in a fuel cell; at a constant cell *iR*-free potential on the RHE scale, the catalytic activity remains almost constant.

3.1.2. Oxygen Reduction on Pt/C Nanoparticles

For practical fuel cells applications, the mass activity of Pt nanoparticles on high surface area support is more important than the specific activity. To obtain a benchmark for Pt/C, two commercial catalysts were chosen: TEC10F60TPM, a 60% wt. Pt/C from Tanaka Kikinzoku Kogyo (TKK) and HiSPEC 13100, a 70% wt. Pt/C from Johnson Matthey. The specific activity and mass activity for the TKK 60% Pt/C are shown in Fig. 4a and b, respectively. The activity is shown without corrections (grey columns), with online Ohmic drop correction (red column) and with both Ohmic drop and capacitance corrections (blue column). The difference in average activity between the background subtracted column and the others increases with scan speeds, due to the capacitive contribution to the current density $j_{DL} = C_{DL} dE/dt$ which increases linearly with scan rate dE/dT and depends on the double layer capacitance C_{DL} [91]. At 5 mV s^{-1}, the background subtraction only changes the activity by 5%; for such low scan speeds the subtraction is not necessary, as reported by Gasteiger et al. [5]. At higher scan rates, such as 50 50 mV s^{-1} the background

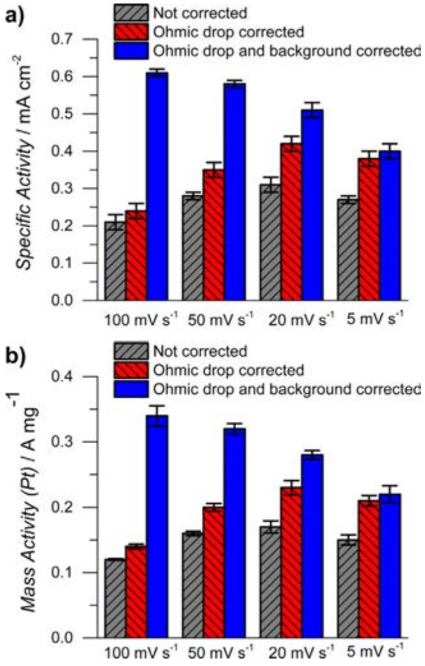

Fig. 4. a) specific and b) mass activity for TKK 60% Pt/C measured in O_2 saturated 0.1 M $HClO_4$ at 23 °C, 1600 rpm and different scan speeds. The different colours indicate different data treatment: First column (grey) have been normalized by ECSA or Pt mass; second column (red) same normalization plus the measurement was performed with 85% online Ohmic drop correction; third column (blue) have in addition been background corrected by subtracting the N_2 CV.

subtraction increases the activity by ~60%, and hence is more significant [87]. Comparing the trend in Figs. 3 and 4, only the background subtracted column increases with scan rates as seen for the polycrystalline Pt disk in Fig. 3 and thus the background subtraction is significant for higher scan rates including at 50 mV/s. An implicit assumption in the background correction is that the capacitive currents in the absence of O_2 are identical to those in the presence of O_2. Impedance spectroscopy measurements performed at our laboratory on Pt-based single crystals confirm this notion: there are only minor changes in the presence of O_2 [95,96].

Fig. 4 shows that the mean value of the activity is up to 40% higher with Ohmic drop correction. The mean values of the activity, calculated with Ohmic drop correction and background subtraction are listed in Table 2. The TKK 60% wt. Pt/C catalyst was also tested at 60 °C and 50 mV/s; the specific activity was 0.73 ± 0.02 mA/cm^2 compared to 0.58 ± 0.01 mA/cm^2 at 23 °C. This corresponds to a 26% increase in activity; it is more significant than for polycrystalline Pt, where the activity difference was within the error. Comparing to the ORR activities reported by Mayrhofer et al. [36] at 0.9 V vs RHE, the trend is the same where the activity increases with temperature.

Gasteiger et al. [5] also showed that the activity measured using the RDE method at low scan rates of 5 or 20 mV/s and at 60 °C, are within a factor 2 of the ones measured for the MEA in the fuel cell. The activity difference observed between 23 °C and 60 °C are negligible in comparison to the difference between RDE measurements and MEA measurements. Therefore, we conjecture that the RDE measurements performed at room temperature and below 20 mV/s are comparable to MEA measurements. However, from a practical perspective, by carrying out the measurements at 50 mV/s, it takes a shorter time to reach a stable electrochemical response. Moreover, model experiments, such as those performed on single crystals, mass selected nanoparticles or polycrystalline extended surfaces, are usually conducted at 50 mV/s [11,90,97–99]. The reason for this is that the electrolyte will always contain some contaminants; the low electrode surface area/electrolyte ratio in model experiments increases the propensity for the contamination of the electrode. Consequently, we take the view that the measurement should ideally be performed at 23 °C, using a scan rate of 50 mV/s; during the data processing we first apply an Ohmic drop correction, if online Ohmic drop compensation was not used, and then perform a background subtraction.

3.2. Hydrogen Oxidation Reaction and CO tolerance

3.2.1. Hydrogen Oxidation Reaction

The cyclic voltammogram in H_2 on a polycrystalline Pt disk is shown in Fig. 5a. The experiment was performed at 60 °C, because the limiting current is temperature dependent [100] as well as the CO poisoning [52] and to be able to compare to literature data [52,100]. The reaction was measured at different rotations speeds (400, 900, 1600, 2500 and 3600 rpm) in both 0.1 M $HClO_4$ (black lines) and 0.5 M H_2SO_4 (dashed red lines). The dotted line is data adapted from [100] which was measured using the same experimental parameters as the solid red line. Fig. 5b shows a Levich plot using the data from Fig. 5a measured at 0.2 V vs RHE in both 0.1 M $HClO_4$ (black points) and 0.5 M H_2SO_4 (red points). The dashed lines in Fig. 5b shows a linear fit to the data points. To verify

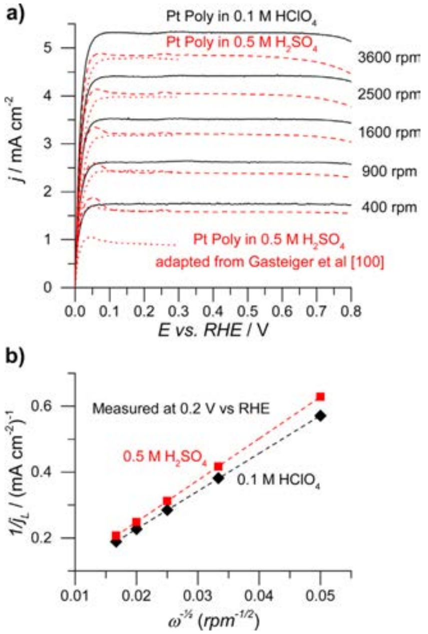

Fig. 5. –a) Hydrogen oxidation reaction on a polycrystalline Pt disk (anodic sweep) at 60 °C, 20 mV/s for different rotations speeds, in either 0.1 M $HClO_4$ (black solid line) or 0.5 M H_2SO_4 (red dashed line). The dotted line is data adapted from [100]. b) Levich plot using the limiting current measured at 0.2 V vs RHE using the data from a). The dashed lines shows a linear regression on the data points.

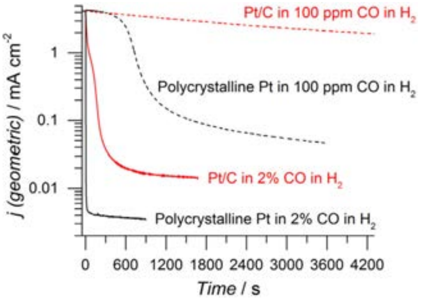

Fig. 6. –Geometric current density measured at 0.1 V vs. RHE for a polycrystalline Pt disk and a TKK 60% Pt/C catalyst at 60 °C and 2500 rpm in 0.1 M $HClO_4$, saturated with either 100 ppm CO in H_2 or 2% CO in H_2.

that the correct limiting current was obtained, the Levich equation [91] was used:

$$i_d = 0.62nFD^{2/3}\nu^{-1/6}c_0\omega^{1/2} = Bc_0\omega^{1/2} \tag{3}$$

In Eq. (3) n is the number of electrons in the process, F is the faraday constant, D is the diffusion constant, ν is the viscosity of the electrolyte, c_0 is the solubility of H_2 in the electrolyte and ω is the rotation speed and B is a constant. From the slope of the Levich plot in Fig. 5, we determined the Bc_0 to for 0.5 M H_2SO_4 to be 7.9×10^{-2} mA cm^{-2} rpm$^{-1/2}$ and for 0.1$HClO_4$ it was 8.7×10^{-2} mA cm^{-2} rpm$^{-1/2}$ .Our data correspond closely to those of Gasteiger for 0.5 M H_2SO_4 at 62 °C, [100] both in terms of the Bc_0 constant and by the fact that the data overlap each other on Fig. 5.

Measurements of the hydrogen oxidation reaction activity on Pt are not possible when using a rotating disk setup in liquid electrolyte because of mass transport resistance, which will lead to an underestimation of the catalytic activity by 1–2 orders of magnitude [44–47]. However, introducing even trace amounts of CO causes a decrease in catalytic activity, and hence a large shift in potential, or overpotential for the HOR, at any given current density, in comparison to pure H_2. This decrease in activity can also be measured using the RDE method. In this study, we focus on the HOR on Pt and Pt–Ru catalysts during CO poisoning conditions.

3.2.2. CO Poisoning on Polycrystalline electrodes

Platinum is the most active pure-metal catalyst for the HOR. However, concentrations as low as 10 ppm CO in the H_2 gas can severely degrade the performance of the fuel cell [4,48,49]. We recommend that the poisoning procedure be benchmarked both on pure Pt and a commercial Pt–Ru catalyst. Although pure Pt based catalysts would not be used in real fuel cells running on CO–H_2 gas mixtures, they provide an useful benchmark for the measurement procedure: should the pure Pt based catalysts exhibit higher than expected CO-tolerance, this would constitute a clear sign that the measurement was not being performed adequately (this could be induced by high amounts of O_2 in the cell). For real applications, the concentration in the fuel feed might be as high as 50–100 ppm [4]. At the outset, we tried to measure H_2 oxidation in the presence of 100 ppm CO. However, the poisoning process was impractically slow. This is shown clearly in Fig. 6, which is a chronoamperometric plot for a smooth polycrystalline Pt disk and a Pt/C nanoparticulate catalyst, at 0.1 V vs RHE, whilst bubbling either 100 ppm or 2% of CO in H_2 in the cell. The electrode was pre-conditioned beforehand as explained in Section 2.3. Each of the catalysts starts with a similar geometric current density of ~4.5 mA/cm^2. On polycrystalline Pt, the current density diminishes rapidly to ~0.1 mA/cm^2 after 30 minutes in 100 ppm CO, after which time it decreases somewhat more slowly. On the other hand, even after 1 hour, the Pt/C catalysts still retain a current density of 2.1 mA/cm^2. This can be explained by the low amount of CO molecules that reach the surface. The surface atom density of Pt (111) is ~1.5×10^{15} atom cm^{-2}; the flux of reactants to surface can be approximated by dividing the limiting current density by the charge of 2 electrons as it is a two electron reaction taking place which yield a flux of 1.38×10^{16} reactants cm^{-2} s^{-1}; only 1/10000 molecules are CO in a 100 ppm CO/H_2 mixtures which makes the flux of CO molecules 1.38×10^{12} CO molecules cm^{-2} s^{-1}. We estimate the poisoning time by dividing the surface atom density by the CO molecule flux, yielding ~18.1 min for the polycrystalline Pt disk surface. For the nanoparticles, we estimate a similar number by multiplying the poisoning time for a smooth surface with the roughness factor, i.e. the real surface area divided by the geometric area, 1.74 cm^2/0.196 cm^2; this yields a poisoning time of 2.7 hours. This crude calculation offers an explanation of the slow poisoning observed in Fig. 6; on this basis, we conclude that it is impractical to use 100 ppm CO in H_2 to study CO poisoning. Instead, we recommend the use of 2% CO in H_2 to achieve fast poisoning of both the nanoparticles and the polycrystalline Pt disk.

During the development of the experimental procedure, we observed that repeating the same measurement several times did not yield the same result. For this reason, we developed a pre-treatment for a polycrystalline Pt disk, as represented in Fig. 7. The upper part of the figure shows the applied potential and the lower part shows the resulting measured current density. The pre-treatment involves cycling the electrode 21 times between 0.0 and 0.8 V vs RHE (not shown in the figure) in the gas mixture of 2% CO and H_2, followed by 30 s at 0.8 V vs RHE to oxidize all CO from the surface, at which point the actual measurement commences. From time, t = 0 to 900 s, the potential is held at 0.1 V vs RHE; the potential is then increased in 50 mV increments, with 300 s at each potential. Clearly, the current density drops three orders of magnitude within 30 s, after which time it is changes little. Upon the beginning of each potential step, there is an initial spike in the current which could be artefacts from the potentiostat, double layer charging or H_2/CO oxidation; we define the steady state current density as the value immediately before the following

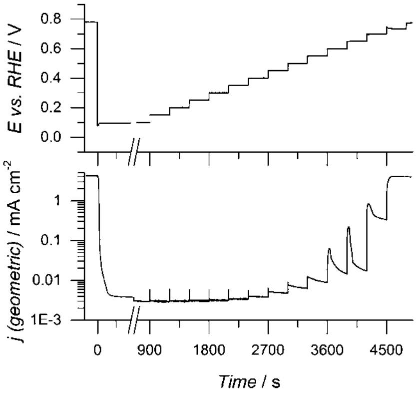

Fig. 7. –The upper part shows the applied potential and the lower part the measured geometric current density on a polycrystalline Pt disk. Before measurement the disk was cycled 21 times between 0 and 0.8 V vs. RHE at 100 mV/s then the potential was held at 0.8 V vs. RHE for 30 s before stepping down to 0.1 V vs RHE for 15 min followed by steps of 50 mV at 5 min intervals. The measurement was performed in 0.1 M $HClO_4$ saturated with 2% CO in H_2 at 60 °C and 2500 rpm.

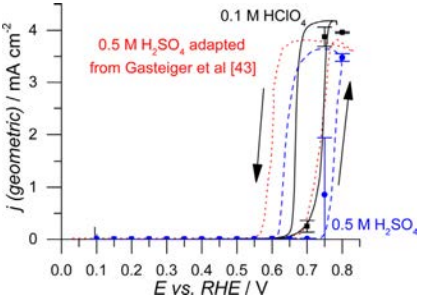

Fig. 8. –H_2–CO electrooxidation on Polycrystalline Pt in 2% CO in H_2 saturated electrolyte either 0.1 M $HClO_4$ (black solid line) or 0.5 M H_2SO_4 (blue dashed line and red dotted line) at 60 °C, 2500 rpm and 1 mV/s after 15 min at 0.1 V vs RHE. The points indicate the average steady-state value from holding the potential 5 min at each of the points. The dotted red line is data adapted from [52].

potential step. There is no significant change in the current density from 0.1 V to 0.55 V vs RHE; however, from 0.55 V onwards, the initial spike is much more pronounced, and there is a slight improvement in the steady state current density over the previous value. However, at 0.7 V vs RHE, the steady state current increases by an order of magnitude. At 0.75 V, the steady state current density is close to the limiting current density.

Fig. 8 shows a combination of the potentiostatic experiment (points showing the steady-state current density from Fig. 7) with cyclic voltammetry of a polycrystalline Pt disk recorded at 1 mV/s after being completely poisoned (15 min). The Figure also shows a digitized CV showing the same experiment by Gasteiger et al. [52]. The difference between the two experiments is that this was performed in 0.1 M $HClO_4$ at 60 °C whereas the other was performed in 0.5 M H_2SO_4 at 62 °C. Although the onset of the oxidation and the anodic going scan are rather similar, the behaviour in the cathodic sweep is different; this may be due to sulphate anion adsorbing strongly on Pt and perchlorate anion adsorbing weakly, if it all [88]. There is also a good relation between the CV recorded at 1 mV/s and the steady-state points, in agreement to previous studies by Gasteiger et al. [52]. The potential required for significant current densities, i.e. >0.1 mA/cm^2, depends on the CO partial pressure, as demonstrated by Gasteiger et al. [52] and Schmidt et al. [101]. Even so, for fuel cell relevant applications, it is more relevant to look at the steady-state current densities at less negative potentials, in particular below 0.2 V. These are plotted in Fig. 9 for the polycrystalline Pt disk in 2% CO in H_2, in either 0.1 M $HClO_4$ (blue) or 0.5 M H_2SO_4 (red) at 60 °C and 2500 rpm. The data used in Fig. 9 are performed under the same condition as Fig. 7. Fig. 9 shows that there is no significant difference in current densities between 0.1 M $HClO_4$ and 0.5 M H_2SO_4. We would like to emphasise that although we tentatively assign the data on Fig. 9 to hydrogen oxidation, the currents are negligible, on the order of the noise level.

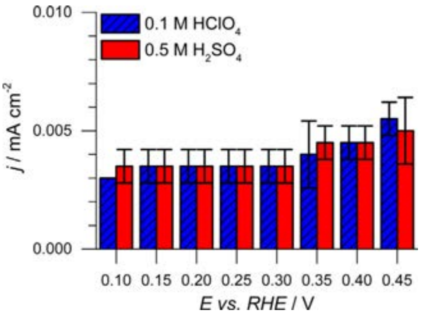

Fig. 9. –Steady-state current densities of polycrystalline Pt disk in 2% CO in H_2 saturated 0.1 M $HClO_4$ (blue) or 0.5 M H_2SO_4 (red) measured at 60 °C and 2500 rpm. The potential was held for 15 min at 0.1 V vs RHE before the first measurement and the potential was then stepped up in 50 mV increments, with 5 minute at each interval. Each measurement is taken immediately before the potential step.

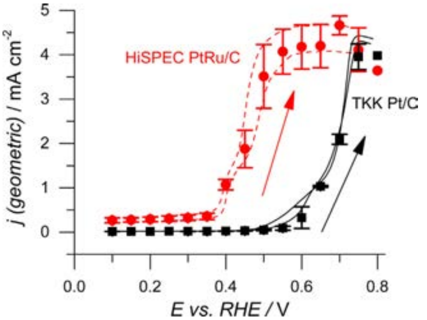

Fig. 10. –CV at 1 mV/s of HiSPEC PtRu/C (red dashed lines) and TKK 60% Pt/C (black solid lines) in 2% CO in H_2 saturated 0.1 M $HClO_4$ at 60 °C and 2500 rpm. The points shows the average steady state current density. The loading was 12 and 13 $\mu g_{Pt}/cm^2$ for Pt/C, and 14 and 18 $\mu g_{Pt}/cm^2$ for PtRu/C. The larger difference in loading is visible for the PtRu/C as there is a clear difference in onset where the sample with higher loading starts earlier.

3.2.3. CO Poisoning on Pt/C and PtRu/C nanoparticles

CO poisoning experiments were also performed on commercially available nanoparticulate Pt/C. The TKK 60% Pt/C catalyst, that yielded the best results for the ORR (see Section 3.1.2), was also benchmarked for CO tolerance. The best CO tolerant commercial catalysts are Pt–Ru alloys, and for this benchmark we chose JM HiSPEC 10100 with a 40% wt. Pt loading. Fig. 10 shows a combination of cyclic voltammetry and steady state current densities for the Pt/C nanoparticles, similar to the experiments described in the previous section for polycrystalline Pt. The experiments were performed in 0.1 M $HClO_4$ saturated with 2% CO in H_2 at 60 °C and 2500 rpm. The solid lines were recorded after holding the potential at 0.1 V vs. RHE for 15 min and the points show the steady-state current after 5 min. The steady state points follow the CV for Pt/C nanoparticles, while for PtRu/C the average steady state current lie in between the two measurements. This shows that both the CV and the steady state measurements yield similar results at low overpotentials, in agreement with the literature [101]. The onset for the rapid post-ignition increase in current density, to values above 0.5 mA/cm^2, occurs at much lower potentials on the PtRu/C catalyst. Indeed the *half-wave* potential, i.e. the potential at half the current density of the limiting current density, is 250–300 mV lower for the PtRu/C compared to the Pt/C. This is consistent to reports for polycrystalline PtRu alloys [52] and also nanoparticulate PtRu/C [53]. The greater magnitude of the error bars on the PtRu/C catalyst can be attributed to the fact that the current density has been normalised to the geometric, rather than microscopic surface area, and the fact that a different loading was used in the two different measurements. The difference is, however, only present when normalizing to geometric area. On the contrary, the error bars are negligible for the PtRu/C in Fig. 11(a) and (b), where the steady state current density has been normalized by either electrochemical surface area (11a) or Pt mass (11b).

The steady state current densities of Pt/C (Fig. 11a) are small, and very close to those of polycrystalline Pt, in Fig. 9. On the other

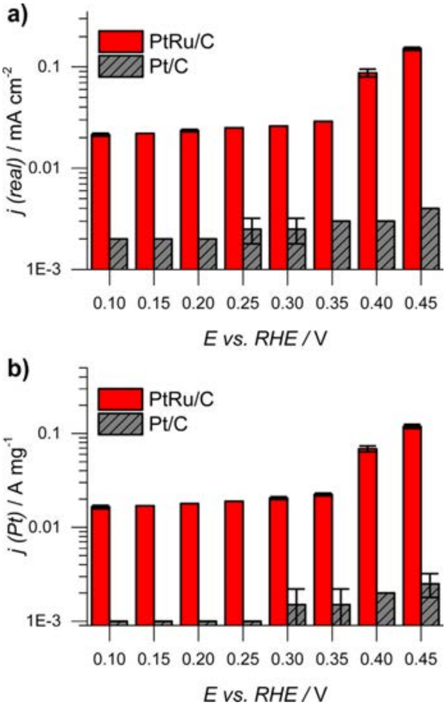

Fig. 11. –Steady state current densities normalized by either CO stripping a) or Pt mass b) for HiSPEC 10100 PtRu/C (red) and TKK 60% Pt/C (grey). The measurement was performed in 2% CO in H_2 saturated 0.1 M $HClO_4$ at 60 °C and 2500 rpm. The potential was held at 0.1 V vs. RHE for 15 min then stepped in 50 mV steps in 5 min intervals. Each measurement was recorded immediately before the next potential step.

hand, at 0.10–0.35 V, PtRu/C shows an order of magnitude higher current density, both in terms of specific activity, as shown on Fig. 11 a, and mass activity, as shown in Fig. 11 b. In the post-ignition region, above 0.45 V, the apparent activity for hydrogen oxidation is highly dependent on the catalyst loading [101]. However, since this region is largely irrelevant for technological applications, we will not peruse upon it any further.

4. Conclusions

In order to compare ORR data it is important that the measurements follow the same experimental procedures. In this study we have shown a benchmark for different commercially available catalysts as well as polycrystalline Pt electrodes measured under different conditions. We observed that there was a small increase in the ORR specific activity 26% for the Pt/C catalyst when increasing the temperature from 23 °C to 60 °C. The same measurement was performed on a polycrystalline Pt electrode but in that case the increase was insignificant compared to the experimental error. It was also shown how Ohmic drop correction, capacitance and scan rate have a major impact on the measured activity. Our recommendation is to correct for Ohmic drop and to measure at either 20 mV s^{-1} or 50 mV s^{-1}.

The experimental conditions for best benchmarking CO poisoning during HOR were also investigated utilizing both cyclic voltammetry, potentiostatic and galvanostatic measurements. We found that potentiostatic poisoning at relevant anode potentials (0.1–0.35 V vs RHE) provides the most optimal conditions for benchmarking the CO tolerance of different electrocatalysts. We showed that there is no significant difference between using 0.5 M H_2SO_4 and 0.1 M $HClO_4$ as electrolyte for CO tolerance experiments. The PtRu/C benchmark exhibits an order of magnitude higher steady state current density for hydrogen oxidation than Pt/C. This method enables rapid catalyst evaluation and will facilitate the future development of new CO-tolerant materials for hydrogen oxidation.

Acknowledgements

We thankfully acknowledge the EU FP7's initiative Fuel Cell and Hydrogen Joint Undertaking's project CathCat (GA 303492), the Danish National Research Foundation's Center for Individual Nanoparticle Functionality (DNRF54) for providing the funding for this research. We also thank the Danish Council for Strategic Research's project NACORR (12-133817) and The Industrial PhD Programme under The Danish Council for Technology and Innovation (DCTI).

References

[1] D.U. Eberle, D.R. von Helmolt, Sustainable transportation based on electric vehicle concepts: a brief overview, Energy Environ. Sci. 3 (2010) 689, doi: http://dx.doi.org/10.1039/c001674h.
[2] U. Eberle, B. Müller, R. von Helmolt, Fuel cell electric vehicles and hydrogen infrastructure: status 2012, Energy Environ. Sci. 5 (2012) 8780, doi:http://dx.doi.org/10.1039/c2ee22596d.
[3] F.T. Wagner, B. Lakshmanan, M.F. Mathias, Electrochemistry and the Future of the Automobile, J. Phys. Chem. Lett. 1 (2010) 2204–2219, doi:http://dx.doi.org/10.1021/jz100553m.
[4] H.A. Gasteiger, J. Garche, Fuel Cells, in: G. Ertl, H. Knözinger, F. Schüth, J. Weitkamp (Eds.), Handb. Heterog. Catal, Wiley-VCH Verlag GmbH & Co. KGaA, Weinheim, Germany, 2008, doi:http://dx.doi.org/10.1002/9783527610044.
[5] H.A. Gasteiger, S.S. Kocha, B. Sompalli, F.T. Wagner, Activity benchmarks and requirements for Pt, Pt-alloy, and non-Pt oxygen reduction catalysts for PEMFCs, Appl. Catal. B Environ. 56 (2005) 9–35, doi:http://dx.doi.org/10.1016/j.apcatb.2004.06.021.
[6] I.E.L. Stephens, A.S. Bondarenko, U. Grønbjerg, J. Rossmeisl, I. Chorkendorff, Understanding the electrocatalysis of oxygen reduction on platinum and its alloys, Energy Environ. Sci. 5 (2012) 6744, doi:http://dx.doi.org/10.1039/c2ee03590a.
[7] A. Rabis, P. Rodriguez, T.J. Schmidt, Electrocatalysis for Polymer Electrolyte Fuel Cells: Recent Achievements and Future Challenges, ACS Catal. 2 (2012) 864–890, doi:http://dx.doi.org/10.1021/cs3000864.
[8] J. Zhang, M.B. Vukmirovic, Y. Xu, M. Mavrikakis, R.R. Adzic, Controlling the catalytic activity of platinum-monolayer electrocatalysts for oxygen reduction with different substrates, Angew. Chem. Int. Ed. Engl. 44 (2005) 2132–2135, doi:http://dx.doi.org/10.1002/anie.200462335.
[9] R.R. Adzic, J. Zhang, K. Sasaki, M.B. Vukmirovic, M. Shao, J.X. Wang, a. U. Nilekar, M. Mavrikakis, J. a. Valerio, F. Uribe, Platinum Monolayer Fuel Cell Electrocatalysts, Top. Catal. 46 (2007) 249–262, doi:http://dx.doi.org/10.1007/s11244-007-9003-x.
[10] A. Bonakdarpour, K. Stevens, G.D. Vernstrom, R. Atanasoski, A.K. Schmoeckel, M.K. Debe, J.R. Dahn, Oxygen reduction activity of Pt and Pt–Mn–Co electrocatalysts sputtered on nano-structured thin film support, Electrochim. Acta 53 (2007) 688–694, doi:http://dx.doi.org/10.1016/j.electacta.2007.07.038.
[11] V.R. Stamenkovic, B. Fowler, B.S. Mun, G. Wang, P.N. Ross, C.A. Lucas, N.M. Marković, Improved Oxygen Reduction Activity on Pt3Ni(111) via Increased Surface Site Availability, Science 80 (2007) 493–497, doi:http://dx.doi.org/10.1126/science.1135941.
[12] J. Greeley, I.E.L. Stephens, A.S. Bondarenko, T.P. Johansson, H.A. Hansen, T.F. Jaramillo, J. Rossmeisl, I. Chorkendorff, J.K. Nørskov, Alloys of platinum and early transition metals as oxygen reduction electrocatalysts, Nat. Chem. 1 (2009) 552–556, doi:http://dx.doi.org/10.1038/nchem.367.
[13] M. Lefèvre, E. Proietti, F. Jaouen, J.-P. Dodelet, Iron-based catalysts with improved oxygen reduction activity in polymer electrolyte fuel cells, Science 324 (2009) 71–74, doi:http://dx.doi.org/10.1126/science.1170051.
[14] K. Sasaki, H. Naohara, Y. Cai, Y.M. Choi, P. Liu, M.B. Vukmirovic, J.X. Wang, R.R. Adzic, Core-protected platinum monolayer shell high-stability electrocatalysts for fuel-cell cathodes, Angew. Chem. Int. Ed. Engl. 49 (2010) 8602–8607, doi:http://dx.doi.org/10.1002/anie.201004287.
[15] P. Strasser, S. Koh, T. Anniyev, J. Greeley, K. More, C. Yu, Z. Liu, S. Kaya, D. Nordlund, H. Ogasawara, M.F. Toney, A. Nilsson, Lattice-strain control of the activity in dealloyed core–shell fuel cell catalysts, Nat. Chem. 2 (2010) 454–460, doi:http://dx.doi.org/10.1038/nchem.623.

[16] C. Wang, M. Chi, D. Li, D. Strmcnik, D. van der Vliet, G. Wang, V. Komanicky, K. Chang, A.P. Paulikas, D. Tripkovic, J. Pearson, K.L. More, N.M. Markovic, V.R. Stamenkovic, Design and synthesis of bimetallic electrocatalyst with multilayered Pt-skin surfaces, J. Am. Chem. Soc. 133 (2011) 14396–14403, doi:http://dx.doi.org/10.1021/ja2047655.

[17] C. Wang, D. van der Vliet, K.L. More, N.J. Zaluzec, S. Peng, S. Sun, H. Daimon, G. Wang, J. Greeley, J. Pearson, A.P. Paulikas, G. Karapetrov, D. Strmcnik, N.M. Markovic, V.R. Stamenkovic, Multimetallic Au/FePt3 nanoparticles as highly durable electrocatalyst, Nano Lett. 11 (2011) 919–926, doi:http://dx.doi.org/10.1021/nl102369k.

[18] J.X. Wang, C. Ma, Y. Choi, D. Su, Y. Zhu, P. Liu, R. Si, M.B. Vukmirovic, Y. Zhang, R.R. Adzic, Kirkendall effect and lattice contraction in nanocatalysts: a new strategy to enhance sustainable activity, J. Am. Chem. Soc. 133 (2011) 13551–13557, doi:http://dx.doi.org/10.1021/ja204518x.

[19] M. Escudero-Escribano, A. Verdaguer-Casadevall, P. Malacrida, U. Grønbjerg, B.P. Knudsen, A.K. Jepsen, J. Rossmeisl, I.E.L. Stephens, I. Chorkendorff, Pt5Gd as a Highly Active and Stable Catalyst for Oxygen Electroreduction, J. Am. Chem. Soc. 134 (2012) 16476–16479, doi:http://dx.doi.org/10.1021/ja306348d.

[20] W. Liu, P. Rodriguez, L. Borchardt, A. Foelske, J. Yuan, A.-K. Herrmann, D. Geiger, Z. Zheng, S. Kaskel, N. Gaponik, R. Kötz, T.J. Schmidt, A. Eychmüller, Bimetallic aerogels: high-performance electrocatalysts for the oxygen reduction reaction, Angew. Chem. Int. Ed. Engl. 52 (2013) 9849–9852, doi: http://dx.doi.org/10.1002/anie.201303109.

[21] S. Choi, S. Xie, M. Shao, J.H. Odell, N. Lu, H. Peng, L. Protsailo, S. Guerrero, J. Park, X. Xia, J. Wang, M.J. Kim, Y. Xia, Synthesis and characterization of 9 nm Pt–Ni octahedra with a record high activity of 3.3 A/mg(Pt) for the oxygen reduction reaction, Nano Lett. 13 (2013) 3420–3425, doi:http://dx.doi.org/10.1021/nl40 1881.

[22] C. Cui, L. Gan, M. Heggen, S. Rudi, P. Strasser, Compositional segregation in shaped Pt alloy nanoparticles and their structural behaviour during electrocatalysis, Nat. Mater. 12 (2013) 1–7, doi:http://dx.doi.org/10.1038/nmat3668.

[23] S. Guo, D. Li, H. Zhu, S. Zhang, N.M. Markovic, V.R. Stamenkovic, S. Sun, FePt and CoPt nanowires as efficient catalysts for the oxygen reduction reaction, Angew. Chem. Int. Ed. Engl. 52 (2013) 3465–3468, doi:http://dx.doi.org/10.1002/anie.201209871.

[24] D. Wang, H.L. Xin, R. Hovden, H. Wang, Y. Yu, D. a Muller, F.J. DiSalvo, H.D. Abruña, Structurally ordered intermetallic platinum–cobalt core–shell nanoparticles with enhanced activity and stability as oxygen reduction electrocatalysts, Nat. Mater. 12 (2013) 81–87, doi:http://dx.doi.org/10.1038/nmat3458.

[25] P. Hernandez-fernandez, F. Masini, D.N. Mccarthy, C.E. Strebel, D. Friebel, D. Deiana, P. Malacrida, A. Nierhoff, A. Bodin, A.M. Wise, J.H. Nielsen, T.W. Hansen, A. Nilsson, I.E.L. Stephens, I. Chorkendorff, Mass-selected nanoparticles of PtxY as model catalysts for oxygen electroreduction, Nat. Chem. (2014) 1–7, doi:http://dx.doi.org/10.1038/nchem.2001.

[26] S.-I. Choi, M. Shao, N. Lu, A. Ruditskiy, H.-C. Peng, J. Park, S. Guerrero, J. Wang, M.J. Kim, Y. Xia, Synthesis and Characterization of Pd@Pt–Ni Core–Shell Octahedra with High Activity toward Oxygen Reduction, ACS Nano 8 (2014) 10363–10371, doi:http://dx.doi.org/10.1021/nn5036894.

[27] C. Chen, Y. Kang, Z. Huo, Z. Zhu, W. Huang, H.L. Xin, J.D. Snyder, D. Li, J. a Herron, M. Mavrikakis, M. Chi, K.L. More, Y. Li, N.M. Markovic, G. a Somorjai, P. Yang, V.R. Stamenkovic, Highly crystalline multimetallic nanoframes with three-dimensional electrocatalytic surfaces, Science 343 (2014) 1339–1343, doi:http://dx.doi.org/10.1126/science.1249061.

[28] C. Baldizzone, S. Mezzavilla, H.W.P. Carvalho, J.C. Meier, A.K. Schuppert, M. Heggen, C. Galeano, J.-D. Grunwaldt, F. Schüth, K.J.J. Mayrhofer, Confined-Space Alloying of Nanoparticles for the Synthesis of Efficient PtNi Fuel–Cell Catalysts, Angew. Chem. Int. Ed. Engl. (2014) 14250–14254, doi:http://dx.doi.org/10.1002/anie.201406812.

[29] A. Velázquez-Palenzuela, F. Masini, A.F. Pedersen, M. Escudero-Escribano, D. Deiana, P. Malacrida, T.W. Hansen, D. Friebel, A. Nilsson, I.E.L. Stephens, I. Chorkendorff, The enhanced activity of mass-selected PtxGd nanoparticles for oxygen electroreduction, J. Catal. (2015) , doi:http://dx.doi.org/10.1016/j.jcat.2014.12.012 accepted.

[30] A. Marcu, G. Toth, R.J. Behm, Electrochemical Test Procedures for Accelerated Evaluation of Fuel Cell Cathode Catalyst Degradation, Fuel Cells 14 (2014) 378–385, doi:http://dx.doi.org/10.1002/fuce.201300138.

[31] B. Han, C.E. Carlton, A. Kongkanand, R.S. Kukreja, B.R. Theobald, L. Gan, R. O'Malley, P. Strasser, F.T. Wagner, Y. Shao-Horn, Record activity and stability of dealloyed bimetallic catalysts for proton exchange membrane fuel cells, Energy Environ Sci. 8 (2015) 258–266, doi:http://dx.doi.org/10.1039/C4EE02144D.

[32] DOE, 3.4 Fuel Cells, in: Fuel Cell Technol. Off. Multi-Year Res. Dev. Demonstr. Plan, 2014.

[33] Johnson Matthey Platinum 2013 Interim Review, 2013.

[34] OICA, 2013 Production statistics, (2014). http://www.oica.net/category/production-statistics/2013-statistics/

[35] L. Dubau, M. Lopez-Haro, L. Castanheira, J. Durst, M. Chatenet, P. Bayle-Guillemaud, L. Guétaz, N. Caqué, E. Rossinot, F. Maillard, Probing the structure, the composition and the ORR activity of Pt3Co/C nanocrystallites during a 3422 PEMFC ageing test, Appl. Catal. B Environ. 142–143 (2013) 801–808, doi:http://dx.doi.org/10.1016/j.apcatb.2013.06.011.

[36] K.J.J. Mayrhofer, D. Strmcnik, B.B. Blizanac, V. Stamenkovic, M. Arenz, N.M. Markovic, Measurement of oxygen reduction activities via the rotating disc electrode method: From Pt model surfaces to carbon-supported high surface area catalysts, Electrochim. Acta 53 (2008) 3181–3188, doi:http://dx.doi.org/10.1016/j.electacta.2007.11.057.

[37] Y. Garsany, O.A. Baturina, K.E. Swider-Lyons, S.S. Kocha, Experimental Methods for Quantifying the Activity of Platinum Electrocatalysts for the Oxygen Reduction Reaction, Anal. Chem. 82 (2010) 6321–6328, doi:http://dx.doi.org/10.1021/ac100306c.

[38] Y. Garsany, I.L. Singer, K.E. Swider-Lyons, Impact of film drying procedures on RDE characterization of Pt/VC electrocatalysts, J. Electroanal. Chem. 662 (2011) 396–406, doi:http://dx.doi.org/10.1016/j.jelechem.2011.09.016.

[39] S. Kocha, Best Practices and Benchmark Activities for ORR Measurements by the Rotating Disk Electrode Technique. 2014 DOE Hydrogen and Fuel Cells Program Review, 2014.

[40] S. Rudi, C. Cui, L. Gan, P. Strasser, Comparative Study of the Electrocatalytically Active Surface Areas (ECSAs) of Pt Alloy Nanoparticles Evaluated by Hupd and CO-stripping voltammetry, Electrocatalysis 5 (2014) 408–418, doi:http://dx.doi.org/10.1007/s12678-014-0205-2.

[41] H. a. Gasteiger, J.E. Panels, S.G. Yan, Dependence of PEM fuel cell performance on catalyst loading, J Power Sources 127 (2004) 127–171, doi:http://dx.doi.org/10.1016/j.jpowsour.2003.09.013.

[42] J.X. Wang, S.R. Brankovic, Y.J.C. Zhu Hanson, R.R. Adžić, Kinetic Characterization of PtRu Fuel Cell Anode Catalysts Made by Spontaneous Pt Deposition on Ru Nanoparticles, J. Electrochem. Soc. 150 (2003) A1108, doi: http://dx.doi.org/10.1149/1.1579481.

[43] S. Chen, A. Kucernak, Electrocatalysis under Conditions of High Mass Transport: Investigation of Hydrogen Oxidation on Single Submicron Pt Particles Supported on Carbon, J. Phys. Chem. B 108 (2004) 13984–13994, doi: http://dx.doi.org/10.1021/jp048641u.

[44] K.C. Neyerlin, W. Gu, J. Jorne, H.A. Gasteiger, Study of the Exchange Current Density for the Hydrogen Oxidation and Evolution Reactions, J. Electrochem. Soc. 154 (2007) B631, doi:http://dx.doi.org/10.1149/1.2733987.

[45] M. Wesselmark, B. Wickman, C. Lagergren, G. Lindbergh, Hydrogen oxidation reaction on thin platinum electrodes in the polymer electrolyte fuel cell, Electrochem. Commun. 12 (2010) 1585–1588, doi:http://dx.doi.org/10.1016/j.elecom.2010.08.037.

[46] C.M. Zalitis, D. Kramer, A.R. Kucernak, Electrocatalytic performance of fuel cell reactions at low catalyst loading and high mass transport, Phys. Chem. Chem. Phys. 15 (2013) 4329–4340, doi:http://dx.doi.org/10.1039/c3cp44431g.

[47] J. Durst, A. Siebel, C. Simon, F. Hasché, J. Herranz, H.a. Gasteiger, New insights into the electrochemical hydrogen oxidation and evolution reaction mechanism, Energy Environ. Sci. 7 (2014) 2255, doi:http://dx.doi.org/10.1039/c4ee00440j.

[48] H.-F. Oetjen, V.M. Schmidt, U. Stimming, F. Trila, Performance Data of a Proton Exchange Membrane Fuel Cell Using H2/CO as Fuel Gas, J. Electrochem. Soc. 143 (1996) 3838, doi:http://dx.doi.org/10.1149/1.1837305.

[49] T.E. Springer, T. Rockward, T.A. Zawodzinski, S. Gottesfeld, Model for Polymer Electrolyte Fuel Cell Operation on Reformate Feed: Effects of CO, H2 Dilution, and High Fuel Utilization, J. Electrochem. Soc. 148 (2001) A11, doi:http://dx.doi.org/10.1149/1.1344516.

[50] S. Gottesfeld, A New Approach to the Problem of Carbon Monoxide Poisoning in Fuel Cells Operating at Low Temperatures, J. Electrochem. Soc. 135 (1988) 2651, doi:http://dx.doi.org/10.1149/1.2095401.

[51] Z. Jusys, R.J. Behm, Simulated Air Bleed Oxidation of Adsorbed CO on Carbon Supported Pt. Part 2. Electrochemical Measurements of Hydrogen Peroxide Formation during O 2 Reduction in a Double-Disk Electrode Dual Thin-Layer Flow Cell, J. Phys. Chem. B 108 (2004) 7893–7901, doi:http://dx.doi.org/10.1021/jp0499171.

[52] H.A. Gasteiger, N.M. Markovic, P.N. Ross, H2 and CO Electrooxidation on Well-Characterized Pt Ru, and Pt–Ru. 2. Rotating Disk Electrode Studies of CO/H2 Mixtures at 62C, J. Phys. Chem. 99 (1995) 16757–16767.

[53] T.J. Schmidt, M. Noeske, H.A. Gasteiger, R.J. Behm, P. Britz, H. Bönnemann, PtRu Alloy Colloids as Precursors for Fuel Cell Catalysts: A combined XPS, AFM, HRTEM, and RDE study, J. Electrochem. Soc. 145 (1998) 925, doi:http://dx.doi.org/10.1149/1.1838368.

[54] P. Liu, a. Logadottir, J.K. Nørskov, Modeling the electro-oxidation of CO and H2/CO on Pt, Ru, PtRu and Pt3Sn, Electrochim. Acta 48 (2003) 3731–3742, doi: http://dx.doi.org/10.1016/S0013-4686(03)538-3.

[55] M. Arenz, V. Stamenkovic, B. Blizanac, K. Mayrhofer, N. Markovic, P. Ross, Carbon-supported Pt–Sn electrocatalysts for the anodic oxidation of H2, CO, and H2/CO mixtures.Part II: The structure–activity relationship, J. Catal. 232 (2005) 402–410, doi:http://dx.doi.org/10.1016/j.jcat.2005.03.022.

[56] B.N. Grgur, N.M. Markovic, P.N. Ross, Electrooxidation of H2, CO, and H2/CO Mixtures on a Well-Characterized Pt70Mo30 Bulk Alloy Electrode, J. Phys. Chem. B 102 (1998) 2494–2501, doi:http://dx.doi.org/10.1021/jp972692s.

[57] B.N. Grgur, N.M. Markovic, P.N. Ross, The Electro-oxidation of H 2 and H 2/CO Mixtures on Carbon-Supported Pt x Mo y Alloy Catalysts, J. Electrochem. Soc. 146 (1999) 1613–1619.

[58] M. Watanabe, New CO-tolerant catalyst concepts, in: Handb. Fuel Cells, 2010: pp. 1–8.

[59] H. Igarashi, T. Fujino, Y. Zhu, H. Uchida, M. Watanabe, CO Tolerance of Pt alloy electrocatalysts for polymer electrolyte fuel cells and the detoxification mechanism, Phys. Chem. Chem. Phys. 3 (2001) 306–314, doi:http://dx.doi.org/10.1039/b007768m.

[60] N.M. Marković, The hydrogen electrode reaction and the electrooxidation of CO and H2/CO mixtures on well-characterized Pt and Pt-bimetallic surfaces,

in: A. Vielstich, H.A. Lamm (Eds.), Handb. Fuel Cells, John Wiley & Sons Ltd., Chichester, UK, 2010, doi:http://dx.doi.org/10.1002/9780470974001.f204027m.

[61] M. Watanabe, S. Motoo, Electrocatalysis by ad-atoms: Part II. Enhancement of the oxidation of methanol on platinum by ruthenium ad-atoms, J. Electroanal. Chem. Interfacial Electrochem. 60 (1975) 267–273, doi:http://dx.doi.org/10.1016/S0022-0728(75)80261-0.

[62] H.A. Gasteiger, N. Markovic, P.N. Ross, E.J. Cairns, CO Electrooxidation on Well-Characterized Pt–Ru Alloys, J. Phys. Chem. 98 (1994) 617–625.

[63] M.T.M. Koper, T.E. Shubina, R.A. van Santen, Periodic Density Functional Study of CO and OH Adsorption on Pt–Ru Alloy Surfaces: Implications for CO Tolerant Fuel Cell Catalysts, J. Phys. Chem. B 106 (2002) 686–692, doi:http://dx.doi.org/10.1021/jp0134188.

[64] T. Iwasita, F.C. Nart, W. Vielstich, An FTIR Study of the Catalytic Activity of a 85:15 Pt:Ru Alloy for Methanol Oxidation, Berichte Der Bunsengesellschaft Für Phys, Chemie 94 (1990) 1030–1034, doi:http://dx.doi.org/10.1002/bbpc.19900940930.

[65] J. McBreen, S. Mukerjee, In Situ X-Ray Absorption Studies of a Pt–Ru Electrocatalyst, J. Electrochem. Soc. 142 (1995) 3399, doi:http://dx.doi.org/10.1149/1.2049993.

[66] J.C. Davies, J. Bonde, Á. Logadóttir, J.K. Nørskov, I. Chorkendorff, The Ligand Effect: CO Desorption from Pt/Ru Catalysts, Fuel Cells 5 (2005) 429–435, doi:http://dx.doi.org/10.1002/fuce.200400076.

[67] P. Piela, C. Eickes, E. Brosha, F. Garzon, P. Zelenay, Ruthenium Crossover in Direct Methanol Fuel Cell with Pt–Ru Black Anode, J. Electrochem. Soc. 151 (2004) A2053, doi:http://dx.doi.org/10.1149/1.1814472.

[68] T.T.H. Cheng, N. Jia, P. He, Characterization of the Degree of Ru Crossover and Its Performance Implications in Polymer Electrolyte Membrane Fuel Cells, J. Electrochem. Soc. 157 (2010) B714, doi:http://dx.doi.org/10.1149/1.3356939.

[69] P. He, T. Cheng, R. Bashyam, A.P. Young, S. Knights, Relative Humidity Effect on Anode Durability in PEMFC Startup/Shutdown Processes, ECS Trans. (2010) 1273–1279, doi:http://dx.doi.org/10.1149/1.3484620.

[70] R. Bashyam, P. He, S. Wessel, S. Knights, Impacts of Cathode Loading on Ru Crossover Related PEFC Durability, ECS Trans. (2011) 837–844, doi:http://dx.doi.org/10.1149/1.3635617.

[71] T.J. Schmidt, H.A. Gasteiger, G.D. Stäb, P.M. Urban, D.M. Kolb, R.J. Behm, Characterization of High-Surface-Area Electrocatalysts Using a Rotating Disk Electrode Configuration, J. Electrochem. Soc. 145 (1998) 2354, doi:http://dx.doi.org/10.1149/1.1838642.

[72] U. Paulus, T. Schmidt, H.A. Gasteiger, R.J. Behm, Oxygen reduction on a high-surface area Pt/Vulcan carbon catalyst: a thin-film rotating ring-disk electrode study, J. Electroanal. Chem. 495 (2001) 134–145, doi:http://dx.doi.org/10.1016/S0022-0728(00)00407-1.

[73] T.J. Schmidt, H.A. Gasteiger, Rotating thin-film method for supported catalysts, in: W. Vielstich, A. Lamm, H.A. Gasteiger, H. Yokokawa (Eds.), Handb. Fuel Cells, John Wiley & Sons, Ltd., Chichester, UK, 2010, doi:http://dx.doi.org/10.1002/9780470974001.f203024.

[74] N. Markovic, Kinetics of Oxygen Reduction on Pt(hkl) Electrodes: Implications for the Crystallite Size Effect with Supported Pt Electrocatalysts, J. Electrochem. Soc. 144 (1997) 1591, doi:http://dx.doi.org/10.1149/1.1837646.

[75] N.M. Markovic, H.A. Gasteiger, P.N. Ross, Oxygen Reduction on Platinum Low-Index Single-Crystal Surfaces in Sulfuric Acid Solution: Rotating Ring-Pt(hkl) Disk Studies, J. Phys. Chem. 99 (1995) 3411–3415, doi:http://dx.doi.org/10.1021/j100011a001.

[76] A. Zana, J. Speder, N.E. a. Reeler, T. Vosch, M. Arenz, Investigating the corrosion of high surface area carbons during start/stop fuel cell conditions: A Raman study, Electrochim. Acta 114 (2013) 455–461, doi:http://dx.doi.org/10.1016/j.electacta.2013.10.097.

[77] A. Rose, E.M. Crabb, Y. Qian, M.K. Ravikumar, P.P. Wells, R.J.K. Wiltshire, J. Yao, R. Bilsborrow, F. Mosselmans, A.E. Russell, Potential dependence of segregation and surface alloy formation of a Ru modified carbon supported Pt catalyst, Electrochim. Acta 52 (2007) 5556–5564, doi:http://dx.doi.org/10.1016/j.electacta.2007.02.023.

[78] A. Velázquez-Palenzuela, E. Brillas, C. Arias, F. Centellas, J.A. Garrido, R.M. Rodríguez, P.-L. Cabot, Carbon monoxide and methanol oxidation on potential-modified Pt–Ru/C electrocatalyst for polymer electrolyte fuel cells, J. Power Sources 208 (2012) 306–315, doi:http://dx.doi.org/10.1016/j.jpowsour.2012.02.064.

[79] V. Čolić, J. Tymoczko, A. Maljusch, A. Ganassin, W. Schuhmann, A.S. Bandarenka, Experimental Aspects in Benchmarking of the Electrocatalytic Activity, ChemElectroChem (2014) , doi:http://dx.doi.org/10.1002/celc.201402295.

[80] F. Maillard, E.R. Savinova, U. Stimming, CO monolayer oxidation on Pt nanoparticles: Further insights into the particle size effects, J. Electroanal. Chem. 599 (2007) 221–232, doi:http://dx.doi.org/10.1016/j.jelechem.2006.02.024.

[81] F.J. Perez-Alonso, D.N. McCarthy, A. Nierhoff, P. Hernandez-Fernandez, C. Strebel, I.E.L. Stephens, J.H. Nielsen, I. Chorkendorff, The Effect of Size on the Oxygen Electroreduction Activity of Mass-Selected Platinum Nanoparticles, Angew. Chemie Int. Ed. 51 (2012) 4641–4643, doi:http://dx.doi.org/10.1002/anie.201200586.

[82] D.F. van der Vliet, C. Wang, D. Li, A.P. Paulikas, J. Greeley, R.B. Rankin, D. Strmcnik, D. Tripkovic, N.M. Markovic, V.R. Stamenkovic, Unique electrochemical adsorption properties of Pt-skin surfaces, Angew. Chem. Int. Ed. Engl. 51 (2012) 3139–3142, doi:http://dx.doi.org/10.1002/anie.201107668.

[83] Q.-S. Chen, J. Solla-Gullón, S.-G. Sun, J.M. Feliu, The potential of zero total charge of Pt nanoparticles and polycrystalline electrodes with different surface structure: The role of anion adsorption in fundamental electrocatalysis, Electrochim. Acta 55 (2010) 7982–7994, doi:http://dx.doi.org/10.1016/j.electacta.2010.03.050.

[84] A.S. Bandarenka, A.S. Varela, M. Karamad, F. Calle-Vallejo, L. Bech, F.J. Perez-Alonso, J. Rossmeisl, I.E.L. Stephens, I. Chorkendorff, Design of an Active Site towards Optimal Electrocatalysis: Overlayers, Surface Alloys and Near-Surface Alloys of Cu/Pt(111), Angew. Chemie 124 (2012) 12015–12018, doi:http://dx.doi.org/10.1002/ange.201205314.

[85] M. Watanabe, Y. Zhu, H. Uchida, Oxidation of CO on a Pt–Fe Alloy Electrode Studied by Surface Enhanced Infrared Reflection–Absorption Spectroscopy, J. Phys. Chem. B 104 (2000) 1762–1768, doi:http://dx.doi.org/10.1021/jp993001q.

[86] U.A. Paulus, A. Wokaun, G.G. Scherer, T.J. Schmidt, V. Stamenkovic, N.M. Markovic, P.N. Ross, Oxygen reduction on high surface area Pt-based alloy catalysts in comparison to well defined smooth bulk alloy electrodes, Electrochim. Acta 47 (2002) 3787–3798, doi:http://dx.doi.org/10.1016/S0013-4686(02)00349-3.

[87] M. Nesselberger, S. Ashton, J.C. Meier, I. Katsounaros, K.J.J. Mayrhofer, M. Arenz, The Particle Size Effect on the Oxygen Reduction Reaction Activity of Pt Catalysts: Influence of Electrolyte and Relation to Single Crystal Models, J. Am. Chem. Soc. 133 (2011) 17428–17433, doi:http://dx.doi.org/10.1021/ja207016u.

[88] J.X. Wang, N.M. Markovic, R.R. Adzic, Kinetic Analysis of Oxygen Reduction on Pt(111) in Acid Solutions: Intrinsic Kinetic Parameters and Anion Adsorption Effects, J. Phys. Chem. B 108 (2004) 4127–4133, doi:http://dx.doi.org/10.1021/jp037593v.

[89] U.A. Paulus, T.J. Schmidt, H.A. Gasteiger, Poisons for the O2 reduction reaction, in: Handb. Fuel Cells, (2010).

[90] D. Strmcnik, M. Escudero-Escribano, K. Kodama, V.R. Stamenkovic, A. Cuesta, N.M. Marković, Enhanced electrocatalysis of the oxygen reduction reaction based on patterning of platinum surfaces with cyanide, Nat. Chem. 2 (2010) 880–885, doi:http://dx.doi.org/10.1038/nchem.771.

[91] A.J. Bard, L.R. Faulkner, Electrochemical Methods: Fundamentals and Applications, second ed., John Wiley & Sons Ltd., 2001.

[92] A. Cuesta, A. Couto, A. Rincón, M.C. Pérez, A. López-Cudero, C. Gutiérrez, Potential dependence of the saturation CO coverage of Pt electrodes: The origin of the pre-peak in CO-stripping voltammograms. Part 3: Pt(poly), J. Electroanal. Chem. 586 (2006) 184–195, doi:http://dx.doi.org/10.1016/j.jelechem.2005.10.006.

[93] M. Nesselberger, M. Roefzaad, R. Fayçal Hamou, P. Ulrich Biedermann, F.F. Schweinberger, S. Kunz, K. Schloegl, G.K.H. Wiberg, S. Ashton, U. Heiz, K.J.J. Mayrhofer, M. Arenz, The effect of particle proximity on the oxygen reduction rate of size-selected platinum clusters, Nat. Mater. 12 (2013) 1–6, doi:http://dx.doi.org/10.1038/nmat3712.

[94] D. van der Vliet, D.S. Strmcnik, C. Wang, V.R. Stamenkovic, N.M. Markovic, M.T.M. Koper, On the importance of correcting for the uncompensated Ohmic resistance in model experiments of the Oxygen Reduction Reaction, J. Electroanal. Chem. 647 (2010) 29–34, doi:http://dx.doi.org/10.1016/j.jelechem.2010.05.016.

[95] A.S. Bondarenko, I.E.L. Stephens, L. Bech, I. Chorkendorff, Probing adsorption phenomena on a single crystal Pt-alloy surface under oxygen reduction reaction conditions, Electrochim. Acta 82 (2012) 517–523, doi:http://dx.doi.org/10.1016/j.electacta.2012.02.095.

[96] A.S. Bondarenko, I.E.L. Stephens, H.A. Hansen, F.J. Pe'rez-Alonso, V. Tripkovic, T.P. Johansson, J. Rossmeisl, J.K. Nørskov, I. Chorkendorff, The Pt(111)/Electrolyte Interface under Oxygen Reduction Reaction Conditions: An Electrochemical Impedance Spectroscopy Study, Langmuir 27 (2011) 2058–2066, doi:http://dx.doi.org/10.1021/la1042475.

[97] S. Kunz, K. Hartl, M. Nesselberger, F.F. Schweinberger, G. Kwon, M. Hanzlik, K.J.J. Mayrhofer, U. Heiz, M. Arenz, Size-selected clusters as heterogeneous model catalysts under applied reaction conditions, Phys. Chem. Chem. Phys. 12 (2010) 10288–10291, doi:http://dx.doi.org/10.1039/c0cp00288g.

[98] I.E.L. Stephens, A.S. Bondarenko, F.J. Perez-Alonso, F. Calle-Vallejo, L. Bech, T.P. Johansson, A.K. Jepsen, R. Frydendal, B.P. Knudsen, J. Rossmeisl, I. Chorkendorff, Tuning the Activity of Pt(111) for Oxygen Electroreduction by Subsurface Alloying, J. Am. Chem. Soc. 133 (2011) 5485–5491, doi:http://dx.doi.org/10.1021/ja111690g.

[99] A. Kuzume, E. Herrero, J.M. Feliu, Oxygen reduction on stepped platinum surfaces in acidic media, J. Electroanal. Chem. 599 (2007) 333–343, doi:http://dx.doi.org/10.1016/j.jelechem.2006.05.006.

[100] H.A. Gasteiger, N.M. Markovic, P.N. Ross, H2 and CO Electrooxidation on Well-Characterized Pt Ru, and Pt–Ru. 1. Rotating Disk Studies of the Pure Gases Including Temperature Effects, J. Phys. Chem. 99 (1995) 8290–8301.

[101] T.J. Schmidt, H.A. Gasteiger, R.J. Behm, Rotating Disk Electrode Measurements on the CO Tolerance of a High-Surface Area Pt/Vulcan Carbon Fuel Cell Catalyst, J. Electrochem. Soc. 146 (1999) 1296, doi:http://dx.doi.org/10.1149/1.1391761.

C

Appendix C - Paper 2 abstract

Probing the nanoscale structure of the catalytically active overlayer on Pt alloys with rare earths

Anders F. Pedersen[a,*], Elisabeth T. Ulrikkeholm[a,*], María Escudero-Escribano[a,b], Tobias P. Johansson[a], Paolo Malacridaa, Christoffer M. Pedersen[a], Martin H. Hansen[c], Kim D. Jensen[a], Jan Rossmeisl[c], Daniel Friebel[d], Anders Nilsson[d], Ib Chorkendorff[a], Ifan E. L. Stephens[a,e**]

[a]Department of Physics, Center for Individual Nanoparticle Functionality, Building 312, Technical University of Denmark, 2800 Lyngby, Denmark

[b]Department of Chemical Engineering, Shriram Center, 443 Via Ortega, Stanford University, Stanford, CA 94305, USA

[c]Department of Chemistry, Univeristy of Copenhagen, Universitetsparken 5, 2100, Copenhagen, Denmark

[d]SLAC National Accelerator Laboratory, 2575 Sand Hill Road, MS31, Menlo Park, CA 94025, USA

[e]Massachusetts Institute of Technology, Department of Mechanical Engineering, 77 Massachusetts Avenue, Cambridge, MA 02139 USA

[*]These authors contributed equally to this work.

[**]Corresponding author.

Email address: ifan@fysik.dtu.dk (Ifan E. L. Stephens)

Pt_xY and Pt_xGd exhibit exceptionally high activity for oxygen reduction, both in the polycrystalline form and the nanoparticulate form. In order to understand the origin of the enhanced activity of these alloys, we have investigated thin films of these alloys on bulk Pt(111) crystals, i.e. Y/Pt(111) and Gd/Pt(111). These surfaces exhibit a 4-fold improvement over Pt(111). We observe the formation of a thick Pt overlayer after the electrochemical measurements, both on Y/Pt(111) and Gd/Pt(111). Using surface sensitive X-ray diffraction we revealed that crystalline closely packed Pt overlayers were formed. The diffraction experiments showed that the strain and crystallinity of the overlayers are strongly dependent on the electrochemical treatment, and in general show lateral compression.

D

Appendix D - Paper 3 abstract

Relating direct methanol fuel cell performance to measurements in a liquid half cell

Christoffer M. Pedersen[a,b], Elisa A. Paoli[a], Oskar Tynelius[a], Torsten Lund-Olesen[a], Jan H. Hales[a,b], Leif H. Christensen[a], Ifan E. L. Stephens[b], Ib Chorkendorff[b]
[a]Department of Physics, Center for Individual Nanoparticle Functionality, Building 312, Technical University of Denmark, 2800 Lyngby, Center for Nano- and Micro technology, Danish Technological Institute (DTI), Gregersenvej, DK-2630 Taastrup, Denmark
[b]Center for Individual Nanoparticle Functionality, Department of Physics, Building 312, Technical University of Denmark (DTU), DK-2800 Lyngby, Denmark

In this study we try to establish how liquid half-cell measurements of catalysts for a Direct Methanol Fuel Cell (DMFC) should be performed in order to achieve comparable measurements to that performed in a DMFC. To accomplish this, DMFC measurements are compared to liquid half-cell experiments. The potential of the anode and cathode electrodes in the DMFC is measured to establish the operating potentials of the DMFC electrodes, which is done by using a specially designed DMFC with a reference electrode. The potential measurements are used to calculate the activity of the catalyst in the electrodes. In addition, measurements of liquid half-cell experiments using both the rotating disk electrode (RDE) and high loading catalyst electrodes on gas diffusion layers are performed to compare the catalyst activity in the different experiments. It is seen that the activity of the methanol oxidation reaction (MOR) in the anode is comparable in all three types of experiments. Contrary, the oxygen reduction reaction (ORR) activity depends on the type of experiment, especially in the case where methanol is present. RDE measurements of methanol poisoning of ORR shows both, a much larger activity loss compared to the DMFC measurements, and that the RDE experiments are more sensitive to the experimental conditions than for the DMFC. The measurements shows that the MOR activity in the DMFC can be predicted from liquid half-cell experiments, whereas RDE measurements of ORR in the presence of methanol does not show the real impact in a DMFC, but rather can be used for qualitative comparison of catalyst under the exact same experimental conditions.